Ice Crystal Icing in Gas Turbine Engines

Jonathan Connolly

Wolfson College

University of Oxford

A thesis submitted for the degree of

Doctor of Philosophy

Trinity 2021

Acknowledgements

I would first like to thank my primary and secondary supervisors, Prof. Matthew McGilvray and Prof. David Gillespie, who have been the best supervisors that I could have asked for. David's endless pool of knowledge coupled with his outrageous, witty comments meant that no meeting was ever a dull affair. Matt's vast experimental experience ensured the success of many experimental campaigns, helped along the way with his ability to magic up a brewski at the most needed moments.

Thanks to the members of the Engine Environmental Protection team at Rolls-Royce, most notably to Rory Clarkson, Geoff Jones and Carol Rance. Their industrial insights and project management ensured that the work kept relevant to the real-world problems.

The staff at the NRC are thanked for their flexibility for our last minute changes, ensuring that all experiments met their target goals.

My friends at the Oxford Thermofluids Institute have provided not only technical support, but most crucially the ability to break off from work and enjoy our time as researchers. Our experiences at conferences and experiments around the world have been one of the highlights of my time as a PhD student. Special thanks to Alex Bucknell for the support in getting me up to speed on the world of ice crystals, and enjoying a beer (or ten). Also to Liam Parker for being there as a mutual venting wall as we transformed ICICLE into its current form, and to Chiara Falsetti with whom I regularly ran away from our stresses in the lab.

Many people outside of the lab have also helped me through the past three years. To Suria, who has been a great friend, and now I am proud to call my partner - she has given me enormous support and I look forward to our many years head. Thanks to my friends from Wolfson, most notably to Thomas Walshe, Ryan Walker, Grigore Gafencu and Andrew "Lego Man" Hyslop, who have kept me sane during the busy schedule Oxford imposes on all of us. My highlights have been the college balls, "Marlborough College" lockdown formals, and our exposure to new and exciting drinks (timișoreana and perrytini) over the soothing sounds of manele. Finally to my friends from OUTriC for our times training, racing and evenings at the pub.

Finally I would like to thank my family for their continued support throughout my whole education which has allowed me to reach this milestone. My Mum and Dad have always been there for me, in providing food for my endless hunger and editing my many; gramatical errors. Finally, thanks to my sister, Sarah, for setting benchmarks for me to strive for.

Abstract

Numerous turbofan power loss events have occurred in high altitude locations in the presence of ice crystals. Ice crystals enter the engine core, partially melt in the compressor and then accrete onto components that are initially warmer than freezing. The ice accretion causes blockage of the flow path, and if it later sheds can damage downstream components and potentially cause flame-out alongside other issues.

Numerical models are currently required for the design and certification of next-generation engines to fly within ice crystal icing conditions. They have successfully predicted ice growth on simplistic geometries, but are often fine-tuned to a single condition or geometry due to the high level of empiricism.

In this thesis a review of the current literature is presented, areas of missing research are indicated, some of which form the basis of the PhD. First, a new method for spatially resolving the three-dimensional ice accretion profile was developed and tested in an ice crystal icing wind tunnel. Historical measurement techniques were either two dimensional or could only be applied after the accretion had formed. This new technique provides transient, three-dimensional, non-intrusive measurement of the accretion during the ice exposure. Such measurements are deemed essential for the development of complex three-dimensional ice accretion models.

The second set of work was the development of the ice crystal icing numerical model, ICICLE. The most notable development was the inclusion of the ability to update the flowfield based on the numerically predicted accretion profile. This change in geometry alters the potential field, leading to changes in the predicted particle trajectories and resultant accretion. The new capabilities of the code were tested using two test pieces: a single compressor stator, and a triple NACA airfoil linear cascade. The results showed that certain conditions require the update of the flowfield for accurate estimation of both the shape and volume of the accretion.

Contents

List of Figures

List of Tables

Symbols

A	Position of laser reflection on clean surface	-
$A_{p,\perp}$	particle area projected normal to the flow	m
A_p	surface area of particle	m^2
B	Position of laser reflection on iced surface	-
b	Equivalent position of laser reflection on iced surface, as observed by the camera	-
c	diameter of a circle of confusion	m
C	critical yield stress coefficient	-
C_D	drag coefficient	-
c	specific heat capacity	$J\,K^{-1}\,g^{-1}$
C_p	Pressure coefficient	-
D	lens aperture diameter	m
d_{eq}	particle equivalent diameter	m
D_{obst}	characteristic length of the obstacle in the flowfield	m
d_p	particle diameter	m
$D_{v,nn}$	diameter where nn% of the population lies below this value	m
E	particle aspect ratio	-
e	coefficient of restitution	-
E^*	equivalent elastic modulus	Pa
F	position on clean surface which is vertically below the laser reflection point on the iced surface	-
f	lens f focal length	m
$\mathbf{F_D}$	drag force vector	N
$\mathbf{g}$	acceleration due to gravity	$m\,s^{-2}$
G_c	critical energy release rate	$J\,m^{-1}$
h_p	heat transfer coefficient of particle	$W\,m^{-1}\,K^{-2}$
h_{film}	water film thickness	m
I	camera focal point	-
k_w	thermal conductivity of water	$W\,m^{-1}\,K^{-1}$
K_c	fracture toughness	$Pa\,m^{1/2}$
$\mathcal{L}$	kinetic energy to surface energy ratio	-
L	laser focal point	-
$\dot{m}_e$	mass flux of water evaporated off the test piece	$kg\,s^{-1}$
$\dot{m}_i$	mass flux of ice stuck to test piece	$kg\,s^{-1}$
$\dot{m}_{run}$	mass flux of water runback on the test piece	$kg\,s^{-1}$
$\dot{m}_w$	mass flux of water stuck to test piece	$kg\,s^{-1}$
m_p	particle mass	kg
N	lens f-number	m

n	body surface normal axis direction	m
O	camera optical center	-
q_{conv}	energy loss per unit area due to convection	$\mathrm{W\,m^{-2}}$
q_{evap}	energy loss per unit area due to evaporation	$\mathrm{W\,m^{-2}}$
q_f	energy gain per unit area due to latent heat of fusion of ice	$\mathrm{W\,m^{-2}}$
q_{freeze}	energy gain per unit area from the test piece heater	$\mathrm{W\,m^{-2}}$
q_{kin}	energy gain per unit area due to kinetic energy transfer of impacting particles	$\mathrm{W\,m^{-2}}$
Q_{loss}	energy loss due to heat losses in the test piece	W
$q_{radiation}$	energy loss per unit area due to radiation	$\mathrm{W\,m^{-2}}$
$q_{sens,imp}$	energy loss per unit area due to sensible heat of impinging particles	$\mathrm{W\,m^{-2}}$
$q_{sens,run}$	energy loss per unit area due to sensible heat of run-back water	$\mathrm{W\,m^{-2}}$
Re_p	particle Reynolds number	-
t	time	s
T_a	air temperature	K
T_p	particle temperature	K
$T_{wb,0}$	total wet bulb temperature	K
U_{attr}	maximum velocity at which only minor breakup occurs	$\mathrm{m\,s^{-1}}$
U_{crack}	critical velocity above which particle breakup occurs	$\mathrm{m\,s^{-1}}$
U_f	distance of a far object from the camera lens	m
U_n	distance of a near object from the camera lens	m
U_y	critical velocity above which particle yields at the contact region	$\mathrm{m\,s^{-1}}$
V_f	distance of a far object image plane from the camera lens	m
V_n	distance of a near object image plane from the camera lens	m
$\mathbf{v_a}$	air velocity vector	$\mathrm{m\,s^{-1}}$
$\mathbf{v_p}$	particle velocity vector	$\mathrm{m\,s^{-1}}$
v_{pn}	particle normal velocity	$\mathrm{m\,s^{-1}}$
λ	Minimum vertical height of the laser or camera relative to the projection plane in the DIP system	m
μ_a	air dynamic viscosity	$\mathrm{kg\,m^{-3}}$
μ_w	water dynamic viscosity	$\mathrm{kg\,m^{-3}}$
ρ_a	air density	$\mathrm{kg\,m^{-3}}$
ρ_p	particle density	$\mathrm{kg\,m^{-3}}$
ρ_w	water density	$\mathrm{kg\,m^{-3}}$
τ_f	characteristic time of the flow	s
τ_p	characteristic time of a particle	s

τ_{wall}	wall shear stress	Pa
σ_y	yield stress	Pa
α	empirical coefficient for Hauks critical crack velocity model	$m^{5/3}\,s^{-1}$
β	empirical coefficient for Hauks critical crack velocity model	$m^{3/2}\,s^{-1}$
e_σ	surface energy per unit area	$J\,m^{-1}$
η	Horizontal separation of laser and camera in the DIP system	m
η_{net}	net sticking efficiency	-
θ	water film temperature	K

Acronyms

AIWT Altitude Icing Wind Tunnel

CFD Computational Fluid Dynamics

DIP Digital Image Projection

DOE Diffractive Optical Element

EMM-C Extended Messinger Model - Crystals

FEA Finite Element Analysis

GE General Electric

HAIC/HIWC High Altitude Ice Crystals / High Ice Water Content

HTC Heat Transfer Coefficient

ICI ice crystal icing

IWC Ice Water Content

LPC Low-Pressure Compressor

LWC Liquid Water Content

MIR Mid Infrared

MMD Median Mass Diameter

MR Melt Ratio

MVD Median Volume Diameter

NACA National Advisory Committee for Aeronautics

NRC National Research Council, Canada

OEM Original Equipment Manufacturer

OGV Outlet Guide Vane

ONERA Office National d'Etudes et de Recherches Aérospatiales

OTI Oxford Thermofluids Institute

PID Proportional Integral Derivative

PIV Particle Image Velocimetry

PSD Particle Size Distribution

PSL Propulsion Systems Laboratory

RANS Reynolds-averaged Navier–Stokes

RATFac Research Altitude Test Facility

RH Relative Humidity

SF Scaling Factor

SLD Supercooled Large Droplet

SLW Supercooled Liquid Water

SND Swan Neck Duct

TWC Total Water Content

URANS Unsteady Reynolds-averaged Navier–Stokes

USQ University of Southern Queensland

1 Introduction

Contents

1.1 Research Motivation

Numerous ice crystal icing induced power loss events (>60) have occurred on turbofan engines since the 1990s [1] which has led to the need for a greater understanding of the ice crystal icing mechanisms and proposal of new legislation's [2, 3].

Ice crystals are formed in deep convective clouds, which have strong updraft cores. Moisture is transported to altitude, creating regions of high ice crystal concentrations. This is typically found in the warm, mid-latitude regions, such as in Southeastern Asia [4], as shown in Figure 1.1. This is especially problematic with the recent growth of aviation within this region. Due to the crystals low reflectivity, high concentrations of ice crystals can go undetected by radar systems, posing additional threat to aircraft safety [1, 5–7].

A schematic of an modern engine architecture is shown in Figure 1.2, where the key engine regions which affect or are effected by engine ice crystal icing are

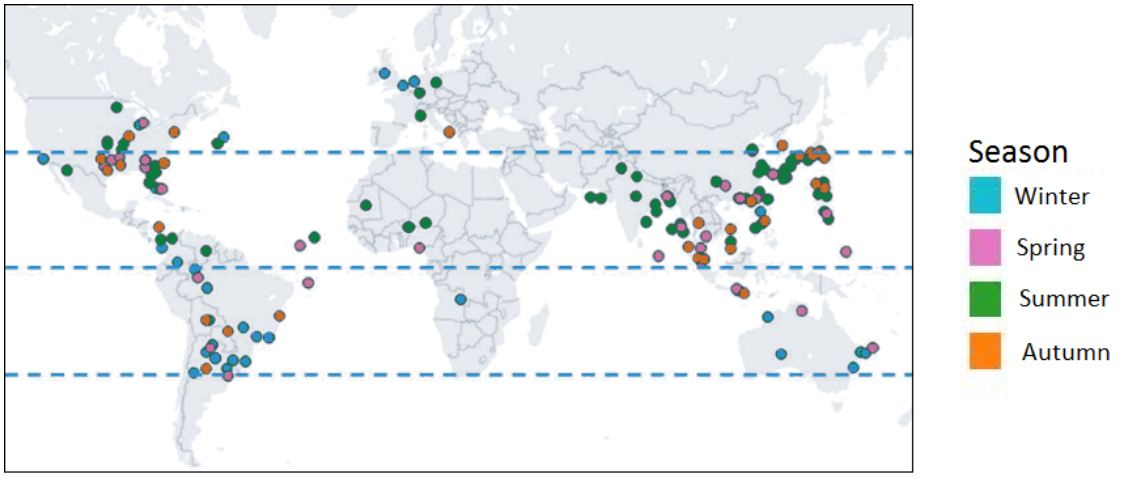

Figure 1.1: Map of Boeing ice crystal icing encounters [8].

indicated. In the atmosphere the crystals are near stationary and isothermal at $\sim$ -40°C. Ice crystals ingest into the nacelle/intake where particles may obtain heat from anti-icing elements (used for supercooled liquid droplet icing, where icing occurs on sub-freezing components). At the fan the particles bounce or shatter upon impact to a blade, depending on the particle size/shape, relative speed and impingement angle. No particle sticking occurs on the fan due to the component sub-freezing temperature. The fan also centrifuges the particles, meaning that some enter the core flow path and the rest are spun out into the bypass. Downstream of the fan, heat transfer from the warm air in the compressor causes the ice crystals to partially melt, increasing the liquid water content of the crystal. Impingement of the partially melted particles onto warm components in the intermediate compressor creates a water film. Successive impact and adhesion of crystals onto the film cools component surface temperatures until the film freezes, creating a mechanical link between the ice and component [9]. Mason et al. [1] theorised that once surface temperatures are sub-freezing, partially melted (mixed-phase) crystals accrete onto the layer of ice on the surface. Therefore ice crystals accrete where the surfaces are initially warmer than freezing, compared to supercooled liquid which can only accrete on sub-freezing components. A summary of the key ice crystal icing physics in each section of the engine is shown in Table 1.1.

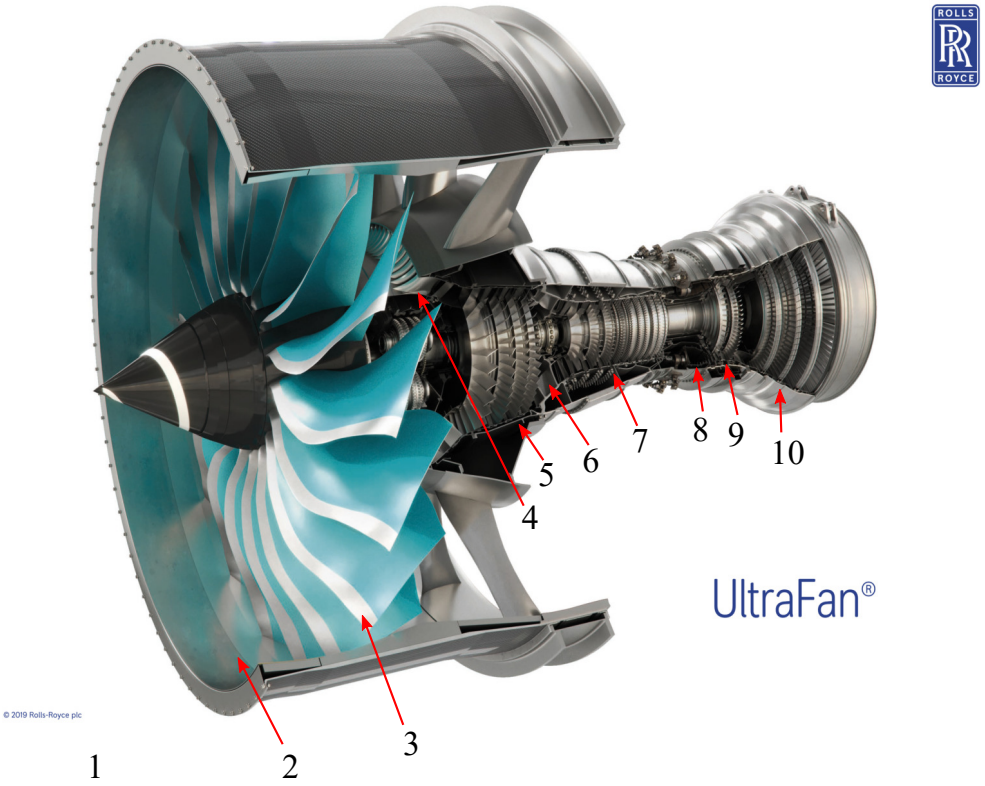

1 - atmosphere
2 - intake
3 - fan
4 - core inlet
5 - intermediate compressor (IPC)
6 - swan neck duct (SND)
7 - high pressure compressor (HPC)
8 - combustor
9 - low pressure turbine (LPT)
10- high pressure turbine (HPT)

Figure 1.2: Architecture of modern geared turbofan engine (UltraFan). Base image taken from [10].

Table 1.1: Ice crystal particle interaction in the atmosphere and with a jet engine. IPC = intermediate pressure compressor.

Region	Crystal state	Surface interaction	Surface heat transfer	Particle slip	Air heat transfer
Atmosphere	Frozen	None	None	None	None
Intake	Frozen	Bounce	Negligible	Medium	Negligible
Fan	Frozen	Shatter, bounce	Negligible	Medium	Medium
Core inlet	Low melt	Bounce, slide	With heated surfaces	Medium	Negligible
IPC	Partially melted	Breakup, bounce, slide	Melting and refreezing	High	Evaporation, melting
Swan neck duct	Partially melted	Bounce, slide	Melting and refreezing	Medium	Evaporation

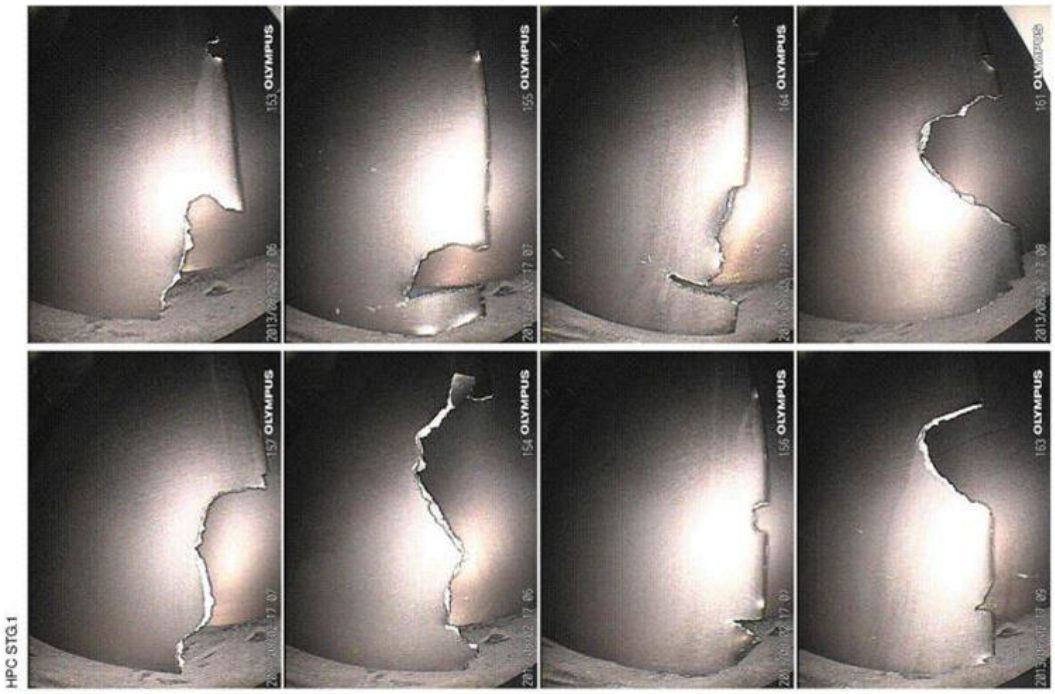

Figure 1.3: Damage of a General Electric GEnx high pressure rotor one blade row. Image taken from [11].

The build-up of ice can cause a range of issues such as significant passage blockage in small engines, loss of thrust, stall and shedding which can cause damage to downstream components and flame out. A documented damage of a high pressure compressor rotor (stage one) blade row occurred to a General Electric (GE) GEnx engine. An AirBridge Cargo 747-8 aircraft was cruising near Chengdu, China, when ice ingestion and large scale shedding occurred. The damage to the blade row is shown in Figure 1.3. If no damage due to shedding occurs, power can typically be restored to the engine after a reduction in altitude [4].

1.2 Effect of Future Designs

Occurrences of ice crystal icing have increased in recent decades, which are likely to have been caused by changes to the engine architecture in the pursuit of a reduction in the specific fuel consumption. Low-pressure ratio fans, high power gearboxes, slender blades with reduced impact tolerance and high-pressure ratio compressors are thought to be contributing to this effect. In previous designs, a large number of

fan blades would have broken up and centrifuged the crystals into the bypass duct, which is less affected by ice crystals due to its low temperatures. Recent engine designs have reduced fan solidity, allowing more crystals to reach the engine core.

The addition of a gearbox in next-generation engines will lead to reduced fan speed, decreasing the centrifugal force experienced by the crystals and causing more to enter the core. The gearbox will be placed in front of the low-pressure compressor, and due to the high heat fluxes emitted from the gearbox, the hub metal temperature will increase. The increased hub temperature has the potential to partially melt incoming crystals, which will allow ice crystal icing to occur in a region that was not previously considered possible [12].

Increased compressor pressure ratio will reduce the high-pressure compressor blade span. A critical parameter in determining compressor stability is the ratio of accretion to passage volume. Therefore, for the same level of icing, the stall margin of the compressor will reduce.

Pilots generally avoid thunderstorms but on certain occasions they need to penetrate the anvil region pf a cloud due to weather or traffic restrictions [4], and often are unaware that they are in regions of high ice water content, meaning that for robust design of the next-generation engines, the effects of ice ingestion must be minimised.

While the use of intercompressor bleeds has been suggested to capture shed ice, and to heat surfaces to prevent accretion, both options (which are currently used in the GE GEnx) are thought to reduce the overall efficiency [1]. Robust solutions can only be created once a more detailed knowledge of the accretion process is known.

1.3 Research Aims

The focus of this PhD is to further develop a numerical code to predict ice crystal icing, to enhance the design capabilities of new, novel engine architectures. It is hoped that with an improved understanding of the ice crystal icing process that integrated designs will be produced which meet environmental targets, while not risking damage or loss of power from the presence of ice crystals in the atmosphere.

The aim is to enhance the ICICLE code, produced by Oxford Thermofluids Institute [13], which is currently based on physics and empiricism. This code in its previous state could not take into account the change in the flowfield solution due to the changing accretion geometry. One main focus of this work is the implementation of an automated re-meshing and CFD solution process. This will create more accurate predictions of the transient accretion behaviour observed in domains where the accretion has noticeable effects on the flow blockage, which other ice-crystal icing codes are not currently able to produce. If the model can be validated in the future by suitable experimental data, such as a planned full compressor test, it will add industrial value to Rolls-Royce.

To validate the numerical model an accurate method for measuring accretion thickness from experimental data is needed. A novel aspect of the work is the use of new optical imaging methods to measure the three-dimensional accretion profile during the icing tests. The method provides experimental validation data at a greater fidelity than was previously possible.

To summarise, the two key contributions to the field by this work are:

1. Implementation of coupling between accretion geometry and flowfield solution

2. Development and validation of a new optical imaging technique for measurement of 3D ice accretion profiles

Publications

The following papers have been published as a direct result of the work in this thesis:

1. J. Connolly, M. McGilvray, D. Gillespie, A. Bucknell, L. Parker, G. Jones and B. Collier, “Two-Way Flow Coupling in Ice Crystal Icing Simulation” SAE Technical Paper 2019-01-1966, 2019, doi:10.4271/2019-01-1966.

2. J. Connolly, M. McGilvray, D. Gillespie, G. Jones and B. Collier. "Digital Image Projection for 3D Ice Crystal Icing Accretion Measurements" AIAA 2020-2812. AIAA AVIATION 2020 FORUM.

3. J. Connolly, M. Choi, X. Yang, L. Doherty, M. McGilvray, D. Gillespie, B. Collier and G. Jones, "Ice crystal accretion in a combined linear cascade and swan neck duct" AIAA 2020-2828. AIAA AVIATION 2020 FORUM.

Collaboration with colleagues in the particulate research group has also led to the following publication:

1. N. Vadgama, J. Connolly, M. McGilvray, D. Gillespie, “Convergence of Spatially Resolved Particle Deposition” 14th European Conference on Turbomachinery Fluid dynamics & Thermodynamics, ETC2021-65.

2
Literature Review

Contents

2.1 Ice Crystal Icing Physics

2.1.1 Particle Shapes

Ice crystals formed in the atmosphere are inherently non-spherical. International collaboration projects have characterised the conditions within convective storms [7, 14–16]. To gather quantitative data of such atmospheric crystals, a field project - High Altitude Ice Crystals / High Ice Water Content (HAIC/HIWC) was formed, which included atmospheric ice crystal measurements in storm clouds around Darwin, Australia. Two-dimensional images of the crystals were taken using optical array probes and binarised, as shown in Figure 2.1. Maximum diameters were extracted for each particle, and the width was defined as the diameter perpendicular to the maximum diameter. The ratio of these two diameters defined the particle aspect

ratio, which for the data-set shown in Figure 2.1, it was found that the mean particle aspect ratio was 0.55. The data matched the previous observation by Heymsfield *et al.* [17], who found that the smallest crystals are generally spherical, and that larger particles are rimed and form aggregates. From these works, it was concluded that in the storm clouds that the crystals typically had a Median Volume Diameter (MVD) of 50-1,000 µm. The largest of crystals have a ballistic trajectory path, meaning that they have a high likelihood of impacting the fan blade and shattering, whereas the smallest of crystals are centrifuged into the bypass. This means that the core of the engine has a smaller range in particle size distribution compared to the atmosphere.

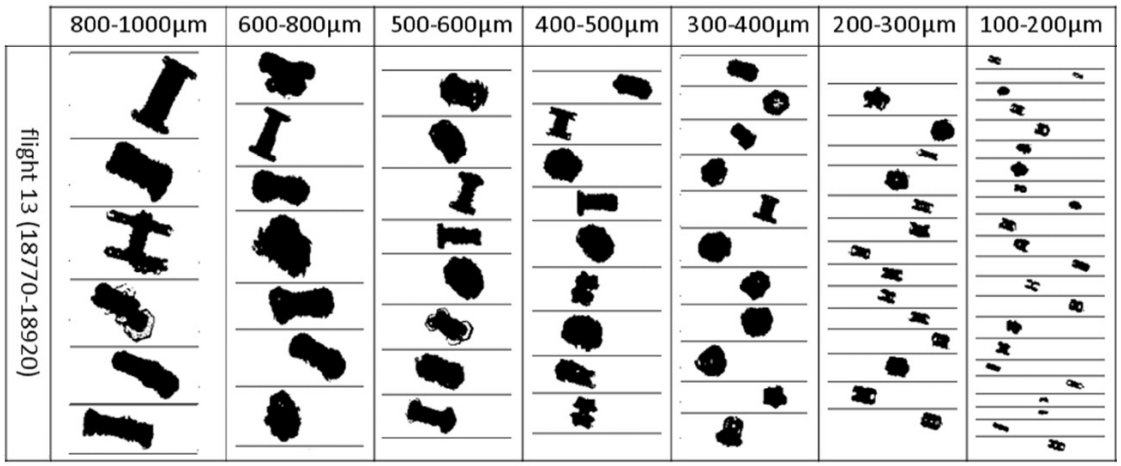

Figure 2.1: Two dimensional images of ice crystals within high ice water content regions, segregated by ice crystal maximum diameter [16].

Numerical analysis of ice crystal trajectories of arbitrary particle shapes such as seen in Figure 2.1 is a numerically intensive task. It is common to approximate the particles as a spheroid, which has a particle aspect ratio (E) of either less than unity (oblate) or greater than unity (prolate) - see Figure 2.2. The particle size can then be defined using the particle equivalent diameter (d_{eq}), which is the diameter that would give a sphere of equal volume to the original particle.

2.1.2 Particle Forces

As a particle traverses through an engine, a range of forces are applied. These forces include drag, gravity, buoyancy, thermophoresis (due to temperature gradients),

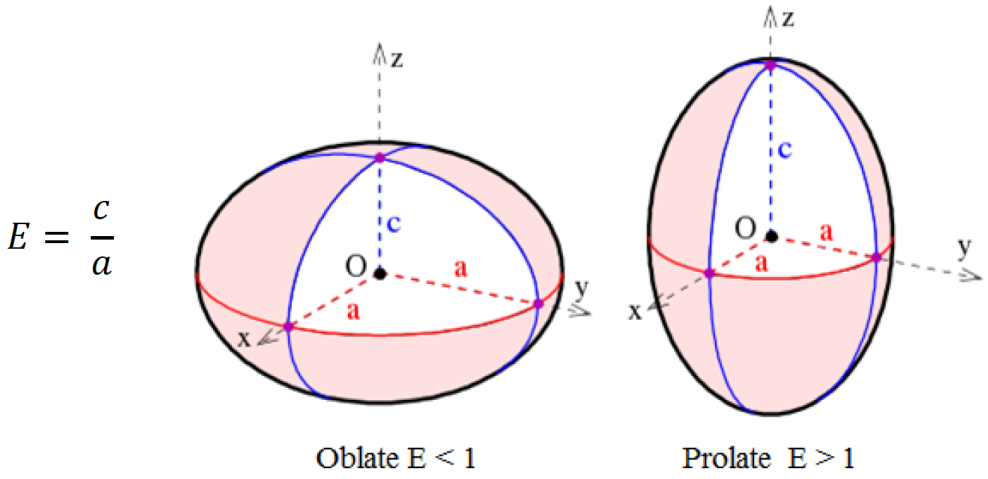

Figure 2.2: Geometry of oblate and prolate spheroids of aspect ratio E [13].

turbophoresis (the tendency of particles to migrate in the direction of decreasing turbulence), Basset force (lagging boundary layer development of accelerating bodies moving through a fluid [18]) Saffman's lift force (due to velocity gradients) and virtual mass force (force required to accelerate the mass of the surrounding fluid phase when the particle accelerates relative to the flow).

The relative magnitude of these applied forces compared to the inertia of the particle determines whether the particle will follow flow streamlines or be inertia dominated (ballistic). This phenomenon is characterised by the non-dimensional group, Stokes number (Stk), defined as the ratio of the characteristic time of a particle (τ_p) to the characteristic time of the flow (τ_f). Assuming Stokes flow (when the particle Reynolds number is less than unity), the Stokes number can be derived for a spherical particle as shown in Equations (2.1) to (2.3), where the symbols are defined as; particle density (ρ_p), air density (ρ_a), particle diameter (d_p), air dynamic viscosity (μ_a), characteristic length of the obstacle in the flowfield (D_{obst}), air velocity vector ($\mathbf{v_a}$). It is generally assumed that particles with a Stokes number of less than unity are streamline following. Buckell *et al.* [13] found that for the typical particle sizes found in an engine (post impact of the cold stages), the particle Stokes numbers were in the range of 1.05-105. This suggested that for the majority of the particles, they will have ballistic trajectories. The result of this (coupled with

the fact that the $\rho_a << \rho_p$), is that all forces apart from drag and gravity can be neglected. This has been further confirmed by Villedieu *et al.* [19].

The largest crystals found in turbofan engines are the most ballistic, meaning that they are more likely to impinge onto cold components in the intake/fan and fracture, reducing the Median Mass Diameter (MMD). The smaller particles are more heavily influenced by the centrifugal forces of the fan, increasing the likelihood of entering the bypass where there are less damaging effects of ice crystal icing.

$$Stk = \frac{\tau_p}{\tau_f} \tag{2.1}$$

$$\tau_p = \frac{\rho_p {d_p}^2}{18\mu_a} \tag{2.2}$$

$$\tau_f = \frac{D_{obst}}{|\mathbf{v_a}|} \tag{2.3}$$

The simplified equation of motion is shown in Equations (2.4) and (2.5), where the symbols are defined as: particle mass (m_p), particle velocity vector ($\mathbf{v_p}$), drag force vector ($\mathbf{F_D}$), acceleration due to gravity ($\mathbf{g}$), drag coefficient (C_D), particle area projected normal to the flow ($A_{p,\perp}$).

$$m_p \frac{d\mathbf{v_p}}{dt} = \mathbf{F_D} + m_p\mathbf{g} \tag{2.4}$$

$$\mathbf{F_D} = \frac{1}{2}\rho_a C_D A_{p,\perp} |\mathbf{v_p} - \mathbf{v_a}| \mathbf{v_p} - \mathbf{v_a} \tag{2.5}$$

The unknown quantity for numerical modelling is the drag coefficient. The assumption that the particles can be approximated as spheroids, allow spheroid drag coefficient correlations to be used. The two main expressions for the drag coefficient used in numerical particulate studies are that of Haider & Levenspiel [20] and Hölzer & Sommerfeld [21]. Haider & Levenspiel's correlation takes into account the particle sphericity and the particle Reynolds number (Equation (2.6)) and is implemented into commercial Computational Fluid Dynamics (CFD) packages such as ANSYS FLUENT. Hölzer & Summerfeld's model is a more recent correlation that

also takes into account the orientation of the particles by considering the particles crosswise sphericity, and is generally considered to be the most accurate model [13].

$$Re_p = \frac{\rho_a |\mathbf{v_p} - \mathbf{v_a}| d_p}{\mu_a} \tag{2.6}$$

2.1.3 Impact Dynamics

Glaciated crystals ingest into the engine and pass through the cool components such as the fan, Outlet Guide Vane (OGV) and early stages of the Low-Pressure Compressor (LPC). In these regions where the component surface temperatures are sub-freezing, the frozen ice crystals do not stick to the surfaces. Upon impact, the particles either rebound as a single entity or shatter and rebound as multiple smaller crystals. The process of particle breakup and plastic losses has a large influence on the particle diameter distribution reaching the LPC and the post-impact trajectory paths.

Four main stages of impact have been defined by Tropea *et al.* [22]. Initial collision first occurs, with a shockwave in the particle and target. Next, elastic deformation of the particle and target occurs. Plastic deformation is present when the local stress is greater than the yield stress, forming a crushed zone near the target surface and a cracked zone where the particle fragments. Finally the fragments/whole particle rebound from the surface. The likelihood of plastic deformation occurring is dependent on the particle size, velocity components, crystal structure and the elastic properties of the substrate.

Hauk *et al.* [23] experimentally studied the impact dynamics of fully glaciated ice crystals on a solid surface. The experiments tested a range of particle sizes and impact velocities, and it was observed that four main fragmentation modes were defined as having: no, minor, major, and catastrophic fragmentation. No fragmentation was defined as a case where the particle rebounded off the surface with no fragments released and no material stuck to the surface. In minor fragmentation the volume of fragments was much smaller than the initial particle, and small levels of rotation occurred after impact. Whereas in major fragmentation, the fragment

sizes were of similar size to the initial particle and significant post-impact rotation occurred. Finally, for catastrophic fragmentation, the particle broke up into a large number of small fragments. These are summarised in Figure 2.3.

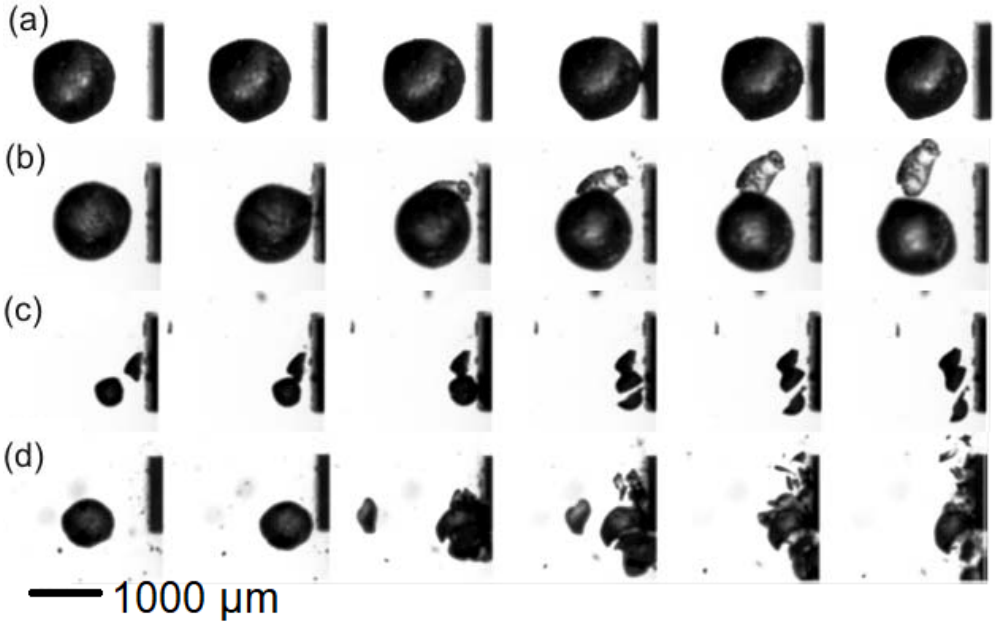

Figure 2.3: Fragmentation modes of ice crystals impacting onto a plate; (a) no fragmentation, (b) minor fragmentation, (c) major fragmentation, (d) catastrophic fragmentation [22].

Vargas *et al.* [24] conducted an experimental study on the impact of spherical ice particles onto a flat plate, set at 45° with respect to the direction of particle motion. The particle diameters ranged from 1-3.5 mm, and velocities from 20-120 $\mathrm{m\,s^{-1}}$. High-speed cameras were used to measure the pre-impact particle diameter and velocity, and the post-impact fragment data. The study aimed to find the post-impact fragment size distributions and the features of the impact/fragmentation.

The experiments showed that upon impact, the particles were initially crushed into small particles, creating a fragment cloud that had a high initial velocity. Cracks then started to develop in the main particle which then created larger fragments.

For all the tests conducted the following trends were observed. At low velocities, high levels of rebound occurred post-impact. At increasing velocities, the level of rebound reduced and the particles trajectories were closer to the impaction plate post impact. It was also found that the fragment sizes reduced with increasing

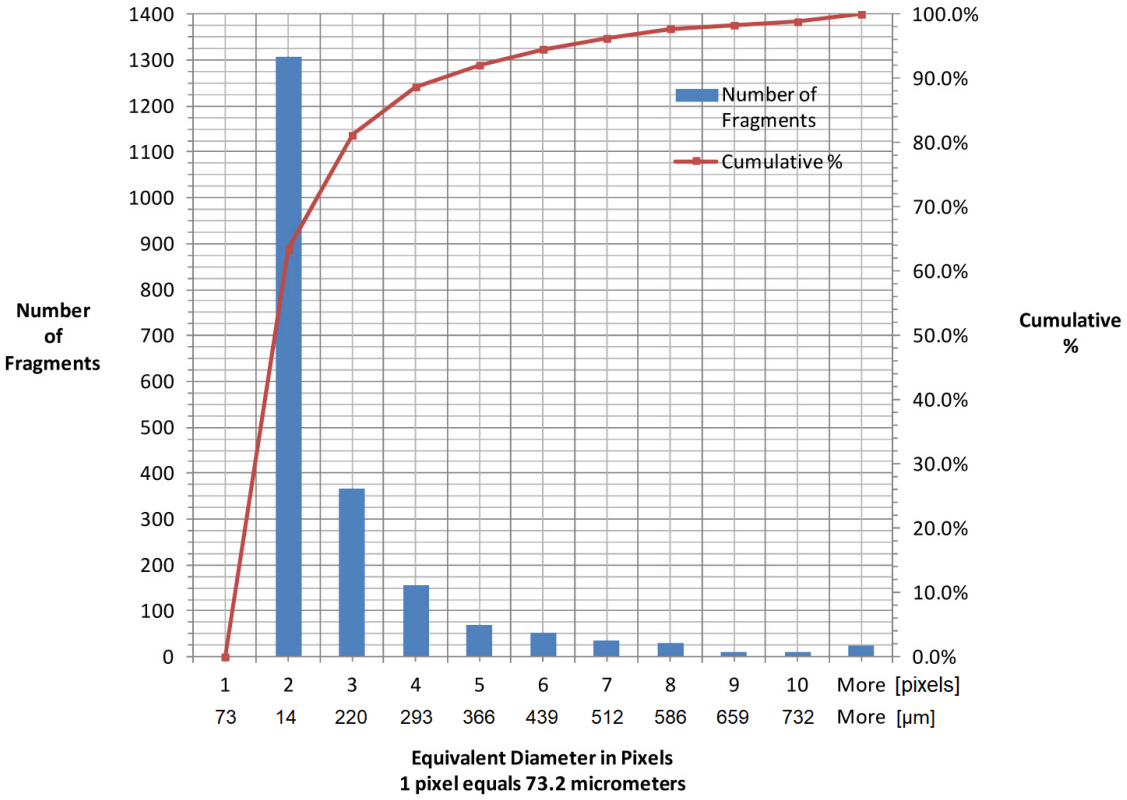

Figure 2.4: Histogram of fragment sizes post impact of a 2.9 mm crystal travelling at 130 $\mathrm{m\,s^{-1}}$ [24]. Additional X axis (µm) overlaid onto original figure for clarity.

velocity. A histogram of fragment sizes for a test with a 2.9 mm crystal, travelling at 130 $\mathrm{m\,s^{-1}}$ is shown in Figure 2.4. The data showed a non-normal distribution with a long tail, and the majority of the fragments were concentrated on the resolution limit of the camera.

Hauk *et al.* [23] studied their experimental data of ice crystal impacts onto a solid surface, to derive a fragmentation model. By relating the length of a lateral crack to the initial diameter of the particle, a critical velocity above which particle breakup occurs (U_{crack}) was derived:

$$U_{crack} = \alpha {d_p}^{-\frac{2}{3}} \,, \qquad \alpha = \frac{{K_c}^{\frac{4}{3}}}{{\rho_p}^{\frac{1}{2}}\ {\sigma_y}^{\frac{5}{6}}} \approx 0.046 \tag{2.7}$$

The author also derived a velocity at which minor fragmentation would occur:

$$U_{attr} = \beta {d_p}^{-\frac{1}{2}} \,, \qquad \beta \approx 0.45 \tag{2.8}$$

The critical velocity had good agreement with experimental data, and due to the tuned parameters being equal to a function of material properties, the model should be applicable to both glaciated and mixed-phase crystals. Unfortunately, the model did not take into account the angle of incidence of the crystal upon the surface, which has since been found to have a dominant effect.

Vidaure *et al.* [25] introduced a non-dimensional number, kinetic energy to surface energy ratio ($\mathcal{L}$), as shown in Equation (2.9), where the symbols are defined as; particle normal velocity (v_{pn}), surface energy per unit area (e_σ). For intermediate values of $\mathcal{L}$ between $\mathcal{L}_{c1}$ and $\mathcal{L}_{c2}$, small cracks form in the particle which dissipates energy and minor fragmentation occurs. For $\mathcal{L} < \mathcal{L}_{c1}$, elastic rebound occurs with no loss of kinetic energy, and for $\mathcal{L} > \mathcal{L}_{c2}$, highly inelastic rebound occurs with major fragmentation. Using experimental data, Vidaure *et al.* found that the onset parameters, $\mathcal{L}_{c1}$ and $\mathcal{L}_{c2}$ equalled 0.5 and 90 respectively. The model showed good agreement with experimental data for a clean geometry with no accretion. As a liquid film starts to form, the onset parameters will need to be adjusted, however, due to a lack of experimental data, this effect has not been accounted for.

$$\mathcal{L} = \frac{1}{12}\frac{\rho_p d_p (v_{pn})^2}{e_\sigma} \tag{2.9}$$

Substituting U_{crack} as the particle normal velocity, a comparison was made between the calculated value of $\mathcal{L}$ and $\mathcal{L}_{c2}$. It was found that for small crystal sizes ($d_p \approx 60$ µm) there was good agreement, however with increasing particle size, Hauk's model under predicted the velocity for major fragmentation.

Once particles have impacted, the rebound velocity is quantified by the coefficient of restitution. It is not feasible to do the solid mechanics to determine the stress state of each crystal, so simplified models based on the underlying physics are numerically utilised.

A general model, based upon modelling of plastic spheres as rigid-plastic particles, was created by Jackson *et al.* [26]. They derived the critical velocity above which particle yields at the contact region (U_y) as shown in Equation (2.10). For velocities above the yield velocity, the coefficient of restitution (e) was then derived, as shown

in Equation (2.11), which is less than unity due to plastic losses. This model has been suggested by Tropea *et al.* [22] as being applicable to ice crystal icing impact, however further work is required to prove this hypothesis.

$$U_y = \frac{C^{\frac{5}{2}}\pi^2}{2\sqrt{10}}\left(\frac{{\sigma_y}^5}{{E^*}^4\rho_p}\right)^{\frac{1}{2}} \qquad where \qquad C = 1.295\, e^{0.736\mathbf{v_p}} \tag{2.10}$$

$$e = 0.62\left(\frac{U_y E^*}{U_0\sigma_y}\right)^{\frac{1}{2}} \tag{2.11}$$

Villedieu *et al.* determined the normal and tangential coefficients of restitution following their previous work on the fragmentation model. They found that for $\mathcal{L} < \mathcal{L}_{c1}$, both the normal and tangential coefficient of restitution should equal unity. For $\mathcal{L} > \mathcal{L}_{c1}$, the normal coefficient of restitution remained equal to unity, but the tangential component equalled $\frac{\mathcal{L}_{c1}}{\mathcal{L}}$. Due to a lack of available data, neither of these models has yet been fully validated.

2.1.4 Particle Melt

In the atmosphere ice crystals are frozen, but as the particles propagate through the compressor heat they melt due to heat transfer from the warm air. Partially melted ice crystals are made up of solid ice and liquid water. The amount of ice and water in a crystal is defined as the Ice Water Content (IWC), and Liquid Water Content (LWC). The sum of these two terms gives the Total Water Content (TWC). Quantification of the Melt Ratio (MR) is defined as the ratio of IWC to TWC (Equation (2.12)).

$$MR = \frac{IWC}{TWC} \tag{2.12}$$

Hauk *et al.* [27] have experimentally studied the melting process of ice particles held in an acoustic levitator. A warm air jet that had an adjustable velocity, humidity and temperature was passed over the particles. The melting was recorded using a high-speed camera to determine the melting time and change in the cross-sectional area. It was found that Relative Humidity (RH) had a significant influence

on the melting time. During the melting process, a reduction in crystal length occurred until the crystal was fully melted and a spherical shape was formed due to surface tension forces. This process is shown in Figure 2.5. The change in particle shape (and hence drag coefficient) and density due to phase change means that the trajectory dynamics can alter vastly during the melting process. It should be noted that the assumption of a spherical water droplet will only be true where there is a limited slip velocity between the particle and the air. If the slip velocity is too high, then drag forces may overcome the surface tension, leading to an elliptical droplet shape.

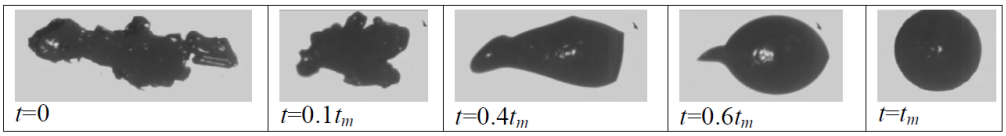

Figure 2.5: Shape evolution of a melting ice crystal held in an acoustic levitator [22]. Surface tension forces reduce the aspect ratio, tending towards a spherical droplet when fully melted.

If mass transfer due to condensation, melting, evaporation and sublimation is neglected, the general heat equation for the particle shown in equation 2.13 can be used. The symbols of Equation (2.13) are defined as; specific heat capacity (c), particle temperature (T_p), time (t), surface area of particle (A_p), heat transfer coefficient of particle (h_p), air temperature (T_a).

$$m_p c \frac{dT_p}{dt} = A_p h_p (T_a - T_p) \tag{2.13}$$

An expression for the heat transfer coefficient can be obtained by determining the Nusselt number, which exists in the literature for non-spherical particles. A correlation by Richter *et al.* [28] is commonly used, and it takes into account the particle sphericity and crosswise sphericity but was only validated against a small range of particle shapes. A more recent model by Villedieu *et al.* [19], based upon the particle sphericity, Prandlt number and Reynolds number has been found to be more accurate over a range of particulate sizes and shapes.

Application of such models to data from wind tunnel tests has been found to inaccurately predict the melting of ice crystals. Yang *et al.* [29] derived a more sophisticated melting model to include the effects of surface blowing and porosity. The model was validated against the time to melt single particles in an acoustic levitator, using data of Hauk *et al.* [27, 30]. It was found that the inclusion of surface blowing from evaporation increased the particle melting time, and was more dominant at higher temperatures. An increase in gas temperature, humidity, slip velocity, aspect ratio and particle temperature decreases the melting time, while an increase in particle diameter, Mach number and porosity factor was found to increase the melting time.

Altitude Scaling

To match engine realistic conditions, it was previously thought that the ice crystal experiments would need to be conducted at sub-atmospheric pressure. Currie [31] attempted to determine whether altitude scaling could be achieved by matching the melt ratio alone. To match the melt ratio, the energy transferred from the warm gas, warm components and particle-particle interaction, was matched from the inlet to the point of impact. If this hypothesis were proven, it would allow for certification of engines in ice crystal clouds at altitude, through testing at sea level conditions.

A test piece with a hemispherical nose and streamlined body was used. The experiment was conducted at pressures of 34.5 kPa and 69 kPa, with a fixed TWC and a range of melt ratios. The experimental aim was to match accretion rates and shapes at both pressures by matching the melt ratio.

By matching MR, the accretion shapes at both pressures were "quite similar", and varied from small to large to small with an increasing melt ratio, as was expected from previous work. A good comparison was seen in terms of the steady state deposited volume and growth rates. For the conditions tested, less than 10% difference in accreted volume was observed. The volume of accretion at the high and low pressures was less than 1.5% different. Figure 2.6 shows the transient ice profiles between the high and low-pressure tests, also for a melt ratio of approximately

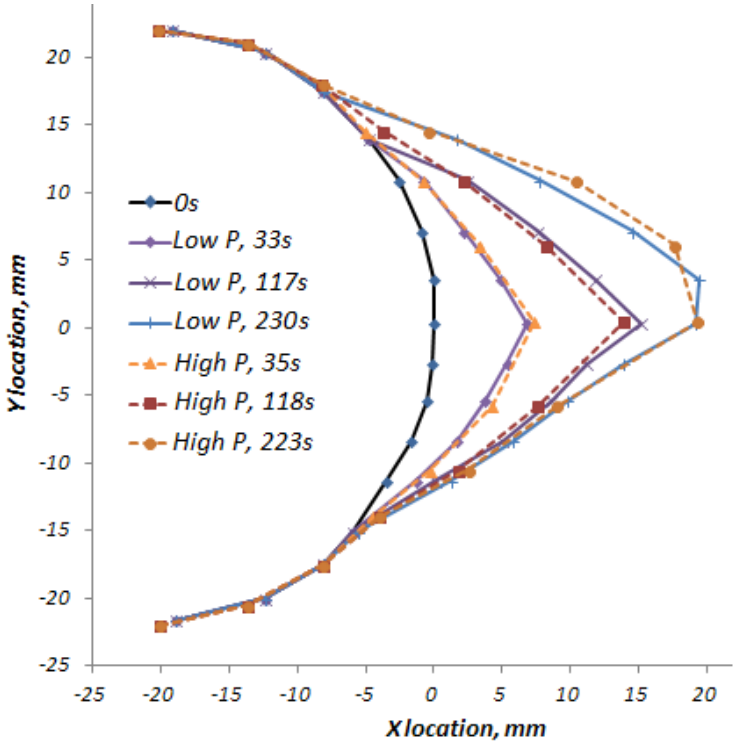

Figure 2.6: Comparison of transient ice accretion profiles at low and high pressure on a hemispherical cone. Altitude scaling achieved by matching the particle melt ratio immediately upstream of the test piece [31].

11%. The data showed good similarity between the two altitudes, however, it is believed that there is insufficient data to conclude over what range of pressures the altitude scaling can be utilised. As a result, to date, all work conducted at altitude representative conditions, have been done in a pressure vessel at reduced pressure, as opposed to using scaling.

Particle-Surface Heat Transfer

Bucknell *et al.* [32] conducted an experiment to determine the thermodynamic processes of ice particles impinging onto warm surfaces. A flat plate was instrumented with thin-film heat flux gauges and thermocouples, embedded between the heater and the icing surface. A Proportional Integral Derivative (PID) feedback loop was used to ensure the plate was both spatially and temporally isothermal. A flat plate was chosen to prevent individual particles from bouncing multiple times, as would occur on curved, concave surfaces. The flat plate was set at a

temperature to represent the heat flux from components in the early core compressor. A titanium coating to the flat plate provided representative coefficient of restitution found in gas turbine compressor blades.

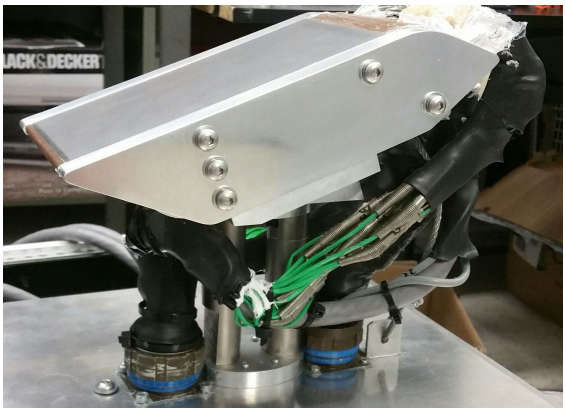

Figure 2.7: Wedge shaped flat plate test piece used in Bucknell's experiment to measure the thermodynamic and mechanical processes experienced by ice particles impinging on a warm surface [32].

Bucknell [32] assumed that the main sources of heat flux in and out of the test piece were from the heater (q_{freeze}), kinetic energy of incoming particles (q_{kin}), convection (q_{conv}), melting of ice (q_f), raising particle temperatures to T_{plate} ($q_{sens,imp}$), evaporation (q_{evap}), losses (Q_{loss}) and radiation ($q_{radiation}$). These terms can be used in a heat balance, as shown in Equation (2.14).

$$q_{freeze}A_h + q_{kin}A_{surf} = (q_{conv} + q_f + q_{sens,imp} + q_{evap})\,A_{surf} + Q_{loss} + q_{radiation}A_{plate} \quad (2.14)$$

The effect of $q_{radiation}$ was neglected as it was two orders of magnitude smaller than q_{conv}. Due to not knowing the amount of melting which would occur before the experiment, $q_{sens,imp}$ and q_f were unknown. The kinetic energy flux, q_{kin} was also unknown, but Particle Image Velocimetry (PIV) data showed that bounce and shatter occurred, so little kinetic energy would have been transferred into the plate. Finally q_{conv} was also unknown. These unknown terms were lumped together to make $q_{mixed,phase}$. The test was conducted in Altitude Icing Wind Tunnel (AIWT) - a closed-loop wind tunnel that reaches near-saturated conditions once the cloud is

initiated. Near saturation conditions mean that the magnitude of the evaporative term would have been low so was also neglected. Assuming that any losses could be ignored, the heat transfer measured by the thin film gauges (q_{TFG}) could be related to the mixed-phase heat loss Equation (2.15).

$$q_{mixedphase} A_{surf} = q_{TFG} A_{surf} \tag{2.15}$$

The $T_{wb,0}$ in the tunnel was kept sufficiently low that no natural melting occurred, meaning that fully glaciated crystals impinged onto the plate. A value for heat transfer enhancement was calculated by normalising the Stanton number by the theoretical Stanton number for dry conditions. Heat transfer enhancement was found to linearly increase with TWC, for the range of 0<TWC<3 gm^{-3}. At increased TWC, the driving temperature difference of the convective heat flux is reduced. Given that the total heat transfer enhancement was linear, the heat flux to the ice and water must have been non-linear to cancel out the reduction in driving temperature. Bucknell explained this by suggesting that there was a water film present at high TWC, which increased the total heat transfer and increased the impact time due to the dampening of the particles. The water film was later confirmed by use of PIV, which showed film splashing at TWC>2 $\mathrm{g\,m^{-3}}$.

2.1.5 Particle Sticking

Research by Struk *et al.* and Currie *et al.* [33, 34] concluded that for ice crystal icing accretion to occur, liquid water has to be present in the crystals, which is commonly known as partially melted, mixed-phase conditions. At zero LWC, glaciated particles have zero sticking efficiency, and either bounce or shatter. At high LWC, the wet particles also have a low sticking efficiency, and are generally blown off the surfaces by aerodynamic forces. Mason *et al.* theorised that a regime exists between these two extreme cases, at which optimum icing occurs [1].

An early study by Boeing and the National Research Council, Canada (NRC), looked at mixed-phase icing in a geometry simulating the s-shaped transition duct between the low and high-pressure compressors [35]. The results showed that

accretion occurred in a range of total temperatures, below and above freezing, provided that the LWC was sufficiently high.

Bucknell *et al.* [36] experimentally determined the net sticking efficiency as a function of MR. The net sticking efficiency (η_{net}) was defined as "the proportion of the impinging mass flux that sticks to the component minus the proportion that bounces or is eroded". An axisymmetric test piece with a conical nose was used for the experiment. A cone was used instead of a hemispherical geometry to minimise the gravitational droop experienced by Currie *et al.*. [31].

When the temperature of the wall was greater than 0°C it was found that η_{net} was most dominated by MR when using particles with small diameter and low velocity, and hence low erosional impact. A model of sticking probability (defined as the sticking efficiency normalised between 0-1) was produced, with a polynomial between 0.02<MR<0.34, and zero elsewhere, as shown in figure 2.8. The model was compared to external data from Struk and Currie [37, 38], and good agreement was found. Regardless of the Particle Size Distribution (PSD) used and hence erosive pattern, the peak sticking probability remained between 9-13% MR, which was in agreement with Currie *et al.* who found the optimum to be 10-20%. If the MR remained constant, the effect of total wet bulb temperature ($T_{wb,0}$) was negligible (for $T_{wb,0} > 0$) as was also observed by Currie *et al.* [31].

The accretion growth rate was proportional to TWC, and the sticking efficiency was found to be constant across the TWC range of 4-12 gm^{-3} range tested, which suggested that particle-particle interactions were negligible at this level of TWC.

2.1.6 Erosion

Knezevici *et al.* [39] found that that larger particles had an increased erosive effect on previously accreted ice, whereas small particulates were more likely to get trapped in a water film and accrete. With increased MMD, the dampening effect of the film reduced, until a critical size at which the film no longer trapped the particle, and erosion occurred. Work by Samenfink et al. [40] had similar findings and found that

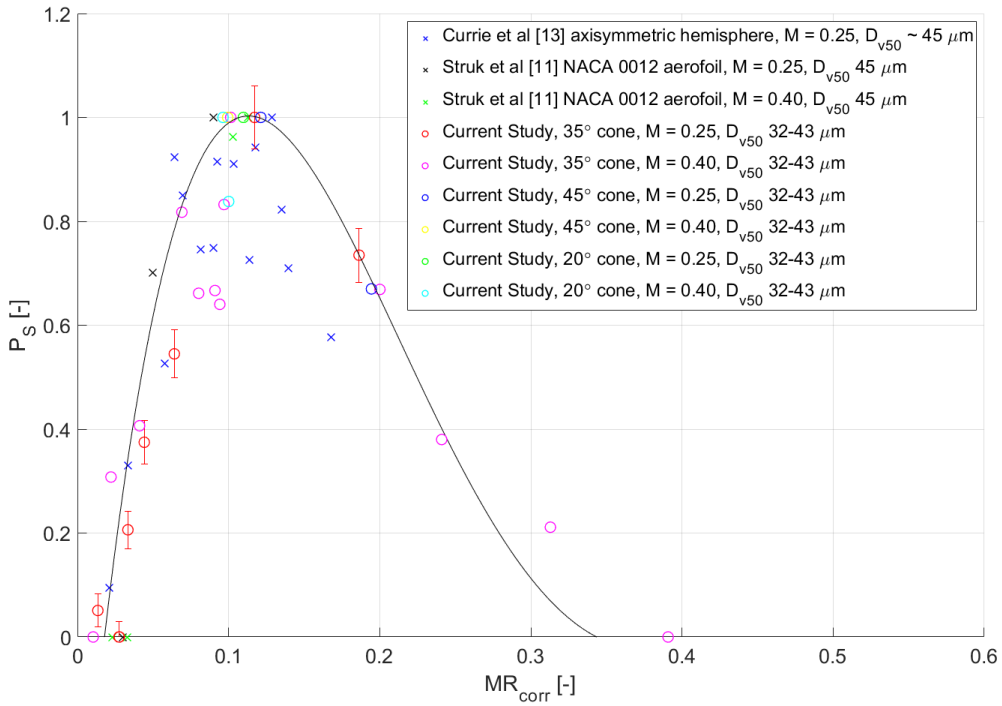

Figure 2.8: Sticking probability of an incoming particle onto an accretion surface, plotted against melt ratio. Created using data from [36], and compared to data from [37] [38].

with increased film thickness, the sticking efficiency of that component increased. For excessively large particles, the erosion rate could exceed the accretion rate.

Later work by Knezevici *et al.* [41] de-coupled the effect of ice particle melt and size distributions by fixing the melt ratio and ice crystal mass flux, but varying the size distribution. Two grinder configurations were tested; A and C, as shown in figure 2.9. Under fully glaciated conditions, the MMD differed by less than 1.5%, however, configuration C had some particles which were up to 1.5 times greater than the largest of configuration A.

For a $T_{wb,0}$ above zero degrees, configuration A produced significantly more accretion compared to configuration C, when equal aerodynamic conditions were used in the tunnel. The key difference between the two configurations was the right-hand tail of the size distribution, and it was believed that this caused differences in erosion, splashing and particle retention times. Only 8% by weight of particles of C were larger than A, however configuration C had a 94% reduction in accretion rate compared to configuration A. The larger particles were less affected by the damping

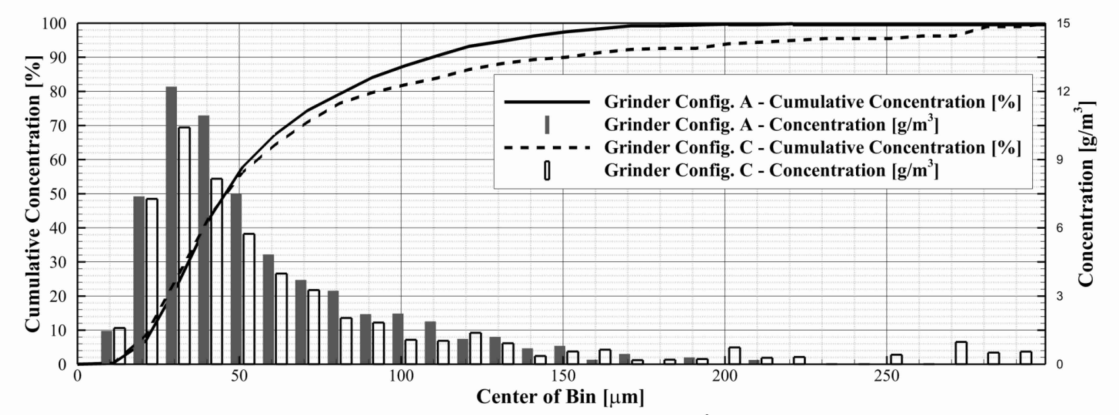

Figure 2.9: Comparison of particle size distributions of grinder configuration A and C under glaciated conditions, with near equal median mass diameter but differing right hand tail distribution characteristics [41].

of the liquid film, meaning that they splashed the film away and eroded the surface.

Previous studies focused on using the MMD to characterise the size of the particulates, but it is now deemed that this parameter alone is insufficient. Knezevici [41] focused on using the variable defined as diameter where nn% of the population lies below this value ($D_{v,nn}$). If all crystals have equal density, the MMD is equivalent to D_{v50}. From the findings of this work, it was found that as a minimum, D_{v50} and D_{v90} or D_{max} are required to accurately describe the size distribution.

Work by Bucknell *et al.* [36] determined the effect of the Particle Size Distribution (PSD) on erosion characteristics. Tests using a transient change in grinder speed allowed for D_{v50} and D_{v10} to remain approximately constant, while increasing D_{v90} and $D_{v,max}$. Reducing the velocity by a factor of 1.6 and increasing the D_{v90} by a factor of only 1.2, the net sticking efficiency decreased. This implied that the erosion was more dependent on the PSD than velocity. A linear fit between D_{v90}^3 and net sticking efficiency was found, which was not too surprising given that erosion occurs when the impact kinetic energy is greater than the surface energy of the ice, and the kinetic energy is proportional to D^3.

A final change increased $D_{v,max}$ by 40%, while all other D_{vnn} were kept within 6% of the previous values. The sticking efficiency dropped by 85%, which showed that a very small number of large particles can have a large effect on overall deposition evolution. Unfortunately $D_{v,max}$ is usually unknown.

These findings further confirmed that a full understanding of the breakup mechanics within the cold components needs to be determined to know what particulate size distribution should be expected within the core compressor and hence determine the accretion regime. This has not yet been completed in open literature.

Numerical erosion models have been suggested by numerous authors [36, 42–45] to include the effects of tangential velocity, IWC, MMD, ice temperature and crystal temperature. The main limiting factor in all models is the use of MMD, and not taking into account the $D_{v,90}$, which is now known to be dominant in the erosion characteristics.

2.1.7 Accretion Dynamics

Once ice crystals have impacted and stuck to a surface, a model needs to be incorporated to determine the growth rate of the ice layer. The first thermodynamic model for ice accretion was produced by Messinger [46] for use in Supercooled Liquid Water (SLW) conditions. The model consisted of an energy balance between the air, ice and liquid film. Energy loss terms included convection, evaporation, and cooling by incoming particles. Energy gain terms included kinetic energy of impinging droplets, the release of latent heat, and aerodynamic heating.

This model has since been updated by Myers [47] to include transient effects, conduction through the ice and to calculate the water film thickness. Wright *et al.* [48] further updated the model to take into account heat transfer from the air to the droplet, allowing for the model to be suitable for use in ice crystal icing.

The most recent formation of this model was created by Bucknell *et al.* [49], who extended it to a three-layer model, allowing for a water layer to exist above and below the ice accretion. The model has two stages: a single water layer on a warm surface, and a three-layer (water-ice-water) once an accretion has initiated. The simulation moves from stage one to stage two when the film surface temperature reaches freezing conditions. Calculation of the water film temperature (θ) profile is done by an energy balance on the film surface (Equation (2.16)), and imposing the boundary condition of the film temperature to be equal to the substrate temperature at the

interface. All particles sticking to the surface are assumed to melt instantaneously. The height of the water film is based on the mass flux of sticking water/ice and evaporation. A quasi-steady assumption is made so that the one-dimensional heat equation can be used (Equation (2.17)).

$$-k_w \frac{\partial \theta}{\partial n} = (q_{conv} + q_{evap} + q_{sens,imp} + q_{sens,run}) - (q_{kin} + q_f) \tag{2.16}$$

$$\frac{\partial^2 \theta}{\partial n^2} = 0 \tag{2.17}$$

Once film surface temperatures reach freezing, an ice layer forms on top and an additional water layer may form on top of the ice layer. The model assumes that the ice layer is isothermal and that the top water layer is sufficiently thin that wall-normal gradients can be neglected, so that it can also be assumed to be isothermal. The growth rate of the ice layer is found from the mass fluxes of ice sticking to the surface and the freezing rate of the above film.

This model can be applied to any general body definition and has been successfully used in ice crystal ice modelling [13]. Its main limitations are the basic form of water run-back model which is based only on mass fluxes and a fixed maximum film thickness. This model could be greatly improved with a more sophisticated water run-back model based on the shear stresses imparted by the local flowfield. Mass conservation modifications also need to be made to this model when it is applied to a non-planar geometry.

2.1.8 Accretion Shedding

During the accretion process it has been found that certain conditions cause the ice formation to break away from the substrate on which it was grown. The shedding falls into two categories; "adhesive failure" and "cohesive failure". Adhesive failure occurs when the inter-facial stress between the ice and its substrate exceeds a critical value. Cohesive failure occurs when the internal stresses of the ice exceed a critical value. These two types are displayed in Figure 2.10.

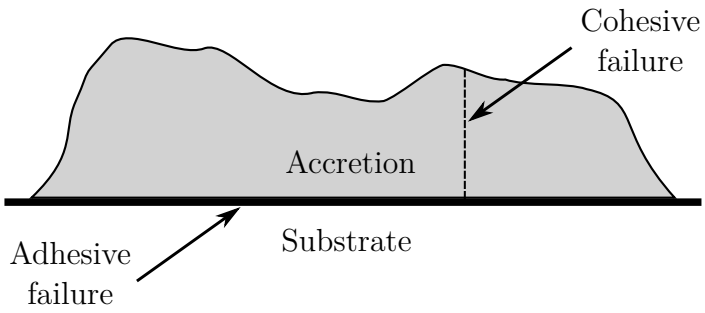

Figure 2.10: Two types of shedding initiation of ice crystal accretion: adhesive and cohesive failure.

Adhesive failure may occur due to an increase in inter-facial stress, or a reduction in the adhesion strength between the ice and substrate. As an accretion grows sufficiently thick, the cooling effect of impinging particles can be outweighed by the heating through the test piece. This creates a water layer on the surface, reducing the adhesion strength to the substrate and generally leads to the bulk movement of the accretion along the test piece. This mode is displayed in Figure 2.11a. Adhesive failure may also occur with an increased aerodynamic load, causing an increased drag force and hence inducing greater stress at the interface, likely causing the accretion to lift off the substrate and escape into the free-stream flow. This mode is shown in Figure 2.11b. Both of these methods generally lead to large-scale shedding, in which a large proportion of the accretion sheds as a near single entity.

Cohesive failure can be caused by increased aerodynamic loading, or due to a change in the accretions yield strength. The change in yield strength can be caused by an increased amount of water in the ice accretion (induced by an increase in humidity or incoming particle MR and/or elevated heat flux into the ice decreasing the ice stiffness) or conversely due to drying of the ice increasing the brittleness. This mode can lead to small sections of ice breaking off on the outer layers, or if hooked around a blunt body, can also lead to large scale shedding, as shown in Figure 2.11c.

Adhesive and cohesive failure generally do not act mutually exclusively. Partial adhesive failure can lead to rotation of the accretion. At a critical level of rotation, the crack propagation can move into the bulk accretion, forming cohesive failure, as shown in Figure 2.11d.

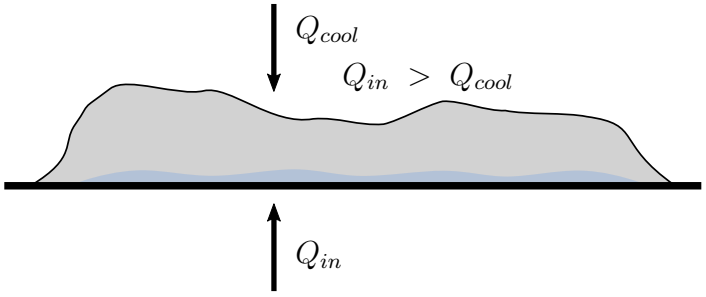

(a) Back heating

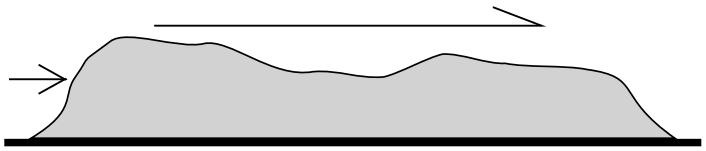

(b) Shear loading

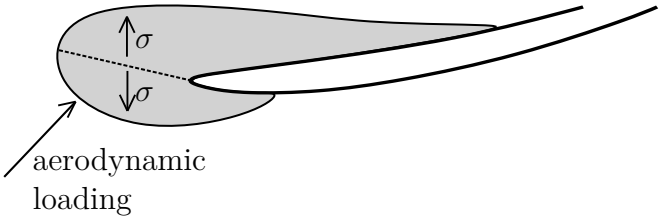

(c) Cohesive stress limit

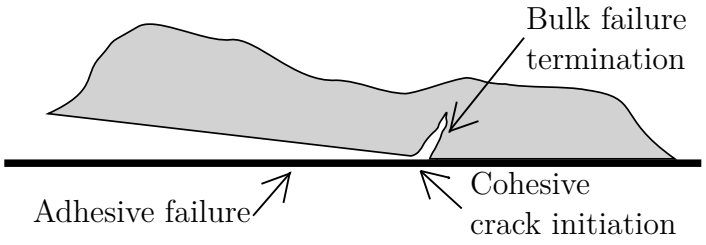

(d) Adhesive failure leading to cohesive failure

Figure 2.11: Mechanisms of shedding of crystal icing.

In an engine, there are generally three reasons that ice will shed. The first is a change in the engine operating point. When an increase in engine power is required, the rotational speed increases, leading to increased dynamic pressure which causes larger pressure drag forces. The change in blade speed will alter the flow angles, altering the accretion loading. The increased compressor work will increase the compressor temperature rise, meaning that increased heat fluxes will pass into the accretion, which if continued for a sufficient amount of time will start to melt the accretion and its interface. A change operating point can also occur due to a change in environmental conditions, such as descending into warmer air, or migration away from an ice cloud leading to an increase in gas path temperature caused by the removal of evaporative cooling. Finally, if the engine is passing through an unstable transient to increase the power, the vibrations may induce further sheds.

The second cause of sheds is the change in accretion geometry. As the accretion grows, new stagnation regions will form, leading to increased pressure being applied to the body, meaning elevated stress levels and hence increasing the probability of fracture.

The final major cause for engine shedding is due to use of auto-thrust. The system is used to maintain aircraft speed during varying conditions and operates by altering guide vane angles [50]. The system is generally under damped leading to large oscillations in flow angles. The change in exit flow angles will alter the accretion loading and may lead to critical stress levels.

In the event of a shed, soft slushy ice can lead to flameout, however, this is not deemed to be an issue due to auto-ignition generally occurring before the pilot can respond to the decrease in engine power. This is commonly termed "avalanche shed" within the industry and would lead to certification failure so needs to be avoided at all costs. The more damaging type of shed is when hardened ice which has been hooked around a body (such as a vane leading edge) separates from its substrate and is carried by the core flow to a downstream location, leading to large levels of damage.

The adhesion strength of ice crystal ice is a dominant parameter to be used in numerical models of ice shedding, unfortunately, its value is currently poorly

understood. Due to the complexities involved in measuring its value, studies have had a large scatter in their data, with results showing adhesion strengths ranging from 0.5-3MPa in dry conditions [51–54], down to only 17 Pa in wet conditions [34]. A range of parameters affect the adhesion strength of ice crystal ice, such as impact velocity, PSD, strain rates, annealing, temperature and critical energy release rate (G_c) [55].

Impact speeds ice of ice crystals can alter the adhesion strength onto rough surfaces. At greater impact speeds, the mixed-phase crystals can penetrate into deeper pores within the substrate forming higher strength of adhesion. For smooth surfaces less variation exists [53, 54, 56]. When testing, the strain rate applied during the loading process can cause up to an order of magnitude difference in the apparent adhesion strength [53–57]. In general, a lower strain rate leads to a decreased adhesion strength due to equilibrium stress states forming. If samples are left for a sufficient amount of time between accretion and testing, annealing of the crystal structure will occur, increasing the adhesion strength to the substrate as well as the tensile strength, reducing the probabilities of both cohesive and adhesive failure [53]. By increasing the MMD the adhesion strength increases for rough surfaces because of a similar argument to the impact velocities - with greater sizes, the increased momentum will help the crystals penetrate deeper into the substrate [53, 56]. For temperatures below freezing, with decreased temperature the adhesion strength increases, until ≈-10°C at which a plateau occurs [51, 54, 56]. At temperatures below -15°C, a reduction in adhesion strength is observed due to an increase in the number of pores and cavities at such low temperatures [58]. The energy release rate determines at what levels of stress a crack is thermodynamically advantageous to propagate. Once the strain energy release rate exceeds G_c then the crack will propagate. Typical values are approximately 1 $\mathrm{J\,m^{-1}}$ [52].

Most adhesion strength tests have either used lap joint shear rigs or centrifugal forces to induce the shed event [51, 53, 54, 57]. In a perfect loading case, the adhesion strength can be determined by dividing the force applied at the moment of the shed, by the inter-facial area. In reality, stress concentrations form on the

accretion-substrate interface which induces local crack propagation at a lower than expected loading level. Accurate adhesion strength measurements can therefore only be determined by utilising Finite Element Analysis (FEA) to determine the stress concentrations for the specific loading case, to then back out the adhesion strength.

To date, ice crystal icing codes have only successfully demonstrated the growth of ice, and no models have been able to accurately determine when the accretion will be shed.

Other similar disciplines such as Supercooled Large Droplet (SLD) and freezer ice have created numerical models to capture ice shedding. While the material properties of these types of ice can not be transferred to ice crystal icing, the basic methodology remains the same. In its most basic form, if the accretion is not hooked around a body, when the water layer covers the whole area interfacing the accretion and its substrate then it is known that it will shed, for any representative air speed. This criterion was further expanded by R. Henry [59], who determined that only 80% of the inter-facial ice needed to melt for a shed event to occur.

The effect of aerodynamic forces in ice shedding was studied numerically by Scavuzzo *et al.* [60] using finite element analysis. Iced profiles of a National Advisory Committee for Aeronautics (NACA) 0012 airfoil were studied, and zero displacement and zero rotations were applied as boundary conditions to the nodes at the interface between the test piece and the accretion. It was found that for air speeds less than Mach 0.45, that the stresses were insignificant and that the most likely reason for shedding is a change in accretion properties (either due to humidity changes or increased heat flux inputs). At Mach 0.6, the maximum shear stresses reached levels of 20% ultimate shear stress, meaning that it is necessary to couple the pressure distribution obtained by CFD with FEA.

More advanced numerical models of ice shedding have been developed to study the ice shedding mechanisms [61, 62]. These include the effect of external aerodynamic forces, and also the hydrostatic pressure equilibrium between the external flow and the internal water film - leading to an additional lifting force. The models show that most shedding events occurred due to detachment of the adhesive

bonding until a critical crack length is reached. At the critical length, the crack propagates through the ice layer leading to bulk failure, matching experimental observations of Wei *et al.* [63].

Recently, higher levels of coupling between the CFD and FEA have been achieved. Zhang *et al.* [64] produced a multi-timestep methodology in which a small level of ice accretion was obtained which was used as boundaries of a new CFD solution. Using this new pressure distribution as boundary conditions for an FEA simulation, the stress field within the ice accretion was obtained. It was assumed that zero displacements between the ice and the substrate occurred (no adhesive failure) and small deformation approximations were applied (and justified with numerical analysis). Using the stress field, if the maximum first principal stress exceeds the tensile strength, then the initial crack is located on that cell. Using the displacement field, the stress intensity factors were calculated and used with the maximum hoop stress criterion [65] to determine the crack growth direction. The computed CFD pressure field is shown in Figure 2.12a and the induced principal stress distribution throughout the ice crack propagation is shown in Figure 2.12b.

While these programs provide an insight into the possible shedding mechanisms for a given accretion profile, none have yet been implemented into a model of predicting the ice accretion. The current limitations of numerical models of ice crystal icing is that the accretion can indefinitely occur as they have not coupled in the analysis of ice shedding.

2.2 Complete Numerical Models

Numerical models for predicting ice crystal accretion are essential for the robust design of new engines and certification testing of engines going into service. The models need to incorporate sufficient thermodynamics to capture the relevant heat transfer from the air and hot components to predict the melt ratio and component surface temperatures. Equations of motion are required to predict the trajectory of the particulates, with heat and mass transfer between both the crystals and the bulk flow. Criteria are then required to determine if particles will bounce, shatter, accrete,

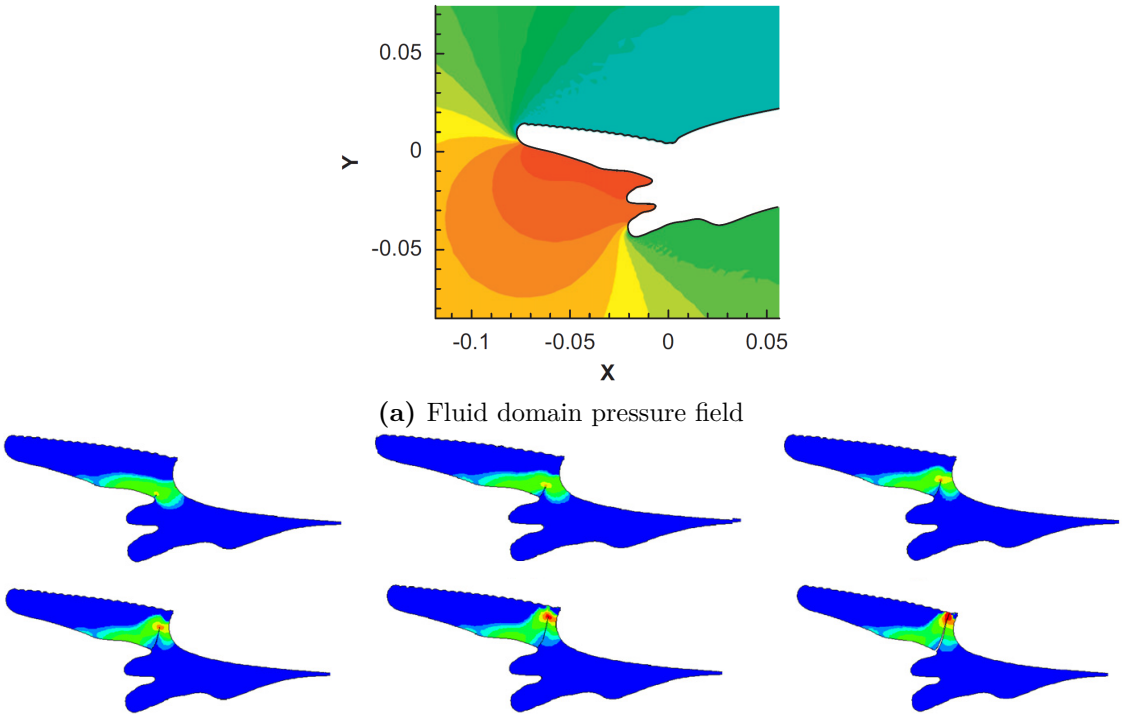

(a) Fluid domain pressure field

(b) Evolution of crack growth, coloured by the principal stress distribution

Figure 2.12: Results from a coupled finite element model and CFD simulation [64].

melt or erode upon impact to a surface. When the mass distribution of crystals onto a surface is known, a model needs to be applied to determine the growth rates of the ice and water layers. Once accretions are formed, shedding models need to be incorporated to determine the transient build-up of ice. Numerical models without removal mechanisms (erosion and shedding) generally over-predict the leading edge accretion by an order of magnitude compared to experimental results [34, 66, 67]. Experimental data has shown that the total air temperature drops significantly and water vapour pressure increases upon the addition of ice crystals [33], and this process needs to be captured within the model.

Before implementing all the necessary components of a model into a system, a level of coupling between the fluid and discrete particle phase needs to be determined. Preliminary work by Wright *et al.* [48] determined that for the conditions expected within an engine environment, that the effects of mass, momentum and energy transfer from the crystals to the air is negligible. From these findings, most models incorporate one-way coupling between the air and the crystals.

The most complete model described in detail in the open literature is the Office National d'Etudes et de Recherches Aérospatiales (ONERA) 2D icing code created by Villedieu *et al.* [19, 43, 68]. They included the effects of non-spherical crystal shapes on drag coefficients, heat transfer and phase change using their correlations as well as others taken from open literature [69]. Impact regimes were determined by the use of the model created by Vidaure *et al.* [25] and the accretion process used the extended Messinger model [47], with further improvements following the work of Wright *et al.* [48]. The model has been successful in qualitatively matching the accretion on simplistic geometries such as an airfoil leading edge as shown in Figure 2.13. It can be seen that for low LWC cases (Cox #19, Cox #20), the numerical code has good agreement with the experimental data. For increased MR, in which the ice layer will have been more affected by the aerodynamic shear and erosional effects, the model failed to accurately predict the ice shape. In their model, the erosion is accounted for using an empirical relationship, which was produced with limited data. This shows the importance of an accurate erosion model, which to date has not yet been produced.

The Oxford Thermofluids Institute (OTI) has created an ice crystal icing numerical program, primarily produced by Bucknell [13]. The model, called ICICLE, was originally based on the work at ONERA [19, 43, 68], but has since been developed to include new models for surface-particle heat transfer, erosion, sticking probability, and ice crystal accretion, all produced using targeted experiments at the NRC. Models from open literature have been incorporated such as correlations for non-spherical particle Nusselt number, Sherwood number, drag coefficient and phase change.

The general structure of the model is shown in Figure 2.14, with the items in white showing sections of the model already produced, items in green being sections implemented during this PhD, and items in red being sections currently missing from the code. The model starts with a definition of the clean geometry from which a flow solution is obtained using CFD. Implicit Lagrangian time-stepping is then used to calculate the trajectories of the particles throughout the domain. Finally,

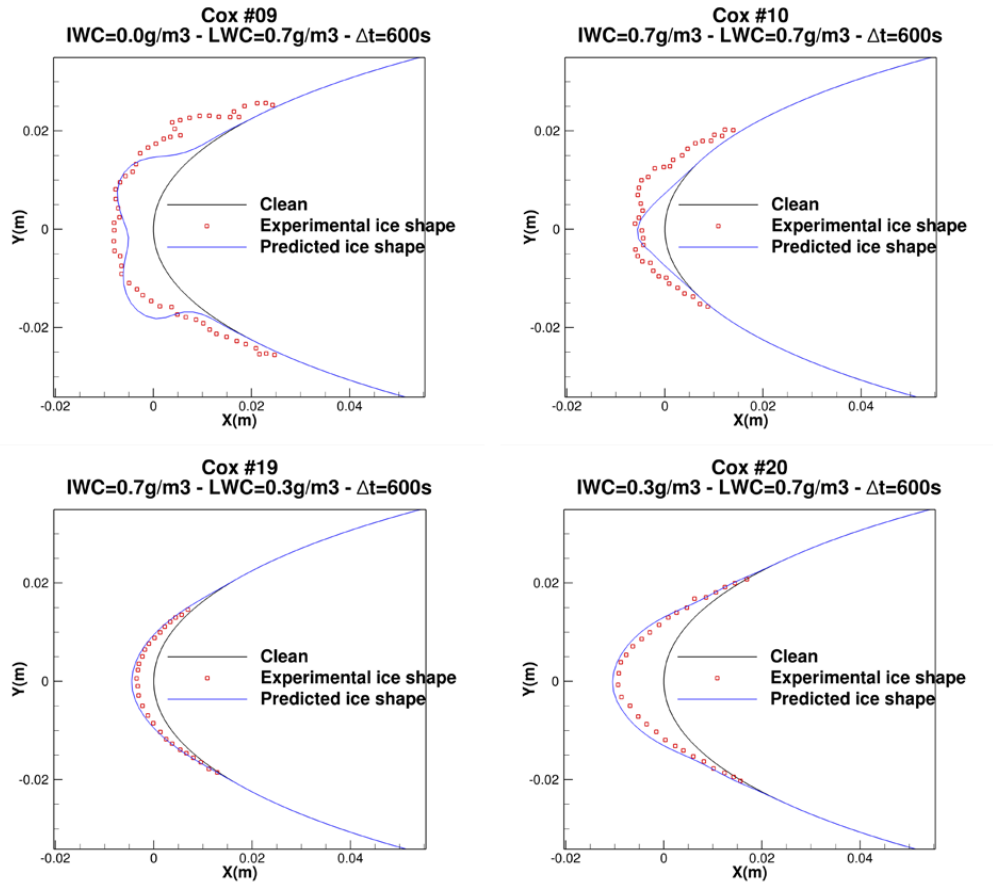

Figure 2.13: Ice shapes computed using the ONERA 2D code, compared to experimental data in the Cox icing wind tunnel [70] using a NACA-0012 airfoil. Figure taken from [43]. IWC = ice water content, LWC = liquid water content.

the Extended Messinger Model adapted of ice crystals - Extended Messinger Model - Crystals (EMM-C) [49] is applied to determine the ice growth.

To validate the model, the data has been compared to an experimental campaign, using a simplified compressor stator vane [71]. Three specific test cases were chosen, which held a constant PSD (D_{v50} = 34 µm) and Mach number of 0.4, and varied the MR from 1% to 10%. These results are shown in Figure 2.15. For the cases with MR of 1% and 4%, good agreement was observed with the experimental data. At the highest MR (10%), the numerical prediction deviated significantly from the experimental data. As found experimentally, this MR produces a maximum sticking probability, meaning that a significant accretion formed. At such large accretion volumes, the accretion itself deviates the local flowfield and hence alters

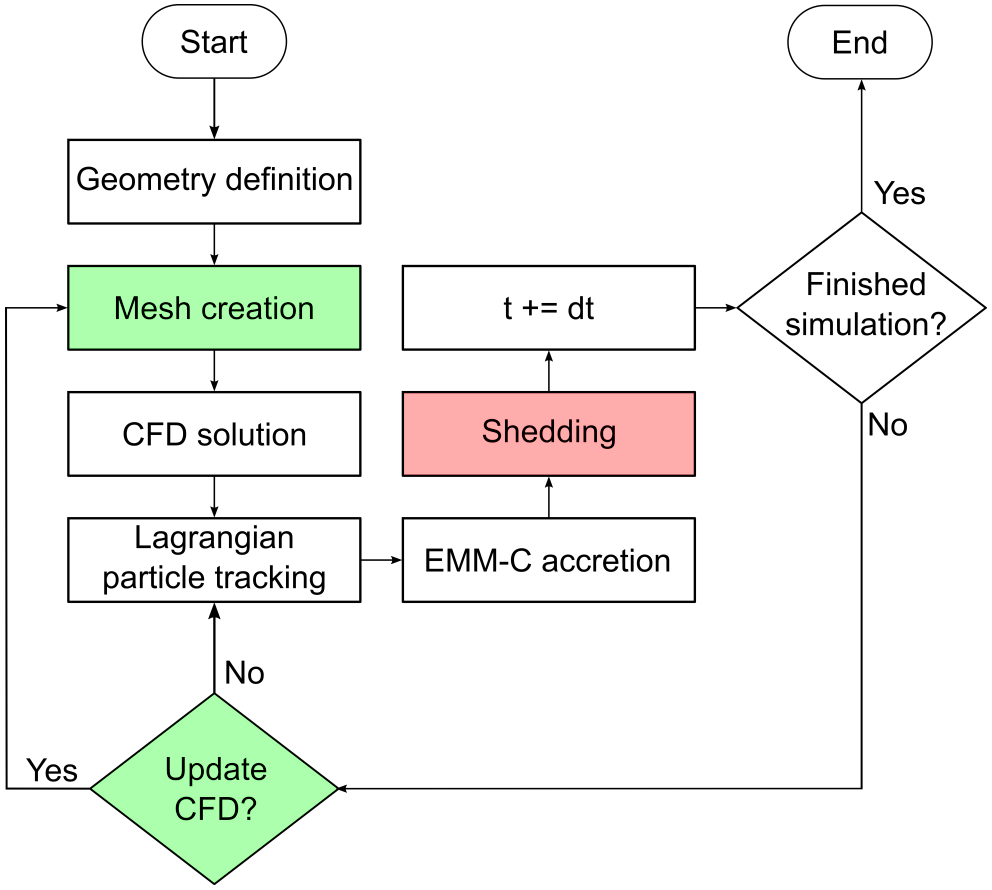

Figure 2.14: Flow chart of numerical code produced in the Oxford Thermofluids Institute, ICICLE. Items in green are sections implemented during this PhD, and items in red are sections currently missing from the code.

the trajectory of incoming particles which could not be accounted for.

One of the main limitations of the old ICICLE model is the lack of update in the CFD flow solution to account for the change in potential field around the accretion. Other sections which need further work, are the film model, inclusion of a shedding model, heat/mass transfer from the particle to the continuous phase, heat transfer from the particle to the test-piece, heat transfer from the test-piece to the particle and a particle impact-splashing model.

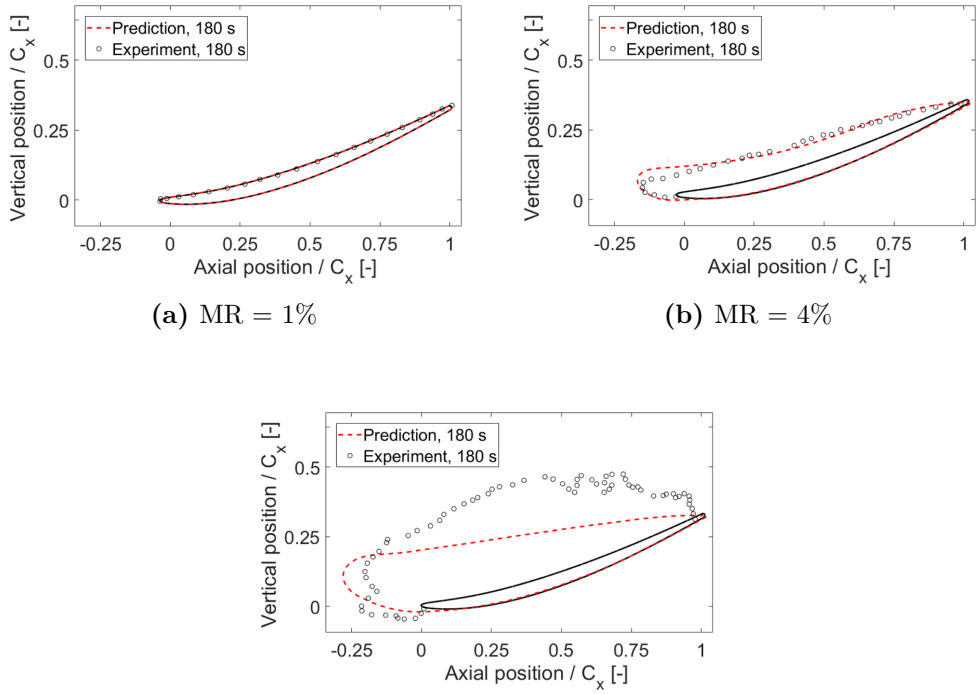

(a) MR = 1%

(b) MR = 4%

(c) MR = 10%

Figure 2.15: Numerical results from ICICLE, all tests at D_{v50} = 34 µm, Mach = 0.4, with varying relative humidity (and hence melt ratio, MR) [13].

2.3 Experimental Methods

Liquid and Total Water Content

Multi-element probes are typically used to experimentally determine the LWC [72]. Wires of different diameter are maintained at a constant temperature of 150°C by independent control systems which alter the voltage across each wire. The wires are cooled by two forms of heat loss; convective loss from the airflow, and heat loss due to interception of cloud water. The second form of heat loss is due to heating of the impinging water to the equilibrium temperature for evaporation, and also latent heat of evaporation. One wire is orientated to follow the direction of the flow and provides a measurement of the heat loss due to convection (assuming no particles collide with the flow aligned element).

Measurement of the liquid water content is done by subtracting the power supplied to each vertical element by the power supplied to the flow aligned element.

Figure 2.16: Multi-wire liquid water content probe. The sensing elements of the Multi-wire, are the 2.1-mm hollow cylinder (left), the 2.1-mm diameter forward facing half-pipe (centre), the 0.5-mm wire (right), and the compensation wire (behind). [73].

Measurements of sensor width, senor length, ambient temperature and airspeed are used to convert the net power into a liquid water content.

A particle is detected by the probe if it intercepts an element and is also held on the probe for sufficient time for particle evaporation. Small crystals may be turned by the potential field around the element, reducing the collection efficiency of the probe. Fully glaciated conditions also produce non-zero LWC readings due to the glaciated crystals receiving heat as they rebound off an element. This secondary error is termed the "false response" of the probe and has been parametrically characterised [36, 74]. These errors of the device are not yet fully understood, and any measurement of liquid water content should be noted as having considerable uncertainty.

Total water content is typically measured using an iso-kinetic probe. By fully evaporating all incoming liquid and ice, the change in specific humidity is measured and correlated to the incoming total water content. The melt ratio can then be found by taking the ratio of the liquid water content (from the multiwire probe), to the total water content (from the iso-kinetic probe).

Figure 2.17: Cross-sectional ice shape tracing method. Section of ice is melted and accretion edge traced on a piece of card [78].

Accretion Measurements

Methods of quantitative measurements of ice accretion profiles have been developed over the past couple of decades. Some experiments have extracted qualitative data from images of the accretion to determine the level of icing severity at specific conditions [75, 76]. The most basic form of quantitative ice measurement is cross-sectional tracing. This method involves melting a section of the accretion with a hot wire, placing a cardboard template of the test piece into the melted slot, and tracing around the accretion profile. This method is depicted in Figure 2.17. Research of two-dimensional test pieces have found that three dimensional accretion profiles are formed due to end wall effects [77]. The shape tracing can be repeated at multiple spanwise locations but is a highly labour intensive task, during which the ice shape may melt and change shape. This technique is intrusive and can only be taken once the ice cloud has been turned off.

Non-intrusive techniques have since been developed to measure ice profiles during the accretion process. Extraction of quantitative data at a single spanwise location for a two-dimensional test piece can be extracted using a back-lit camera view. Edge detection algorithms can then be utilised to extract the high contrast edge of the accretion in the camera view. This process has been utilised in many experimental campaigns [34, 36, 71, 79], and an example image is shown in Figure 2.18. The limiting factor is the assumption that the accretion is uniform along the length

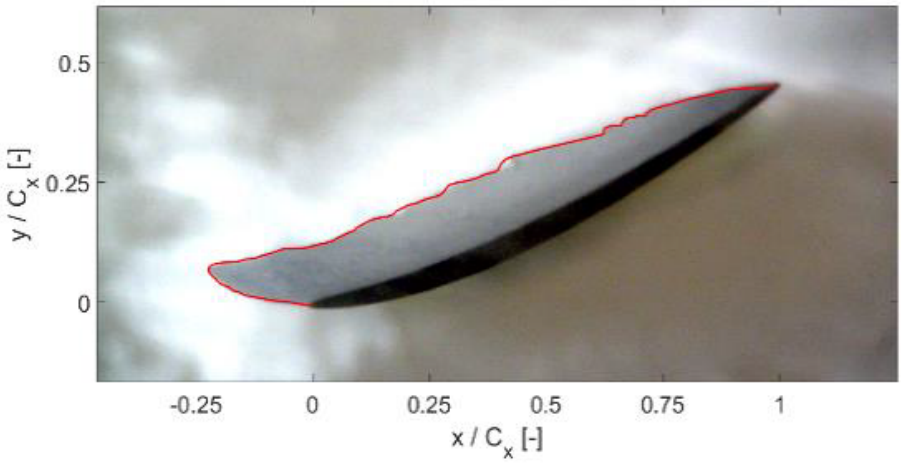

Figure 2.18: Backlit shadography method on a two dimensional (prismatic) stator airfoil test piece. Edge detection algorithm used to extract the accretion profile, as shown in red [71].

of the test piece. Three-dimensional flows induced by end wall effects and other non-idealities can lead to a non-uniform accretion profile. Unless a very short depth of field can be obtained, backlit shadography generally extracts the largest accretion profile along the span of the test article at each circumferential position. For axisymmetric test pieces it is possible to rotate the object on its major axis, record the edge profile at each rotated position and merge these profiles to produce a three-dimensional model of the ice accretion. This method has been successfully employed by Currie *et al.* [31] but is only applicable to axisymmetric geometries, not commonly found in engine realistic components.

Three-dimensional accretion shapes have been documented using casting methods [80], but this fails to obtain quantitative data. Laser scanning of the accretion using stereo vision has been conducted once the test piece has been removed from the tunnel, such as shown in Figure 2.19. Successful three-dimensional maps of accretion have been obtained using such device. However, this method requires the ice to be rapidly frozen to increase the surface reflectively and also the placement of circular stickers. These requirements prevent the method being used during the accretion process. Use of the Mid Infrared (MIR) spectrum has been found to produce good results when imaging ice formed by super-cooled water. However, infrared cameras have large physical size compared to visible spectrum cameras, due to the inherently

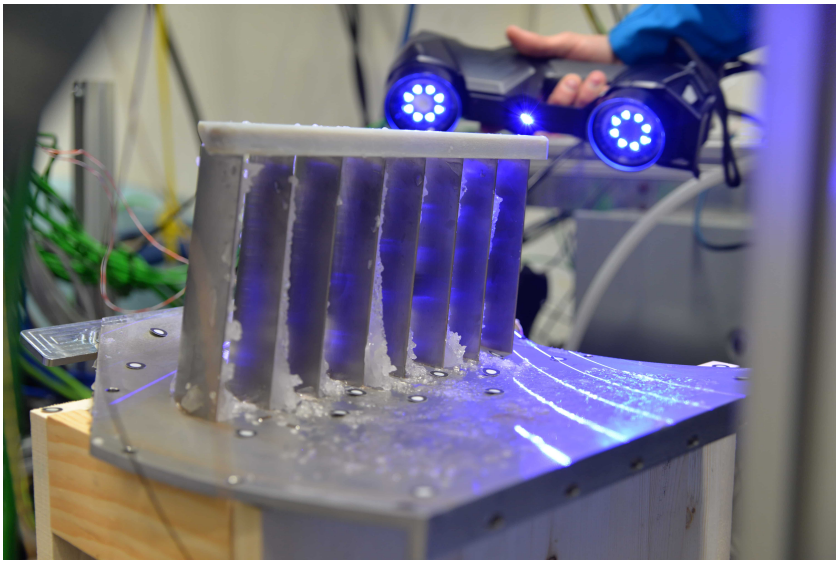

Figure 2.19: Laser scanning of an ice accretion of a complex test piece after ice exposure using a HandySCAN device. Method requires the ice to be fully frozen and for circular marker stickers to be placed around the test piece.

larger pixel size in infrared cameras. This limits the applicability of the method due to the small space constraints often imposed on both engine and wind tunnel tests.To date, no technique for quantitative, transient and three-dimensional ice accretion measurements for ice crystal icing exist in the open literature in the visible spectrum, and is a key element missing for obtaining essential experimental data.

2.4 Experimental Facilities

Experimental facilities for ice crystal icing are subdivided into two groups; stationary single component facilities and whole engine test beds.

University of Southern Queensland

The facility at the University of Southern Queensland (USQ), is an open circuit, ambient total pressure wind tunnel. The overall facility is shown in Figure 2.20a, and the ice generation system is detailed in Figure 2.20b. The maximum air speed in the ice core is 28 $\mathrm{m\,s^{-1}}$ (Mach 0.08), and total water content of 12 $\mathrm{g\,m^{-3}}$. Ice crystals are made by atomisation of water passed through a cloud of evaporated

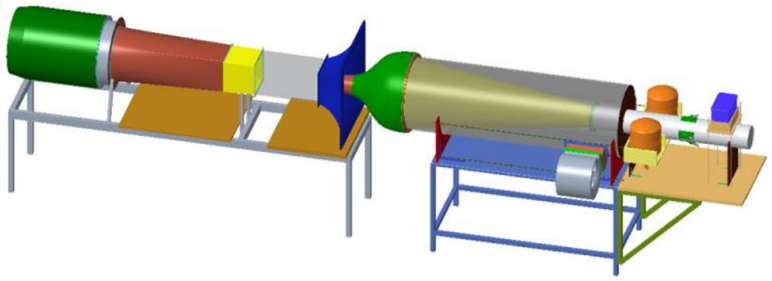

(a) Whole icing wind tunnel.

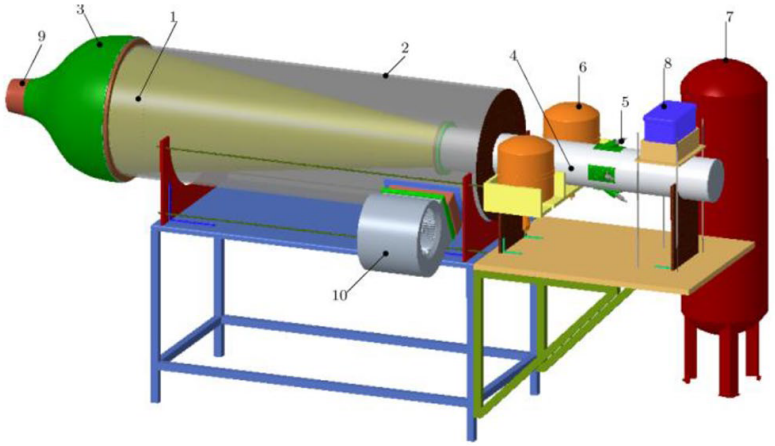

(b) Icing jet hardware consisting of: (1) perforated diffuser; (2) shell; (3) nozzle contraction; (4) spray guide pipe; (5) ultrasonic atomiser nozzle; (6) pressurised water tank; (7) compressed air vessel; (8) liquid nitrogen tank; (9) contraction nozzle lip; and (10) fan.

Figure 2.20: Icing wind tunnel at the University of Southern Queensland [81].

liquid nitrogen. The tunnel relies on natural melt of the ice crystals within a diffuser and does not have the capability of injecting supplemental water.

Altitude Icing Wind Tunnel

The AIWT is a closed-loop altitude facility, capable of reproducing icing conditions representative of up to 40,000 ft and Mach 0.55. Liquid nitrogen is used to freeze water droplets, produced via an atomisation process, and is capable of producing total water contents of up to 3.5 $\mathrm{g\,m^{-3}}$ [82]. Figure 2.21 shows a schematic of the wind tunnel.

Research Altitude Test Facility

Research Altitude Test Facility (RATFac) is an altitude chamber divided into two sections. On the cold side, ice particles are generated by an ice grinder system. On

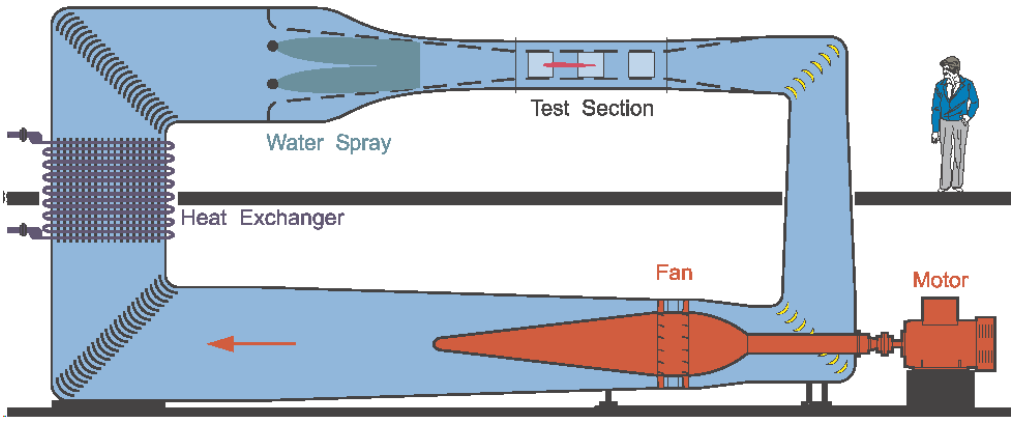

Figure 2.21: Drawing of the Altitude Icing Wind Tunnel (AIWT), at the National Research Council of Canada (NRC) [83].

the warm side, in which the test piece is situated, the humidity is controlled by steam injection and the total temperature is also controlled. Between these two sections is the transition, in which the crystals are transported from the cold section via an injection pipe, to the warm side where they are mixed with additional liquid water, to set the required melt ratio. The tunnel is capable of reaching altitudes of 40,000 ft and Mach 0.5. The wind tunnel is summarised in figure 2.22.

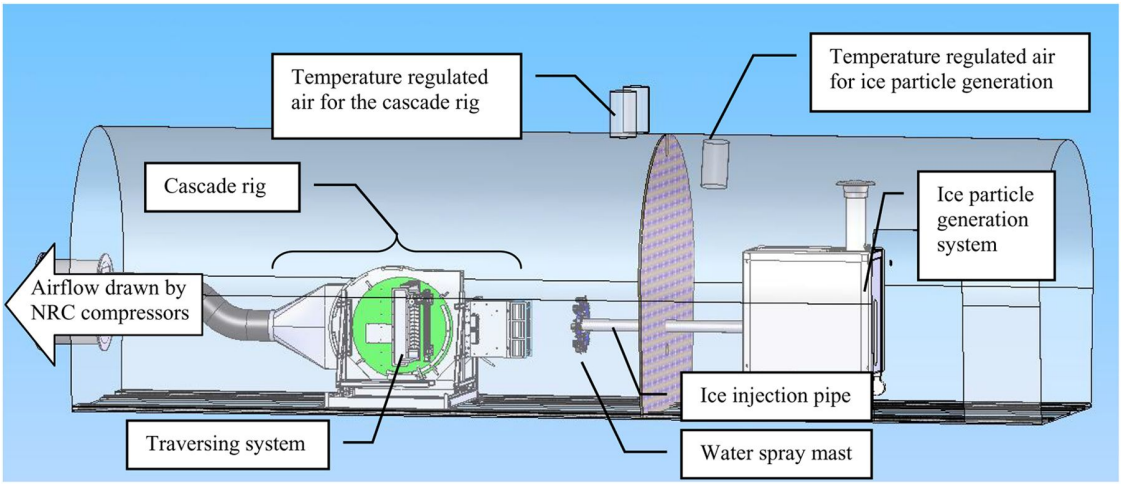

Figure 2.22: Schematic of the Research Altitude Test Facility (RATFac), at the National Research Council of Canada (NRC). Facility shown in its cascade configuration [84].

Icing Wind Tunnel Braunschweig

A novel wind tunnel has been produced at Technische Universität Braunschweig, where ice crystals are produced in a cloud chamber. This ice generation system is

thought to be more representative of natural ice in convection clouds. The tunnel is closed-loop, with a maximum speed of Mach 0.11 and maximum total water content of 1.1 $\mathrm{g\,m^{-3}}$. The tunnel can only be operated at ambient pressure. A schematic of the tunnel is shown in Figure 2.23.

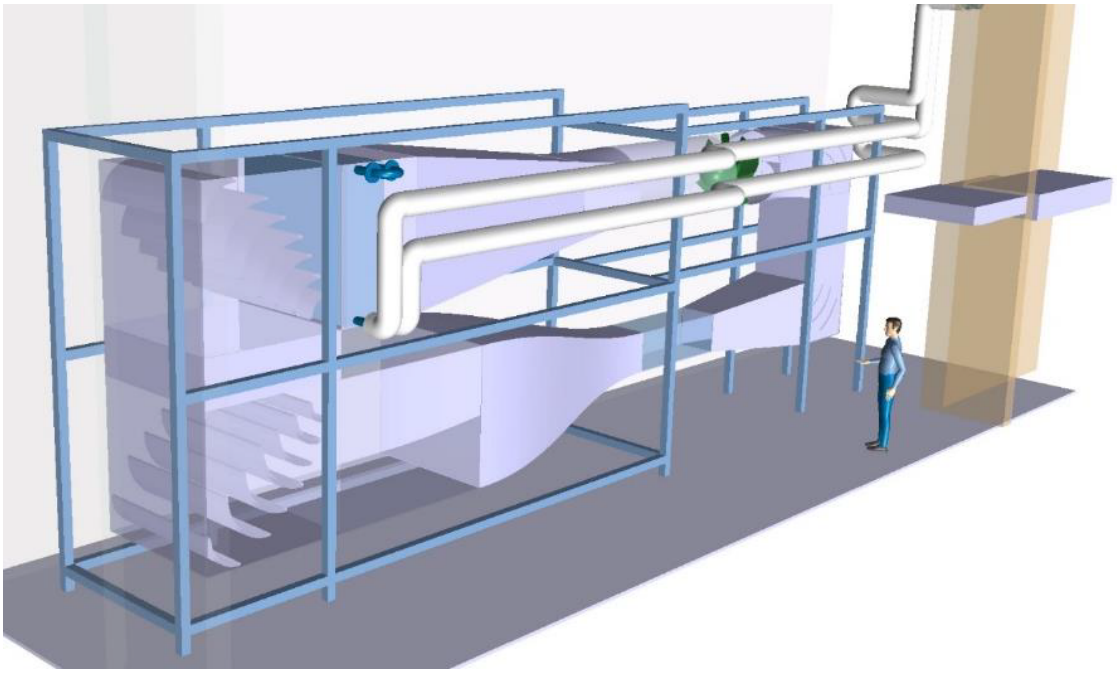

Figure 2.23: Schematic of the icing wind tunnel at Technische Universität Braunschweig [85].

Propulsion Systems Laboratory

The Propulsion Systems Laboratory (PSL), situated at the NASA Glenn research center, has two alitude test chambers which were previously used for research of gas turbine engines. One of the two altitude chambers (PSL3) has since been upgraded to have a water spray bar system and liquid nitrogen injection to simulate ice crystal icing using a freeze out process. It has the capability of testing full engines, with engine diameters up to 2.13 m, at altitudes up to 40,000 ft and Mach numbers to 0.8. A schematic of the facility spray bars, test section and exhaust is shown in Figure 2.24.

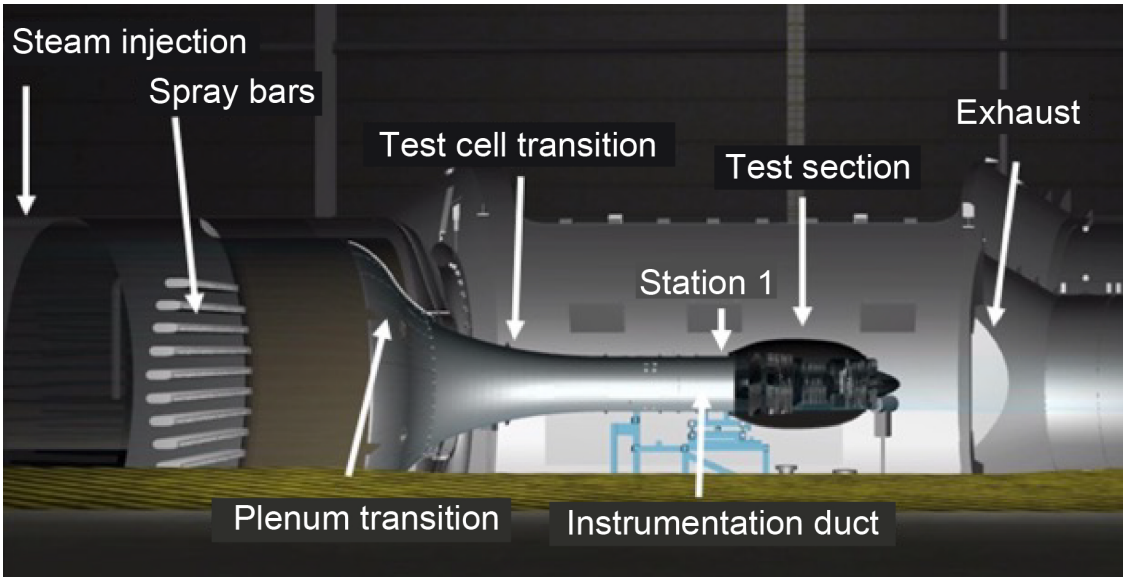

Figure 2.24: Schematic of the Propulsion Systems Laboratory (PSL) wind tunnel, with an engine connected [86].

Summary

A summary of the operating conditions of each facility is shown in Table 2.1.

Table 2.1: Operating conditions of the main ice crystal icing wind tunnels

Parameter	USQ		AIWT		RATFac		Braunschweig		PSL	
	Min	Max	Min	Max	Min	Max	Min	Max	Min	Max
T0 [°C]	-9	10	-30	45	-40	35	-20	20	-50	10
P0 [kPa]	94	94	19.4	101	15.3	93.1	101	101	11.1	87.5
Mach number [ ]	-	0.08	0.025	0.55	0.15	0.5	-	0.11	0.15*	0.8*
Relative Humidity [ ]	no control		no control		0.05	0.95	no control		no control	
$D_{v,50}$ [µm]	76	108	20	100	24	300	12	50	15	100
Ice Water Content [$g\,m^{-3}$]	0	0	0	0	2	12	0	20	0	0
Liquid Water Content [$g\,m^{-3}$]	0	12	0.1	3.5	0.5	4	0	1.5	0.5	8
Working Section [mm]	305x305		520x330		254x132		500x500		609x609 - 1828x1828	
Ice generation method	freeze-out		freeze-out		mechanical grinder		cloud chamber		freeze-out	

* Equivalent flight speed (calculated from the pressure ratio across the test vehicle).

2.5 Summary

After covering the relevant literature, it has been found that considerable work has gone into the study of ice crystal icing. The models produced have been able to predict accretion with reasonable accuracy in certain accretion regimes. However, it is clear that the models use large levels of empiricism to cover up a lack of knowledge of the physical process, and that certain processes are not included.

Most noticeably, the models lack realistic terms for breakup mechanisms, erosion and shedding, and the coupling between the accretion profile and surrounding flow field solution. Numerical ice crystal prediction programs assume that the flowfield is invariant with accretion, which is expected to be a false assumption for more complex geometries. The implementation of flowfield coupling is one of the two key contributions of the work in this thesis.

To build more sophisticated models, three-dimensional surface maps of the accretion will be required, as opposed to traditional two-dimensional methods. The second contribution of this work was chosen to be a development of a new measurement technique to capture transient changes in accretion profiles during the test.

3
Test Pieces

Contents

3.1 Stator Airfoil

A prismatic stator airfoil was designed and studied by Bucnkell *et al.* [71]. It was designed to be representative of a compressor airfoil but with constant radial profile. The geometry was chosen to provide geometric features such as a leading edge and concave pressure surfaces, which were more engine representative than previous geometries such as wedges and cones.

The chord length was 42 mm, span of 90 mm and camber of 27.5°. It was machined from solid Ti90-Al6-V4, with a surface roughness of approximately 2 µm Ra. Three span-wise thermocouples were located at mid chord positions.

It has been experimentally tested at RATFac in un-ducted flow. The blade root was attached to a rotary window for angle of attack control. A gap of 30 mm existed between the blade tip and adjacent window to prevent any accretion from building up on the window.

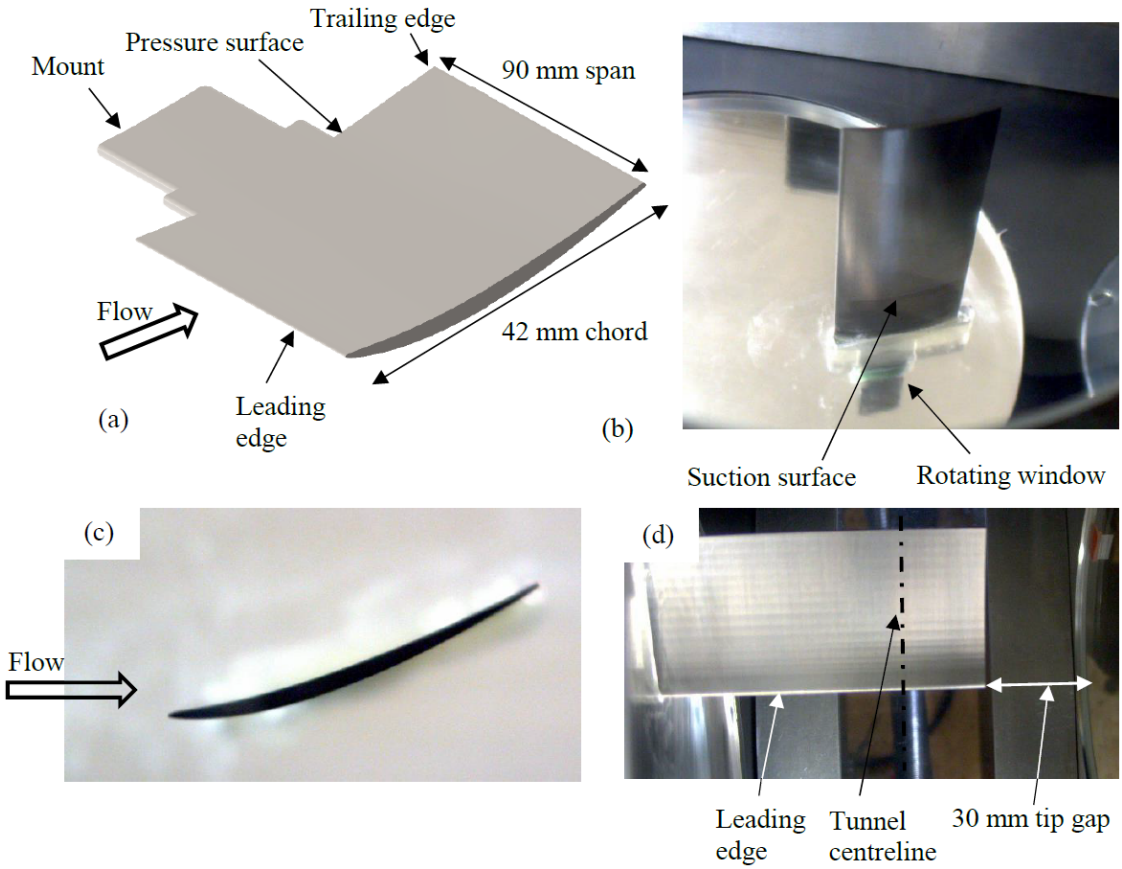

Figure 3.1: Stator test piece installed in RATFac. Images shown with the following views: (a) Isometric; (b) suction surface; (c) side (tip); (d) top down. Flow is left to right in all images [71]. Note: image has been distorted to hide geometric detail of the airfoil.

The test piece was backlit from behind the window holding the blade root, and a camera viewed down the axis of the blade span from the opposing window. The shadow formed by the accretion was recorded by the camera, allowing for the accretion profile to be extracted using numerical algorithms.

Back-lit shadography accretion measurement data from the 2017 tests conducted by Bucknell *et al.* [71] is used in this thesis for validation of the flowfield coupling of the stator test piece. Further tests were performed using the stator test piece as part of the work for this thesis to validate the three-dimensional accretion measurement techniques. These results are detailed in Chapter 4.

3.2 Swan Neck Duct

There has been a large range of high-quality experiments undertaken at the fundamental end of the spectrum of test piece design. These have focused on simple geometries, such as flat plates [32, 37], cones [36, 38], aerofoils [34, 79] and individual stator blades [71]. In comparison, there is limited experimental data in the open literature of more engine representative three-dimensional geometries. Several linear cascades have been used in ice crystal icing (ICI) experiments [84, 87], which have provided valuable qualitative insight into the effects of ICI in more engine like flowfields. However, there is a lack of quantitative engine representative data-sets needed for validating ice accretion codes.

With engine architecture from all Original Equipment Manufacturers (OEMs) moving towards geared fans, this leads to the inclusion of aggressive turning in the inter-compressor ducting typically referred to as Swan Neck Duct (SND), in the early stages of compression. This can be a location of particularly severe ice accretion due to the radial centrifuging of the ice and concave surface for impact. Although there has been testing of individual components, there is no testing that has coupled the turning effects of a linear cascade and a swan neck duct.

The test geometry used reproduces a typical civil turbofan S-shaped inter-compressor with features that can lead to the accretion on not only stator vanes but also the outer annulus of the swan neck duct passage. The linear cascade includes 8 stator vanes upstream of the swan neck duct with a positive lean angle. The vane profile selected was representative of that in an intermediate pressure compressor, with negative geometric incidence and positive lean. The inner annulus was simplified to be a flat plate to reduce the complexities involved in calibrating the Digital Image Projection (DIP) system with distorted optics. The test piece is shown in Figure 3.2a and a view of the stator cascade from inside the tunnel is shown in Figure 3.2b, where the blade camber and outer annulus curvature is visible. In Fig. 3.2b it can be seen that one of the blades has a penny feature at the

intersection with the outer annulus, representative of that in a variable incidence stator. The test piece and the mounting into RATFac is shown in Figure 3.2c.

One of the aspects of work for this thesis was the design of the complex testpiece in collaboration with colleagues from the OTI and I was solely responsible for the design, integration and analysis of the accretion measurements. The analysis of the accretion measurements are detailed in Chapter 4, and the full results of the experiment are detailed in Appendix A.

3.3 Triple Airfoil

Current numerical capabilities do not allow for complex geometries such as the swan neck duct test piece to be analysed. To bridge the gap between non-ducted geometries and a complex cascade, a triple airfoil cascade was designed as part of this thesis to capture the effects of the change in aerodynamic flowfield in response to the accretion. The blade profile was a NACA 0018 airfoil, with a 200 mm chord and 570 mm span (with 1 mm tip/root gap) when mounted in the tunnel windows. The trailing edge was cut to have a 1 mm thickness for achievable machining thickness. The use of different mounting windows allow the blade pitch to be set at either 60 or 80 mm, and angle of attack to be either 0 or 10°. The test piece can also be tested in a single airfoil configuration at zero angle of attack.

The main section of the airfoil has a hollow cross-section, with a 3 mm wall thickness. To mitigate warping during the manufacturing process, three span-wise ribs were added at mid chordal positions. End caps of the same outer profile are connected with the main airfoil section to connect onto the windows. Tie rods were used to connect the whole assembly. The test piece is shown schematically in Figure 3.3.

Thermocouples were mounted to the internal surface at three chordal positions (TC1, TC2, TC3 as seen in Figure 3.3), at mid-span and 75% span.

This test piece has been designed and built as part of the thesis, for a test that was not able to be conducted during the time frame of the PhD due to international boarder constraints for access to Canada, caused by the COVID 19 pandemic [88].

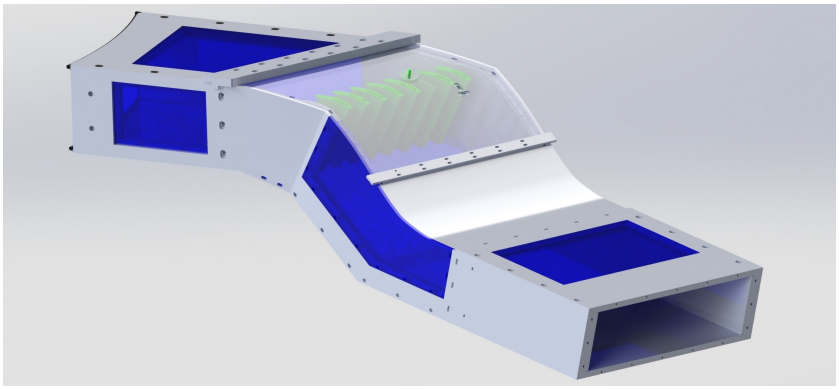

(a) Schematic of the test piece with the outer annulus section transparent for clarity

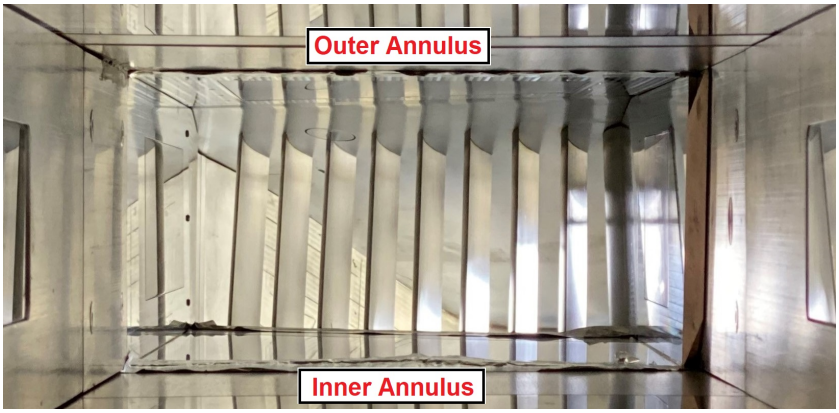

(b) View of cascade blade row from the RATFac cascade bell-mouth inlet.

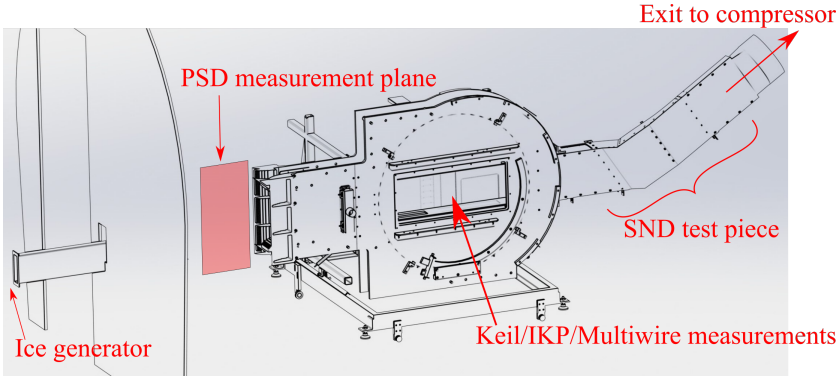

(c) Schematic of test piece connected onto the cascade rig in RATFac.

Figure 3.2: Swan neck duct (SND) test piece.

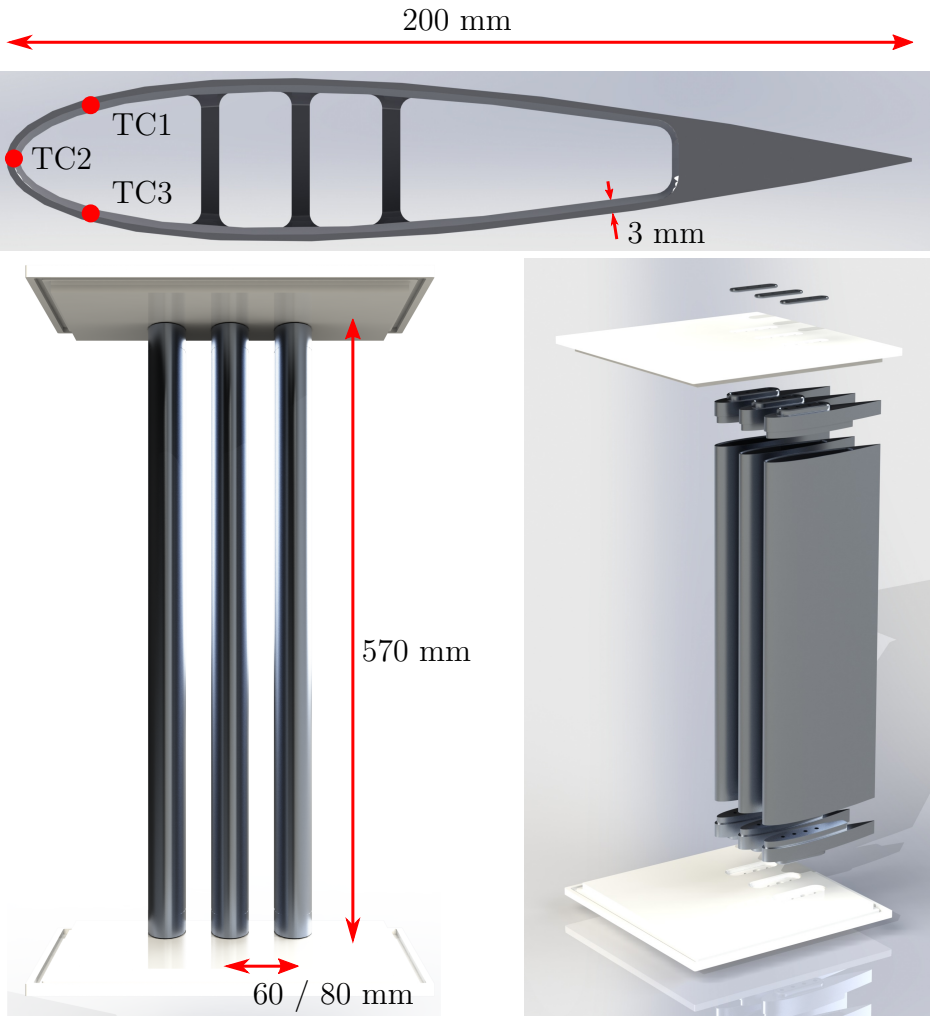

Figure 3.3: Design of triple airfoil test piece.

The test piece geometry has been used in this thesis to show the functionality of the updated numerical model. To validate the flowfield coupling of this test piece the experimental data will be required, which will be conducted after thesis submission when international borders reopen.

4

Development and Validation of three-dimensional Accretion Measurements

Contents

4.1 Measurement Techniques

Previous research has used camera views for qualitative information of icing severity, or backlit shadography methods for two-dimensional quantitative measurements.

For more advanced analysis of test data and validating three-dimensional numerical models, a three-dimensional accretion thickness needs to be measured. The method needs to be non-intrusive and be able to record live during the experiment (i.e not require re-working of the ice post test, generally involving rapid freezing of the ice to increase its opacity). In machine vision, stereoscopic imaging has been utilised to obtain three-dimensional images using two independent cameras. Both cameras image the same object but are offset and angled relative to each other. This methodology dates back to the second world war in which image pairs were used to view three-dimensional images of the enemy zones. To determine depth information, known objects need to be compared between both image data sets. The comparison of both data sets to find commonality, known as the correspondence problem, is non-trivial and is especially difficult for moving objects, which is the case for dynamic ice accretion analysis. To aid this problem, it is common to overlay a pattern onto the object being measured. This allows for automated algorithms to more easily cross compare data-sets over the temporal morphing of the imaged object. Salvi *et al.* found that one of the cameras could be replaced by a projector [89], creating a system termed Digital Image Projection (DIP). This method has previously been used to measure water transport over an airfoil [90] using their in-house developed optical system and to SLW icing on a wind turbine blade using a commercially available system [91].

This work focuses on developing two optical systems; a system with a single camera and single laser and a stereo system with a pair of cameras and a single laser. In this thesis these two systems will be referred to as DIP and stereo.

4.2 Ice Reflective Properties

Surface reconstruction of objects with low surface texture requires the imaging of a projection pattern reflected off the object's surface. Assuming that the surface is fully reflective, the direction of the reflected ray is dependant on the incidence angle and local surface normal. Perfectly smooth surfaces create a specular reflection, whereas a rough surface will create highly scattered reflection, termed a diffuse

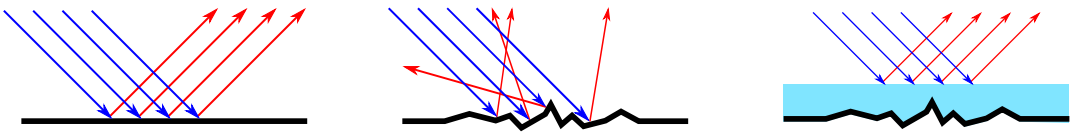

Figure 4.1: Diffuse vs specular reflection on a smooth (left), rough (middle) and wetted (right) surface. Ice crystal icing accretion typically has a rough accretion surface with a water film flow on top, leading to a mostly specular reflection.

reflection. A water film on a rough surface creates a smooth outer surface which creates a specular reflection, as summarised in Figure 4.1. Typical test pieces used in ice crystal icing have a low roughness leading to a specular reflection prior to accretion. As the accretion initiates a dominant water film runback is observed which again leads to a mostly specular reflection. In the latter stages of accretion, for conditions with low melt ratios, a relatively dry rough surface can form, which have a diffuse reflection of the incoming light rays.

For a purely specular reflection, the laser node on the surface is only viewable if the camera axis is directed at the reflected ray. A surface with infinitely small isotropic roughness creates an equal intensity of reflected light in all directions, and can therefore be viewed from any direction. In real experiments, the reflection characteristics are between these two extremes, and therefore the viewing angle of the camera should be located close to the reflectance angle of the central beam.

Ice and water are not fully reflective, meaning that some of the incoming light will transmit through the accretion. In a typical ice crystal icing accretion, there is a layer of water on top of the ice. Some of the incoming ray will reflect off the water surface, with the remainder transmitting into the water layer. Further reflections also occur at density changes; at the ice-water interface and also the ice-substrate interface. This is shown schematically in Figure 4.2. In some conditions further reflections also occur at the inner water layer and impurities in the ice layer such as air bubbles and grain boundaries. This work aims to measure the spatial position of the outer accretion surface and not the points of sub-surface reflections. If such

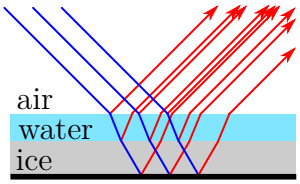

Figure 4.2: Schematic of reflectance and transmission of an incoming ray onto an accretion surface with water layer. Typical ice thicknesses vary from 1-40 mm and water film thicknesses vary from 20 µm to 1 mm. Distance between accretion surface and measurement system is typically greater than 100 mm.

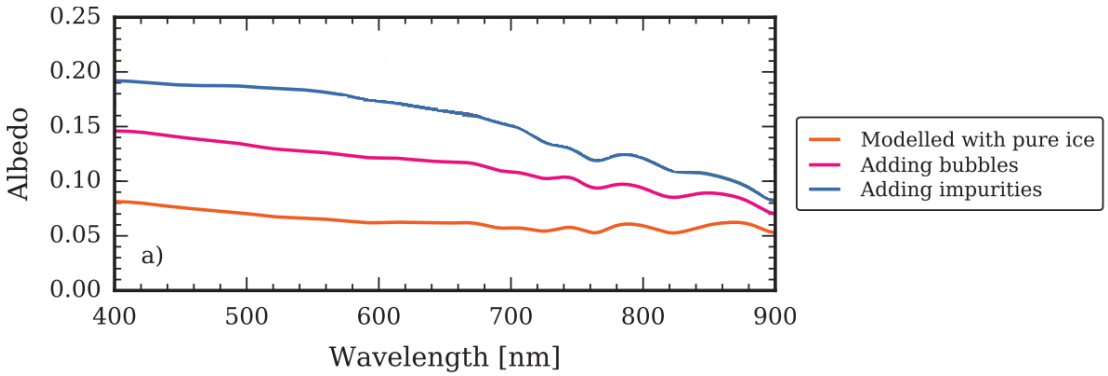

Figure 4.3: Effect of wavelength on the reflectance of light upon ice in the visible spectrum [92].

sub-surface measurements were desired, the calibration would need to account for beam refraction within the accretion, which is out of the scope of this work.

Research in the geology community has studied the albedo (percentage reflectance) of pure ice and ice with bubbles and impurities, as shown in Figure 4.3 [92]. With only a maximum of 20% of the incident light ray being reflected, a large proportion is left to be reflected off deeper impurities and the base surface. The optical power of the projection needs optimised such that a sufficiently strong reflectance of the top surface can be measured by the camera sensor, while also minimising the intensity of the sub-surface reflections.

It should be noted from the data in Figure 4.3 that the reflectance of ice does not significantly vary in the visible spectrum, and therefore the wavelength of the projection should not have a strong influence on the system accuracy if kept within this range.

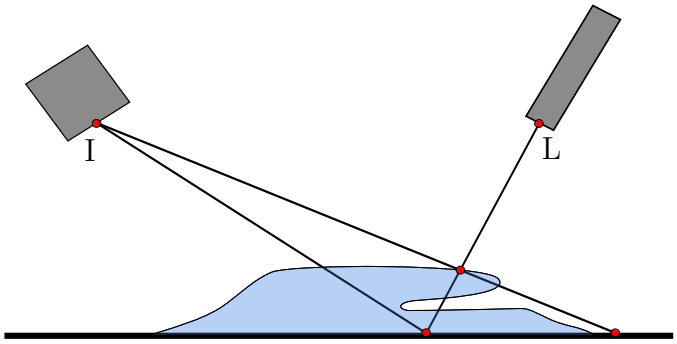

Figure 4.4: Over-hanging ice surface which cannot be measured using a single, static laser.

4.3 Optical Measurement Limitations

A system with a single laser and only one or two cameras has inherent limitations on the shapes which it can accurately measure. If there are complex accretion shapes with overhangs or large variations in ice thickness, the camera may be optically blocked from observing the whole accretion profile. For example, in Figure 4.4, only the top surface over the overhang will be captured, and the inner surface will be omitted from the measured accretion profile. This will lead to an over-predicted accretion volume, essential for the prediction of the impact of shed ice. Alternatively, there may be large scale changes in surface topology along the accretion such as shown in Fig. 4.5. In this condition, the laser path is not blocked by the ice, however, the light path from the laser reflection to the camera is blocked by an adjacent large scale accretion site. The calibration will not have taken the diffraction through the adjacent ice into account, meaning that the true ice thickness will not be accurately measured.

To minimise these effects a traversable laser/camera system, or multiple static laser/camera systems can be utilised, however, this is out of the scope of this work. For a single laser/camera system, the devices need careful positioning to minimise these effects for the expected accretion profile topology.

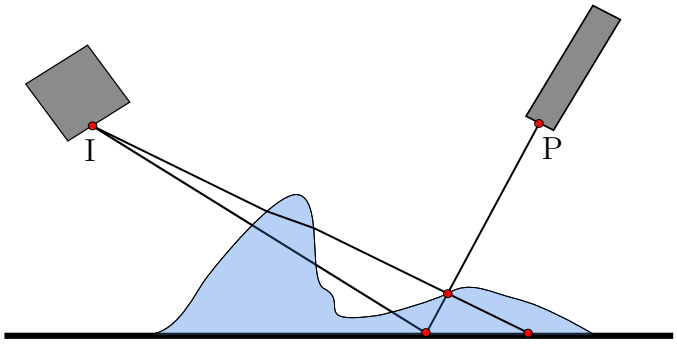

Figure 4.5: Optical path of the laser light between the point of reflection on ice surface and the camera is blocked by an adjacent ice peak. Light path will be diffracted through the adjacent ice peak which is unaccounted for in the calibration.

4.4 Optical Calibration

4.4.1 DIP

Figure 4.6 shows an idealised DIP system. For clarity, only a single node of the projection array is shown in the diagram. The laser has a focal point, L (position where all laser ray lines diverge from), and the camera has a focal point I. The horizontal separation between the camera and projector is defined as η and the vertical height of the projector/laser from the reference plane as λ.

When the laser node is projected onto a reference plane it is positioned at point A. When a thickness of ice is present above the reference plane, the node originally located at A moves to point B, and again to C with further accretion. From the perspective of the camera, when the node spatially moves from point A to B, the camera observes a translation of the node from point A to b. Point F is defined as the point vertically below B on the projection plane.

The goal of the method is to determine ice thickness, $\vec{FB}$, by measuring the displacement of projection nodes, $\vec{Ab}$. From similar triangle relationships, the ratio between $\vec{Ab}$ and $\vec{FB}$ can be related to geometrical parameters of the relative positions of the camera and projector and the ice thickness (Eq. 4.1). By re-arranging Eq. 4.1, the relationship between ice thickness, $\vec{FB}$ and node displacements, $\vec{Ab}$ is found (Equation (4.2)). A similar analysis can also be performed for when the camera and projector are not vertically aligned.

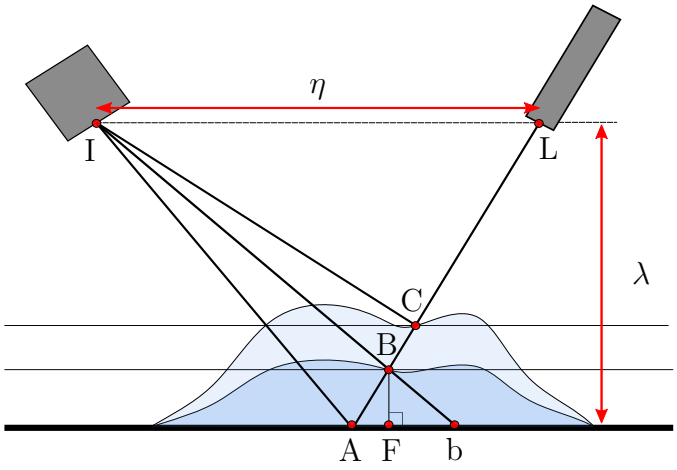

Figure 4.6: Simplified DIP system showing the relative position of imaging plane (I), laser ($\mathcal{L}$), laser node position at three heights (A, B, C), and equivalent imaging position (b).

$$\frac{\vec{Ab}}{FB} = \frac{\eta}{\lambda - \vec{FB}} \tag{4.1}$$

$$\vec{FB} = \frac{\frac{\lambda}{\eta}\vec{Ab}}{1 + \frac{\vec{Ab}}{\eta}} \tag{4.2}$$

Direct measurement of parameters η and λ is not feasible due to being located within the camera lens/laser. Instead, a calibration is performed by traversing a reference plane through known distances using a linear traverse and measuring the node displacements observed in the images. The parameters η and λ are then optimised to get the correct fitting relationship.

To find the spatial position of the node backward ray tracing is used. If the initial position of each node on the test piece and the bream spreading angle is known, then the position of the laser can be found using ray intersections. By backward tracing of each ray from the test piece to a position where the vertical height above the test piece is equal to $\vec{FB}$, the position of the new node location is found. Typically the laser is located outside of the wind tunnel to prevent flow disturbances and therefore the light is diffracted through a window. This can be accounted for if the location of the window and its diffractive properties are known.

4.4.2 Stereo

The calibration of a stereo system involves calibrating a camera pair. Unlike in DIP, the laser is only projected onto the field of view for the experiment and is not included in the calibration. The calibration procedure involves taking photos of a checker-board target of known grid size at a range of positions around the whole field of view of the cameras. Estimates of the intrinsic parameters (lens focal length, optical center, lens skew) and extrinsic parameters (relative translation and rotation of the camera pair) can be calculated using techniques such as [93] which is incorporated into the MATLAB Computer Vision Toolbox [94].

Figure 4.7 shows a simplified stereo camera system, where the left camera has an optical center of O and the right camera has an optical center O'. The aim of stereo-vision is to locate corresponding pairs of pixels between two (un-distorted) camera views and use triangulation to locate the real-world coordinate. For a pixel in the left-hand image, x, the real-world point could be located at any position along the ray containing the points X. The spatial positions X correspond to pixel locations x' on the right-hand image plane. The line connecting the possible locations of x' is termed the epipolar line. For a given pixel in the left-hand image, x, the corresponding pixel in the right hand image is located along the epipolar line, thus reducing the search space from the total sensor area to a 1D line. Re-projecting both image planes onto a common plane which is parallel to the line connecting the optical centers (a process called image rectification), the epipolar lines become horizontal and therefore corresponding pixel pairs lie on the same row.

Finding the corresponding pixel between the left image and the right-hand epipolar line requires image texture so that cross correlation algorithms can be used. The texture in some applications come from the surface texture of the imaged object. In other applications, such as when imaging ice accretion where limited surface texture exists, additional texture can be imposed by projecting laser light onto the object.

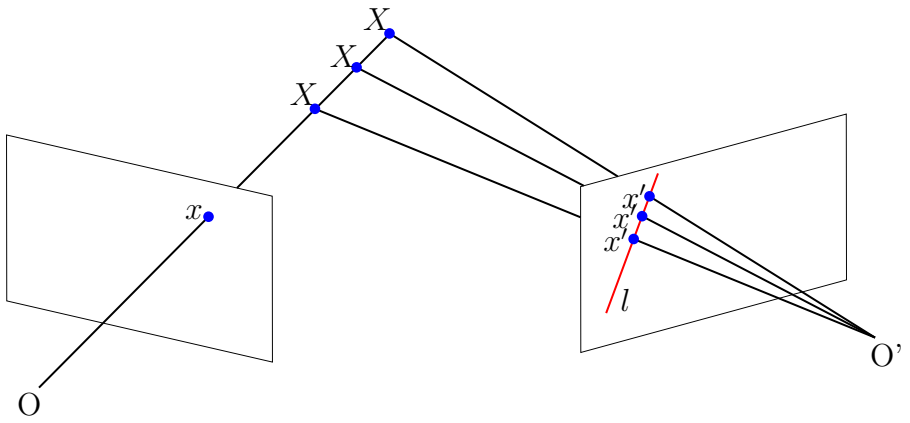

Figure 4.7: Schematic of a simplified stereo-vision system. For a given pixel position, x, in a camera with optical center O, all posible pixel positions in a second camera with optical center O' is shown by the epipolar line in red.

4.5 Post Processing

4.5.1 DIP

The post-processing of DIP data requires the knowledge of the displacement of the node centroids. This can be computed using spatial auto-correlations of successive frames if the reflectance of the body is spatially and temporally invariant. When imaging ice, fast changes in surface state can occur due to run back of water films, or the impingement of large agglomerates. In such scenarios, the image of the reflected ray of light will be observed differently. If these changes occur between successive frames, then the application of an auto-correlation to find the node translation will likely provide a poor result, and a manual method will need to be applied.

Beam divergence and camera lens distortions mean that the calibration for each laser node is unique. The beam therefore needs to be identified and can be performed by using a known laser beam position on the clean test piece surface. During the accretion process, some light rays can get optically blocked by peaks in adjacent accretion, meaning that the post-processing needs to identify missing nodes and be able to assign them to the correct light ray once the obstacle is removed. This can be overcome when imaging non-transparent objects by using a coded projected pattern [95], however the poor reflectivity of the ice accretion means that the reflected image of the projection is highly distorted, reducing their usefulness. These complexities

often lead to a large degree of manual input to process the DIP data, which can be very time consuming when a projected pattern has a high spatial resolution of nodes.

4.5.2 Stereo

In stereo-vision spatial auto-correlations are also used when calculating the disparity, however both images are taken at the same moment in time but viewed from different angles. If the light reflected from the object is not perfectly diffuse, each camera will observe a different light pattern. Whilst developing the optical system, a projection screen designed to have a uniform textured surface was used to limit the need for optimal camera viewing angles. Two cameras imaged a laser node reflected off the screen, viewing at an angle normal to the surface, and an angle equal to the reflectance angle (as shown in Figure 4.8). Even with a surface designed for a diffuse reflection, the observed node shape of the undistorted images was different. If the stereo post-processing did a row-based cross-correlation to compute the image disparity (commonly known as block matching), errors are introduced because of the difference in the observed reflection. An improved method computes line optimisations along multiple directions and sums the cost of each - a method known as semi-global matching. This method has increased computational cost but reduces the errors induced by cameras observing a different reflected pattern. This method has been implemented following the work of Hirschmüller [96].

The positioning of stereo camera pairs needs to consider the relative angle of each camera with respect to the laser to maximise the amount of specular reflection received by each camera, whilst maximising the relative angle between the camera pair.

Stereo vision calculates the spatial position of each pixel in the cameras field of view. In scenarios with sufficient image texture between the laser nodes, this creates a dense surface reconstruction. Typically there is little image texture between the laser nodes when imaging ice crystal icing, which can lead to anomalous disparity calculations. If the node spacing is too large, then post-processing is required to only accept the data in regions around each node.

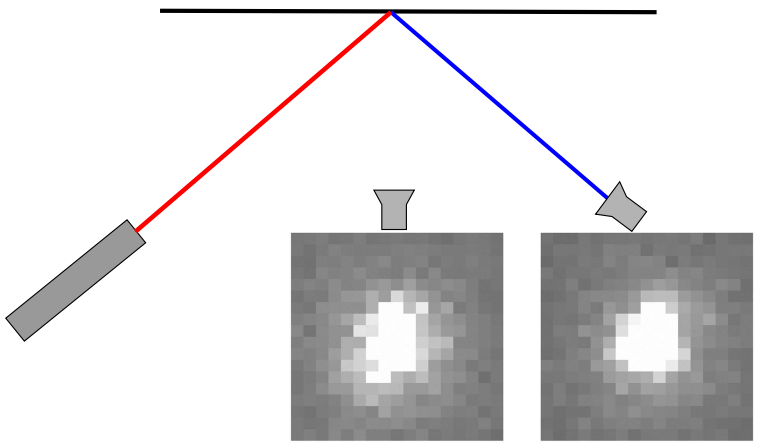

Figure 4.8: Change in observed node shape at different viewing angles. Camera optical axis normal to surface (left) and aligned with the reflectance angle (right).

4.6 Comparison of DIP vs SteroVision Errors

To compute the minimum achievable error of both the DIP and stereo-vision systems, a non-transparent projection screen was traversed through known distances using a linear scale and the projection pattern was recorded. The use of a flat non-transparent projection screen causes the reflective behaviour of the laser pattern to be invariant of the displacement, therefore leading to increased temporal autocorrelation accuracy in the DIP system, and also improved spatial autocorrelation in the stereo system. A system of two cameras and a single laser was set-up, for which the laser and camera-1 were used for DIP, and camera-1 and camera-2 were used as a stereo pair. The relative angle between the laser and camera-1 was set to equal the angle between the camera pair. This system is shown in Figure 4.9 where the working distance and relative angles are representative of that achieved in icing wind tunnels.

Figure 4.10 shows the error of both the stereo and DIP systems for a displacement from 0-10 mm. The error of the DIP system was lowest, with the stereo having roughly twice the error. The error is of similar magnitude when a window is placed between the optics and the test piece.

For both systems the error can be reduced by; increasing the angle between the opposing camera/laser, increasing the camera resolution, increasing lens focal length and decreasing the working distance. The advantages of the DIP system

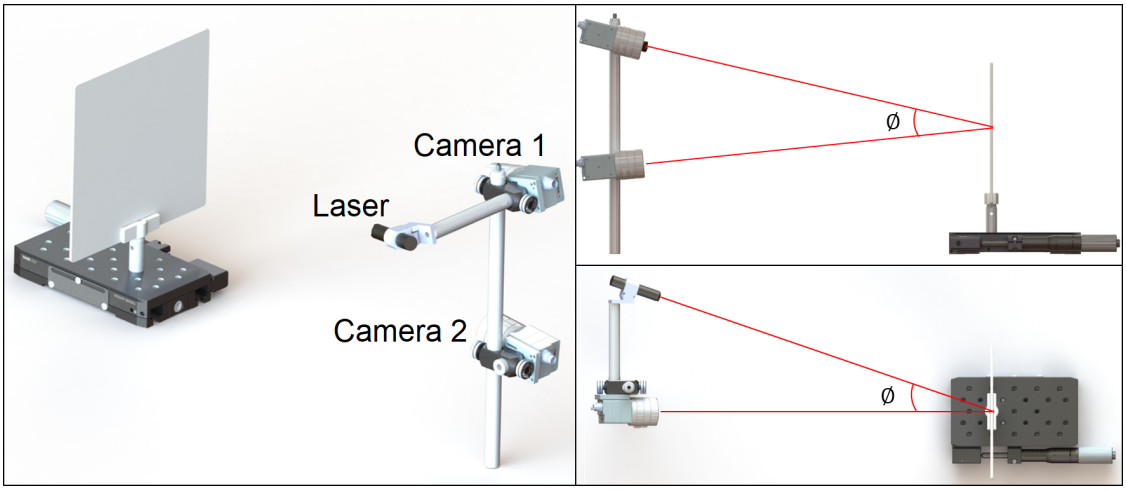

Figure 4.9: Experimental setup for DIP vs stereo comparison. Isometric view (left), side view (top right), top view (bottom right). Angle between the two cameras is set to be the same as the angle between the laser and the camera.

are the accuracy and simplistic system design, however is limited by its tedious post-processing and the calibration procedure being difficult to conduct when there is limited available space. Conversely, the stereo system is easier to calibrate and post-process but has higher error measurements in lab conditions.

Distortion of the reflected laser light with the introduction of a water film on the ice surface increases the error in the DIP system due to poor spatial auto-correlations of successive frames of the node positions. In such scenarios, the error of the DIP is comparable to that of stereo systems, for which the light distortion does not influence the post-processing to the same extent due to both frames being taken at the same moment in time.

4.7 Effects of Aperture

4.7.1 Depth of Field

A simple camera model consists of a lens, aperture and a sensor. Figure 4.11 shows a point source of light, P1 (with P1 located at the tip of the arrow). Light is emitted from P1 in all directions, with some of these light rays passing through the lens. A perfect lens has a single intersection point of all incoming rays, and the sensor in Figure 4.11 has been located so that it matches the ray intersection point. For

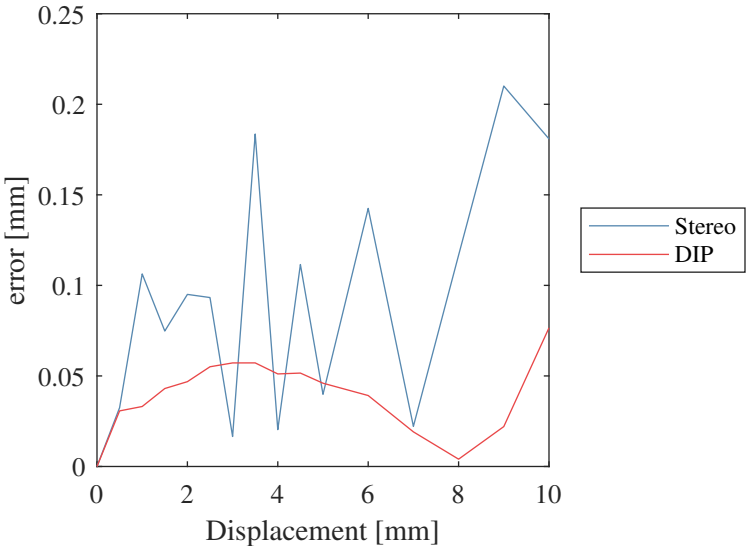

Figure 4.10: Plot of error in the measurement of both the stereo and DIP systems at displacements between 0 to 10 mm.

this configuration, P1 is in focus. Moving the light point source to position P2, the light rays no longer converge on the sensor plane, meaning that a circle of light reaches the sensor as opposed to a single point. The circle of light is commonly known as the "circle of confusion". Similarly, moving the point source rearwards to position P3, an out of focus beam of light reaches the sensor.

Placing an aperture in front of the lens (bottom diagram of Figure 4.11) reduces the angles of rays passing through the lens causing a reduction in the diameter of the circle of confusion.

In the application of accretion measurements, calibrations are conducted for a given sensor position, meaning that the focus cannot be altered. The depth of field of the lens must be sufficiently large for the expected accretion size, and it is desirable for the clean test piece and largest expected accretion to be equally de-focused. Such focal point is not the midpoint of the two extents and needs to be estimated.

Estimation of the circle of confusion for a given aperture and distance between in-focus image planes was studied by Peterson [97]. Figure 4.12 shows a lens and two objects at a distance U_f and U_n from the camera lens, which has an aperture of diameter D. Each object is in focus at the image planes at a distance V_f and

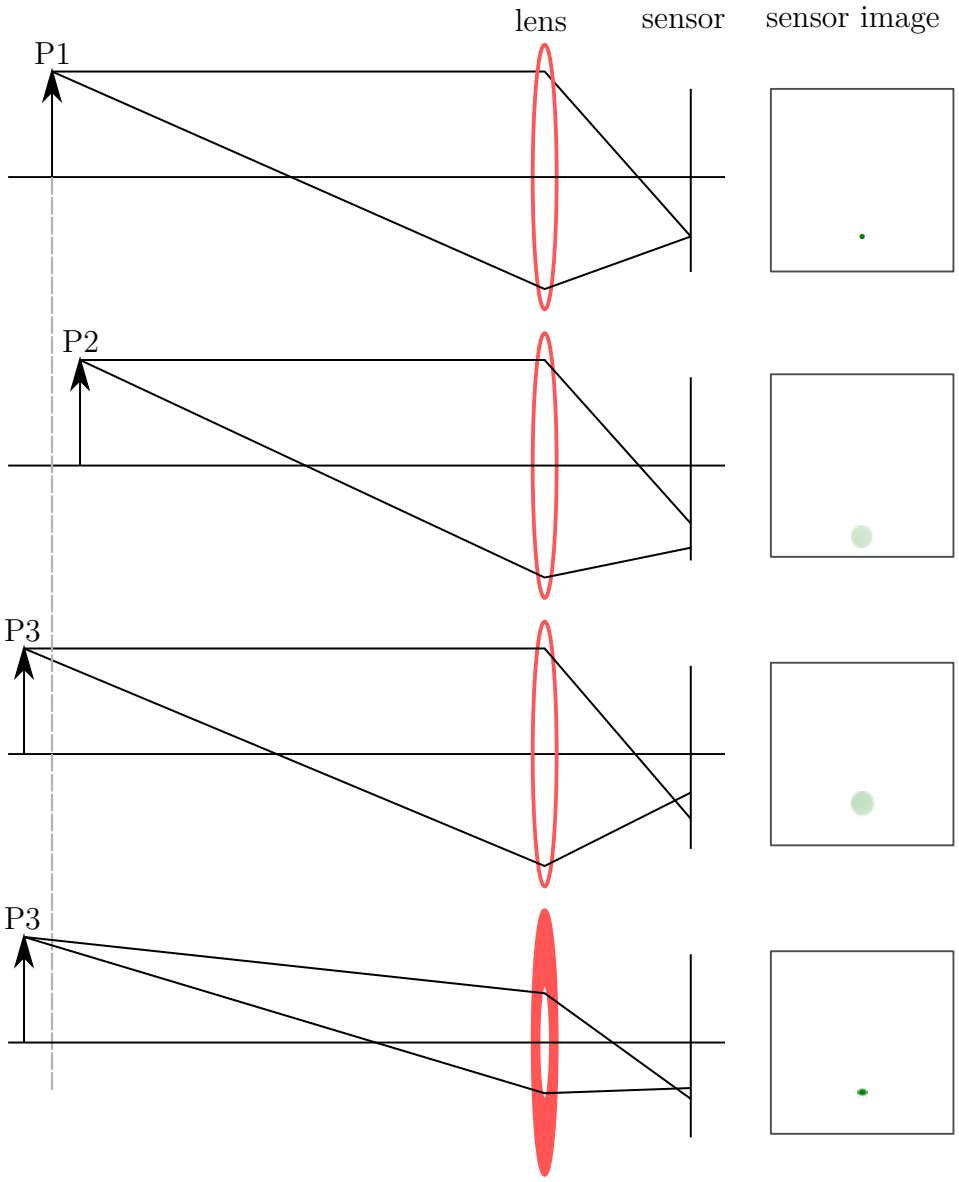

Figure 4.11: Effect of aperture on depth of field. Point source of light is located at P1, P2 and P3. Lens and sensor remain stationary. Out of focus point sources P2 and P3 have a finite circle of confusion which is reduced with the application of an aperture.

V_n respectively. The sensor is situated at image position V and is focused at object position U.

To have equal de-focus at the object distances of U_f and U_n, they must have an equal circle of confusion size, c. From similar triangle relationships, the relationship between V_f to V, D and c can be found (Equation (4.3)), and similarly for V_n (Equation (4.4)).

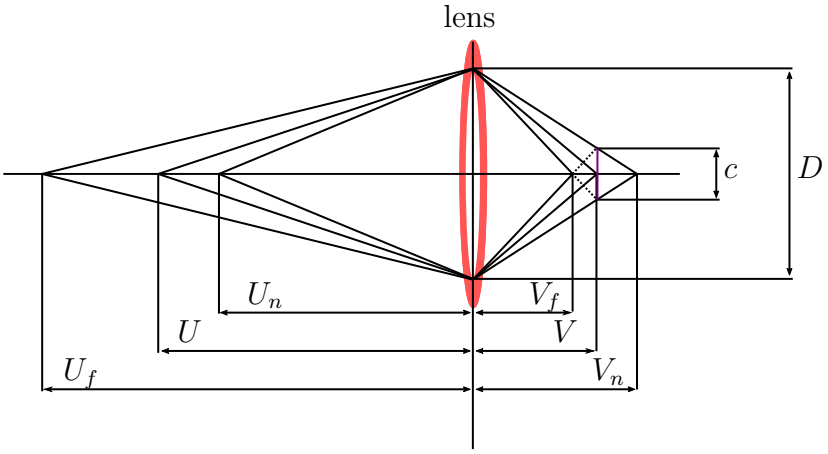

Figure 4.12: Schematic of the relationship between image and object planes for a symmetric lens.

$$\frac{V_f}{D} = \frac{V - V_f}{c}, \quad V_f = \frac{VD}{D + c} \tag{4.3}$$

$$\frac{V_n}{D} = \frac{V_n - V}{c}, \quad V_n = \frac{VD}{D - c} \tag{4.4}$$

Combining Equation (4.3) and Equation (4.4) gives the image distance to provide an optimal focus of both the far and near objects (Equation (4.5)). Use of the thin lens equation (Equation (4.6)), where f is the lens focal length, gives the required focusing object distance (Equation (4.7)). which is found to be the harmonic mean of the two image distances. For a DIP system measuring ice accretion, U_f is known from the distance to the test piece, and U_n can be estimated from the expected ice accretion size so that the required focusing object distance can be calculated.

$$V = \frac{2V_nV_f}{V_n + V_f} \tag{4.5}$$

$$\frac{1}{U} + \frac{1}{V} = \frac{1}{f}, \quad V = \frac{Uf}{U - f} \tag{4.6}$$

$$U = \frac{2U_nU_f}{U_n + U_f} \tag{4.7}$$

Digital cameras have a finite pixel size, meaning that if the circle of confusion is less than the pixel width, then the light rays are observed as being in focus. The

maximum distance between objects that are in focus is termed the depth of field. To determine if the level of de-focus between the limits of the desired field of view is acceptable, it can be compared to the size of the pixel in the camera sensor.

Equating the common variable of V in Equations (4.3) and (4.4) gives Equation (4.8). This can be re-arranged to find c (Equation (4.9)) in terms of the unknown image distances. Using the definition of lens f-number, N (Equation (4.10)), and the thin lens equation (Equation (4.6)) gives the size of the circle of confusion in terms of known object distances and lens f-number (Equation (4.11)). This can be used to determine what f-number is required to get sufficient depth of field to ensure the circle of confusion is less than the size of a sensor pixel.

$$V = \frac{V_f\,(D + c)}{D} = \frac{V_n\,(D - c)}{D} \tag{4.8}$$

$$c = \frac{D\,(V_n - V_f)}{V_n + V_f} \tag{4.9}$$

$$N = \frac{f}{D} \tag{4.10}$$

$$c = \frac{1}{N}\frac{U_n\,(U_f - 1) - U_f\,(U_n - 1)}{U_n\,(U_f - 1) + U_f\,(U_n - 1)} \tag{4.11}$$

While these equations are for a simplified symmetrical lens, they provide a good starting point for finding the required lens f-number for the desired depth of field and the position of where to focus the lens.

4.7.2 Ray angles

Figure 4.13 shows a schematic of a diffuse and specular reflection with an open and closed aperture. Diffuse reflections rebound light in all directions, meaning that even with a small aperture the reflected light will reach the camera sensor. A specular reflection rebounds at a single angle, meaning that with a reduced aperture diameter, the likelihood of the light reaching the sensor is reduced.

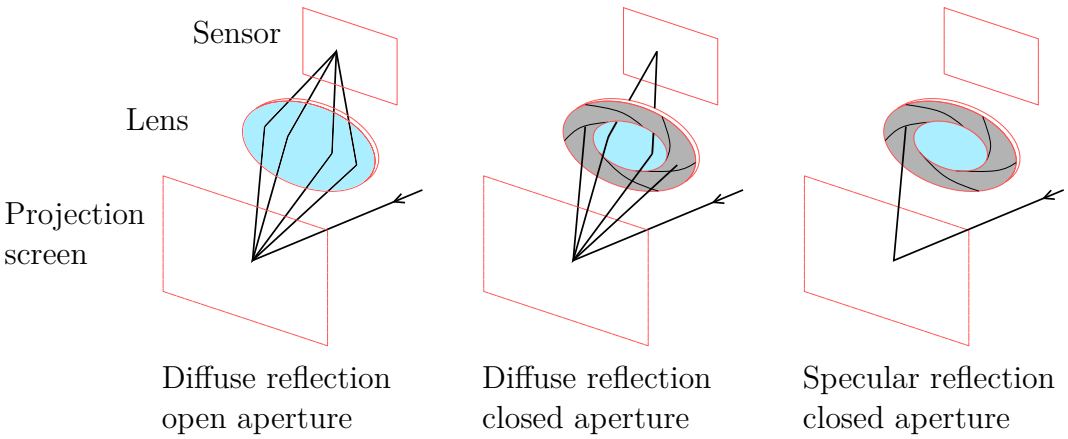

Figure 4.13: Diffuse vs specular reflection with open and closed apertures.

Engine realistic test pieces are made out of metallic compounds and are machined to have a low surface roughness. The reflective properties of such surfaces are closer to specular than diffuse, meaning that the reflected laser light has a greater intensity in certain directions. This reflective property is similar to what is observed when imaging accretion with a water layer. The use of small apertures can prevent the reflected rays from reaching the sensor, thus inhibiting the accretion measurement. Figure 4.14 shows the observed laser reflection off a polished metal surface (close to a specular reflection) at a range of lens f-numbers. Camera exposures were adjusted to account for the change in aperture diameter. At the widest aperture setting (f/2), a poor image of the laser reflection was observed. As seen in the next section, this will have been caused by lens aberrations. Increasing the f-number (decreasing aperture size), created good images of the reflected node at both f/4 and f/8. At the minimum aperture size (f/22), the peak laser intensity was not recorded. This will have been caused by the imperfect alignment of the optical axis and reflection axis, and also due to diffraction.

4.7.3 Image Sharpness

Lens defects prevent rays of light converging at a single focal point and are typically named lens aberrations. The most common defect is imperfect lens curvature which is most dominant on the outer edges of the lens where the lens normal is furthest away from the optical axis. When a lens is used at a maximum aperture, the

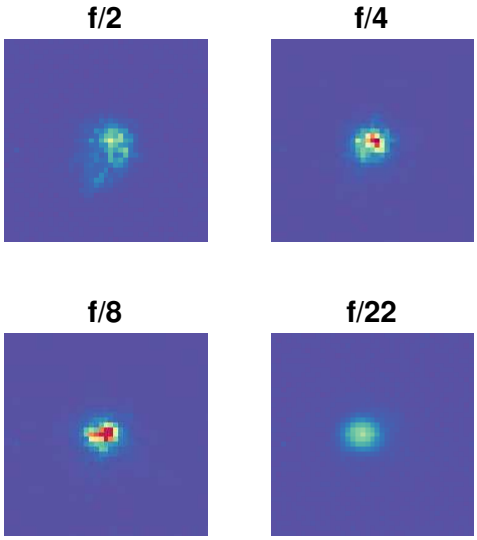

Figure 4.14: Observed laser reflection off a reflective metal surface with varying lens aperture. Aperture size set by the f/# setting, defined as the focal length of the lens normalised by the aperture diameter.

effects of the aberrations are most dominant. Reducing the aperture size means that the defects on the outer edges of the lens are not observed on the image, reducing the effect of the aberrations.

Another form of light distortion is due to the diffraction of the light passing through the aperture. A point source of light is diffracted to form an airy disk, and if the diameter is greater than the circle of confusion, then the image quality is reduced. The angle at which the first minimum in intensity occurs of the airy disk for a light wavelength of λ and aperture D, can be approximated, as shown in Equation (4.12) [98]. For small angles, this can be further approximated to calculate the radius of the first minimum - Equation (4.13), where f is the lens focal length and N is the lens f-number (ratio of the focal length to aperture diameter).

$$sin(\theta) = 1.2197\frac{\lambda}{D} \tag{4.12}$$

$$c_{diffraction} = 2.4394\frac{\lambda f}{D} = 2.4394\lambda N \tag{4.13}$$

Assuming that our desired circle of confusion is a pixel width (to prevent superposition with the neighbouring pixel), we can calculate the aperture size

which will give a diffraction width equal to a pixel width for light in the visible spectrum (centred around 600 nm). For the cameras used in the experiments (Ximea MC050MG-SY), the pixel size was 3.45 µm, giving a diffraction limit f-number of 1.99.

In reality, the effect of lens aberrations dominates over the influence of diffraction, meaning that the aperture with maximum image sharpness - termed the lens sweet spot, is often at an aperture smaller than the diffraction limit. To quantify these effects, images were taken of a checkerboard at a range of apertures. Analysing the number of pixels taken to rise from minimum pixel intensity to maximum intensity over the checkerboard pattern interface, a level of sharpness was determined. Figure 4.15 shows the image of an interface between a low and high in a checkerboard image, and a plot of the intensity along a single row of the image. A linear curve fit was fit to the data on the low and high regions of the image. The point at which the image intensity was greater than two standard deviations from the linear curve fit was deemed to be the edge of the checkerboard image, and a rise time was defined as the separation between these two points. The process was repeated for a range of apertures (f/1.6, 2, 2.8, 4, 8, 22) and the results are shown in Figure 4.16. The minimum rise distance was assumed to be associated with the maximum image sharpness, which occurred at a lens aperture of f/4. Note that this is the aperture to give maximum sharpness for the specific lens tested, and needs to be verified for each lens. This maximum sharpness is only for a planar object, and alterations will need to be made if a finite field of view is desired.

4.7.4 Optimum Aperture

The optimum aperture for a measurement system needs to provide sufficient depth of field while also being wide enough for specular reflections to reach the camera sensor but limit the effects of diffraction and lens aberrations. Peterson [97] assumed that the compounding errors induced by defocus and diffraction could be accumulated by taking the square root of the sum of the square of each error. The effects of lens aberrations were also omitted, assuming that the lens would not be operated at

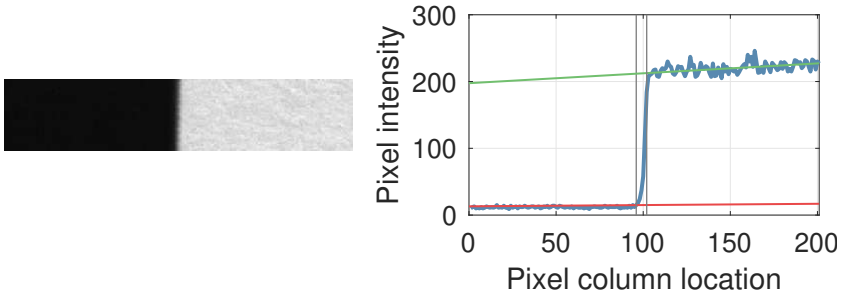

Figure 4.15: Image of the interface of between a black and white checkerboard square (left). Variation in pixel intensity of the central row of the left hand image along all columns (right). Red line shows the linear fit to the the black region, green line shows the linear fit to the white region. Grey lines show the pixel position at which the pixel intensity was greater than two standard deviations from the linear sections.

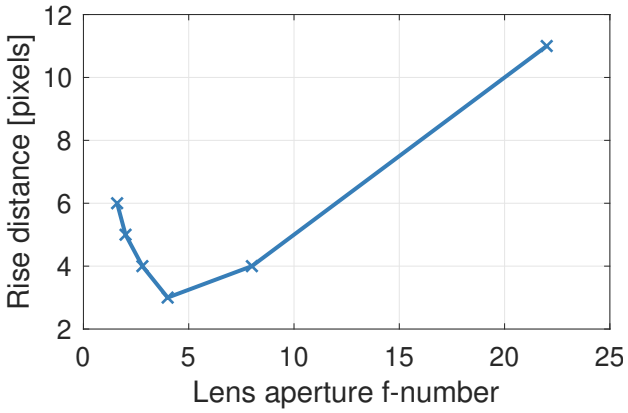

Figure 4.16: Variation of image sharpness as a function of lens aperture size for the specific lens tested (Basler C11-1620-12M-P).

maximum aperture. To reduce the complexity of the equations, the wavelength of light in this section is assumed to be 600 nm. This simplifies Equation (4.13) to be $\sim$ N/750. Equation (4.14) shows the total error induced by the circle of confusion due to defocus and diffraction. Calculus can find the value of f-number, N, which minimises the error induced by defocus and diffraction, resulting in Equation (4.15). Substituting in the thin lens equation (Equation (4.6)), the optimum aperture for given object distances can be found (Equation (4.16)).

As mentioned before these equations are for single symmetric lenses, but provide sufficiently accurate results for a first estimate of the optimal aperture.

$$c_{total} = \sqrt{c_{defocus}^2 + c_{diffraction}^2} = \sqrt{\frac{\delta V}{2N}^2 + \frac{N}{750}^2} \tag{4.14}$$

$$N_{optimum} = \sqrt{375\delta V} = \sqrt{375\left(V_f - V_n\right)} \tag{4.15}$$

$$N_{optimum} = \sqrt{375\left(\frac{U_f f}{U_f - f} - \frac{U_n f}{U_n - f}\right)} \tag{4.16}$$

4.8 Effects of Camera Separation

The distance between the two cameras, known as the stereo baseline, and the object distance alters the disparity observed between the two data sets of a stereo system. The two parameters can be combined to calculate the angle between each camera optical axis, known as the stereo angle. Increasing the stereo angle increases the disparity between each camera view, which decreases the system error. If large stereo-angles are used, cross-correlation of the camera views may be inaccurate due to large perspective differences leading to enhanced errors in the image rectification process. Generally, small stereo angles are most suitable for in-plane measurements but have larger errors in out of plane measurements. Increasing the stereo angle improves out of plane performance at the cost of increased in-plane uncertainties.

Camera pairs at increasing stereo angles were calibrated and tested for in-plane and out of plane accuracy. A checkerboard pattern of known size was traversed in the direction approximately parallel to the average of the two optical axes, and also at approximately 30 degrees to this line. The displacement of each checkerboard node in the direction of travel was extracted, and node separations (in the plane perpendicular to travel) were quantified. The experimental set-up is shown in Figure 4.17.

The systems were calibrated at a working distance of around 450 mm, with baselines of approximately 50, 100, 150 and 200 mm - creating stereo angles of 6.6, 11.4, 18.7 and 21.4 degrees. Baselines were approximately measured during the set-up and stereo angles were extracted from the extrinsic properties of the stereo calibration. The node separations of the checkerboard were 11.56 mm.

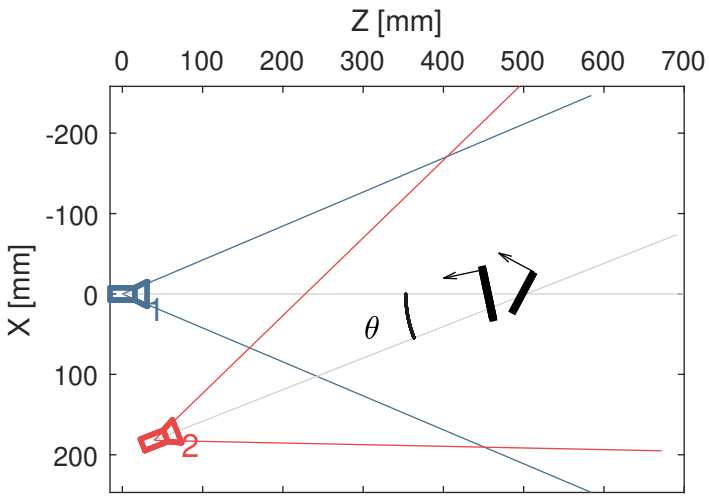

Figure 4.17: Experimental set-up for determining the effect of stereo angle (θ). The field of view of each camera is shown by the radial lines from each camera optical center. Checkerboards are moved in the direction shown by the arrows.

The results for error in measured node displacement and separations for an in-plane traverse are shown in Figure 4.18. The three smallest stereo angles had low error of less than 0.05 mm in measured displacement over the 15 mm traverse. The largest stereo angle had the largest error, and this is thought to be caused by perspective differences. The measured node separations had error of less than 2 µm.

When the direction of projection screen travel was rotated by approximately 30°, the error in measured displacement reduced, but at the cost of increased error in node separations, as shown in Figure 4.18. These results show that the stereo calibration produces most accurate measurements in the plane perpendicular to the optical axis, so if possible the stereo system will be placed off-normal to the measured surface to obtain more accurate results in both the normal and transverse directions (but not far from normal otherwise perspective distortions become dominant).

These experiments utilised a uniform checkerboard grid for which highly optimised algorithms exist for determining the grid node locations at sub-pixel accuracy. When imaging arbitrary objects for which sub-pixel algorithms are less effective, additional error is induced into the system. With increasing stereo-angle, the change in world coordinates decreases for a 1 pixel error in disparity. For the stereo angles used in this study, the error in world coordinates induced by a 1 pixel disparity error

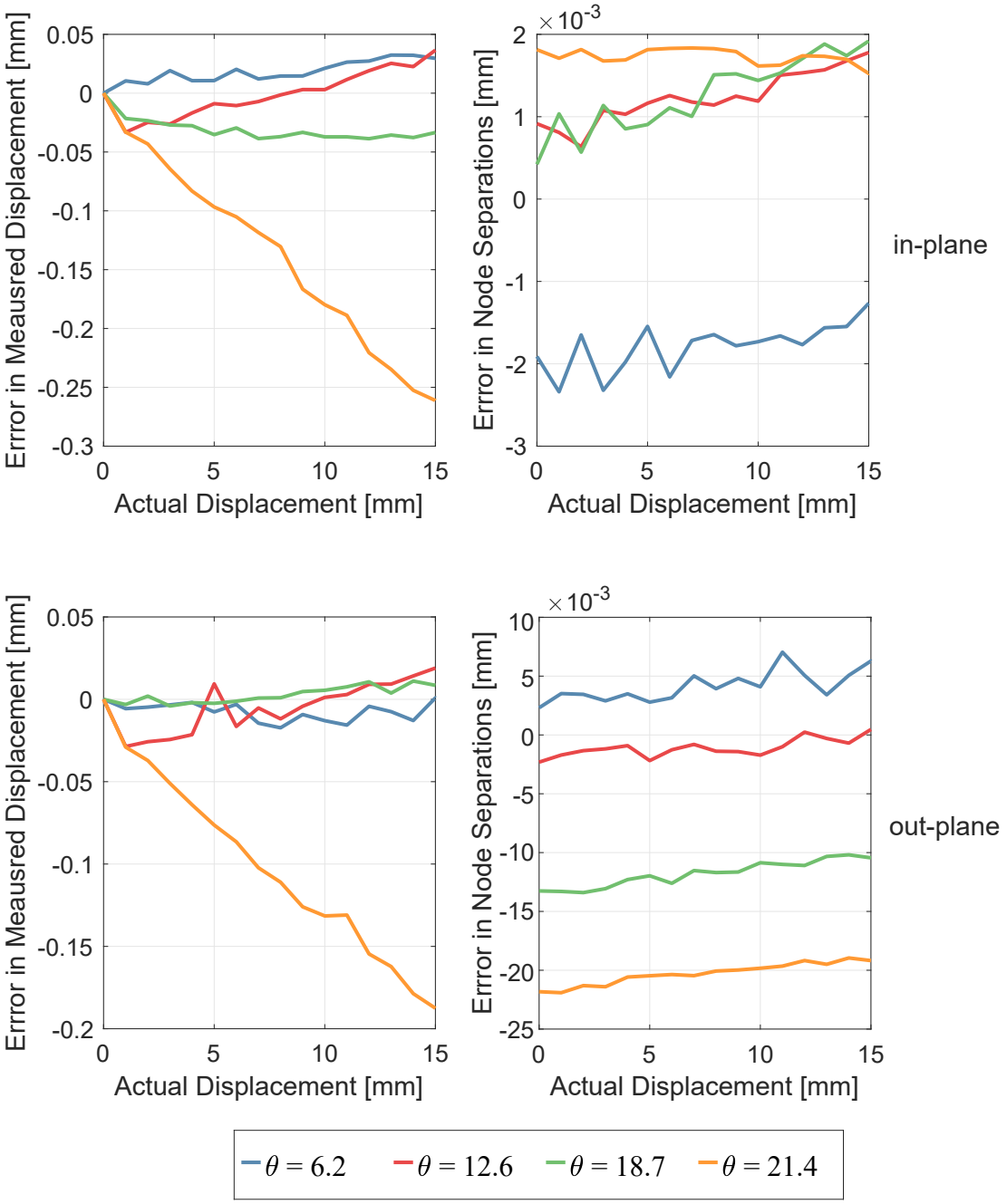

Figure 4.18: Error in measured plane displacement and node separations for in-plane measurements (top) and out of plane measurements (bottom).

was calculated to be 0.96, 0.47, 0.32, 0.24 mm. The difference in observed laser reflection from different viewing angles increases the error in disparity calculations, potentially past the point of sub-pixel error. Therefore, for imaging ice accretion the stereo angle should be kept sufficiently large (>12 degrees) to minimise the effects of disparity errors and errors in depths along the optical axis.

4.9 Effects of Projection Pattern

Objects with strong surface texture can be used in stereo vision without additional projection patterns. Ice crystal icing accretions typically have low levels of surface texture and therefore require a projection pattern to obtain correspondence. If the data in regions with no projection pattern are assumed to be invalid, then using a greater spatial density projection pattern increases the spatial density of the point cloud. The use of high density uniform dot patterns can also lead to errors if the pattern is aligned with the epipolar lines, due to disparity searches along the epipolar line detecting incorrect nodes. If the spatial density is too high, the reflections of multiple nodes may intersect a single pixel of the sensor, preventing the distinction of the projection pattern. This effect is more severe when the optical axis is not aligned with the viewing surface.

Work in the field of stereo vision has found optimal characteristics of the projection pattern. Reu [99] found that the feature size of the projected pattern should be between 3-5 pixels. If projection patterns are smaller than this recommended range, then for small displacements, signal noise can be a dominant error. If larger than this threshold then larger window sizes are required for the disparity calculations, reducing the spatial resolution of the point cloud.

Reu found that the spacing between projection nodes should be approximately the feature size, for non-transparent objects [100]. Ice accretion is transparent, allowing light to propagate through the ice layer to the test piece surface, leading to internal reflections. If the internal reflections align with neighbouring projection nodes, then it is not possible to find correspondence. For application to ice crystal icing, the node spacing should be set greater than the suggested value for non-transparent objects.

The projection pattern criteria found in the literature has good applicability to measurements of non-transparent objects. When imaging ice crystal icing which is semi-transparent, the optimum projection pattern is likely to be different. The effect of different projection patterns when imaging ice crystal icing is one of the

aims of the future testing of the triple airfoil test piece, however is out of the scope of this work. Research into optimised pattern types have been conducted [101, 102], however, this work will focus on standard patterns (regular dot arrays, regular line arrays, irregular dot arrays).

4.10 Laser Intensities

The laser intensity required for the projection pattern is a variable that currently cannot be calculated due to a lack of understanding of the accretion surface reflectivity properties. It is also likely to be dependant on the conditions of the ice accretion (water film thickness, porosity, thickness), which is not known without measurement of the accretion surface. To mitigate this problem a variable power output laser has been utilised in this work. The output power was controlled via a voltage output of a DAQ, and the same DAQ was also used for triggering of the cameras. Multiple images were taken of the same laser intensity so that a time average of the images can be computed to limit the effects of testpiece vibration and sensor noise. An example waveform and timings of the camera trigger is shown in Figure 4.19. Assuming that a limited proportion of the laser intensity levels produce good images, the period of oscillation must be sufficiently small so that if only one laser level returns good data, that sufficient time resolution of accretion growth is captured. Typical accretion tests last >180 s, so it was concluded that an oscillation should take no more than 10 s.

4.11 Stator Test Results

The stator test piece was used for this experiment, as detailed in section Section 3.1. Previous research by Bucknell *et al.* measured the ice thickness by using backlit shadography viewing down the axis of the blade span. This method relies on the assumption that the accretion is uniform along the span. In reality the tip gap and end wall effects produced 3D flows, causing non-uniformity's in accretion

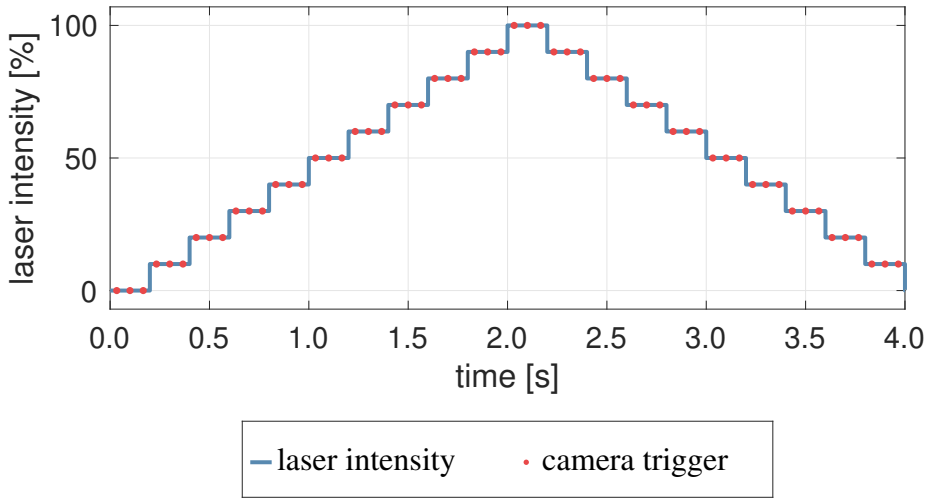

Figure 4.19: Variation in laser intensity and timings of camera trigger. Camera frame rate of 15 Hz, 10 levels of laser intensity and 3 images per laser intensity.

levels. These effects were observed using qualitative camera views, but could not be quantified with the simplistic backlit shadography approach.

At a non-zero aerodynamic angle of attack, increased aerodynamic forces are applied to the stator. Because the stator was not in a cascade configuration, highly separated flow occurred off the suction surface, causing unsteady aerodynamic loading leading to vibrations. The vibrations cause the DIP system to observe a non-physical oscillating ice thickness. To minimise this effect, the stator was set close to the aerodynamic 0° angle of attack.

4.11.1 Optical Equipment

An array of dots were projected onto the test piece using a 632 nm, 5 nW, Flexpoint® laser produced by Laser Components. A Diffractive Optical Element (DOE) was placed on the front of the laser module to produce a dot array from the single laser beam. For this experiment, an array of 6x6 nodes was chosen which covered near full chord, and part span of the stator. The array of dots were recorded using 5 MP miniature cameras produced by Ximea; model MU9PM-MH for low speed image capture (5 fps) and MC050MG-SY for a higher frame capture (70 fps).

This test was conducted before the development of the stereo system, so only includes the results of a single camera single laser DIP system.

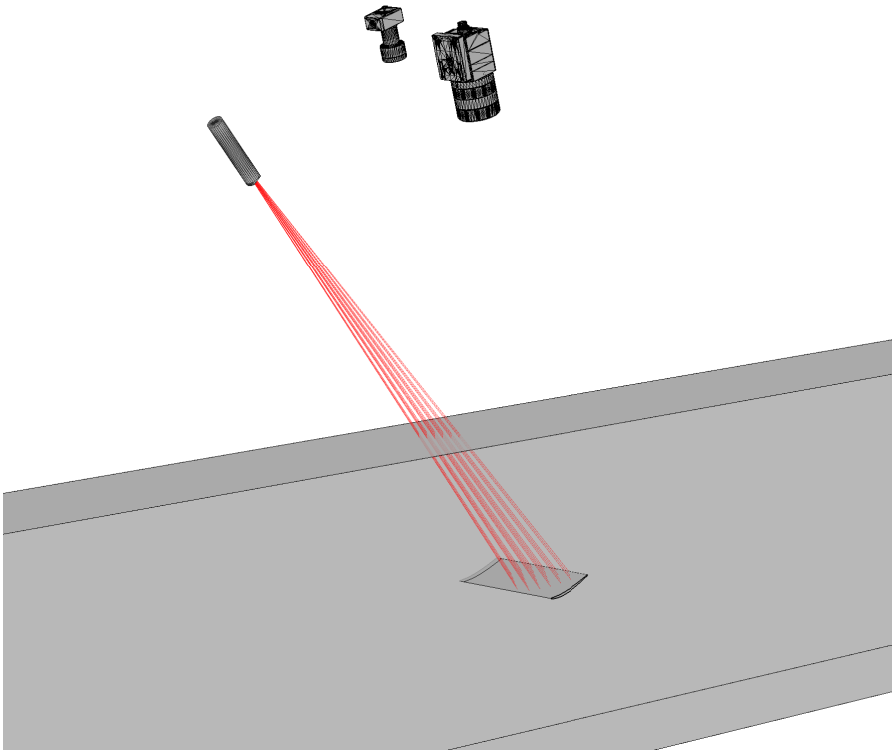

Figure 4.20: Positions of laser and cameras relative to the stator test piece in the RATFac wind tunnel. Each camera is independently calibrated with the laser.

Figure 4.20 shows the relative positions of the stator, cameras and laser. The larger camera was the higher frame rate camera, used for all tests. As discussed later, the second smaller camera was also used on some test points to produce a second data-set to improve the accuracy of the system. Figure 4.21 shows a visual representation of where nodes were positioned on the stator prior to ice accretion. To minimise the computational power required to compute the three-dimensional accretion profiles, it was decided to use a coarse 6x6 grid. The 6x6 grids commercially available were square in shape and the maximum spreading angle available produced a projection which covered the whole chord and part span of the blade. The region closer to the free end was deemed more interesting than the cantilevered end due to tip vortices creating the largest variations in spanwise accretion, meaning that the free end was imaged with the DIP system.

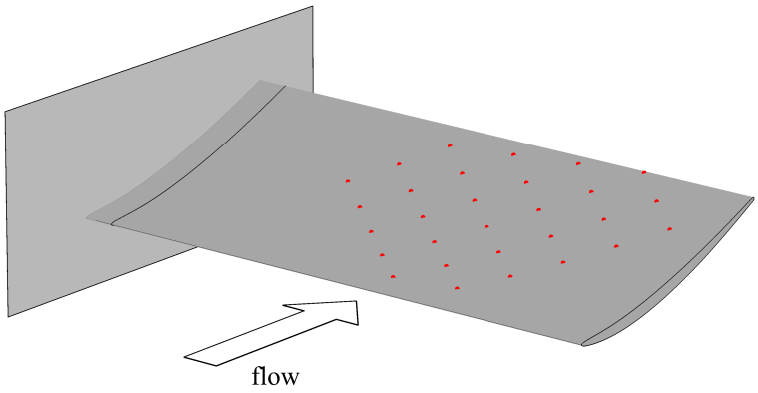

Figure 4.21: Initial node positions of the laser pattern on the stator test piece.

4.11.2 Test Conditions

During the experiment, a total of 16 test runs were completed. All test points were nominally set at a total pressure of 34.5 kPa (∼27,000 ft) and total temperature of 10 °C. Due to limitations in the fine control of tunnel valves, the actual total temperature in the tunnel varied between 10-12 °C but remained approximately constant for each test point.

Steam injection was controlled inside the chamber to adjust the relative humidity between 30-50%. The ice crystals were ground to have the same particle size distribution for all tests. The cloud distribution was analysed using PIV, and it was found that the cloud had a $D_{v_{10}}$, $D_{v_{50}}$ and $D_{v_{90}}$ of 18, 32 and 54µm respectively. All tests had a total ice content of 4 $\mathrm{g\,m^{-3}}$, which was fully glaciated at the exit of the ice injection pipe. As the crystals propagated through the "warm" section of the chamber, the crystals naturally melted. At the test section, it was measured that the average melt ratio of the crystals varied between 5-15% when the relative humidity was adjusted from 30-50%. All tests were conducted at a Mach number of 0.4, creating a dynamic pressure of 3.46 kPa. This section will analyse the results of three test points from the experiment. The actual conditions for each test is shown in Table 4.1, where $\mathrm{RH_0}$ and $\mathrm{TWB_0}$ are the relative humidity and total wet bulb temperature, both calculated using total conditions.

Table 4.1: Tunnel conditions for each test point analysed as part of the stator DIP tests.

Test #	Angle of Attack	RH_0 (%)	TWB_0	MR (%)
1	-1.5°	35	1.0°	6.8
2	0°	40	1.4°	7.5
3	+1.5°	38	1.2°	7.1

4.11.3 Results

Frames were extracted from the DIP video camera at intervals of approximately 30 seconds, analysed and compared to data from a side on backlit camera view. The cameras viewed through windows over which ice passed, meaning that ice periodically stuck to the window, blocking optical access before the ice then shed away. Frames for DIP analysis were chosen such that there was a clear view of the test piece.

The data produced from the DIP system was compared to a backlit camera view down the span axis of the stator blade, as shown in Figure 4.22. In this figure, the blue line shows the extracted profile from the side view. The backlit measurements were taken during the same experiment as the DIP measurements, and were triggered simultaneously. The laser light was continuously projected onto the test piece, with some light reflecting off the top surface and the rest propagating through the ice layer. This caused the ice accretion to glow a red colour, incidentally improving the contrast between the accretion and the background, allowing the accretion edge to be more easily extracted from the image of the backlit view. This data set was used to pseudo-validate the DIP data. It cannot be taken as a "true" measurement of the ice thickness, but was the most accurate widely adopted method for ice measurement during the test.

Figure 4.23 shows the accretion profile after 90 seconds for test #2 (angle of attack of 0°). At small levels of accretion there was relatively poor agreement between the side view data and the DIP data. This can be explained due to two reasons. Firstly, the accretion profile which the side on camera observes is that of the maximum accretion along the span of the blade. After 90 seconds of accretion at this test point, ice had accreted more heavily at the cantilevered end

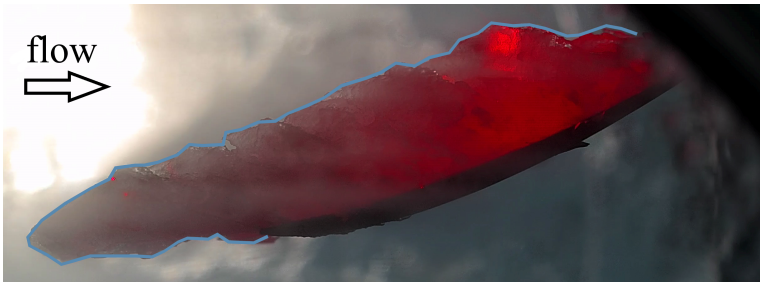

Figure 4.22: Backlit shadography data of the accretion profile. Light source and camera optical axis aligned with the spanwise direction. Image taken after 185 seconds of accretion of Test #3. Accretion profile, as extracted with edge detection algorithms is shown in the blue line.

than the free end of the stator. An isometric camera view of the accretion after 90 seconds is shown in Fig. 4.24. Overlaid on top of this image is the extracted accretion profile from the backlit shadography (projected onto the isometric frame of reference) and also the pressure surface profile of the clean stator at the side wall intersection. While this view is not a perfect visualisation, it gives insight into the non-uniform thickness of ice over the stator, with thicker ice at the fixed end than the mid-span or free end during the initial stages of accretion. Because the DIP was only recording data in a region closer to the free end, it captured a lower value of ice accretion thickness compared to the backlit data set.

At small accretion levels, the laser light has to travel a smaller distance through the ice to reach the underlying metal surface. If a significant amount of laser light reaches the metal surface then a large amount of internal reflection occurs which makes it more difficult to identify the node reflected from the top surface of the ice. This causes further error in the measurements at small accretion levels, but its effect was minimal once larger amounts of accretion had occurred due to less light reaching the metal surface.

Figures 4.25 to 4.27 show the accretion profiles from the three test cases at four moments in time. After the initial transient growth of ice along the span of the stator, better agreement was observed between the DIP data and the side on camera. It can be seen that there is scatter in the DIP data, implying that

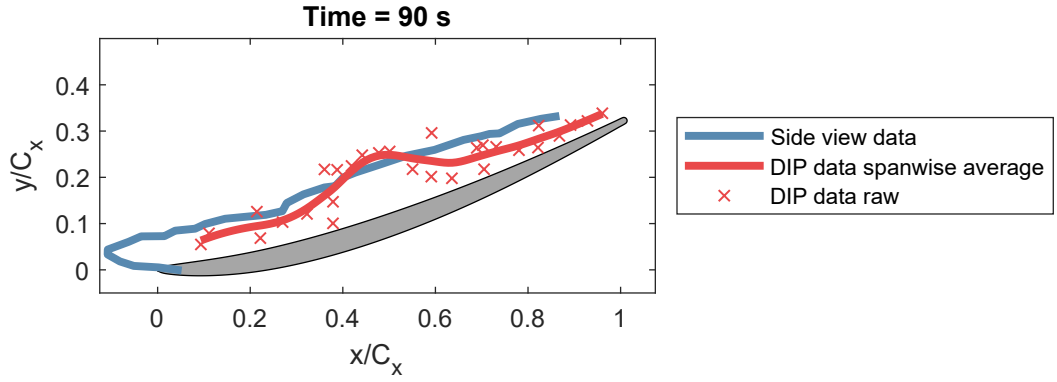

Figure 4.23: Side view and DIP data accretion profiles at small accretion levels for Test #2.

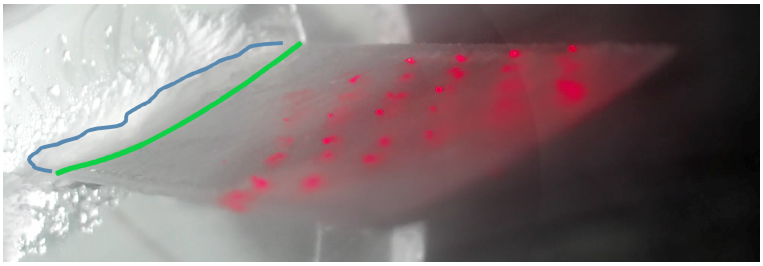

Figure 4.24: Accretion after 90 seconds for Test #2. Profile from backlit shadography is shown in blue, and the underlying stator profile shown in green.

there are spanwise variations in accretion thickness, which previously could not be quantitatively measured.

The remainder of the analysis focuses on Test #1. To further quantify the accuracy of the DIP data, it was compared to measurements taken with a Creaform HandyScan 7000. It has a rated accuracy of 0.025 mm for a part size in the range of 0.05-4 m [103]. The device uses a dual camera system with a single structured light source. The method of determining similarity between the two camera sets utilises targets (circular stickers) which are placed onto the object to be scanned and also uses natural features of the object being scanned, such as geometrical/colour texture. The device has poor performance when measuring glaze ice with high transparency. To get the best results, the ice was treated with a low temperature gas to freeze the ice in a non-equilibrium state leading to a surface finish more closely matching rime ice - enhancing the reflectivity. The need to place targets and freeze the ice

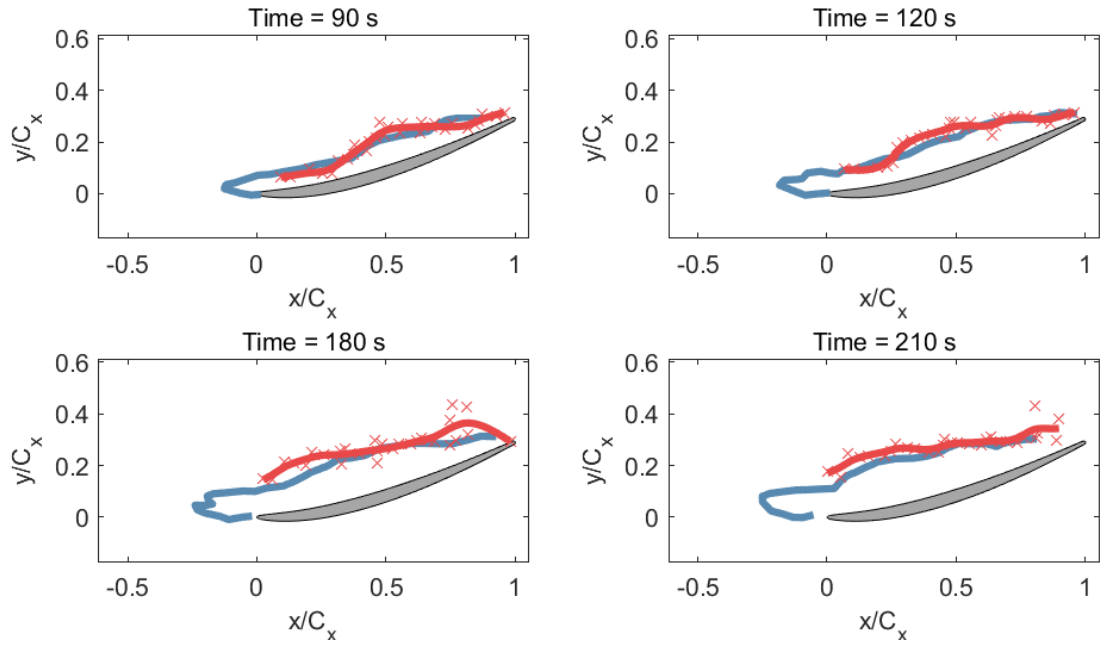

Figure 4.25: Test #1: -1.5° Angle of Attack. Side view camera data shown in blue, individual DIP node data in red crosses, and spanwise averaged DIP data shown in red line.

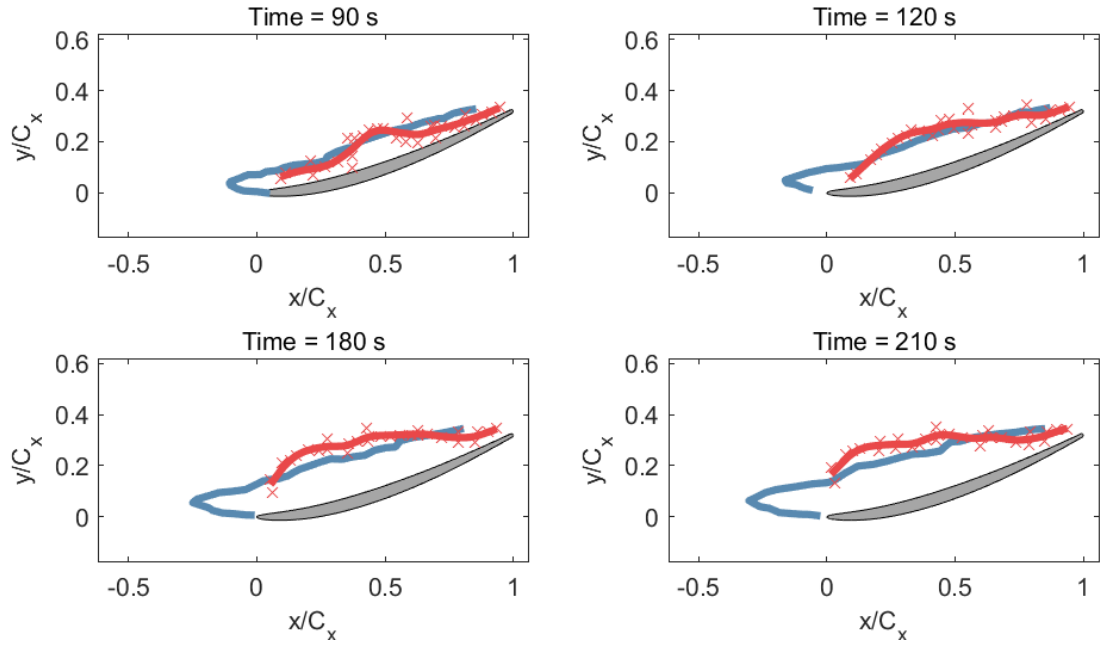

Figure 4.26: Test #2: 0° Angle of Attack. Side view camera data shown in blue, individual DIP node data in red crosses, and spanwise averaged DIP data shown in red line.

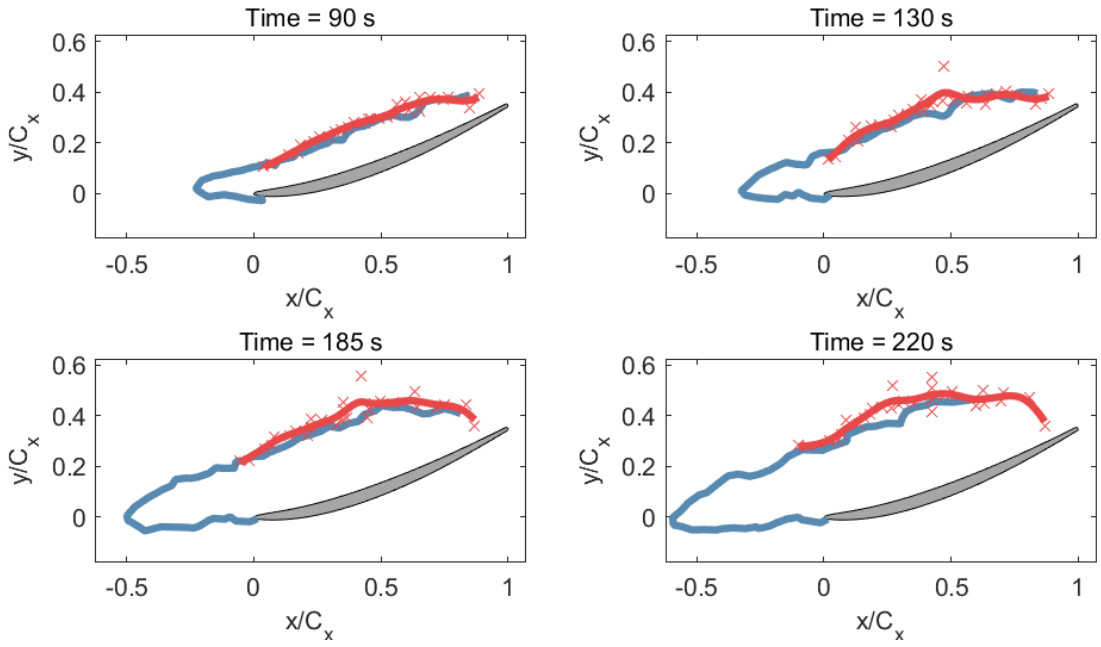

Figure 4.27: Test #3: +1.5° Angle of Attack. Side view camera data shown in blue, individual DIP node data in red crosses, and spanwise averaged DIP data shown in red line.

structure meant it was not possible to measure the ice thickness during the accretion process. Instead, at the end of the test day the altitude chamber was re-pressurised to atmospheric pressure while maintaining sub-freezing conditions (~ -10 °C). The test article was then removed from the wind tunnel and scanned. The ice being scanned is shown in Figure 4.28, and the results are shown in Figure 4.29, where the HandyScan results are shown in the blue mesh, and the coarse mesh measurements are from the DIP system. Regions where the HandyScan mesh has no data was caused by insufficient reflectivity of the structured light source in that region.

Immediately before the test piece was removed for scanning, a final DIP measurement was taken to account for any changes in accretion caused by sublimation and evaporation during the chamber re-pressurisation. The measured accretion profile via the side view camera and DIP is shown in Fig. 4.30. It should be noted that this test point had 240 seconds of accretion, meaning that the accretion profile in Fig. 4.30 was taken 365 seconds after ice off.

Few data points from the DIP match the side view data in Figure 4.30, which based on the historical assumption of uniform thickness along the span would

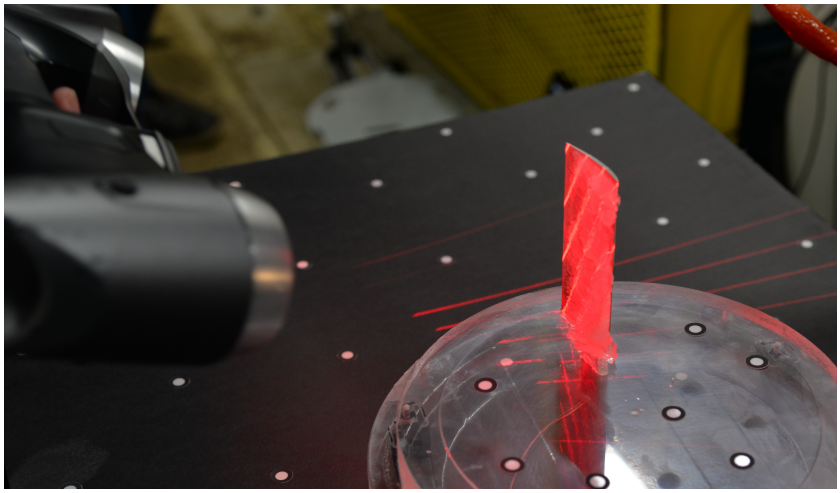

Figure 4.28: Scanning of accreted ice using the Creaform HandyScan 7000.

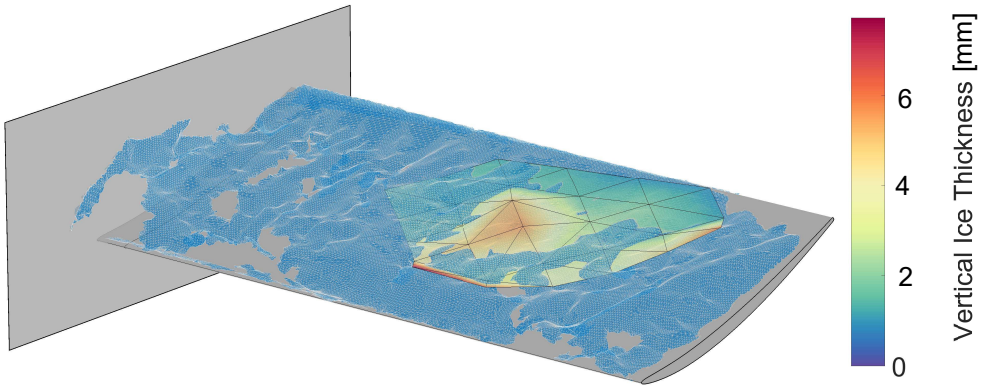

Figure 4.29: Comparison of DIP (coarese mesh) and Creaform HandyScan data (fine blue mesh) on Test #1. DIP data coloured based on vertical ice thickness.

suggest that the DIP had poor accuracy. However, comparing the DIP profile to the data from the Creaform HandyScan (Figure 4.29) it can be seen that the DIP was able to predict the surface non-uniformities along the span axis. It was found that on average that the deviation between the DIP dataset and the HandyScan normalised by the chord length was within 0.64 mm. The DIP data points which match the side view camera data-set were nearest to the free end, showing that the side view had only detected the ice thickness on the free tip of the stator and not captured the average profile along the span of the blade.

To visualise the span-wise variations, accretion profiles were extracted along the span axis at 25%, 50% and 75% chord, as shown in Figure 4.31. These profiles are shown in Fig. 4.32, where 0% span is defined as the free end of the stator, and ice

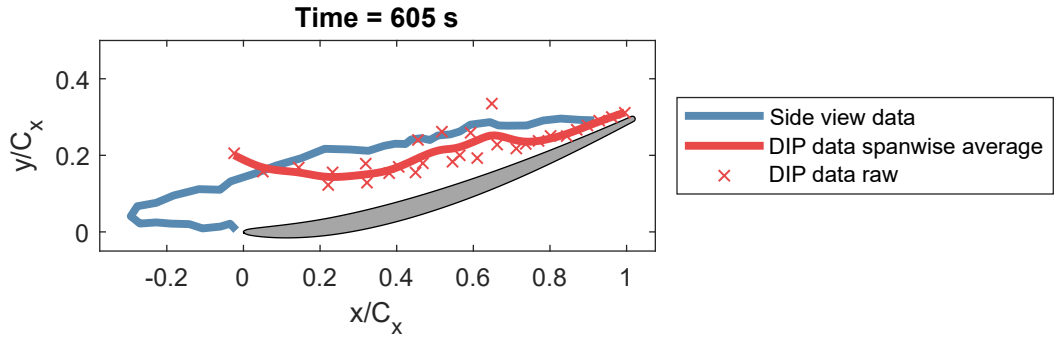

Figure 4.30: Accretion profile measured by side view camera and DIP system in Test #1. Data captured after ice off, immediately before the test piece was scanned with the Creaform HandyScan.

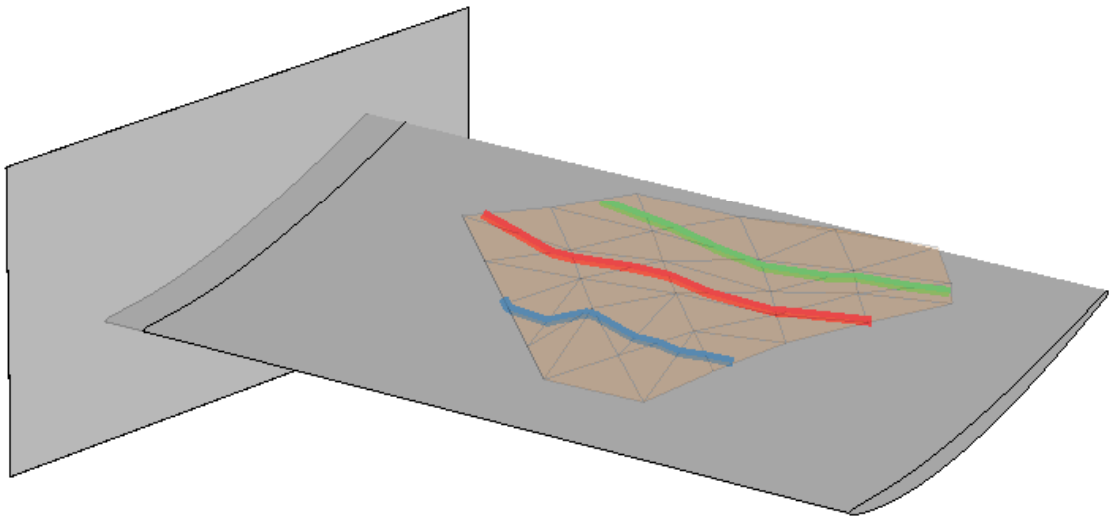

Figure 4.31: Spanwise variation of ice thickness in Test #1 in isometric view of test piece.

thickness is defined as the vertical height of the ice above the stator surface. These profiles show a general trend of there being a greater thickness of ice at the ends of the stator (free and fixed ends) compared to the mid-span. At the free end, where a 20% span clearance gap existed between the tip and the other side wall, three-dimensional flows occurred around the tip which likely led to the enhanced accretion.

To minimise the system complexity it was decided that this test campaign would primarily use a single camera and single structured light source. For some

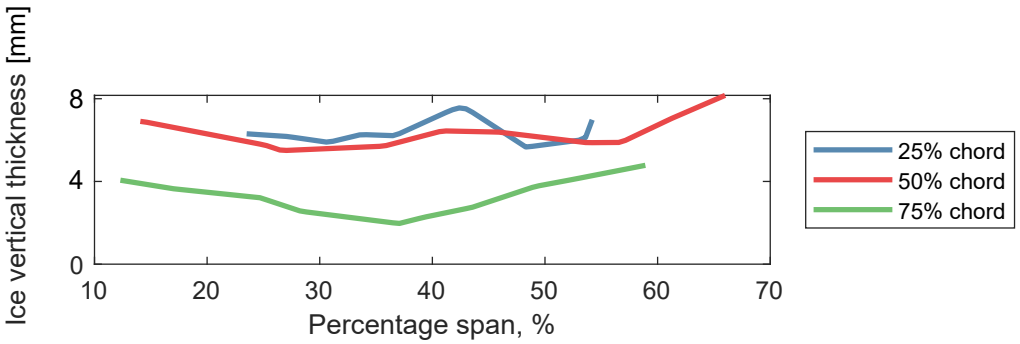

Figure 4.32: Spanwise variation of ice thickness in Test #1.

tests, there was a secondary camera with a viewing angle different to that of the first camera. The cameras were calibrated using the same calibration piece and structured light source and produced two independent datasets. Figure 4.33 shows the accretion profile produced by averaging the two datasets, taken immediately before the test piece was removed for scanning. The colour of the profile is based on the deviation between the two DIP datasets. It can be seen that for the majority of the surface that the deviation between each dataset was less than 0.8 mm, however, there are some nodes with much greater deviation. The mean deviation was found to be 0.56 mm. Surface irregularities caused some nodes of the structured light source to be optically blocked by surrounding ice peaks. Due to the semi-transparency of the ice, it was still possible to view the laser node, but the calibration did not take into account the diffraction of the light through the adjacent ice. This partially optically blocked node produced an inaccurate measurement, leading to high deviation between the dataset of each camera. By averaging the datasets of each camera, the DIP measurements had a mean deviation (normalised by the chord length) from the handheld scanner of 0.34 mm, hence making the dataset more accurate compared to the single camera system (which had a deviation of 0.64 mm).

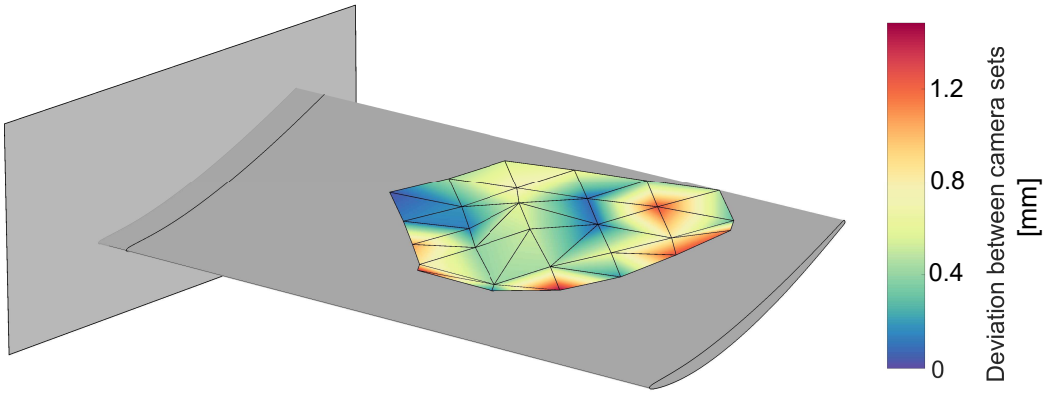

Figure 4.33: Averaged profile of the two DIP datasets. Colour of mesh based on deviation between the two datasets.

Table 4.2: Aerothermal conditions for each test case. The values of total pressure have been rounded to the nearest 0.5 kPa, Mach number to the nearest 0.01, and total temperature to the nearest degree.

Test #	P_0 [kPa]	M	T_0 [°C]	MR	$T_{wb,0}$ [°C]
1	34.5	0.3	10	0.11	0.53
2	34.5	0.4	10	0.06	-1.64
3	34.5	0.4	10	0.12	0.21
4	49	0.3	10	0.11	0.64
5	49	0.4	10	0.02	0.44
6	49	0.4	10	0.05	0.65
7	49	0.4	10	0.11	1.43

4.12 SND Test Results

The same optical system used in the stator test was used in a more complex test piece consisting of a combined linear cascade and swan neck duct. It is believed to be the first study involving the streamline curvature imparted by the blade camber, outer annulus radius and blade lean. An overview of the test and DIP results are shown in this section, but the full details of the test and experimental results are in Appendix A.

A range of conditions were studied, where the total pressure, mach number and relative humidity were varied to adjust the accretion characteristics. A summary of the conditions analysed as part of this thesis is shown in Table 4.2.

It was found that in the conditions studied that there were common features

in the accretion, notably the peaks of accretion on the outer annulus in the wakes downstream of the blade row. The location of accretion initiation in most conditions occurred at the intersection of the pressure surface trailing edge and the outer annulus. By varying the total pressure the location of accretion changed, with less pressure surface accretion occurring at the higher total pressure of 49 kPa compared to the lower total pressure of 34.5 kPa. The outer annulus upstream of the blade row also had reduced accretion at the higher total pressure. By increasing the Mach number from 0.3 to 0.4, a more significant variation in leading edge accretion occurred, with less accretion occurring at the inner annulus compared to the outer annulus. By varying the melt ratio from 2% to 11% an increase in accretion occurred, matching with the sticking probability distribution predicted by Bucknell *et al.* [36]. In the experiments three-dimensional effects were observed. One condition (test #1) saw the leading edge accretions being bent into the adjacent suction surfaces - blocking the flow path of that passage. This had knock on effects, significantly changing the adjacent flow field and undoubtedly altering the future accretion. These observations were made using videos recorded using conventional cameras.

Additional data was also gathered using two measurement systems; DIP (developed in this thesis) and also using the commercial Creaform Handyscanner. The Handyscanner could only be used once the tunnel was turned off but obtained data over the whole test piece surface, producing a full 3D dataset on the formed accretion. The DIP system also operated during the accretion, allowing for transient data to be gathered. A DIP system was positioned on the inner annulus of the swan neck duct, directed at the outer annulus, immediately downstream of the blade-row trailing edge - a position susceptible to accretion due to the annulus curvature. The position of the laser, camera and laser nodes is shown in Figure 4.34. Quantitative ice thickness measurements of the outer annulus have not been possible in previous studies due to the side walls obstructing backlit measurements.

As mentioned previously, the HandyScan device was not able to record accretion sizes during the test, and required a tunnel shut-down to atmospheric pressure, and a rapid cooling of the ice. The tunnel shut-down in RATFac takes approximately

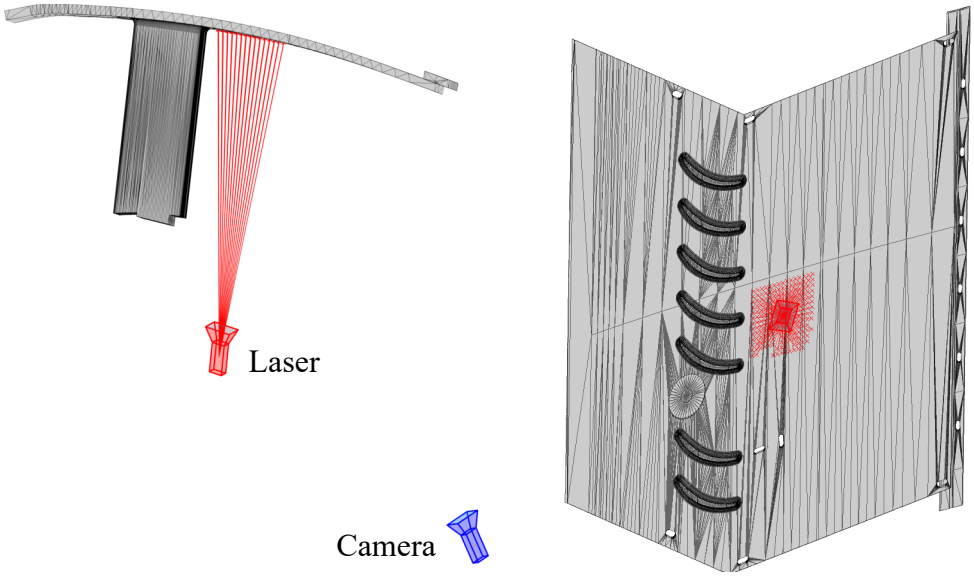

Figure 4.34: Laser and camera position for measurement of the outer annulus of the swan neck duct test piece.

10 minutes, and during this period shedding events occurred. The accretion measurement results are shown after the shutdown period. Two conditions are shown in this section; Test # 6 and Test # 7, where the baseline conditions of 49 kPa total pressure, Mach 0.4, 10°C total temperature, and a melt ratio of 5 and 11% respectively. Figures 4.35 and 4.36 shows a comparison of the DIP and Creaform HandyScan data. The red square in Figures 4.35 and 4.36 shows the region analysed by the DIP system.

This data further shows overall, that the accretion was larger with increasing melt ratio in the conditions studied. Good agreement was observed between the Creaform HandyScan data and the DIP data. The Creaform device has not officially been validated for measuring ice crystal icing accretion thicknesses but is regarded as being an accurate measuring device. The data shows self-similarities between the two datasets, which even though it cannot be used as a validation of the DIP system, suggests that it captures the correct trends.

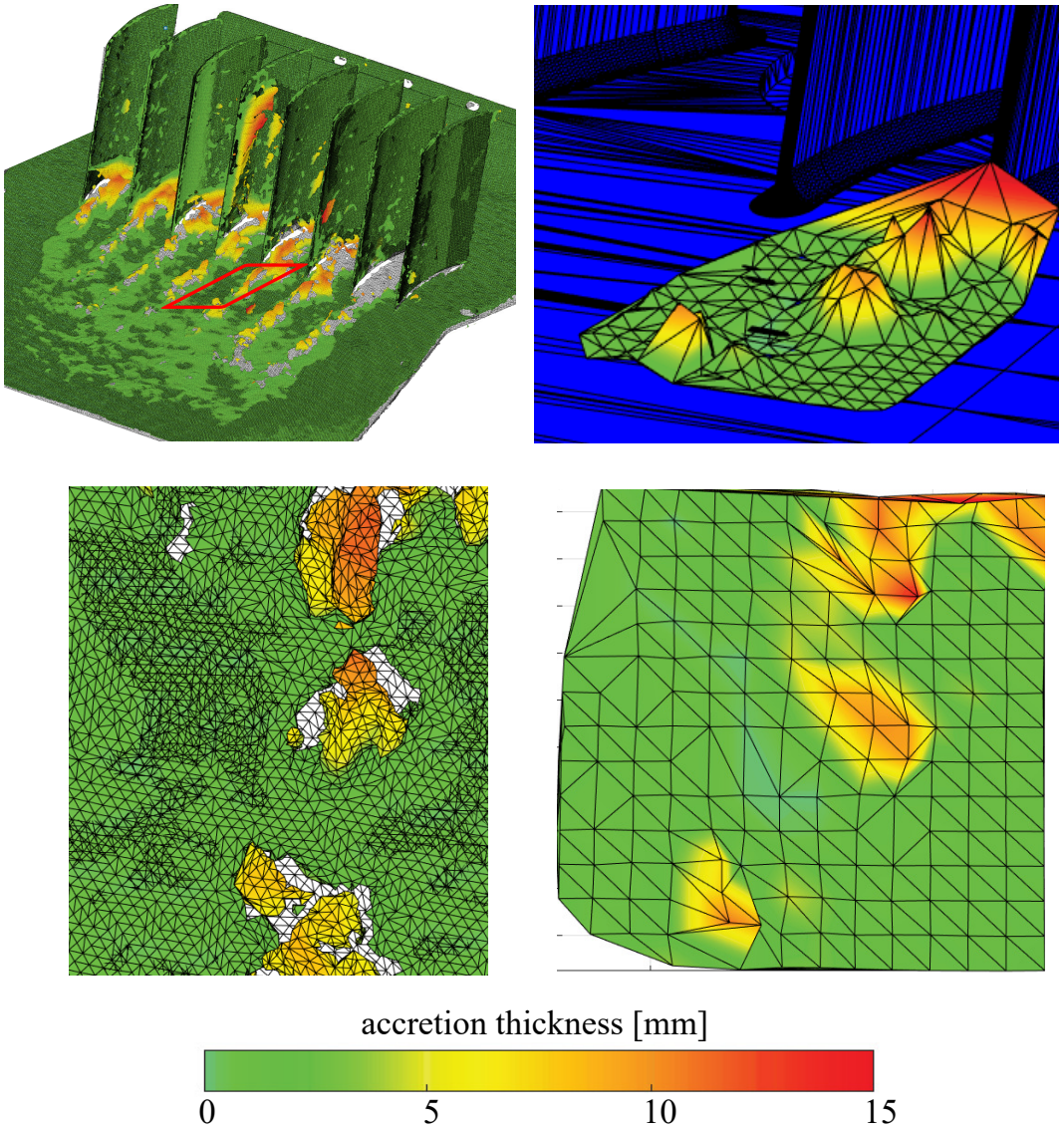

Figure 4.35: Test # 7.Isometric view of downstream ice thickness measurements (top row) from the Creaform HandyScan (left) and DIP system (right), and top down view (bottom row) at melt ratio of 11%. Conditions: $T_0 = 10°C$, MR = 11%, Mach = 0.4.

4.13 Plenoptic Imaging

An alternative method of measuring three-dimensional accretion profiles using plenoptic imaging was studied at the USQ icing facility. The results can be found in Appendix B.

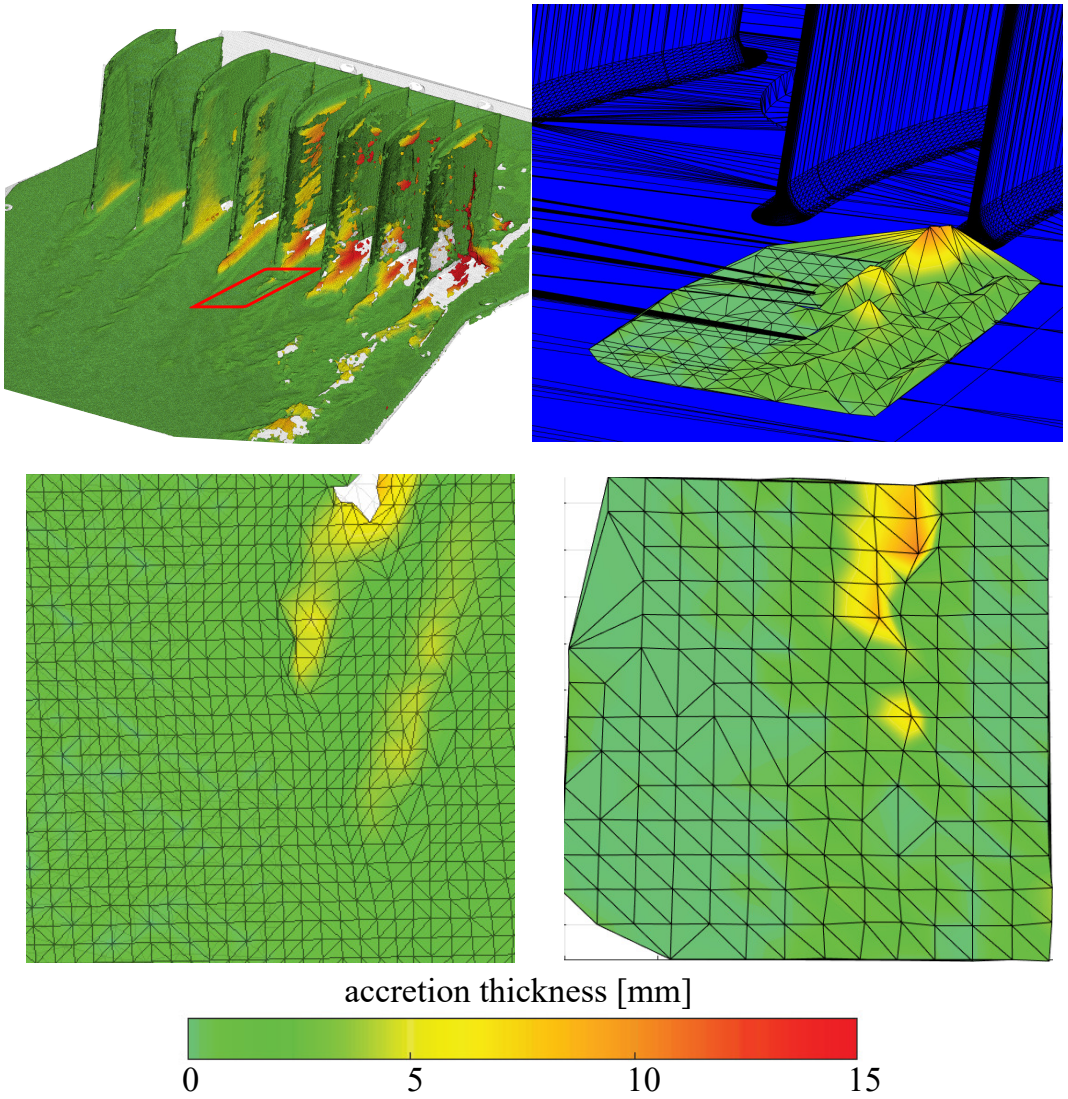

Figure 4.36: Test # 6. Isometric view of downstream ice thickness measurements (top row) from the Creaform HandyScan (left) and DIP system (right), and top down view (bottom row) at melt ratio of 5%. Conditions: $T_0 = 10°C$, MR = 5%, Mach = 0.4.

4.14 Summary

This chapter has detailed the development and test of a three-dimensional ice accretion measurement system. A system comprising of a single laser and single camera was tested under ice crystal icing conditions and was found to have reasonable agreement with the previous measurement technique of backlit shadography. It was found that the system had good accuracy when the accretion was sufficiently thick (>1 mm). Below this threshold the internal reflections of the laser light prevented an accurate being obtained. The discrepancies between the two datasets

were caused by spanwise variations in accretion thickness, which verifies that a three-dimensional measurement technique is needed. Comparison to a commercial 3D scanner showed an averaged error of 0.34 mm. This scanner could only be used at the end of the test due to not being capable of taking measurements of the low reflectivity accretion, unlike the DIP system. This verifies the requirement of the DIP system being able to record during the test to obtain transient data.

The ability to capture quantitative data is critical for validating ice crystal icing codes in complex environments, especially in three-dimensional models. This data shows that the DIP method is capable of gathering this data, and once it is suitably validated it will be used extensively in future tests for numerical validation of complex accretion geometries.

A second system comprising of a duel camera, single laser system has also been developed in house and compared to the DIP system using bench-top testing. Future testing at the NRC will compare the two systems under ice crystal icing conditions. Testing of plenoptic imaging was conducted at USQ and it was found that the system was capable of producing high spatial resolution results with sub-millimetre resolution. This method will also be tested in future tests to be validated and compared to the two systems developed in this PhD.

5

Development and Validation of the Ice Crystal Icing Numerical Model

Contents

This chapter details the development of the ice crystal icing numerical program, ICICLE. The program has been re-written to improve computational efficiency and numerical stability. From the findings of the literature review, it was decided to include new physics, such as coupling between the accretion profile and the CFD flow solution used in the particle tracking. Most of the chapter uses the stator test piece for which the most validation data exists. A summary of the sub-models developed as part of the thesis is shown in Table 5.1.

Table 5.1: Comparison of the pre-existing and developed ICICLE code. Additional components split into work conducted as part of this thesis, and additional work completed by colleagues of the ice crystal icing group.

	Original ICICLE	Updated in thesis	Updated by colleagues
particle-continuous phase heat transfer	none	experimental data used to artificially reduce the continuous phase temperature	
film model	constant thickness	shear driven film thickness	
substrate cooling	none	heat transfer caused by particle melting	
accretion growth method	planar	generalised	
flow coupling	none	accretion-flow coupling	
Lagrangian particle tracking time integration	explicit Euler		implicit Euler
particle rotation	none		non-spherical rotation lift forces
particle phase change	non-spherical Nusselt number		new model to include surface blowing, based on an external experimental data-set

5.1 ICICLE Derivation

This work further develops the ice crystal icing numerical model produced by Bucknell *et al.* [13]. The key equations used in this model are detailed in Appendix C, and references are made to the relevant publications.

5.2 Suitability of RANS CFD

Numerical CFD solutions of iced profiles are often unsteady due to an increase in surface roughness and change in geometric shape. To determine if Unsteady Reynolds-averaged Navier–Stokes (URANS) simulations were necessary to accurately predict the accretion behaviour of such geometries, a comparison between Reynolds-averaged Navier–Stokes (RANS) and URANS was made. Experimental video data from a 2017 test of the stator test piece in RATFac [71] was analysed to determine a representative accretion profile to be studied (taken after 90 seconds of accretion). A RANS and URANS simulation was completed using the same geometry and boundary conditions ($T_0 = 10°C$, Mach = 0.4). The unsteady wake from the iced stator is shown in Figure 5.1, as computed in the URANS calculation. A time-averaged Pressure coefficient (C_p) distribution over the accretion and stator suction surface was calculated from the URANS data, and compared to RANS data, as shown in Figure 5.2. The transparent red curves show the C_p distributions for each time-step computed, and the dark red line is the time-averaged C_p distribution. The error bars show one standard deviation in C_p for all computed time steps. The data showed that the RANS simulation was close to one standard deviation from the URANS for the pressure surface, however a much greater difference occurred on the suction surface.

For analysis of ice crystal icing, a sufficiently accurate flow solution is required in the regions where particles are expected to pass through the numerical domain. For the cambered bodies studied in this thesis, particle impact is only expected on the pressure surface and not on the suction surface. The unsteady flow structures formed in the wake reduce the accuracy of the RANS flow solution on the suction

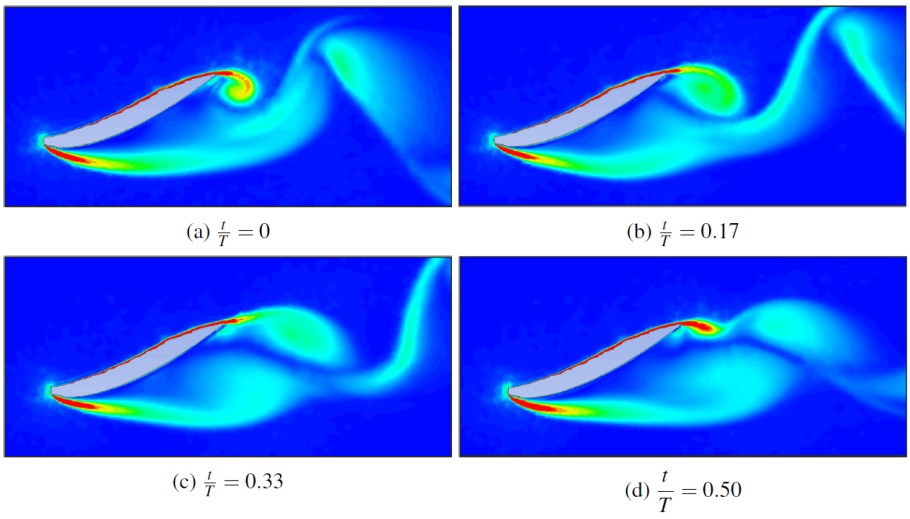

Figure 5.1: Contours of vorticity as calculated through a URANS simulation of the stator test piece, showing the convection of the trailing edge vortex.

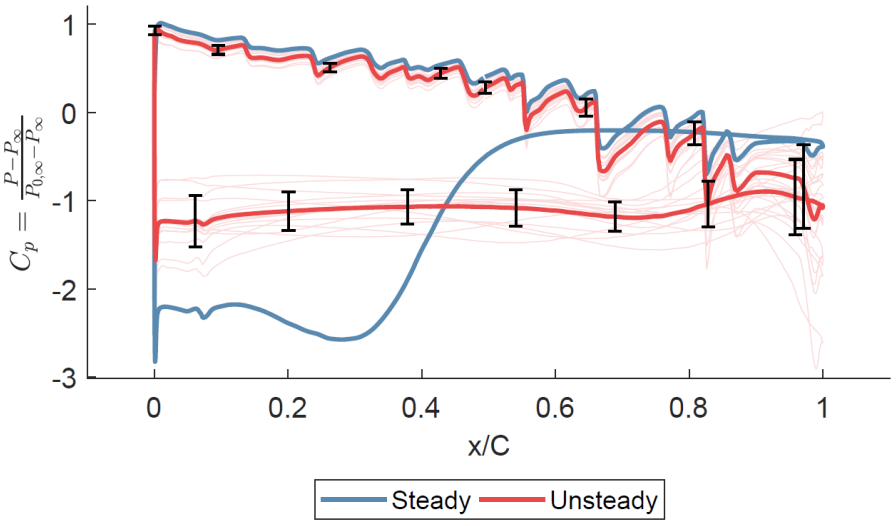

Figure 5.2: Pressure coefficient distribution over the stator for the steady (RANS) and unsteady simulation URANS.

surface, however as particles are not expected to pass through this section of the domain, the flow solution does not need to be a accurate. It should be noted that the wake flow structures do need to be sufficiently resolved in RANS to prevent inaccurate total pressure losses altering the mass flow rate induced by pressure inlet/outlet boundary conditions. For the work conducted in this thesis, it was assumed that as the test pieces are only located in one axial position, the flow structures downstream of the blade row does do not need to be accurately predicted,

allowing for a RANS solver to be used.

For the simulations of the triple airfoil linear cascade at a non-zero angle of attack, there is a possibility of the wake of one blade interfering with the adjacent blade's pressure surface, therefore reducing the accuracy of the RANS solution on the neighbouring blade. It was found that the limited flow separation of this geometry led to only marginal interference between the wake and the region of expected accretion on the adjacent airfoils pressure surface. However, this will not be the case for cascade geometries with more aggressive flow turning, so should not be taken as a general rule.

From these findings it was concluded to use a RANS solver for the simulations in this thesis, but it was noted that the particle trajectory calculations downstream of the trailing edge could not be considered accurate.

5.3 Mesh Dependency

A baseline mesh was created such that the geometric features of the airfoil body were sufficiently captured and prism layers grown from each wall produced y+ < 1 globally. Mesh density regions were situated around the body in regions of expected pressure gradients and also following the blade trailing edge to capture the wake. A mesh dependency study was conducted, where the size of the density region, the growth ratio away from the density, and also the mesh size inside and outside of the density region was adapted.

5.3.1 Flow solution

To ensure that the flow solution was independent of the mesh, a line profile was extracted from the CFD solution at a position 5 mm upstream of the leading edge. Mass weighted averages were computed for the Mach number, static and total pressure. These parameters were chosen as they have the largest influence on the particle trajectory calculations and therefore the accretion behaviour. The results of this study are shown in Figure 5.3, from which it was concluded that the simulation with a mesh count of 400,000 was sufficient for this geometry.

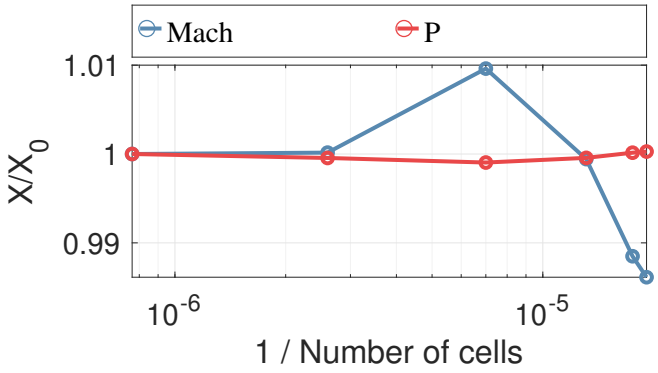

Figure 5.3: Variation of mass averaged flow parameters (X) at a location 5mm upstream from the airfoil leading edge, normalised by the value from the simulation with maximum cell count (X_0).

5.3.2 Particle Tracks

Calculation of the particle trajectories in ICICLE uses one-way coupling - where aerodynamic forces are imparted onto a particle, but forces are not imparted by the particle onto the fluid. This means that a CFD flow solution can be computed without inclusion of the particles into the flow domain, and the flow solution is then used in Lagrangian particle tracking. CFD solvers use high order spatial discretisation during the flow solving process. Particle tracking within ICICLE uses the CFD solution parameters at the nearest cell centre. If pressure gradients exist, adjacent particle streams with different neighbouring cell centres may diverge. While a mesh may be sufficient for convergence of the flow solution, if the mesh density were further increased, the neighbouring particle streams would probe more similar flow parameters, leading to less particle stream divergence. Increasing the mesh density past the level required for flow convergence and mesh independence increases the computational cost, so an alternative method is proposed - interpolating the flow parameter based on the distanced weighted average of the particle to the N nearest cell centres. A quad-dominant meshing strategy was implemented, so N=4 was deemed most suitable. Three particle tracking simulations were conducted; (case 1) baseline mesh with nearest cell centre flow parameters; (case 2) baseline mesh with flow parameter interpolation; (case 3) increased mesh density with nearest cell centre flow parameters.

Figure 5.4 shows 400 particle trajectories at the point near impact for both case 1 and case 2. The modelled particle streams in case 1 split into groups depending on which cells they passed through during their trajectory. Case two did not split into groups, and a more uniform set of particle streams reaching the body was found.

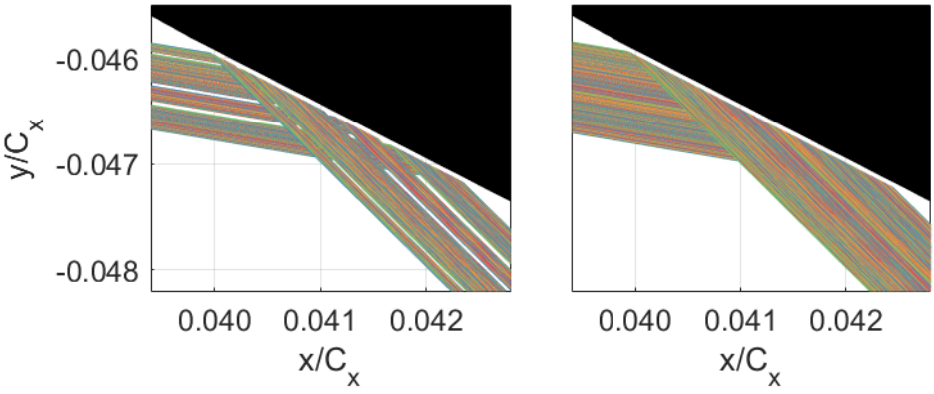

Figure 5.4: Particle trajectories near the point of impact onto the body using two different flowfield interpolation methods. Nearest neighbour interpolation - case 1 (left) and linear interpolation with four nearest elements - case 2 (right).

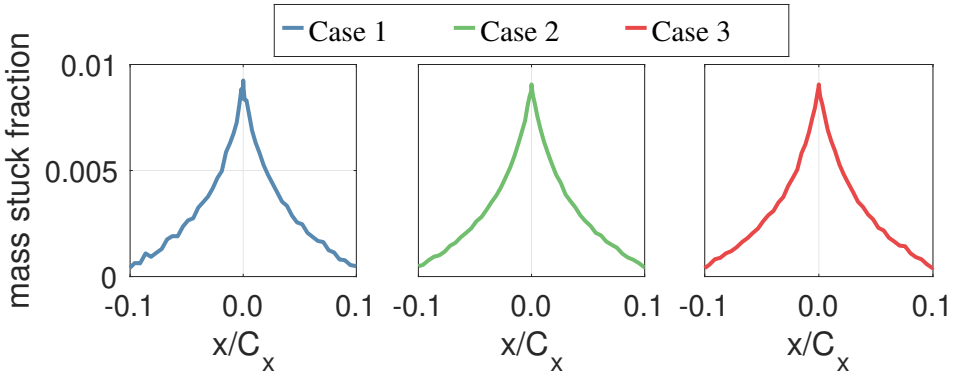

Figure 5.5: Distribution of mass flux stuck to a NACA-0018 airfoil geometry for three different flowfield interpolation methods. Case = 1 - mesh converged N = 1 (nearest neighbour), Case 2 = mesh converged N = 4 interpolation, Case 3 = nearest neighbour interpolation with an increased density mesh.

Figure 5.5 shows the distribution of mass flux stuck to the test piece surface as a function of the axial chord position (with the suction surface coordinates having a negative value). Case 1 had a non-smooth mass distribution, however the use of flow parameter interpolation (case 2) smoothed out the resulting stuck mass distribution. Comparing to the increased mesh density simulation (case 3), it was

found that the use of flow parameter interpolation produced comparable results to using an increased mesh density solution. To save on computational costs, it was decided to use spatial interpolation in future simulations.

5.4 Particle Trajectory Calculation

5.4.1 Validation

Particle tracking functionality exists in the commercial CFD program, ANSYS FLUENT. To validate the output of the ICICLE trajectory calculations, comparisons were made to an equivalent simulation in FLUENT. A suitable validation test case is one in which pressure gradients exist and multiple particle impacts occur. It was decided to use the hub and casing profile of the swan neck duct test piece, with the blade rows removed, and the effects of flow turning in the camber direction neglected, creating a two-dimensional domain. Contours of static pressure at the baseline condition (Mach = 0.4, T_0 = 10 °C), are shown in Figure 5.6. Particles were injected over the inlet surface and tracked until the domain exit. The time-step size for the Lagrangian time-stepping was matched between ICICLE and FLUENT, and implicit time integration was used.

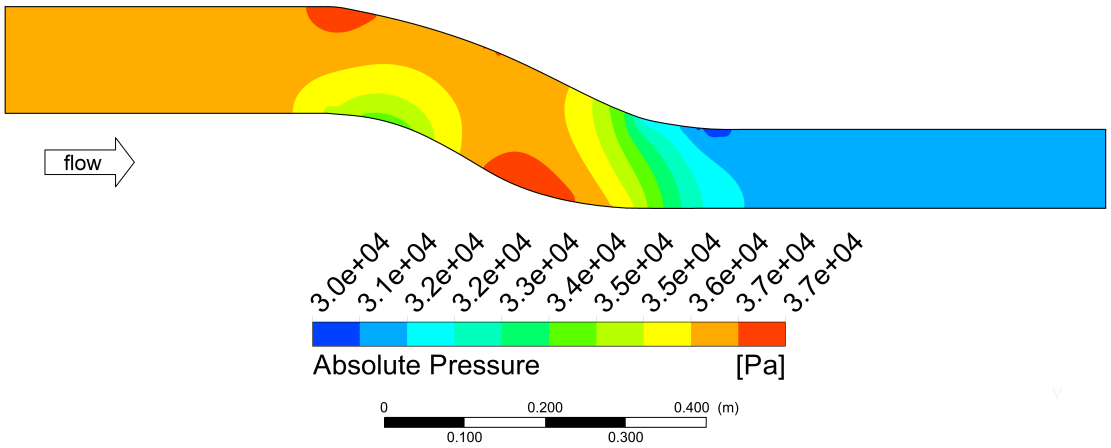

Figure 5.6: Static pressure contours the in swan neck duct test piece. Conditions: P_0 = 40 kPa, T_0 = 283 K, $Mach$ = 0.4

In ICICLE, the bounce/shatter model by Villedieu *et al* [19] has been implemented to account for the effects of plastic losses and fragmentation during the

rebounding process. To save implementing this model as a user defined function into FLUENT, for the means of validating the particle trajectories, it was decided to fictitiously set the coefficients of restitution to be equal to unity.

Figures 5.7a to 5.7c show the trajectory paths of both the ICICLE and FLUENT simulations at five spanwise positions for three different particle sizes; 15, 40, 80 μm. The FLUENT data-set has been re-sampled to show every 40 timesteps for clarity. Qualitatively, a good match is observed between the ICICLE and FLUENT data. Quantification of the difference between the datasets was found by computing the minimum distance between the two trajectory paths at each position. An averaged distance between paths was calculated at each axial position (for all 200 particle streams simulated) and is shown in Figure 5.8. Step changes in error occurred at impact locations, where small differences in particle paths at pre-impact led to larger differences in post-impact trajectory, as shown in Figure 5.9. It was found that the distance between the trajectory paths of the ICICLE and FLUENT simulations were within one particle diameter, which was deemed sufficiently accurate for this analysis. While this does not validate ICICLE for the trajectory of ice crystals, it does validate it for general particulate trajectories of spherical objects. Further physics is then utilised in ICICLE to account for the complexities of ice crystal trajectory dynamics.

5.4.2 Particle Stream Count Convergence

Ice crystal icing experiments inject large quantities of particles. Experiments from RATFac have a general upper limit on the particle feed rate of $\sim 8\ \mathrm{g\,m^{-3}}$ at Mach 0.4, which is in excess of 2×10^9 particles per second. Current computational resources do not allow such large simulations to be computed in reasonable time frames. Instead, "streams" of particles are injected into the numerical domain at discrete points in space. These streams represent multiple real particles, for which it is assumed that their mean trajectories are equal, and therefore only need to be computed once. The mass associated with each stream is the product of the mass of the particle and the number of particles contained within the stream. The ratio of the mass of the particle and the mass associated with the stream is termed the

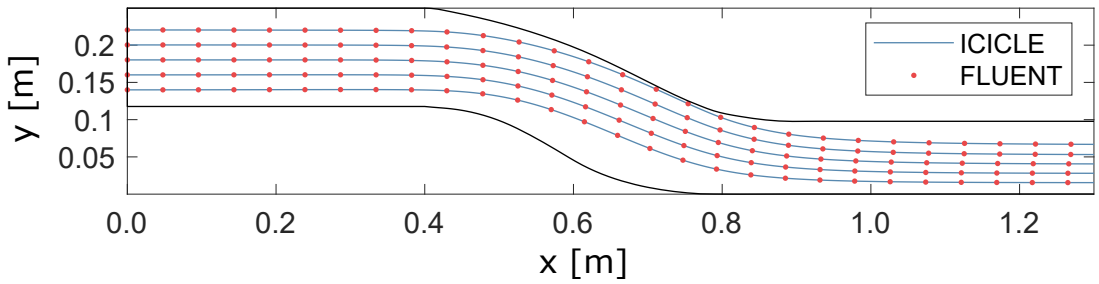

(a) $D_p = 15$ µm.

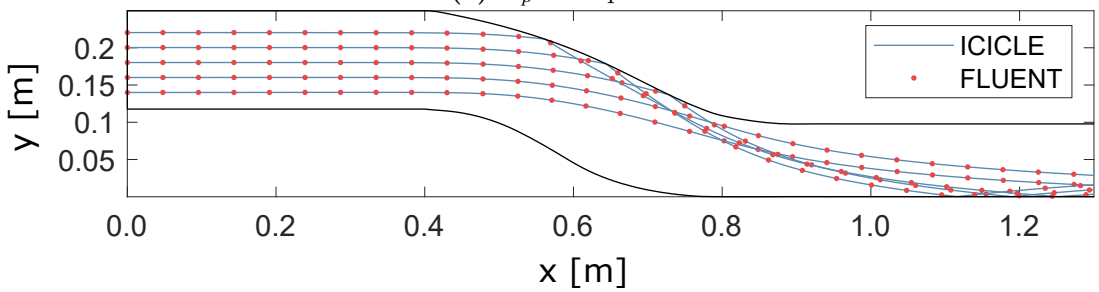

(b) $D_p = 40$ µm.

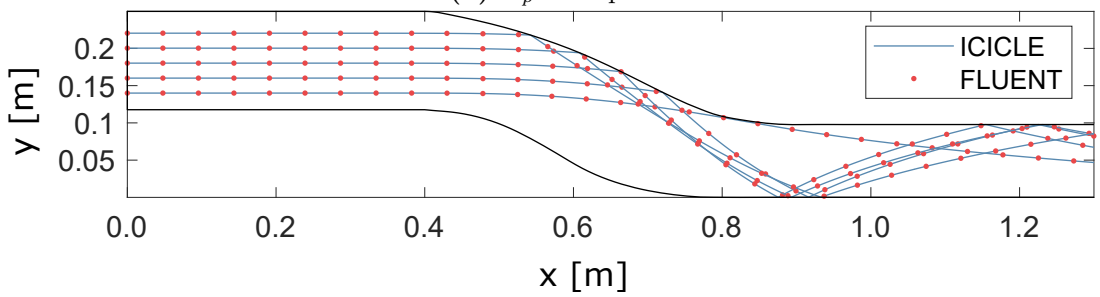

(c) $D_p = 80$ µm.

Figure 5.7: Comparison of ICICLE and FLUENT trajectory paths at varying (monodispersed) particle sizes. Note that coefficients of restitution were set to be unity for this particle trajectory validation case.

particle Scaling Factor (SF). An exact solution would be obtained if each stream contained a single particle (SF=1), but if only a small number of particle streams are simulated (high SF), then the numerical simulation is likely to incorrectly predict the distribution of mass sticking to the test piece.

The value of SF required for suitable accuracy needs to be found through a convergence study. Suitable convergence criteria for particle count convergence has been studied by Vadgama *et al.* [104], who found that convergence based on mass deposited on the test piece at an integral level was insufficient. Instead, a comparison of the change in the distribution of mass deposited around a test piece with increasing particle stream count is required. By discritising the NACA-18

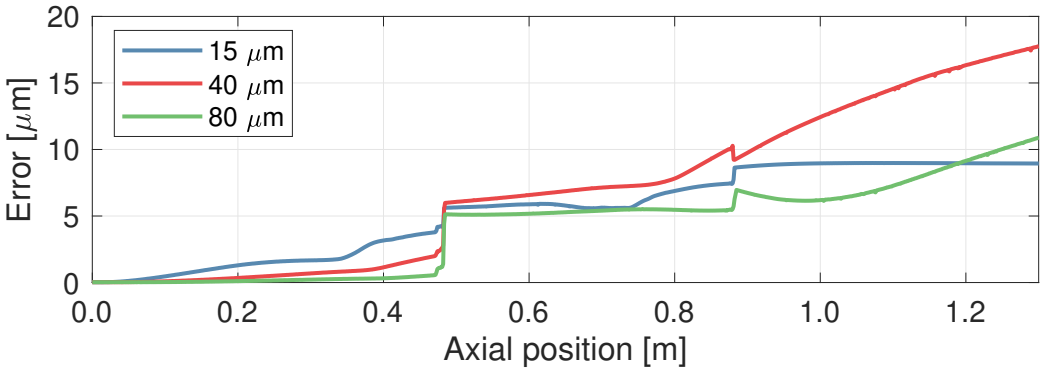

Figure 5.8: Distance between trajectory paths of the ICICLE and FLUENT simulations at three particle sizes.

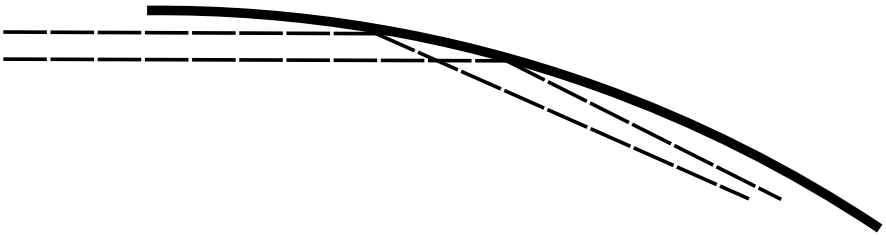

Figure 5.9: Effect of difference in incoming parallel particle trajectory paths on post-impact trajectory path.

airfoil test piece into a uniform mesh of size 0.5 mm ($0.0125C_x$), the distribution of mass fraction stuck on each mesh element was found (mass stuck normalised by the total mass injected). Each successive simulation had double the number of streams of the previous (half the scaling factor), and the difference in mass deposited to each mesh element was compared to the previous simulation. A summation of the difference in stuck mass fraction of each mesh element has been found to provide a suitable convergence parameter [104].

The number of streams required to reach convergence is dependant on the particle size due to changes in their ballistic nature. Three sets of simulations were conducted with mono-dispersed particle sizes of 12, 35 and 45 µm (a typical $D_{v,10}$ $D_{v,50}$ $D_{v,90}$). Convergence was assumed to be at the point of less than 0.5% change in deposited mass fraction with increasing particle stream count. The results are shown in Figure 5.10. The number of streams was increased from 200 to 3.3×10^5, which for the 35 µm case related to a scaling factor of 1×10^7 to 6,700 (injection of 8 g m^{-3}, Mach = 0.4, 1 second exposure). It was found that similar convergence

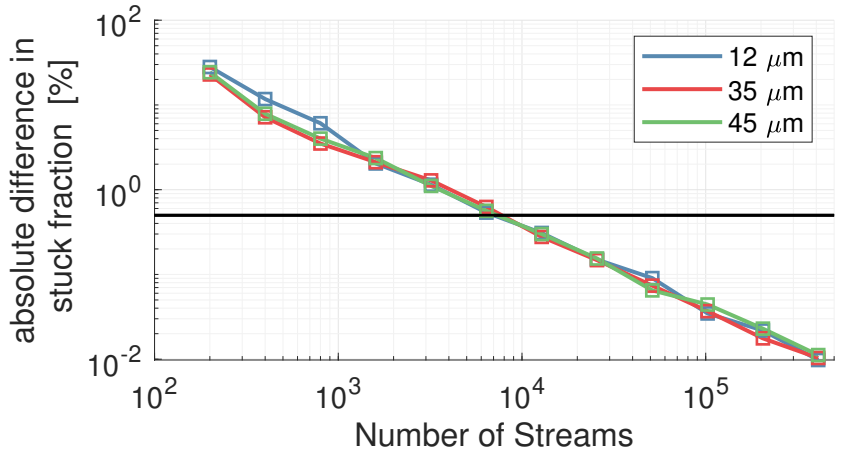

Figure 5.10: Effect of the number of streams on the change in predicted stuck fraction of particles onto the stator test piece. Statistical convergence assumed when the change in stuck fraction was below 0.5% (shown as the horizontal black line).

rates were observed for each particle size tested, with convergence being reached at approximately 10,000 streams. It should be noted that new convergence studies need to be conducted when changing operating conditions or test piece geometry. The convergence studies for each condition analysed in Chapter 6 is shown in Appendix D.

When injecting representative particle clouds, a non-uniform particle size distribution is injected. The size distribution can be sampled at different sizes to calculate the probability of the particle being of that size. By injecting streams of particles at each of these sampled sizes, the scaling factor of each stream can be adjusted to account for the varying amount of each size in the true distribution. For simulations with a distribution of particle sizes, a converged number of particle streams at each particle size needs to be injected so that the whole distribution is converged.

5.4.3 Numerical Efficiency Increase

The number of particle streams required to reach statistical convergence is high, meaning that significant computational demand is required to compute the particle trajectories. The previous implementation of ICICLE was written in MATLAB code, and on each timestep looped through each particle stream to compute the new particle state. As part of this work the code was rewritten in a vectorised

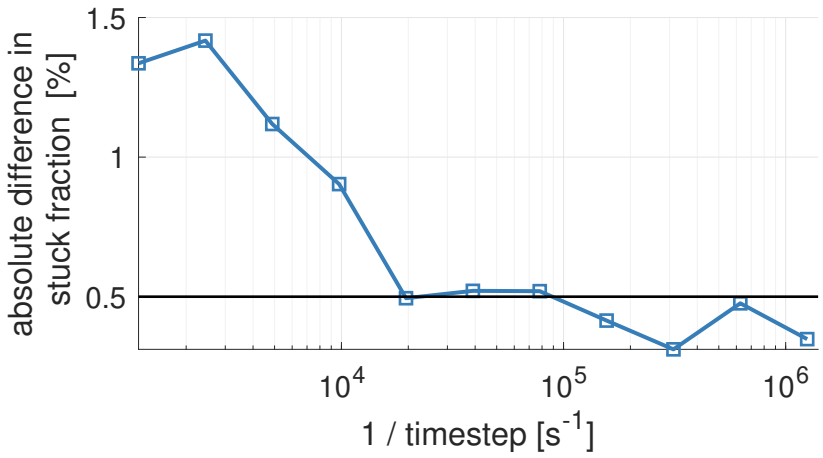

Figure 5.11: Effect of timestep size on change in predicted stuck fraction of particles onto the stator test piece. Statistical convergence assumed when the change in stuck fraction was below 0.5%.

format [105] which reduced the computation time by over an order of magnitude. Further computational gains were achieved through the use of GPU enhanced code for certain demanding functions. Through this work, the number of particle streams which could be tracked in a feasible time frame was dramatically increased.

5.4.4 Lagrangian Time-step Convergence

Lagrangian particle trajectory calculations integrate the equations of motion over a finite time-step size. Large time-step sizes fail to capture gradients in flowfield properties, reducing the accuracy of the solution. For improved efficiency the model has a variable time-step size; fixed duration in the freestream, and when in the proximity of a domain surface it is linearly decreased from the freestream value down to the required time-step size to move a particle by one diameter in a single time-step when at the wall. Using the same convergence method as for particle stream count, the freestream time-step size was reduced on successive simulations. The simulation results are shown in Figure 5.11, from which it was concluded to use a time-step size of 50 μs. It should be noted that the required time-step size is dependant on both the flow conditions and particle size distribution.

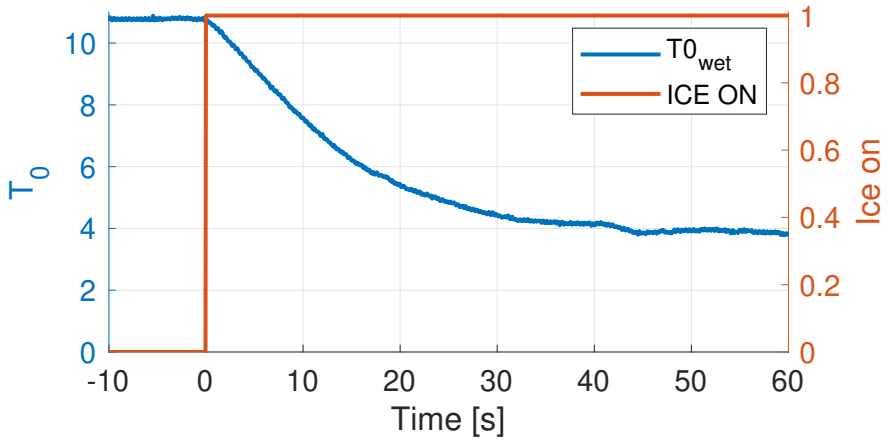

Figure 5.12: Experimental reduction in total temperature when ice is added to the gas path flow. Conditions: Mach = 0.4, T_0 = 10 °C (prior to ice on), relative humidity = 45%, ice water content = 4 g m^{-3}.

5.5 Mass and Energy Transfer between Crystals and Continuous Phase

When the ice cloud is turned on, energy is transferred between the air and ice crystals. In the current implementation of the model, one-way heat transfer occurs from the warm air to the crystals. Heat and mass transfer also occurs due to evaporation/sublimation of the crystals, however this is currently not transferred back into the continuous phase solution space. To account for this, the relative humidity and temperature of the domain are adjusted according to experimental data of the simulated conditions. Figure 5.12 shows a typical reduction in total temperature when the ice cloud is turned on, at conditions of 8 g m^{-3}, Mach 0.4, $T_{wb,0} \approx 1°C$. Future work will implement two-way coupling between the particles and the continuous phase to predict the air cool-down so that experimental data is not required.

5.6 Substrate Cooling

Ice crystal icing typically starts with with a warm test piece which cools due to the impingement of ice crystals. Predicting the cooling of the substrate is essential to determine whether ice formation can occur, or whether only a water layer will form.

The heat flux drawn away from the substrate can be found from the temperature gradients of the inner water layer, computed within the EMM-C. It was decided to impose the computed heat flux as a boundary condition into a finite element model to predict the test piece cool down.

ICICLE makes the assumption that the liquid water from a partially melted ice crystal is fully shed onto the surface upon impact. A criterion needs to be applied to determine if the ice core will stick to the surface or bounce/shatter. Bucknell experimentally derived the sticking probability of ice crystals as function of the melt ratio, but is only suitable when an ice layer is preexisting and over-predicts the sticking probability onto a liquid film. In the substrate cooling model presented by Currie [106] a critical stokes number was used to determine the post impact behaviour of the crystals into the liquid film, taken from the work of Ma *et al.* [107]. A modified stokes number was proposed by Ma, defined as the ratio of the initial particle momentum normalised by the viscous force of the film, as defined in Equation (5.1), where V_i is either the normal or tangential component of velocity relative to the film surface normal, μ_w is the film dynamic viscosity, and h_{film} is the water film thickness. Experimental results of Ma showed that the normal coefficient of restitution could be approximated as zero for a normal modified stokes number below 2000, and the tangential coefficient of restitution could be approximated as zero for a tangential modified stokes number below 500. In this work, a particle was assumed to stick if both of these criteria were met.

$$St_N = \frac{m_p V_i}{\mu_w d_p h_{film}} \tag{5.1}$$

A modification to the stokes number definition is proposed for use with non-spherical particles. Non-spherical ice shapes are typically approximated as either being prolate or oblate. Upon impact with the water film, it is assumed that the particle rotates so that the major axis is tangential to the film, meaning that the minor axis is dominant in the impact behaviour. The diameter used in the denominator of Equation (5.1) is therefore replaced with $2c$ for oblate particles, and $2a$ for prolate particles (see Figure 2.2). When an ice flow is first exposed

to the surface no water film exists, so it can only be formed by the splashing of partially melted particles. As the film grows in thickness with further splashing, the critical modified stokes number is reduced, meaning that crystals can get trapped in the film, further adding to the film growth. Any particle which is trapped by the water film is assumed to instantaneously melt. This has been implemented into ICICLE within a multi-timestep approach.

While the testpiece cools, experimental evidence shows that a stable water film is produced. The previous version of ICICLE assumed all the water accumulated at a thickness greater than a critical film thickness (based on the test-piece surface roughness) would be transported downstream on the next time-step of the numerical model. An improved method was derived by Currie [106], where the film thickness was based on the mass flux onto the surface and the local wall shear stress. By integrating the velocity profile, and substituting in the equation for the shear at the free film surface, the film thickness was derived. In Currie's work a simple linear velocity profile was assumed. Research in other fields has resolved velocity profiles in shear driven films [108, 109], however their applicability to films being impinged by particles has not been studied. For the model used in this work a linear velocity profile is assumed however further work may look into proposing an alternative profile. For a linear velocity profile, the film thickness is a function of the film dynamic viscosity, mass flux of impinging particles, mass flux of evaporating moisture from the film, mass flow rate of film run-back from upstream panels, film fluid density, and local aerodynamic wall shear stress (Equation (5.2)).

$$h_{film} = \sqrt{\frac{2\mu_w \left(\dot{m}_i + \dot{m}_w - \dot{m}_e + \dot{m}_{run}\right)}{\rho_w \tau_{wall}}} \tag{5.2}$$

5.6.1 Model Validation

The stator test piece was used in further tests in 2019 [110] for the validation of the DIP system. In this test piece surface thermocouples recorded temperatures 0.3 mm below the icing surface, located at the positions shown in Figure 5.13. The primary aim of the experiments was to validate the DIP system using repeated conditions.

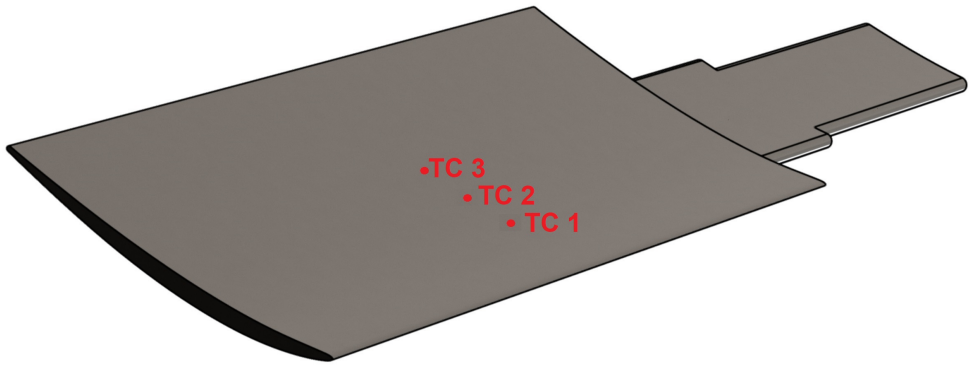

Figure 5.13: Stator test piece, with thermocouple locations shown in red.

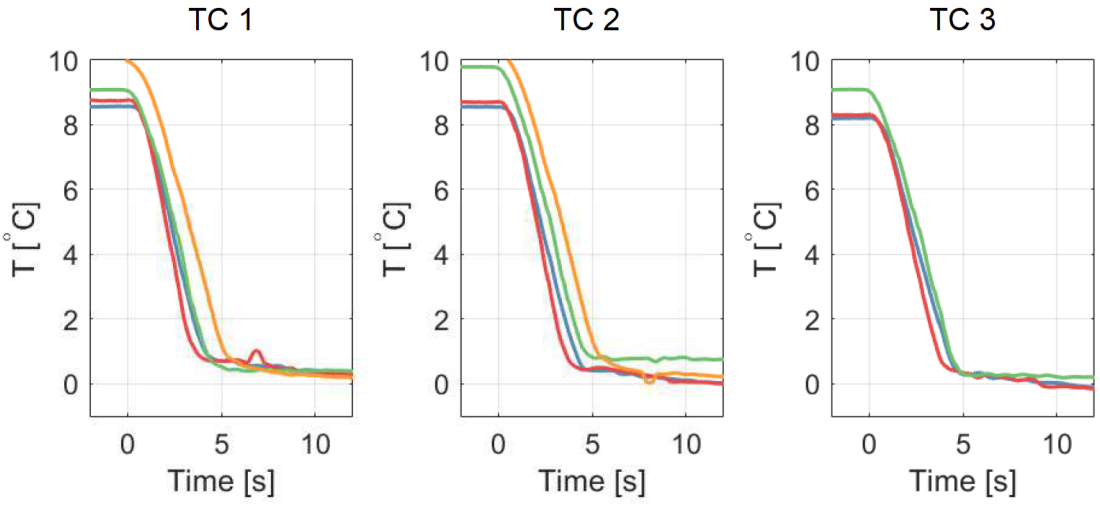

Figure 5.14: Thermocouple readings from stator test piece. Time referenced to the moment the ice cloud was initiated. Sub-figures from left-right are thermocouples 1-3. Each line (red, green, blue, orange) is a different experimental run at the same nominal test conditions.

It was not possible to exactly match the conditions of successive runs due to tunnel drift and hysteresis but the total temperature remained within 1°C of the baseline condition. Figure 5.14 shows the measured surface temperatures from the point of the ice cloud being turned on for four repeat tests of the same condition. It was found that a rapid decrease in temperature occurred in the first five seconds, and then slowly decayed until $\approx$ 8 seconds at which freezing conditions were met. The thermocouple nearest the leading edge had a slightly reduced time period to reach freezing conditions due to the test piece having varying blade thickness and also spatially dependant collection efficiency.

The numerically predicted heat flux was implemented into an FEA model

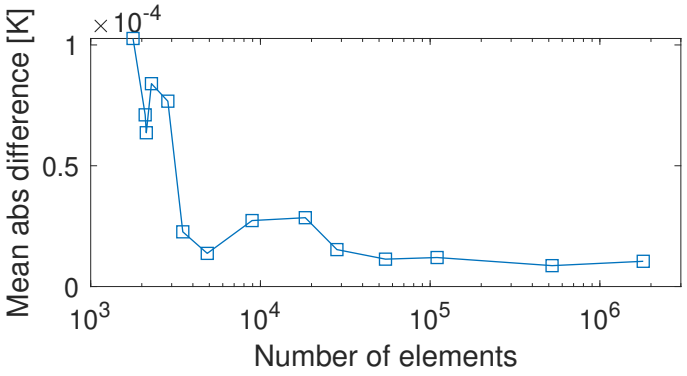

Figure 5.15: Change in body surface temperature with increasing mesh count of the stator test piece FEA model.

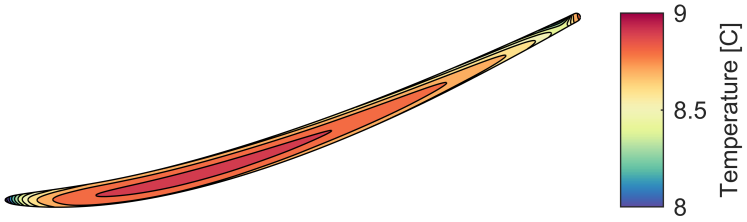

Figure 5.16: Numerically predicted temperature profile after 0.1s of ice exposure.

using the partial differential equations toolbox from MATLAB. The initial body temperature in the model was set equal to the mean surface thermocouple reading prior to ice-on. A mesh dependency study compared the change in body surface temperature with increasing mesh resolution. From the results of the mesh dependency (Figure 5.15), it was decided to use a mesh with 50,000 elements. To validate the output of the MATLAB toolbox, the solution was compared to data produced by COMSOL Multiphysics©, a well documented commercial multi-physics modelling software. Comparisons of the two datasets were made using heat fluxes typical of the baseline condition, applied for 0.1 s of ice exposure. The temperature profile predicted in MATLAB is shown in Figure 5.16, and a comparison of the body surface temperature distribution between the two models in Figure 5.17, where the maximum deviation was less than 0.002 °C. Due to high latency in data transfer between COMSOL and ICICLE, it was decided to compute the FEA heat transfer in MATLAB.

The results of the numerically predicted test piece surface cool-down at the

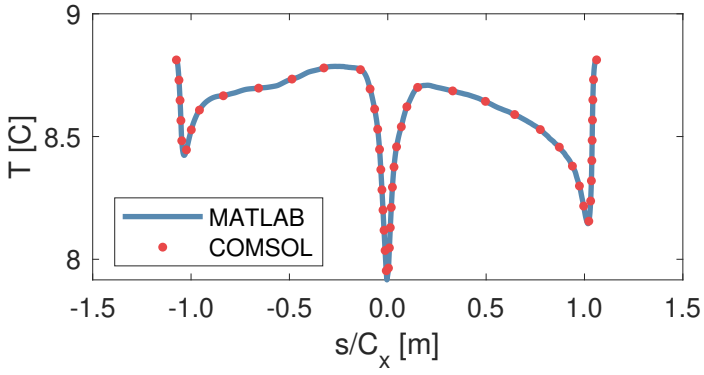

Figure 5.17: Comparison of surface temperatures predicted using MATLAB and COMSOL FEA models.

positions of the three thermocouples are shown in Figure 5.18. After two seconds of exposure the numerically predicted cooling rate was -1.6 °C s^{-1}, which was 41% lower than the experimental cooling rate. Freezing conditions were reached after 7.2 s, which had good qualitative agreement with the experimental data. It was not possible to precisely define the time at which freezing conditions were met in the experimental data due to a slow decay in temperature below 0.5 °C, likely caused by the thermocouples being placed at a small offset from the test piece surface and the cantilevered end of the stator mounted into the wind tunnel acting as a thermal mass. A secondary simulation was conducted with a time-step size of a quarter of that in the current simulation (reduced to 0.075 s down from 0.3 s). The results of this simulation are shown in Figure 5.18, and the good agreement between the two data sets suggest that further reducing the time-step size would not alter the time to reaching freezing conditions. When the timestep of 0.3 seconds was used, a slight oscillatory response in surface temperature was predicted. Over a time-step a heat flux is computed for a given impingement mass flux and previously predicted film surface temperature. If the time-step size were too large then an over-cooling of the test piece would occur, which would then be heated up due to the run-back of the film from the previous time-step.

If the sticking criteria of ice crystals onto the water film was assumed to be the same as sticking criteria onto an ice accretion, the sticking mass was found to be an order of magnitude larger than using the modified stokes number criteria.

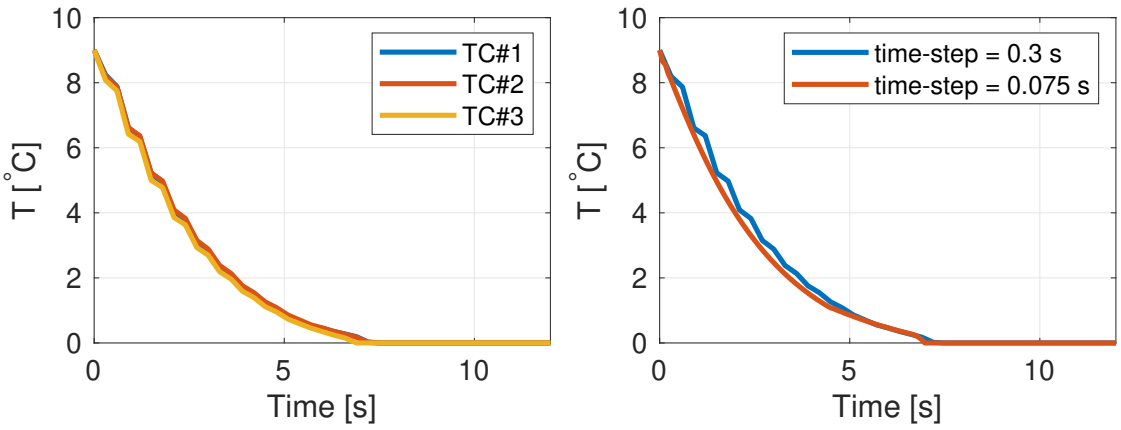

Figure 5.18: Numerically predicted cooling of test piece using two dimensional model. Comparison of surface temperatures at positions of thermocouples (TC) 1-3 (left), and comparison of surface temperature at position of TC 2 at different numerical time-step sizes (right)

.

The large increase in latent heat of fusion to melt this additional stuck ice caused the cooling rate to be substantially over predicted, leading to an initial cooling rate of -940 C/s. Because of the melting term being dominant, it is thought that the sticking criteria based on a modified stokes number is the largest source of error in predicting the substrate cooling rate. Another key source of error is the prediction of the Heat Transfer Coefficient (HTC), which was derived using a two point method; two simulations at the same aerodynamic condition but different isothermal wall temperatures. The HTC was calculated by taking the ratio of the difference in wall heat flux to the difference in wall temperatures. The CFD predictions of surface heat flux were extracted from RANS simulations, which typically struggle to accurately predict near-wall heat fluxes. No experimental data of HTC for this test piece is available, so quantification of the errors induced from the HTC predictions is not possible.

5.7 Accretion Growth Methods

Domain discritisation is required for accretion modelling, and it is assumed that the accretion behaviour within each discritisation element is constant. With finer discritisation, high particle streams counts are required to reach convergence. Coarse

discritisation can over-simplify the geometry, altering the local surface normal and hence altering the impact dynamics.

The previous version of ICICLE [13] utilised two levels of domain discritisation - a fine discritisation to define the geometry and surface normals, and a coarse discritisation where multiple domain points were grouped into "panels", over which the accretion was assumed constant. This method required low stream counts to reach convergence, while also maintaining the true surface normals. Figure 5.19 shows a representative panel distribution around the stator test piece, where multiple domain points are associated with each panel. Most test pieces have a spatially dependant collection efficiency and erosion rate, causing step changes in growth rates of adjacent panels. If the geometry of each panel is simply extruded on each timestep, then step changes in geometry occur at the intersection of panels (as seen in (b) of Figure 5.20). To obtain accurate results, most accretion codes use a "multi-shot" approach, where small duration's of ice exposure are simulated, and particles are re-injected onto the iced profile so that the sticking mass distribution can be updated. Step changes in geometry at panel intersections cause non-physical impact dynamics, reducing the solution accuracy. Panel growth rates can be interpolated to the underlying geometry to create smooth transitions between adjacent panels (as seen in (c) of Figure 5.20). This can be well implemented for planar geometries but can lead to uncontrolled smoothing in geometries of high curvature, making mass conservation difficult unless sophisticated smoothing methods are applied [111].

These numerical issues would be mitigated if a fine domain discritisation were used with a statistically converged stream count. Simulating streams of particles that represent a greater number of real particles inherently creates a non-smooth surface distribution of sticking mass. If this distribution of mass flux onto a surface was used to determine the ice growth, a non-physical surface roughness would form. A rough surface will then alter the impact calculations on the next injection, and also alter the direction of successive ice layer growth which can lead to numerical instabilities in colliding mesh elements.

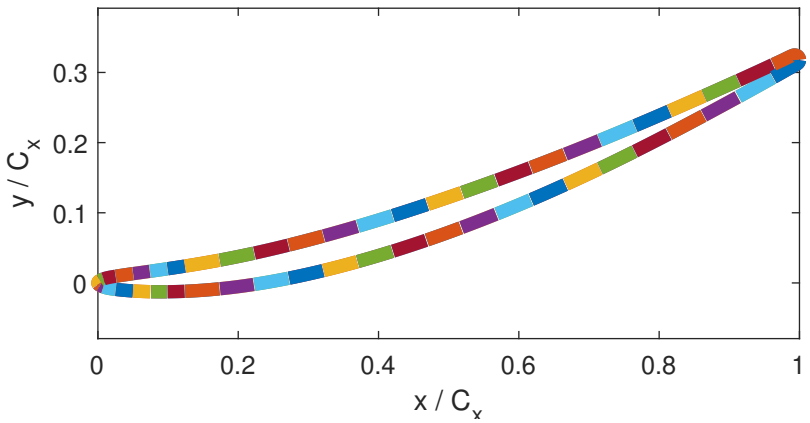

Figure 5.19: Distribution of panels around the stator test piece.

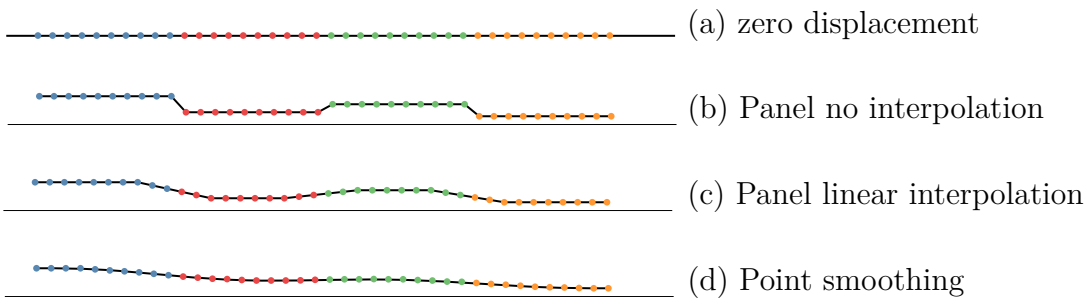

Figure 5.20: Comparison of different accretion growth methods. Legacy ICICLE code utilised panels, new proposed method uses a point based method.

An alternative method has been incorporated into this work - deposited mass is associated with the underlying geometry nodes. Growth of the accretion is then done on a nodal basis, which is post-smoothed using a mass conserving smoothing method [111], creating a smooth accretion (as seen in (d) of Figure 5.20). Removing the need for computation of panels simplifies the code and bring it in line with traditional mesh morphing techniques. This method would not have been possible with the previous version of ICICLE, as the required number of particles to reach statistic convergence would have taken excessive timescales to compute.

Equations defining the growth of the three-layer water-ice-water accretion are as found in [49], and have been used in this work on a nodal basis rather than a panel basis as before. The equations were originally derived for planar geometries so need altered for general geometries. Three main assumptions are used in the model;

- linear temperature profile of the inner water layer in the normal direction

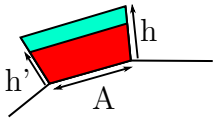

Figure 5.21: Conversion of a planar height from EMM calculations, (h), to nodal translation distance for a non planar geometry , (h').

- isothermal ice layer (at freezing temperature)
- isothermal top water layer (at freezing temperature)

Because of the isothermal ice layer assumption, the equations of growth of the bottom and top surface of the ice layer can be decoupled. For non-planar geometries the surface normal of each node is non-equal to its neighbour. The equations for the EMM produce a height over which that node should be displaced on that timestep for a planar cell. Multiplying the planar displacement (h) by the cell area (A), the volume of the new accretion is found. Using the planar-height as an initial guess, an iterative approach calculates the true displacement (h'). For converging node normals this increases the node displacement, and decreases it for diverging normals. This is shown schematically in Figure 5.21.

The additional benefit of this method is the guaranteed conservation of mass. The previous panel-based method assumed an extrusion normal to the underlying geometry. Because the points associated with each panel were unlikely to be planar, a multiplication of the panel area by the extrusion height does not equal the area of the true extrusion. The iterative method described above accounts for the arbitrary normal directions so that mass is conserved.

5.8 Accretion Time Discritisation for Ballistic Particles

An underlying assumption in the accretion modelling is that the mass flow rate of stuck particles to each cell of the body remains constant until the trajectories are re-calculated. Once sufficient accretion has formed, the collection efficiency distribution around the body will alter, meaning that the trajectories need to be

re-computed. For a constant mass flow rate onto a convex geometry, the rate of increase of accretion thickness decreases, due to the increased surface area. If the trajectories were re-computed, the larger area of the body cell face would likely capture more particles, increasing the growth rate. The two opposing factors in the magnitude of the growth rate mean that the particle tracks need to be updated sufficiently often for accurate predictions.

A fictitious test case was simulated of an infinite cylinder in cross flow. To reduce the complexity, it was assumed that all particles would behave balistically and have 100% sticking efficiency, meaning that the mass sticking to each body cell was proportional to the cell's frontal area. The first simulation only computed the sticking mass distribution once, and each successive simulation doubled the number of times that it was computed. For each simulation a fixed total mass of particles was injected, but the number of times that the trajectories were recomputed was altered.

Figure 5.22a shows the predicted accretion profiles for a number of particle sticking mass distribution recalculations. If the mass distribution is only calculated once, a large accretion forms at the upper and lower sections of the geometry. If the mass distribution is recomputed, these areas are shielded by the upstream accretion, meaning that only the central regions capture incoming particles. Re-computing the mass distribution over increasingly small time durations converges on a predicted accretion geometry. The cell displacement of the accretion geometry (relative to the clean geometry) was calculated for each cell of the body. The cell displacement was compared to that of the previous simulation with half the number of time-steps. The mean percentage change in cell displacement compared to the previous simulation is shown in the right-hand of Figure 5.22a. The solution was assumed to be converged when the mean difference was less than 5%, and this profile is shown in red on the left-hand side of Figure 5.22a.

The same simulation study was repeated for an ellipse with a major horizontal axis twice that of the minor vertical axis. The results are shown in Figure 5.22b. The number of time-steps to reach convergence for this geometry was ~ 50, and the circular geometry was $\sim$60, showing that it is geometry dependant. The maximum

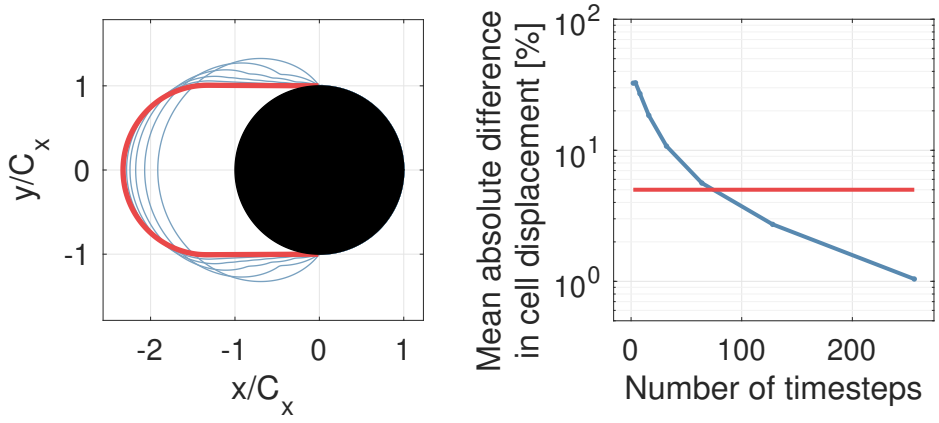

(a) Cylinder.

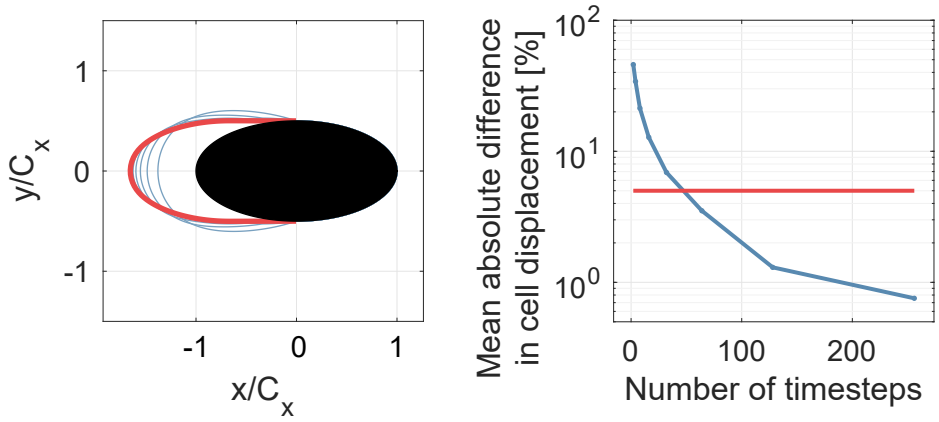

(b) Ellipse (with axis ratio of two).

Figure 5.22: Predicted accretion profiles of a sphere (a) and ellipse (b) in cross flow with ballistic particles. Simulations with increasing number of re-injection of particles is shown in blue, with the converged solution in red (left). Mean difference in accretion mesh displacement between successive simulations (right)

area increase of a cell on each timestep (compared to the previous timestep) for the converged solution of both geometries was found to be ∼2%. From these results it was decided to set the criteria for when the particle trajectories are re-computed to be based on the maximum area increase on that timestep rather than a fixed time duration. While a limit of 2% area change was found to be necessary for a 5% accuracy in accretion profile, it is expected that the limit will be somewhat geometry dependant, so will need to be studied for each geometry.

5.9 Inclusion of Flow Field Coupling

Figure 2.14 (Chapter 2) shows a flowchart of the different subsections which make up the ice crystal icing numerical model, ICICLE. A key missing component was the ability to update the flowfield based on the predicted accretion profile.

To update a flow solution, a new mesh needs to be created, conforming to the geometry of the accretion profile. This mesh can be created from scratch, or morphed based on the mesh of the clean body. Various methods of mesh morphing have been applied in previous literature, and have been summarised by El-Batsh [112]. In the early work by ONERA, the accretion was represented as a deformation of the original mesh, and it was suggested that the deformed mesh could be reused in the icing code to perform multi-stepping ice growth [113], however the results of this method were not published. It has since been found that this method of mesh adaption is limited to relatively small accretions [114], which makes this method unsuitable for ice crystal icing in which excessive accretion can occur. ONERA have published recent data on the effect of flow field updating for SLD accretion [68], however to date, however this has not been seen in the open literature for ice crystal icing.

Due to the limitations of mesh morphing, it was decided to create new meshes on each iteration of the code based on the current accretion profile. An appropriate meshing software had to have a command-line interface for batch processing (to mitigate user input) and be able to produce high quality meshes on uneven iced profiles. After studying a range of meshing programs, it was found that boxerMesh had the best stability. Automated macro scripts were written to define the geometry and mesh parameters for the meshing program.

A top level loop was then implemented into ICICLE so that these scripts could be sent to boxerMesh, and then import the created mesh into FLUENT for the calculation of the flowfield. The flow solution was then extracted in the region of interest and re-imported into ICICLE. The process of mesh creation and CFD computation was fully automated, to prevent the need for user interaction.

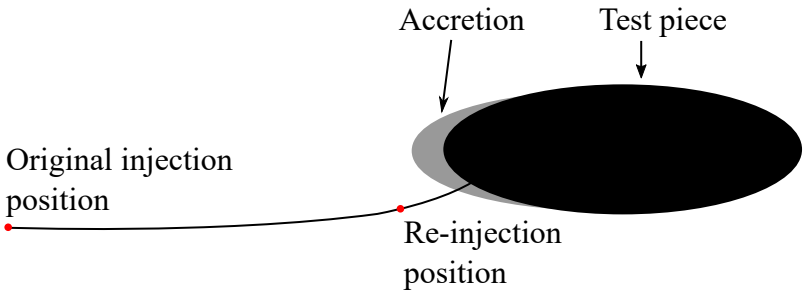

Figure 5.23: Particle re-injection position for computation of particle tracks when the flowfield has not been updated.

5.9.1 Particle Re-injection

From the results of Section 5.8 it is expected that the particle trajectories will need to be re-computed at regular intervals. If only a small amount of accretion has occurred between the trajectory calculations, sufficiently accurate results may be obtained by re-using the flow solution of the previous timestep. The regularity at which the flowfield needs updated is studied in Chapter 6. For the timesteps which have not updated the flowfield solution, there is no need to inject the particles at the start of the numerical domain. Instead, using the particle histories calculated in the last computation of the whole numerical domain, the intersection of the particle stream and the accretion edge can be computed. The new injection point can then be defined as the position a few time-steps upstream of the accretion edge, with the particle state (diameter, shape, velocity, melt ratio etc.) set as the particle state calculated in the previous simulation. This is shown schematically in Figure 5.23. Implementing this particle re-injection provides large numerical efficiency gains, in not repeating unnecessary calculations.

5.10 Comparison to Legacy Code

To ensure that the model still behaves in the expected manor after these changes, it was compared to results from the previous version of the code "ICICLE 1.8". The new code is now at version 4.0. The stator test piece was chosen as validation data exists, and this subset of data was not used as training data when tuning the parameters in the stick/erosion model. The simulation matched experimental conditions, which

were measured to be; Mach number of 0.4, 10°C total temperature, 34.5 kPa total pressure, $D_{v,10} = 18$ µm, $D_{v,50} = 34$ µm, $D_{v,90} = 54$ µm and relative humidity of 45% (creating a mass averaged melt ratio of 4%, 50 mm upstream of the leading edge).

The comparison of the legacy ICICLE code to the updated version, also compared to experimental data is shown in Figure 5.24. Good agreement to experimental data is observed from all models in the region $x/C_x > 0.2$. In the leading edge region there is a worse agreement between the two versions of ICICLE and also to experimental data. Version 1.8 of ICCILE used a panel based accretion method, for which large step changes in accretion was observed on adjecent panels. To create a smooth accretion profile, excessive levels of smoothing was implemented, and the smoothing was applied manually to obtain a result which looked physically correct. Whilst this method had good performance when the expected accretion shape was known, this method of manual smoothing would not be appropriate for simulations of new geometries where experimental data doesn't exist - for example the certification of new engines which have not been through expensive experimental testing. This level of manual user interaction for the smoothing is also not appropriate when flowfield coupling is utilised, as the profile would need to be smoothed on every timestep of the model.

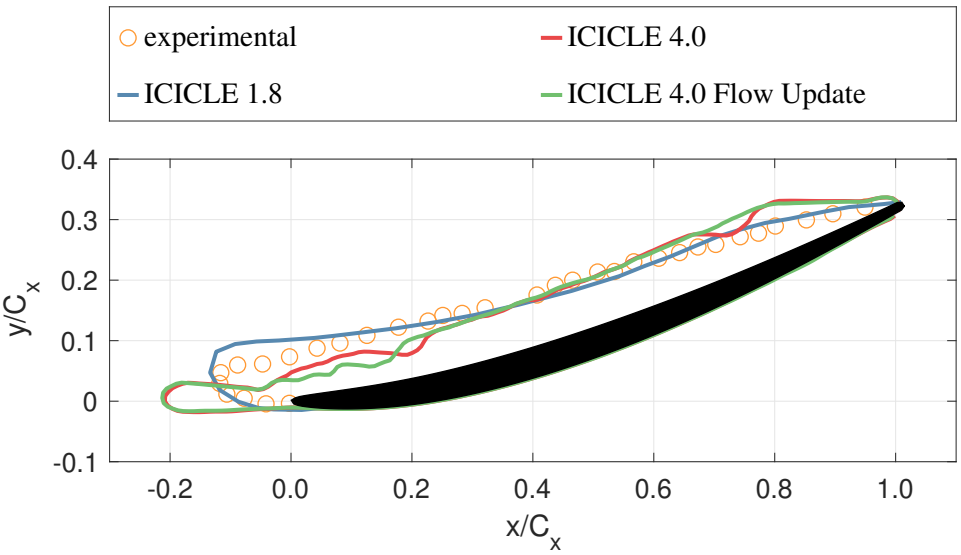

Figure 5.24: Comparison of the previous version of the ice crystal icing numerical model (ICICLE 1.8) to the current version (ICICLE 4.0) with and without flowfield coupling.

The lack of heavy smoothing in version 4.0 means that the leading edge accretion is not smoothed into the main body accretion. The reduction in smoothing in version 4.0 makes the model more physics based, however shows that there are sub-models of the code which are not accurately predicting the accretion process. It is thought that improvements to the water film model, shedding model and accretion bending model are needed to more accurately match the experimental data. To summarise; while the results for ICICLE 4.0 looks to have a reduced accuracy compared to version 1.8, this is due to the increased fidelity and reduced smoothing implemented into 4.0. It is hoped that by improving on the suggested sub-models this version of the code will be suitable for analysis of more complex geometries, something which would not have been possible with the legacy code.

For the simulation of the stator test piece with ICICLE 4.0, for which the point based accretion method was used, it was found that 500,000 particle streams had to be injected each second of physical time in order to reach statistical convergence. If the same level of fidelity were to be modelled in ICICLE 1.8 (500k particle streams injected each second of physical time), the total simulation time would have been approximately 140 days. The improved performance of the new code reduces the simulation time down to 15 hours, improving the performance by over two orders of magnitude.

5.11 Summary

This chapter has shown the development of the ice crystal icing numerical model, ICICLE. The numerical efficiency has been improved by over an order of magnitude, allowing for more complex simulations to be conducted in realistic time-frames. New functionality has been added; inclusion of flowfield coupling, substrate cool down and increased stability & mass conserving accretion growth.

6

Test and Validation of Flowfield Coupling

Contents

This chapter studies the effect of the accretion geometry on the surrounding flowfield and hence future growth. This is first tested on the stator test piece and also on the NACA 0018 airfoil. The effect of updating the particle trajectories is de-coupled from the effect of updating the flowfield by re-using the flowfield of the clean geometry. The aim of the chapter is to determine criteria for when particle trajectories need to be recalculated, and how often these trajectories need to be computed using a new flowfield of the updated accretion geometry.

6.1 Simulations

Three different types of simulations were carried out for the analysis in this thesis.

1. A baseline study was computed with no flow field updating. This simulation will be referenced as “no update”.

2. The geometry of the body in the simulation was updated at discrete time-steps according to the numerically predicted accretion growth. The new geometry was used to determine new particle impact locations, but the flowfield of the clean geometry was used. This method will be referenced as "geometry update".

3. Simulations were computed with flowfield and geometry updating at discrete intervals, and will be referenced to as "flowfield update".

Each successive method has increased computational demand, but the increased levels of fidelity is expected to increase the solution accuracy. Geometry update can be an efficient method if the trajectory history is stored. When the accretion profile computed in the EMM is known, particles can be injected immediately upstream of this location, using the particle tracks of the first timestep. Because the flowfield has not been updated, there is no need to re-compute their trajectories up until this point. Flowfield update requires a large increase in computational demand (meshing, flow solution, trajectory calculations), and therefore should only be used in conditions for which it is necessary.

6.2 Stator test-piece

Work was conducted early in the PhD focused on the effect of flowfield coupling using the stator test piece, using validation data from previous research [71]. The version of ICICLE produced by Bucknell [13] was adapted to include the effects of flowfield coupling, but at this stage of the PhD the other numerical developments shown in Chapter 5 had not been implemented. The non-smooth surface profiles shown for the stator test-piece results are due to numerical instability of the previous version of ICICLE. The results of this work were published at the 2019 SAE Icing Conference.

6.2.1 Motivation

To determine if the change in geometry caused by the growing accretion had an influence on the trajectory calculations, the accretion profiles from experimental

Table 6.1: Particle size distributions for the data shown in Figure 6.1.

	$D_{v,10}$	$D_{v,50}$	$D_{v,90}$
PSD 1	18	34	54
PSD 2	28	40	80
PSD 3	25	50	93
PSD 4	35	68	131

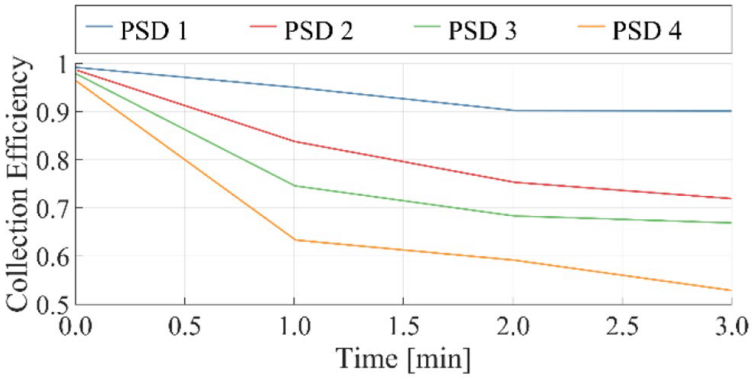

Figure 6.1: Plot of collection efficiency (normalised by clean geometry values) against ice exposure time for a range of Particle Size Distributions (PSDs). Definition of PSDs is shown in Table 6.1.

data was studied. The accretion profiles were extracted from backlit shadography data of the stator testpiece, conducted by Bucknell [71] in RATFac. A baseline condition of zero degrees angle of attack, Mach 0.4, 10 °C total temperature, 34.5 kPa total pressure and 45% relative humidity was chosen. At this condition four PSDs were tested, as detailed in Table 6.1.

Two-dimensional accretion profiles were extracted at a range of time intervals, to be used as geometry for manual mesh creation. These meshes were then used in CFD analysis to compute the continuous phase solution. Discrete phase trajectories were calculated for each accretion profile using ICICLE.

The collection efficiency of each accretion geometry was calculated for each PSD used, and the results are shown in Figure 6.1. The data showed that a change in collection efficiency occurred during the experiment. This indicated that numerical simulations should consider the effect of accretion growth on the surrounding flowfield.

6.2.2 Numerical Boundary Conditions

From the above results, a single condition was chosen for analysis of the effects of flowfield coupling. The aerodynamic conditions were; inlet total pressure of 34.5 kPa, inlet total temperature of 10 °C, free-stream Mach number of 0.4, relative humidity of 45% and a melt ratio of 5% (50 mm upstream of the stator leading edge). The ice crystals were injected with D_{v10}, D_{v50}, D_{v90} of 18, 34, 54 µm respectively. The numerical simulations discussed in this work matched the experimentally measured boundary conditions. The stator was set to a geometric angle of attack of 0°. These conditions were chosen for this paper as previous numerical simulations of such conditions had poor agreement with experimental data, and this was attributed to the lack of geometry/flowfield update [13].

6.2.3 Mesh Creation

The mesh for the stator test piece was produced using ANSYS ICEM. The mesh of the clean geometry (without accretion) of the stator testpiece is shown in Figure 6.2. Prism elements were extruded from the surfaces of the tunnel and body walls. A mesh density was created around the blade to capture the necessary vortical structures. A mesh dependency study was conducted for this clean geometry, and the same meshing parameters were used for all successive simulations of the testpiece.

6.2.4 Flowfield Solution

The flow solution was calculated using the commercial CFD software, ANSYS FLUENT. Symmetry boundary conditions were applied to prevent end wall effects in the spanwise direction.

Inlet and outlet pressure boundary conditions were set to match the freestream velocities to the experimental data. The flow solution was solved using a three-dimensional RANS solver, using the kω-SST turbulence model, with second order discretisation. Due to the experiments operating at Mach 0.4, a compressible solver was used.

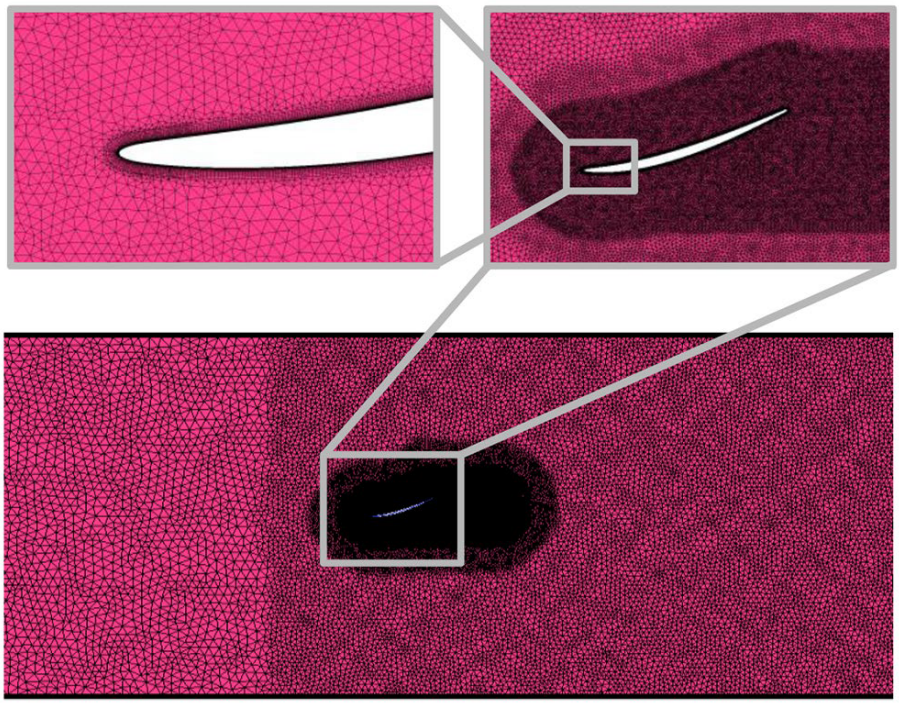

Figure 6.2: Computational mesh of the initial "clean" geometry of the stator test piece. Prism elements grown from test piece surface and a mesh density located around the airfoil and in the downstream wake region.

6.2.5 Accretion Profiles

Figures 6.3a to 6.3c show the accretion profiles of the numerical predictions and experimental data, at the times 30, 60, 90 s.

In the early stages of the accretion, the accretion size was sufficiently small that there was little change in passage blockage, nor a change in the surrounding flow field. As a result all three simulation types had similar results and the numerical simulations had good agreement with experimental data.

In the latter timesteps, for the no update simulation the collection efficiency did not change causing the shape of accretion to also not vary during the simulation, and instead grew in volume.

A large difference in accretion profile between the no update and geometry update solutions on successive time-steps. Because the flow solution had not been updated, the particles did not decelerate in the boundary layer flow, meaning that the particles had an increased erosion in the leading edge region. Shielding of the

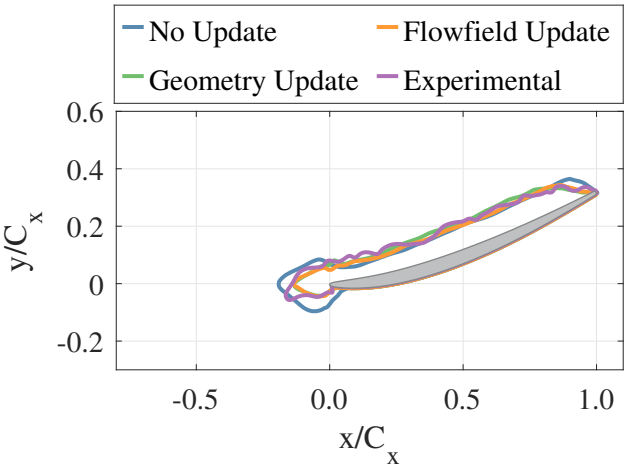

(a) t = 30s.

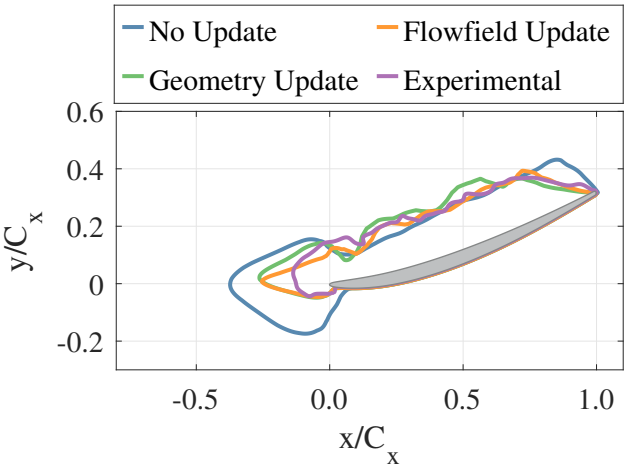

(b) t = 60s.

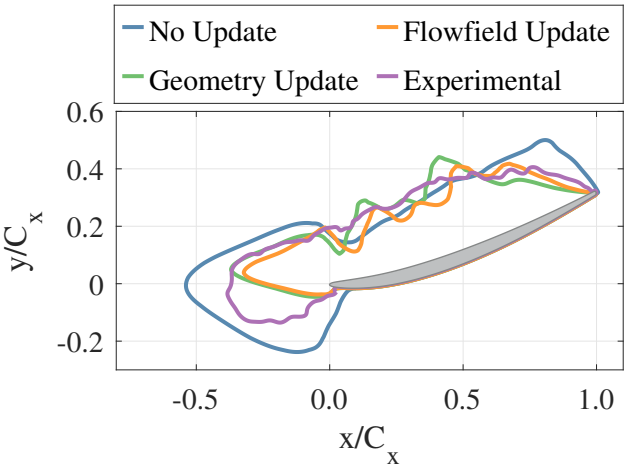

(c) t = 90s.

Figure 6.3: Comparison of the no update, geometry update and flowfield update solutions to experimental data. Conditions: Mach 0.4, T_0 = 10 °C, relative humidity = 45%.

accretion in the leading edge region prevented the unrealistic leading edge bulge created in the no update solution. Further changes between the no update and geometry update solutions also occurred on the pressure surface. This was primarily caused by the change in surface angle affecting the impact behaviour but also caused by shadowing effects of the leading edge accretion on latter timesteps. The shielding effect also limited the growth rate at the trailing edge in the geometry update solution, which was not captured in the no update solution. Good agreement was observed between the experimental and numerical data on the pressure surface, with a significant improvement over the no update simulations in the leading edge region.

With flowfield updating, little changes in the accretion profile were observed compared to the geometry update solution for t $<$ 30 s. Between 30 and 90 s the leading edge accretion differed, with flowfield update having a reduced growth rate compared to the geometry update. Updating the flow solution adjusted the location of the boundary layer, meaning that the particles decelerated prior to impact, reducing their potential to erode. This was outweighed by the enlarged stagnation region reflecting the particles away from the leading edge accretion, reducing the number of particles impacting onto the surface.

The key difference between the numerically predicted profiles with at least geometry update (simulation type 2 & 3) compared to the experimental data was at the suction surface leading edge. In the experiment, due to the high relative humidity (45%), the leading edge accretion was relatively wet and hence had a low stiffness. This led to the leading edge accretion bending downwards under the aerodynamic load. At 50 s in the experiment, the leading edge accretion had deflected sufficiently far that it was overcome by the aerodynamic loads and shed. The bending of accretion and prediction of shedding is not accounted for in ICICLE, and hence explains the difference in predicted accretion profiles in this region.

6.2.6 Growth Rates

Figure 6.4 shows the predicted growth rates for each simulation type, alongside the experimental data. With no flowfield or geometry update, a nonlinear growth

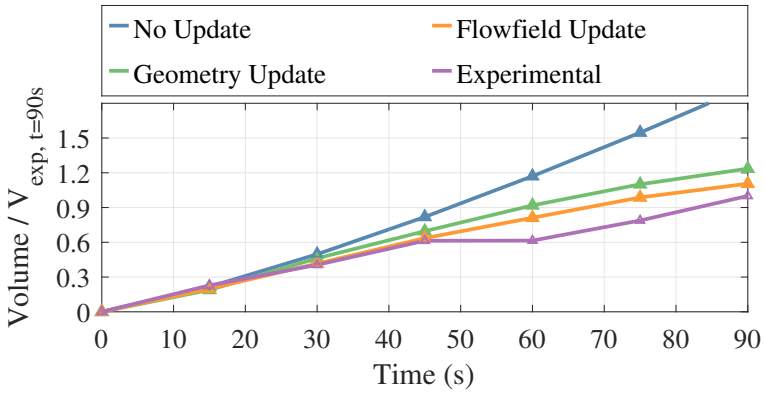

Figure 6.4: Comparison of numerical and experimental growth rates, normalised by the experimental value at 90 seconds. Note that a shed event occurs at 50s in the experimental data.

rate initially occurred as the blade temperature decreased and ice started to form. Once an ice layer had stabilised (>30 s), the growth rate remained approximately constant. With geometry updating the growth rate was lower than the baseline simulation and remained roughly constant for the first 40 seconds and then started to decrease. With flow field updating the growth rate most accurately matched the experimental data. As previously mentioned, a shed event occurred at 50 seconds which was not numerically predicted, explaining the difference in volume after this time. The decrease in growth rate with the updated simulations more closely match the experimental data, indicating that an update of the particle trajectories based on the updated geometry is necessary for accurate numerical predictions.

6.2.7 Collection Efficiency

The average collection efficiency of each panel in the computational domain was calculated at the first time step and at the final time-step of the flow field update simulation. Collection efficiency was defined as mass stuck to each panel, normalised by the total mass stuck to a panel out of the two simulations. Figure 6.5 shows the results of this study. In the no update solution the collection efficiency remained constant for the whole simulation. The peak collection efficiency of the clean stator occurred at the leading edge, which was the cause of the leading edge bulge which formed in the baseline simulation. For the flowfield update solution, as the

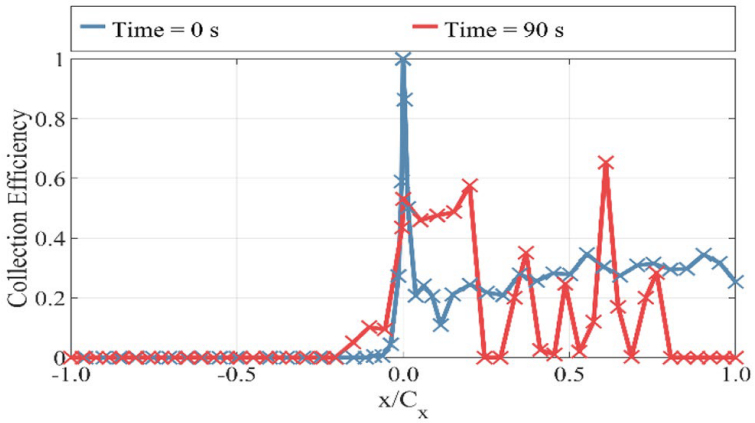

Figure 6.5: Distribution of collection efficiency over the stator for the initial "clean" geometry and final accretion profile predicted after 90 seconds of ice exposure.

accretion grew each panel collected a different percentage of incoming particles due to the change in incoming particle velocity, relative angle between impact velocity and adjacent surface. On the latter time steps a lower proportion of particles were collected by the stator, which can also be seen by the reduced growth rate in Figure 6.4.

6.2.8 Summary

The work showed that the ice crystal icing accretion profiles predicted by numerical codes are highly dependent on the geometry and flow solution. As an accretion forms, the local surface angle of the body relative to the incoming particle streams changes, affecting the post-impact behaviour (stick/bounce/shatter). For the conditions studied in this paper, the change in geometry had the most dominant effect on the final accretion profile. The inclusion of flowfield updating had a minor influence on the accretion in the leading edge region due to the change in stagnation point. The lack of difference between the geometry update and flowfield update solutions is thought to be caused by the high particle velocities, and because the stator was isolated with the accretion leading to little change in flow blockage.

6.3 Single NACA Airfoil

The low levels of flow blockage of the stator test piece in RATFac meant that limited flow coupling occurred. The triple NACA 18 airfoil test piece was designed to be more flow-coupled and is numerically assessed in this section. A single blade was first tested to form a baseline solution of the test piece. The geometry was set at zero angle of attack.

6.3.1 Mesh Creation

The analysis of the stator airfoil was meshed using ANSYS ICEM. For non-iced geometries, high quality unstructured meshes were created using automated scripts. However for non-uniform accretion surfaces, it was found that ICEM required some manual alteration of the meshing parameters. To overcome this issue, an alternative meshing software, BOXERmesh was chosen for the remainder of this work. BOXERmesh is an octree mesh tool, which has been designed to mesh arbitrary geometries making it very suitable for iced geometries. The software uses distributed memory parallel processing, allowing for complex geometries to be meshed in relatively small time scales.

The mesh created for the "clean" geometry of the single NACA airfoil is shown in Figure 6.6. Similar to the stator airfoil, prism elements were extruded from the body and a mesh density surrounded the body and wake regions. A mesh sensitivity study was conducted to verify the effect of the global mesh size, density region size, and expansion ratio between the density and the global mesh.

6.3.2 Numerical Boundary Conditions

The aerodynamic conditions were; inlet total pressure of 34.5 kPa, inlet total temperature of 10 °C, relative humidity of 45% and a melt ratio of 10%, 50 mm upstream of the airfoil leading edge. For the following analysis the Mach number was varied between 0.2 and 0.3, and mono-dispersed spherical particles were injected with sizes between 20-60 µm. A fixed inlet total pressure and outlet static pressure

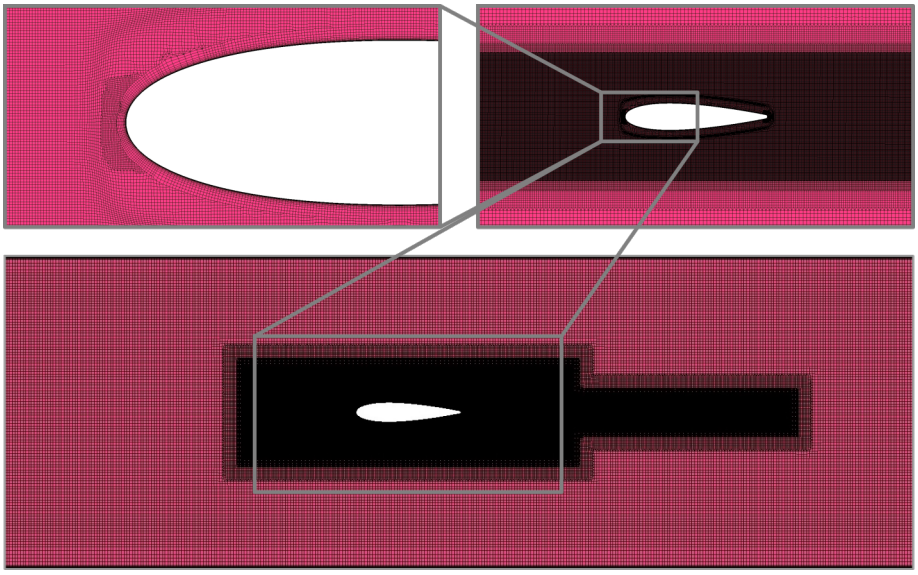

Figure 6.6: Computational mesh of the initial "clean" geomtry of the NACA-0018 aifoil testpiece. Prism elements grown from test piece surface and a mesh density located around the airfoil and in the downstream wake region.

was used, meaning that the Mach number reduced slightly during the simulation due to the change in flow blockage and loss induced by the accretion.

6.3.3 No update

A baseline simulation was conducted where there was no update to the particle trajectories nor the CFD solution, to study the effect of the time-step within the accretion modelling (EMM) subset of the code. If the accretion growth rate was proportional to the mass stuck to the surface, there would be no time-step dependence. Because the growth rate is also affected by the state of the internal/external water layers, heat transfer from the flowfield and energy transfer from the particles, a non-linear growth occurs, making it time-step dependant.

Figure 6.7 shows the predicted accretion growth after 180s of exposure to a mono-dispersed ice cloud of 8 g/m^3 and diameter 20μm, when an EMM timestep of 180, 8 and 1 seconds is used. Using a timestep size of fewer than 18 seconds was found to produce a converged solution. For the remainder of this work an EMM timestep size of 1 second was chosen.

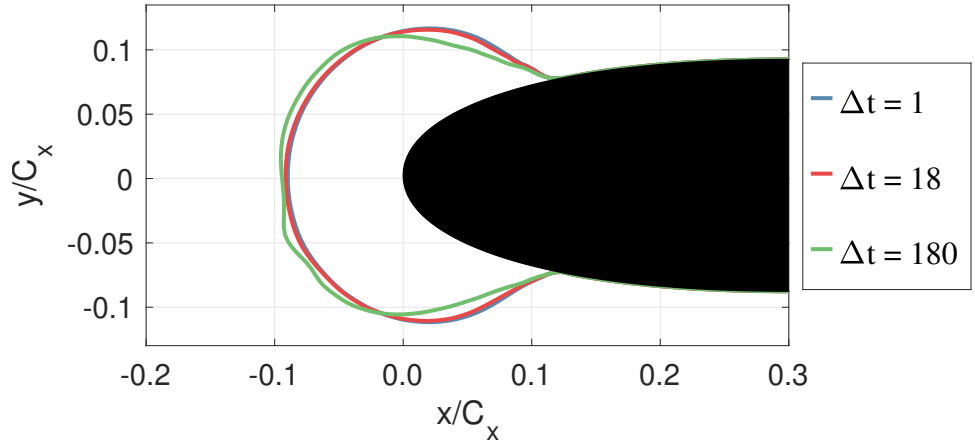

Figure 6.7: Numerically predicted accretion profiles after 180s of ice exposure (TWC=8g/m^3, mono dispersed d=20μm) with varying EMM timestep size, with no update of the particle trajectories nor flow solution.

6.3.4 Geometry Update

Updating the particle trajectories during the growth of the accretion leads to more accurate results. The limit for when to update the particle trajectories was set based on the maximum change in area of the mesh of the body/accretion. This was quantified by the parameter, A_{limit} (Equation (6.1)), where A_{cell} is the cell area, and $A_{cell,0}$ is the cell area at the start of the timestep. A maximum of the two fractions is taken to account for if the adjacent wall-normal is diverging (locally convex), or converging (locally concave).

$$A_{limit} = MAX(\frac{A_{cell}}{A_{cell,0}}, \frac{A_{cell,0}}{A_{cell}}) \tag{6.1}$$

The limits of A_{limit} were set based on a 100%, 50%, 25%, 12.5% and 6.25% change in face area, and the predicted accretion profiles can be seen in Figure 6.8a. If the update of the particle trajectories (and hence sticking mass distribution) occurred too infrequently, the accretion grew in locations that would have been shielded by upstream accretion had the particle tracks been updated.

Accretion growth in non-planar regions caused changes to the cell area, meaning that the mass flux decreases on the convex surface. If the particle tracks had been updated, the larger cell area would have captured a larger proportion of the particles.

When the trajectories are recalculated sufficiently often, a converged solution is obtained, which for this geometry was found to at $A_{limit} = 1.0625$.

The EMM assumes that the stuck mass associated with each cell of the body discretisation remains constant during the accretion until the trajectories are recalculated. An alternative assumption is that the mass flux remains constant so that area changes do not alter the growth rates. The results with this assumption is shown in Figure 6.8b. It was found that the use of constant mass flux resulted in gross over-estimation in the transverse direction but more accurate prediction in the streamwise direction, but was also less numerically stable. To ensure mass conservation, it was decided to use an assumption of a constant mass of stuck water/ice to each mesh cell during the EMM accretion prediction.

6.3.5 Flowfield Update

When the particles were updated in the previous simulations, their trajectory paths were predicted using the flowfield solution of the clean geometry. Far from the accretion site this CFD solution will be close to the true solution, but near to the body the stagnation region moves and alters the local flowfield. Figure 6.9 shows the particle tracks for a particle injected on the blade centerline and a position away from the centerline using the flowfield of the clean geometry and also using a new flowfield based on the accretion geometry. The flowfield of the clean geometry was near axial at the position of the accretion leading edge, so the particles directly hit the body with little turning. The centerline injection was pushed back into the body after the first impact due to the high flow velocity. The particle lost momentum during each bounce, leading to many rebounds. An assumption in ICICLE is that all the liquid water is shed onto the surface upon impact. Between impacts, the short residence time meant that little particle melt occurred, meaning that the sticking efficiency was near zero for successive bounces.

Using the updated flow solution, the mid line injection rebounded back further in the negative axial direction due to the reduced flow velocity decreasing the drag imparted onto the particle, allowing the particle to reach the main gas path and

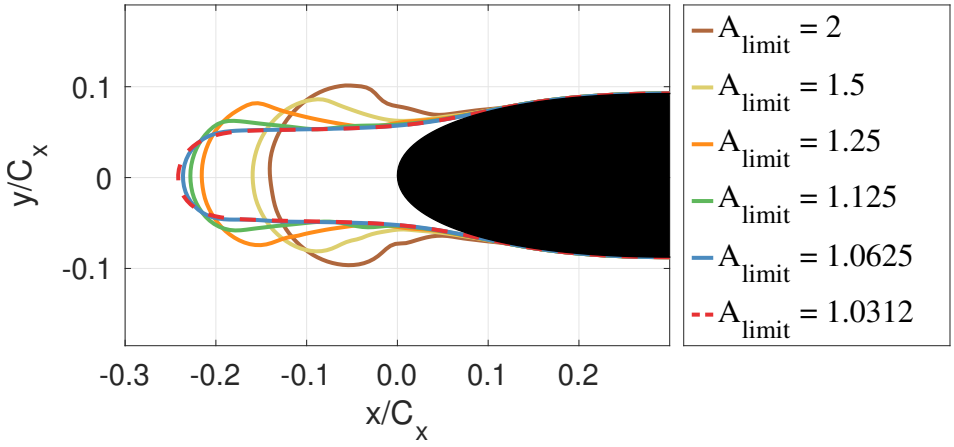

(a) Constant mass assumed for calculating the growth rate.

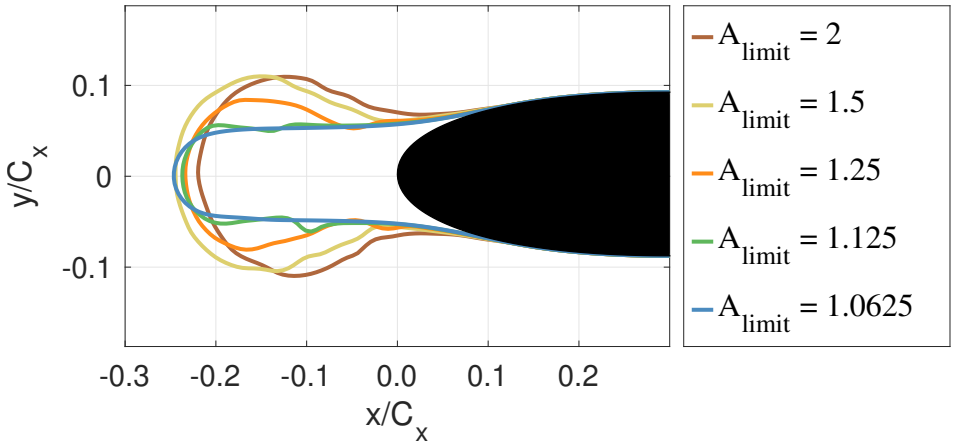

(b) Constant mass flux assumed for calculating the growth rate.

Figure 6.8: Numerically predicted accretion profiles after 180s of ice exposure (TWC=8g/m^3, mono dispersed d=20μm) with varying duration between updates of the particle tracks, with no update flow solution. Growth rates calculated using either constant mass (a) or constant mass flux (b) for each cell of the body discritisation.

be turned away from the body. The top injection was accelerated away from the accretion due to the flow turning in this area, which was not captured when using the flowfield solution of the clean geometry.

The differences in particle trajectories between the clean and updated flowfields altered the distribution of sticking mass on the body. Figure 6.10 shows the difference in mass distribution around the body with the original and updated flowfield solution. The flow turning around the accretion reduced the number of particles impinging onto the body, globally reducing the stuck mass. Downstream of the accretion leading edge, the flowfield of the clean geometry was still axial,

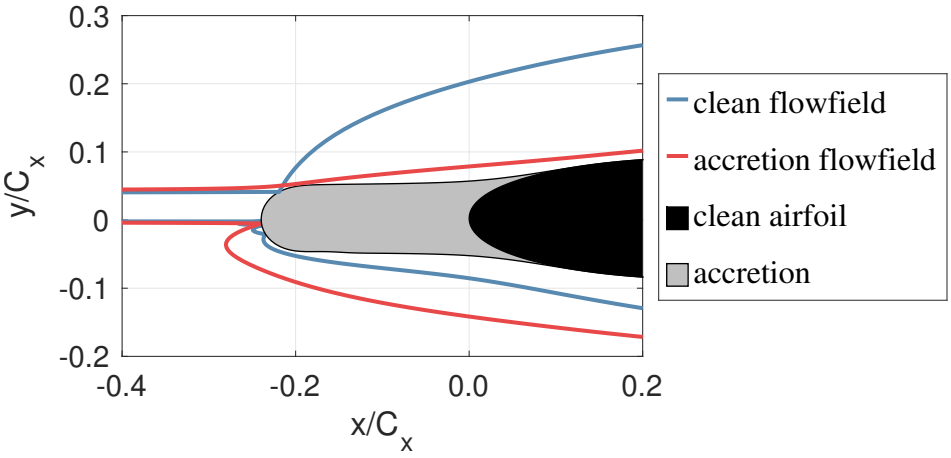

Figure 6.9: Particle trajectories upon the accretion geometry after 180s of ice exposure (TWC=8g/m^3, mono dispersed d=20μm), using the flowfield solution of the clean geometry and an updated flow solution based on the accretion geometry.

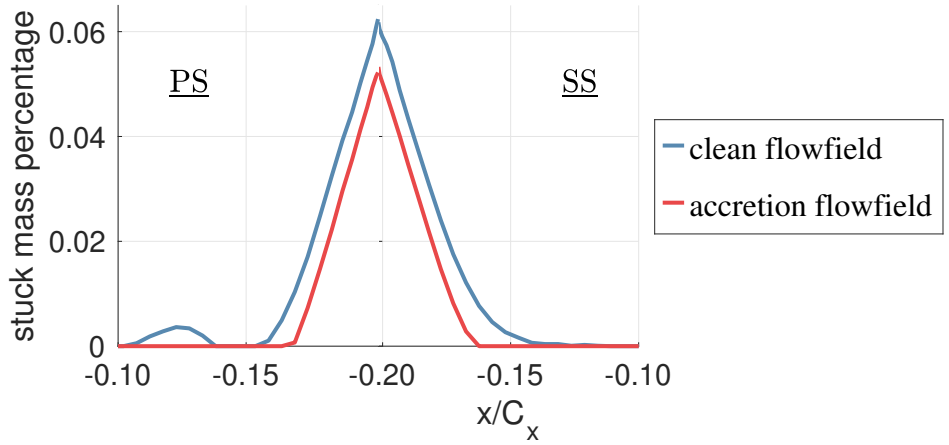

Figure 6.10: Sticking mass distribution around the iced accretion profile (after 180s of ice exposure; TWC=8g/m^3, mono dispersed d=20μm). Distributions shown for the particle tracks calculated using the flowfield of the clean geometry, and an updated flow solution based on the accretion geometry. Data shown for the pressure surface (PS) and suction surface (SS).

meaning that further impingement happened (at $x/C_x = -0.125$ on the pressure surface, PS), which did not occur with the updated flow solution.

A simulation was conducted where the flow solution was updated after every call of the EMM, ensuring that all particle trajectory calculations were using the correct flow solution. The profiles at time intervals of 30, 60, 120 and 180s are shown in Figure 6.11, and the volume of accretion as a function of time is shown in Figure 6.12. At the early stages of accretion (<60 s), good agreement was found between the solutions with and without flowfield coupling. As the accretion

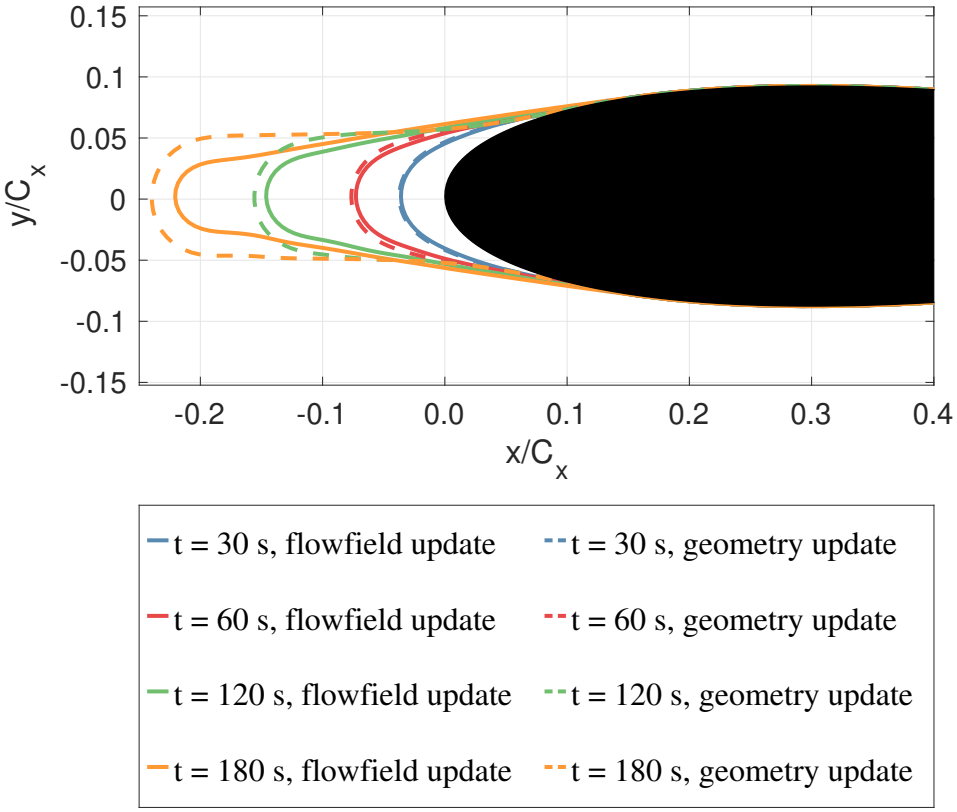

Figure 6.11: Accretion profiles with and without flowfield coupling after 180s of ice exposure (TWC=8g/m^3, mono dispersed d=20μm).

grew out of the stagnation region, deviations occurred between the two solutions, most notably that the tip of ice growth became sharper with flowfield coupling, whereas it stayed axial without flowfield coupling.

In this scenario, flowfield coupling produced a conservative estimate of the level of accretion on the body, but due to the test piece tip and local flow being axial and low levels of flow blockage, the deference's were not too significant.

6.3.6 Effect of Smoothing

To aid numerical robustness, a smoothing step is implemented after each call of the EMM. This provides a continuous surface that can be easily re-meshed and also stabilises the growth on the next timestep. The improvement in numerical stability cannot be justified if the smoothing process inherently alters the accretion profile. The accretion profile after 180 s of ice exposure using flowfield coupling was extracted and smoothed multiple times. The numerical simulation had re-injected

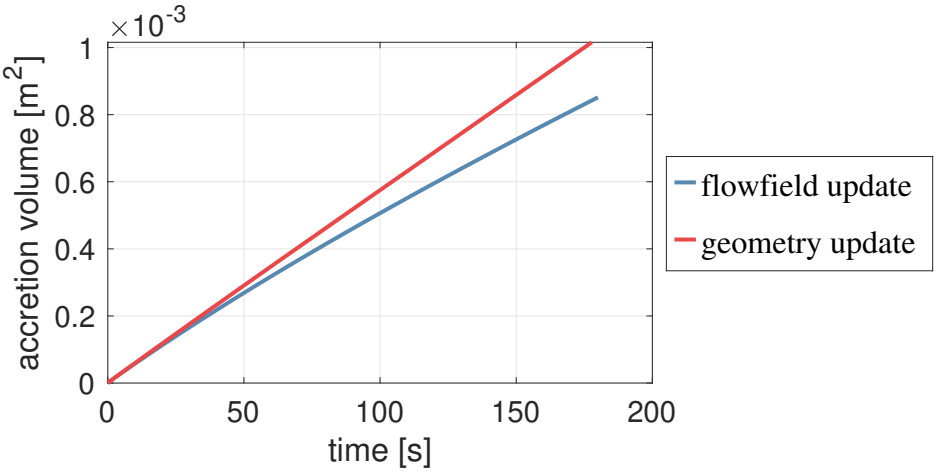

Figure 6.12: Accretion volume with and without flowfield coupling after 180s of ice exposure (TWC=8g/m^3, mono dispersed d=20μm) for the single NACA-0018 airfoil at 0° angle of attack.

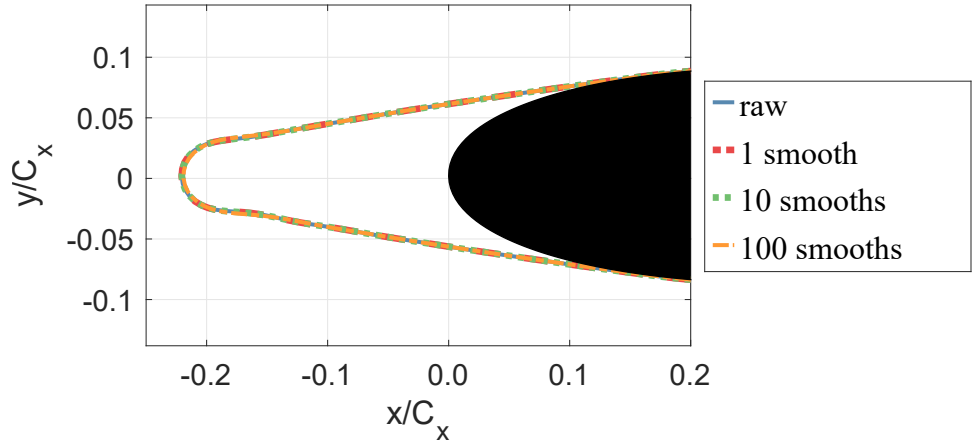

Figure 6.13: Effect of smoothing the end accretion profile after 180s of ice exposure (TWC=8g/m^3, mono dispersed d=20μm) for the single airfoil at 0° angle of attack.

particles and ran the EMM 78 times by the point of reaching this accretion profile, meaning that it had already been smoothed 78 times. Figure 6.13 shows the accretion profile, and the output from smoothing the profile 1, 10 and 100 times. It was found that even after 100 smoothing steps, that the overall surface shape had not dramatically changed, and it was therefore accepted that a smoothing step after each call of the EMM would not be detrimental to the end result.

6.4 Triple NACA Airfoil

To increase the local flow blockage, a 3-blade linear cascade configuration was tested with a pitch of 60 mm. The following simulations vary the degrees of freedom in the experiment; angle of attack, Mach number and particle size. The baseline conditions were Mach 0.2, 10 °C total temperature, 34.5 kPa total pressure, 10% melt ratio (50 mm upstream of the leading edge), 20 µm mono-dispersed particle diameter, 8 $\mathrm{g\,m^{-3}}$ total water content.

6.4.1 0° Angle of Attack

A particle convergence study was conducted, and it was found that 60k particle streams were required to reach a 1% level of convergence. Having only three blades in the linear cascade meant that the central blade observed a symmetrical flowfield, whereas the outer blades had an asymmetrical flowfield. The accretion profiles numerically predicted after 180 seconds of ice exposure to a cloud of mono-dispersed 20 µm, 8 $\mathrm{g\,m^{-3}}$ is shown in Figure 6.14. Similar to what was found in the single blade configuration - a good agreement was observed up until 60 seconds of accretion, and then deviations between the geometry update and flowfield update solutions occurred. The main difference between the datasets is that the geometry update starts to grow as an axial extrusion of the leading edge accretion, due to the accretion growing out of the range of the near body pressure gradients. The flowfield update solution maintained a sharp leading edge accretion and grew in the direction of the local streamlines. By the later stage of the accretion, the flow streamlines were less turned vertically, meaning that the accretion grew closer to the axial direction compared to at the start of the accretion. This is shown in Figure 6.15, where the streamlines are displayed over a contour plot of the absolute vertical velocity for both the clean geometry and final accretion profile. With the iced profile, a much smaller region of high vertical component of velocity existed, reducing the vertical acceleration imparted onto the particles.

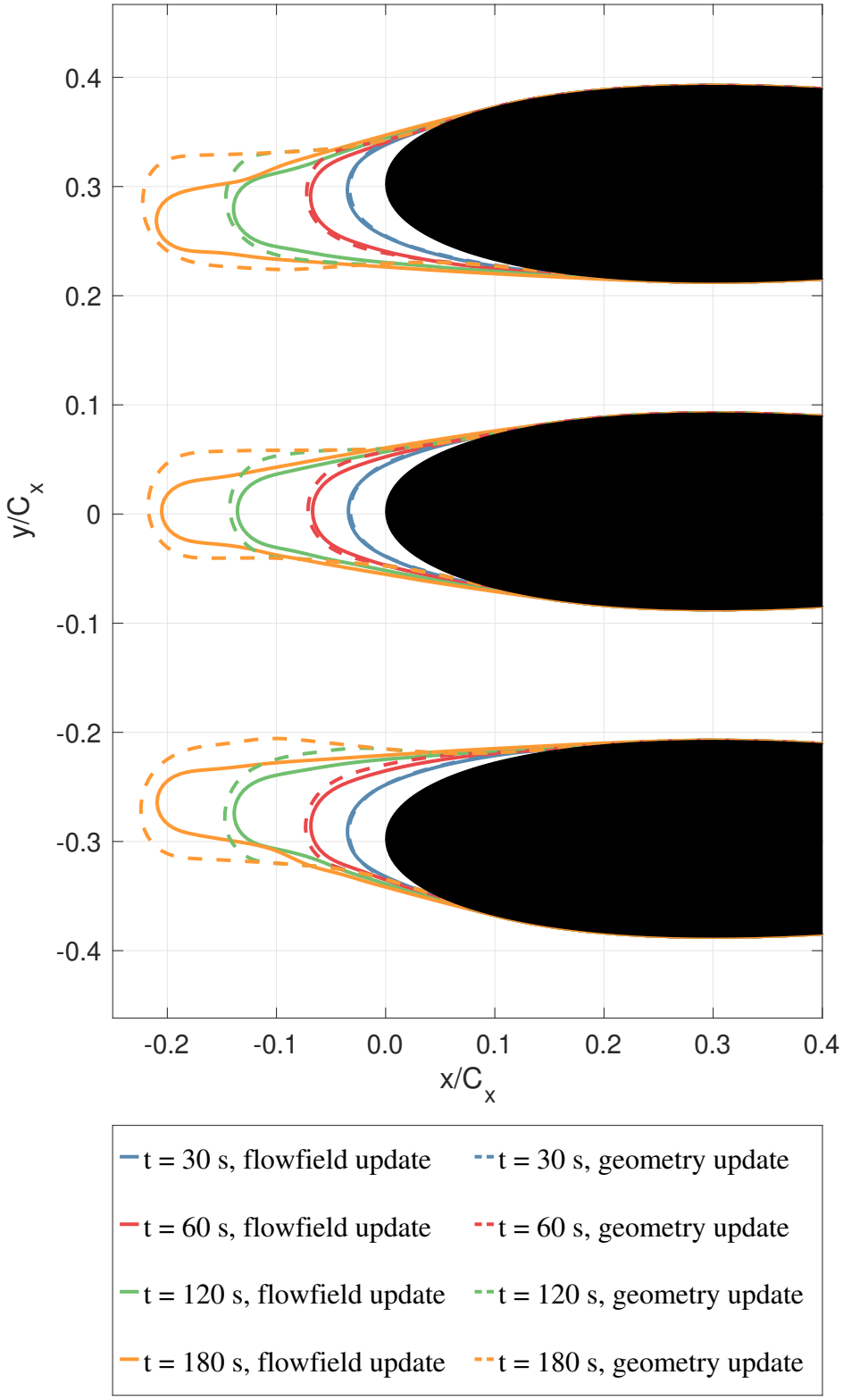

Figure 6.14: Accretion profiles with and without flowfield coupling after 180 s of ice exposure (TWC=8 g m^{-3}, mono dispersed d=20 µm) for the triple airfoil at 0° angle of attack.

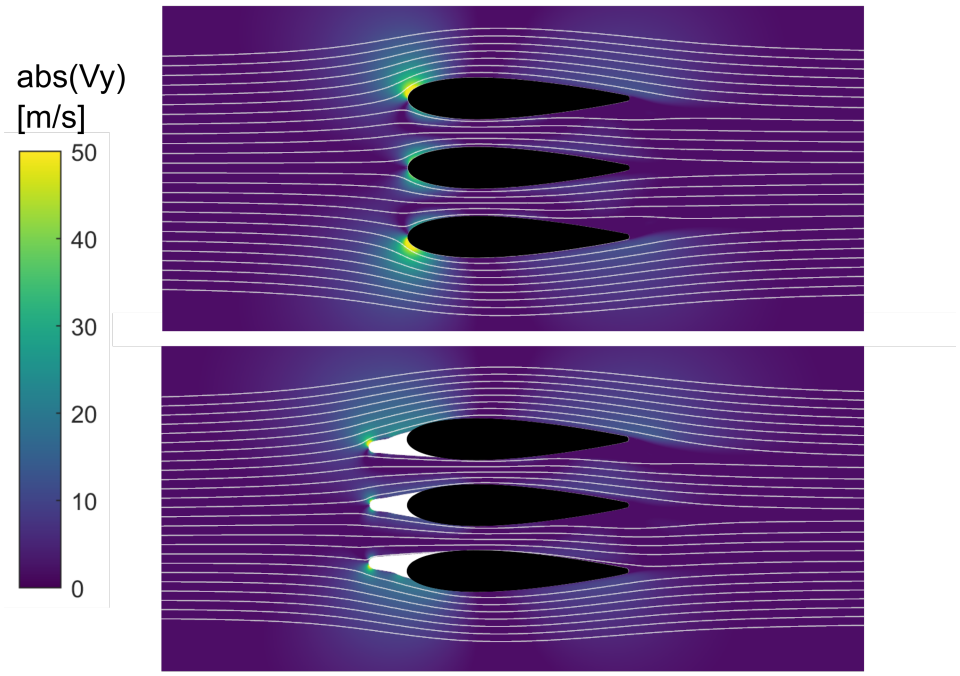

Figure 6.15: Comparisons of the flow streamlines between the initial clean geometry (top) and final iced geometry taken from Figure 6.14 (bottom) overlaid onto contours of vertical component of velocity.

The volume of accretion as a function of time for both the flowfield update and geometry update solutions is shown in Figure 6.16. For the geometry update solution, in which no change in the flowfield occurs, the accretion soon exists the region of pressure gradients near the clean body stagnation region. After this point, as the accretion moves further upstream, the flow conditions on the new accretion stagnation point are invariant of the axial position, meaning that the incoming particles on future timesteps have the same properties, leading to a constant growth rate. The changing flowfield in the flowfield update solution led to a gradual reduction in in growth rate over the time period simulated.

6.4.2 10° Angle of Attack

To increase the cross-passage pressure gradient, the 3 blade configuration was set to a 10° angle of attack. The increased frontal area of this configuration meant that 80k particle streams were required to reach a 1% convergence.

The predicted accretion profiles and volumes for the geometry update and

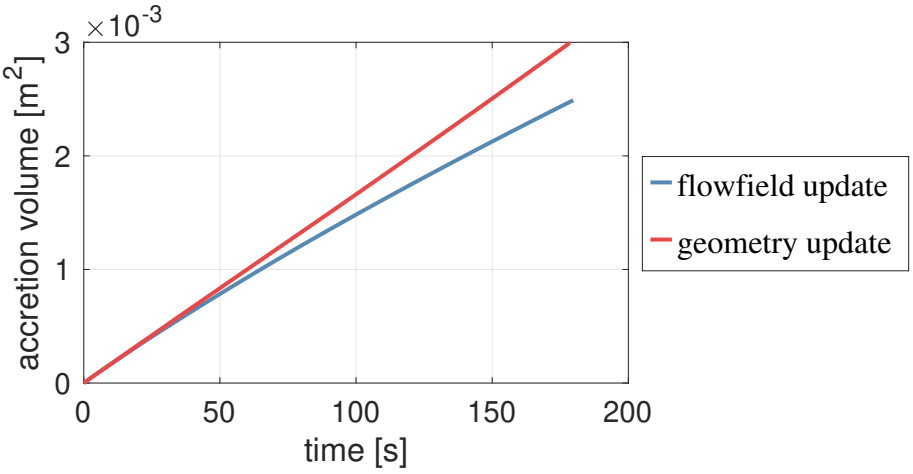

Figure 6.16: Accretion volume with and without flowfield coupling after 180 s of ice exposure (TWC=8 g m^{-3}, mono dispersed d=20 µm) for the triple airfoil at 0° angle of attack.

flowfield update simulations are shown in Figure 6.17 and Figure 6.18 respectively. At a non-zero angle of attack, a substantially different potential field exists in front each of the three airfoils. On the top airfoil, the stagnation region is far round to the pressure surface, and the pressure gradients cause the particles to obtain a high spanwise acceleration. In the initial stages of accretion this causes both solutions to grow away from the axial direction. This pressure gradient in the clean solution is localised to the near body region, meaning that the geometry update solution starts to bend towards the axial direction as the accretion progresses. The lack of pressure gradient in this upstream location means that the particles are not deviated away from the accretion, leading to gross over-estimation of the accreted volume.

In the flowfield update solution, the accretion grows at a non-axial direction for a greater distance. But the non-aerodynamic shape of such accretion leads to a reduction in pressure gradient near the accretion stagnation point, meaning that the accretion slowly moves towards the axial direction, albeit at a slower rate than the geometry update solution.

These differences again caused an overestimate in accretion volume, as shown in Figure 6.18.

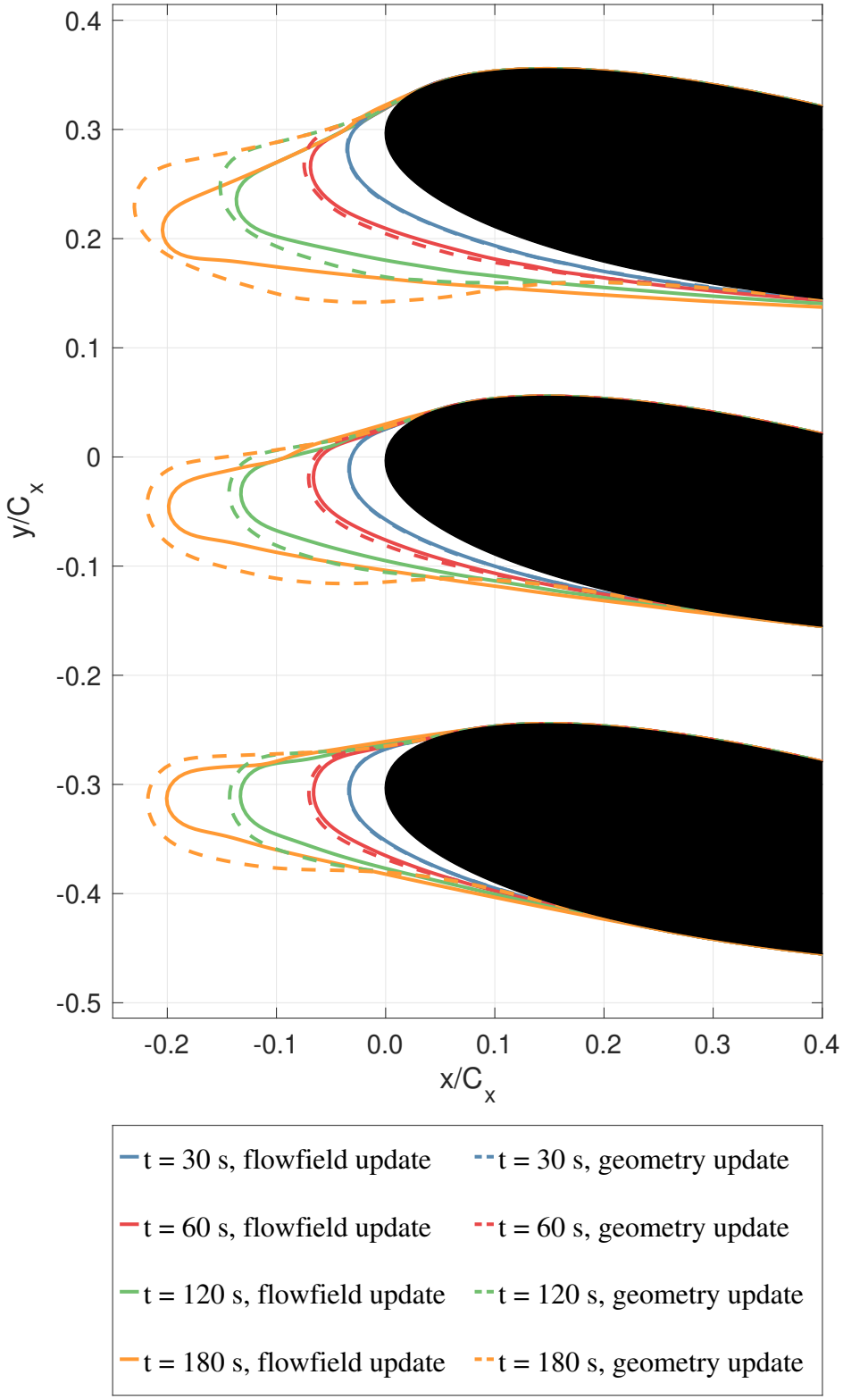

Figure 6.17: Accretion profiles with and without flowfield coupling after 180 s of ice exposure (TWC=8 g m^{-3}, mono dispersed d=20 µm) for the triple airfoil at 10° angle of attack.

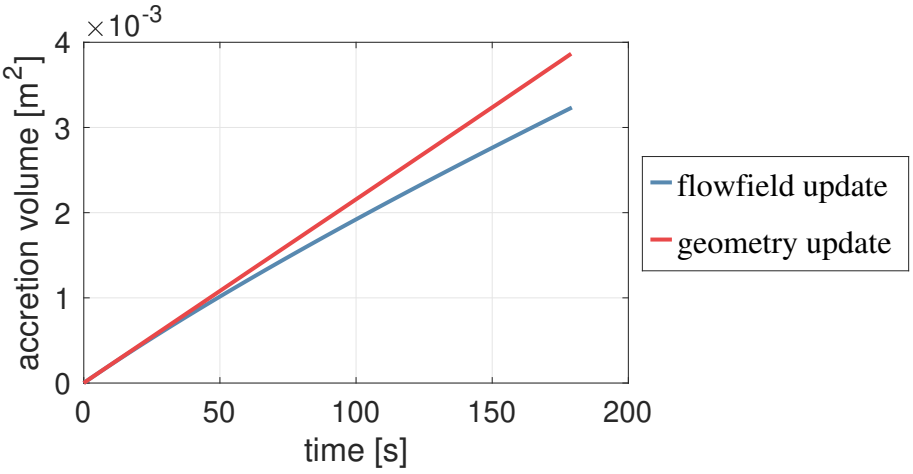

Figure 6.18: Accretion volume with and without flowfield coupling after 180 s of ice exposure (TWC=8 g m^{-3}, mono dispersed d=20 µm) for the triple airfoil at 10° angle of attack.

6.4.3 15° Angle of Attack

Further increasing the angle of attack to 15° was found to have similar accretion behaviour to at 10°. The accretion profiles are shown in Figure 6.19, where the direction of leading edge growth differed between the geometry update and flowfield update solutions, and an overestimate in accretion on the pressure surface accretion near the leading edge occurred in the geometry update solution. Another key difference between the two solutions is that the accretion extends further towards the trailing edge in the flowfield update solution. While the accretion in this region is not thick compared to the leading edge accretion, it will dramatically increase the contact area of the interface between the accretion and the substrate. This increase in inter-facial area could have large influences on the potential of the accretion to shed from the surface.

Whilst the geometry update solution failed to capture the accretion in this downstream section of the airfoil, it largely over-predicted the accretion growth in the leading edge region. Overall the geometry update solution over-predicted the accretion growth, as shown in Figure 6.20.

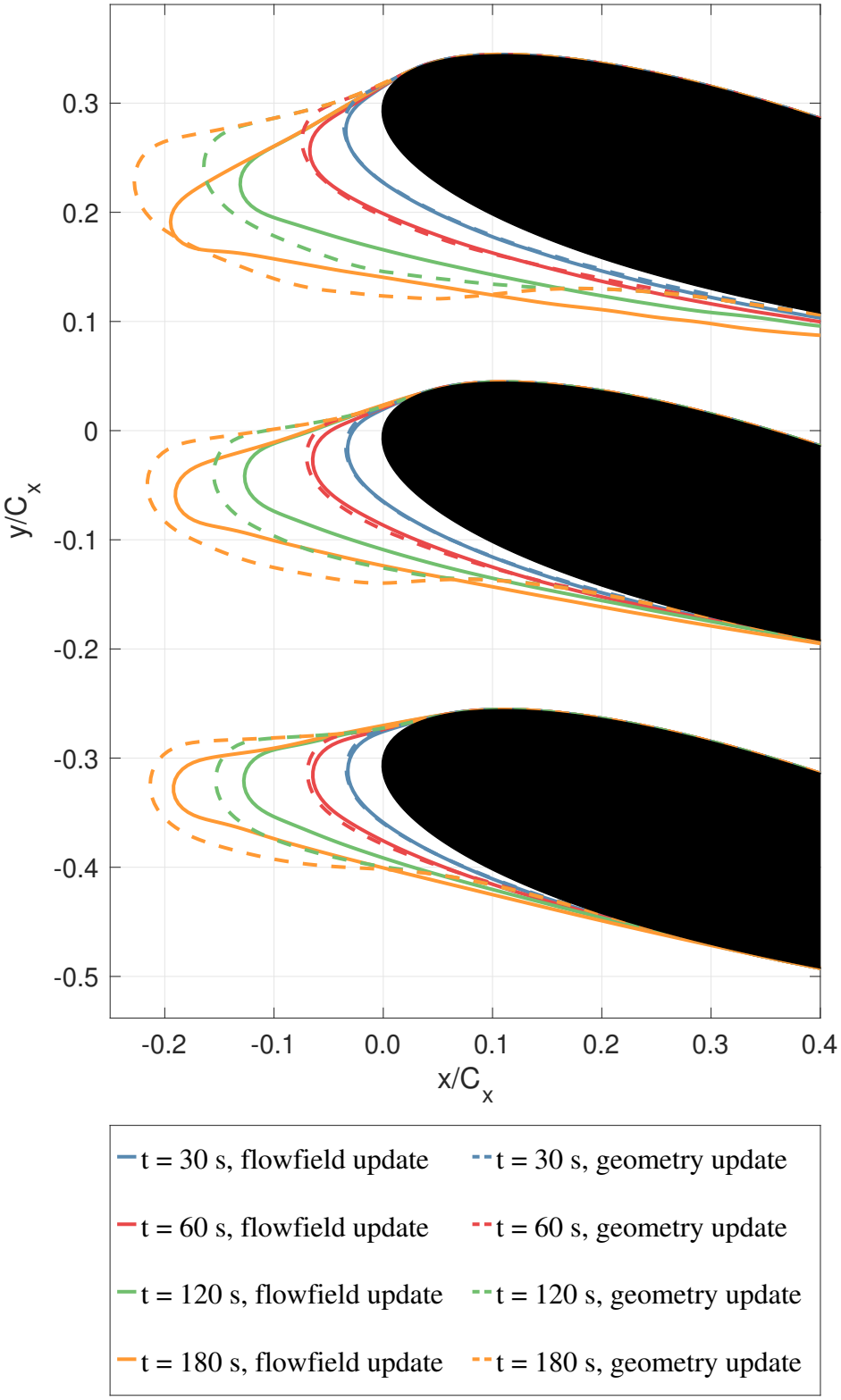

Figure 6.19: Accretion profiles with and without flowfield coupling after 180 s of ice exposure (TWC=8 g m^{-3}, mono dispersed d=20 µm) for the triple airfoil at 15° angle of attack.

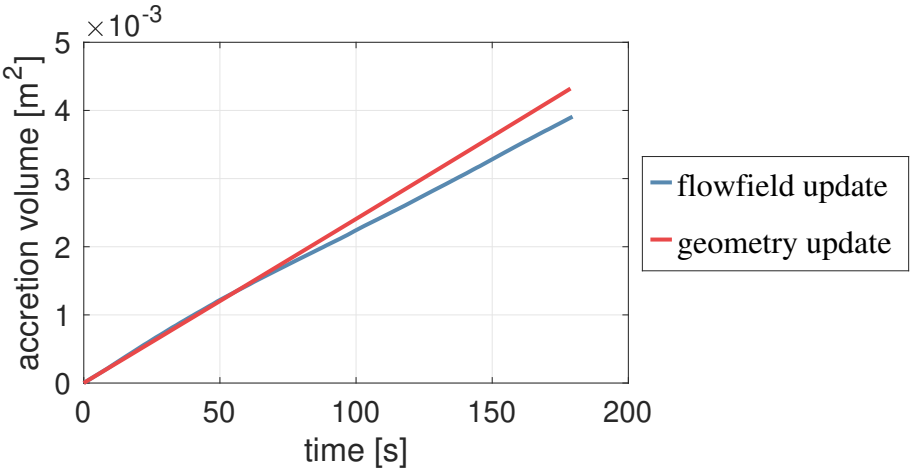

Figure 6.20: Accretion volume with and without flowfield coupling after 180 s of ice exposure (TWC=8 g m^{-3}, mono dispersed d=20 µm) for the triple airfoil at 15° angle of attack.

6.4.4 10° Angle of Attack, Mach 0.3

Increasing the freestream Mach number to 0.3 increases the strength of the drag force imparted on the particles in the near body region due to increased slip velocities. The typical observation in the previous test cases of a deviation in accretion growth direction was also seen in this case. The key difference in this case was the change in accretion behaviour on the pressure surface. Unlike the 15° case, where the flowfield update solution had enlarged mid chord pressure surface accretion, in this case the geometry update solution had enhanced accretion in this region. The result of this was that a large over-estimate in accretion volume was seen with the geometry update compared to the flowfield update solution, as seen in Figure 6.22.

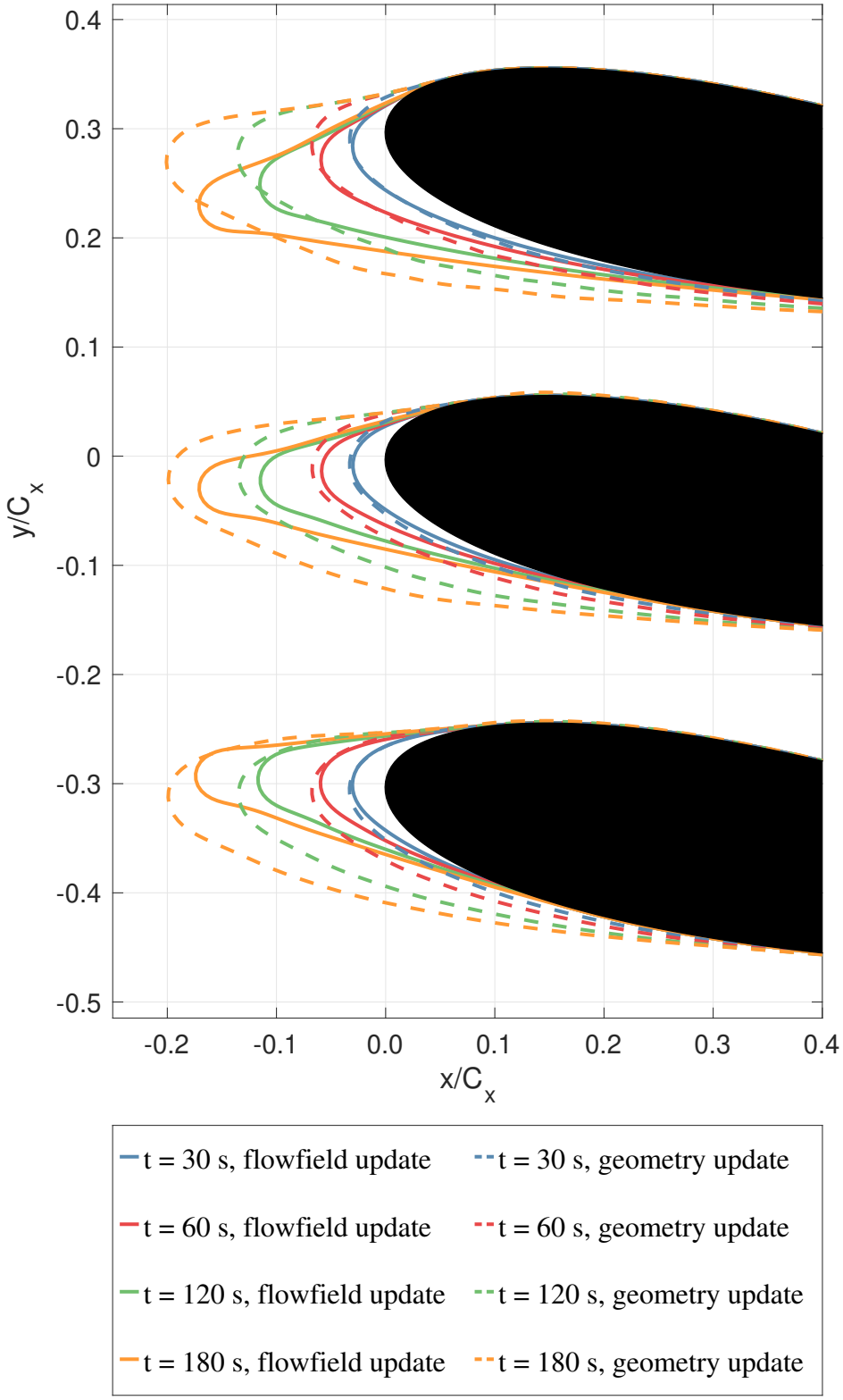

Figure 6.21: Accretion profiles with and without flowfield coupling after 180 s of ice exposure (TWC=8 g m^{-3}, mono dispersed d=20 µm) for the triple airfoil at Mach 0.3, 10° angle of attack.

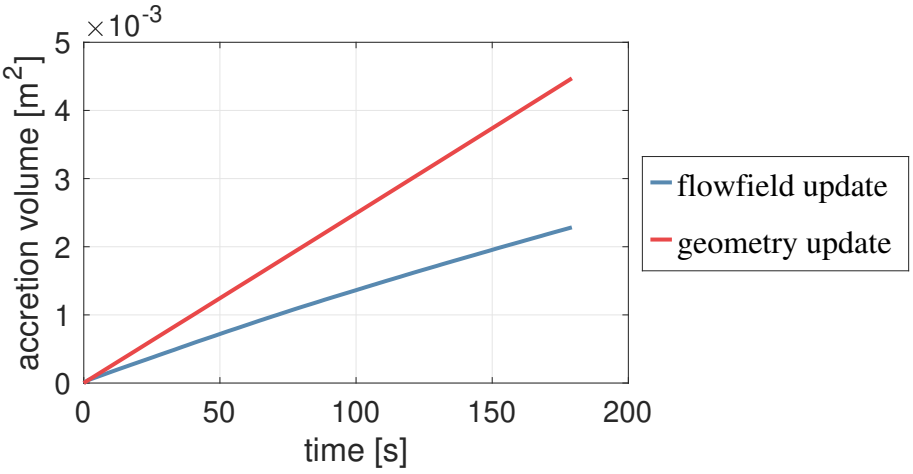

Figure 6.22: Accretion volume with and without flowfield coupling after 180 s of ice exposure (TWC=8 g m^{-3}, mono dispersed d=20 µm) for the triple airfoil at Mach 0.3, 10° angle of attack.

6.4.5 10° Angle of Attack, 40µm diameter

A final test case of this geometry was tested with an increased particle size of 40 µm. When the diameter of the particles is increased, the increased momentum alters their behaviour within the flow. This phenomenon is characterised by the non-dimensional group, Stokes number (Stk), defined as the ratio of the characteristic time of a particle to that of the flow (Equation (2.1)). For the baseline simulation case of Mach 0.2, 20 µm, 10% MR, $\mu_a(T) = \mu_a(283K) = 1.75 \times 10^{-5}$ Pa s, the Stokes number is 2, and for 40 µm is 8.3. It is generally assumed that particles with a Stokes number of less than unity will be streamline following, which suggests that the larger particle size of 40 µm will have a more ballistic trajectory.

The accretion profiles are shown in Figure 6.23, where it can be seen that a much closer agreement is seen between the flowfield update and geometry update solutions. The increase in ballistic nature of the particles meant they were less deviated by the local pressure field, reducing the effect of the updated flow solution in the flowfield update case.

Figure 6.24 shows the growth rate of these two solutions, showing that a much closer agreement in accreted volume was found between the two cases.

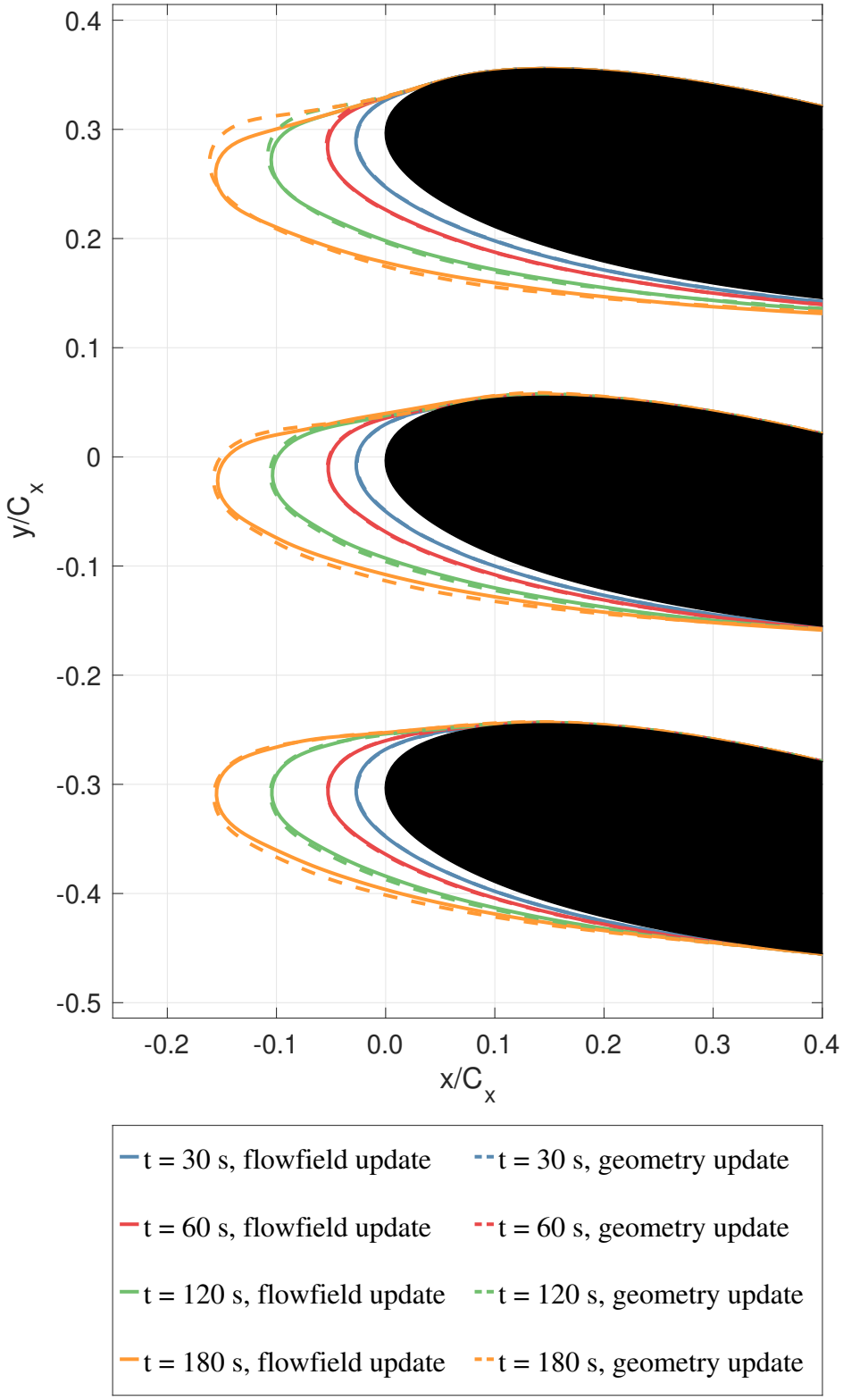

Figure 6.23: Accretion profiles with and without flowfield coupling after 180 s of ice exposure (TWC=8 g m^{-3}, mono dispersed d=40 µm) for the triple airfoil at 10° angle of attack.

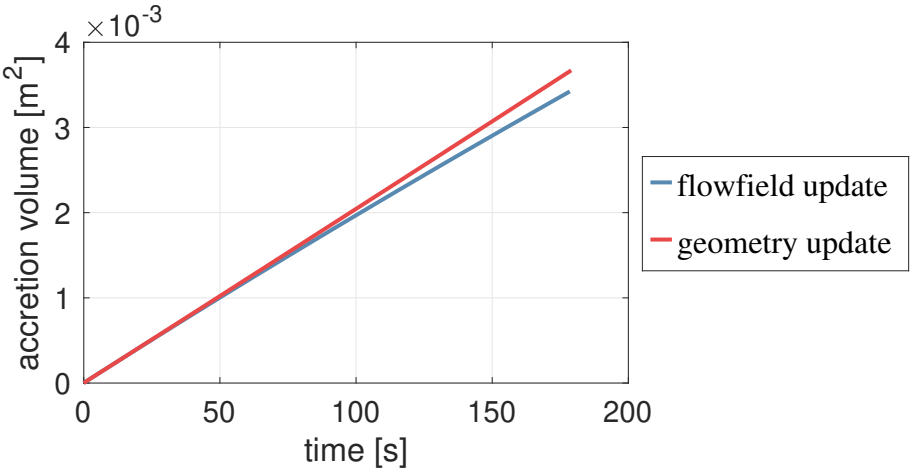

Figure 6.24: Accretion volume with and without flowfield coupling after 180 s of ice exposure (TWC=8 g m^{-3}, mono dispersed d=40 µm) for the triple airfoil at 10° angle of attack.

6.4.6 10° Periodic

A final geometry was tested of a periodic cascade configuration. The angle of attack was kept at 10 ° and pitch of 60 mm. The accretion profiles are shown in Figure 6.25. When infinite blade rows were studied in such configuration, the flow upstream of the blade-row was found to be more axial than that found of a finite linear cascade, leading to an axial accretion growth - similar to what was seen in the zero degrees angle of attack case. However because the pressure gradient in the mid-blade passage was stronger in this periodic case, the particles were deviated away from the accretion much more in the flowfield update case, reducing the number of impacts onto the accretion, decreasing the growth rate substantially compared to the geometry update solution. This meant that the flowfield update solution had a decreasing growth rate, leading to significant differences in accretion volume, as seen in Figure 6.26.

In reality the accretion observed in this case is unlikely to be strong enough to overcome the aerodynamic forces applied. It is expected that this accretion would regularly shed due the small thickness of the leading accretion.

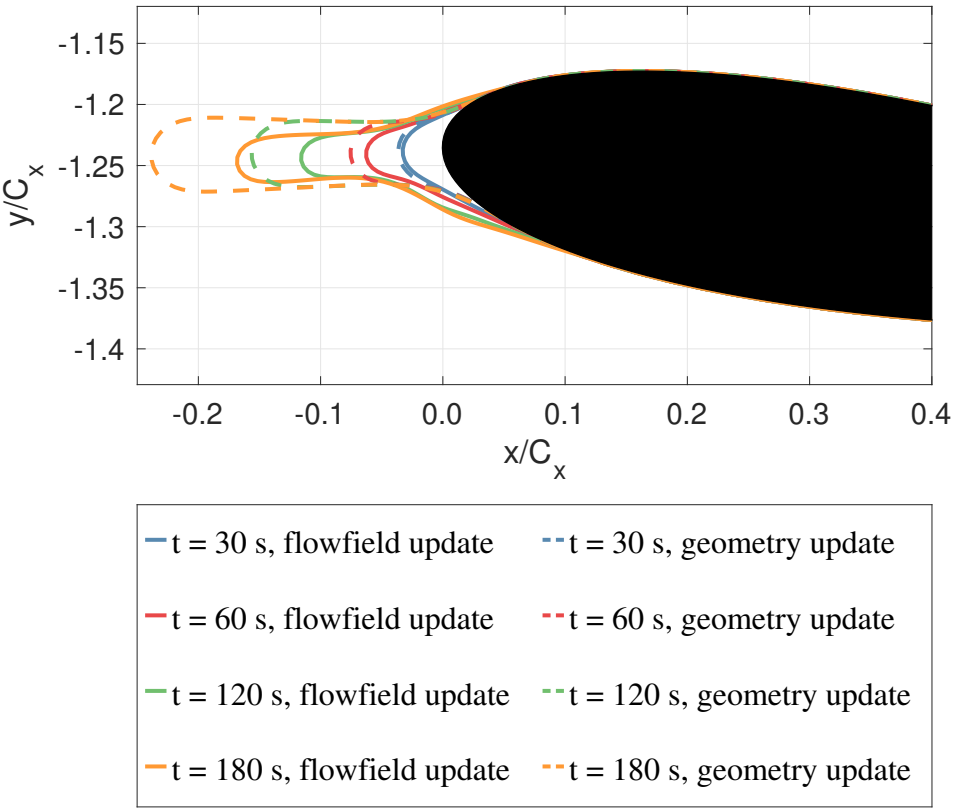

Figure 6.25: Accretion profiles with and without flowfield coupling after 180s of ice exposure (TWC=8g/m^3, mono dispersed d=40μm) for the periodic boundary condition airfoil at 10° angle of attack.

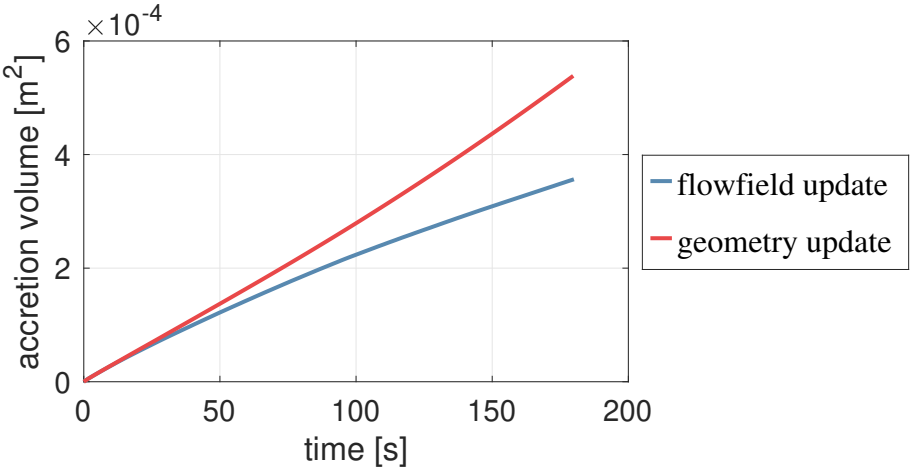

Figure 6.26: Accretion volume with and without flowfield coupling after 180s of ice exposure (TWC=8g/m^3, mono dispersed d=40μm) for the period boundary condition airfoil at 10° angle of attack.

6.4.7 Effect of flowfield update frequency

The results of this section have shown the difference between only updating the geometry compared updating the geometry and flowfield solution each time the particle trajectories are recalculated. An alternative method to save on computational cost is to update the geometry on every timestep, and on every n-timesteps also update the flowfield solution. The previous data has all shown that in the early stages of the accretion that there is a good agreement between the geometry update and flowfield update solutions, suggesting that during this stage of the accretion that only the geometry needs updated. Unfortunately this is only known once a full study has been completed on the effects of flowfield updating, so for a new geometry/condition, all the user can specify is the frequency at which to update the flowfield solution compared to just updating the geometry.

The geometry of 10° angle of attack, 20 µm was tested at both Mach 0.2 and 0.3 for this study . The flowfield was updated on every n times the geometry was updated. For this study, n was chosen to be 1, 2, 4, 8, 16, 32, 64 and overall there was approximately 140 timesteps.

Figures 6.27 and 6.28 shows the accretion profiles predicted at Mach 0.2 and Mach 0.3 with increasing time periods between flowfield update after an ice exposure of 180 s. Note that a flowfield update period of infinity is the geometry update solution. For both cases it was found that updating the flowfield solution every 4 timesteps produced a qualitatively similar accretion profile compared to updating it on every timestep. Updating the flowfield more often than every four timesteps did not have a significant effect on the predicted accretion profile. When the flowfield was updated less frequently than every four timesteps the accretion profile morphed towards the geometry update solution.

To gain quantitative insight into the changes in the accretion profile when the frequency of flowfield update was altered, the accretion volumes were studied. Figures 6.29a and 6.29b shows the accretion volume at 180 s for Mach 0.2 and 0.3 respectively. It can be seen that with a decreasing period between flowfield updates, a the accretion volume converges on a solution. The data again shows

that with the flowfield being updated more often than every four timesteps, that there is an insignificant change in accretion volume.

This data shows that updating the flowfield at decreasing time periods increases the solution accuracy. For the two conditions studied it was found that the flowfield needed to be updated every four times the geometry was updated. It is thought that this is highly dependant on both the test piece geometry and flow condition tested, and should not be taken as a general rule of when the flowfield needs updated. It is therefore deemed necessary to conduct a convergence study to determine the frequency at which the flowfield needs updated.

6.5 Summary

This chapter has numerically explored the effects of updating the geometry and flowfield on the predicted accretion behaviour. It was found that updating the geometry so that particle tracks can be re-computed was essential for reasonable accretion shapes to be predicted. If the end goal of the numerical analysis is to predict a conservative estimate of the total mass of accreted ice, then updating the geometry on its own may be sufficient.

However, if an accurate estimate of the accretion mass is required, then the flowfield needs to be updated at regular intervals - requiring a large increase in computational resources. The level of influence of updating the flowfield is heavily dependant on the geometry, flow condition and particle size. If the flowfield is aligned with the test piece leading edge then it is likely that the accretion will grow in the flow direction. This will allow for reasonable estimates on the shape of the accretion using geometry update, however flowfield update will still be required for accurate prediction. When local flow curvature exists in the near body region then the effects of flowfield updating lead to a large difference in both accretion shape and volume. Increasing the particle diameter was found to make it more ballistic, reducing the influence of the update of the flowfield.

The frequency at which flowfield coupling is required was studied for 10° angle of attack, 20 µm at Mach 0.2 and 0.3. It was found that by updating the flowfield

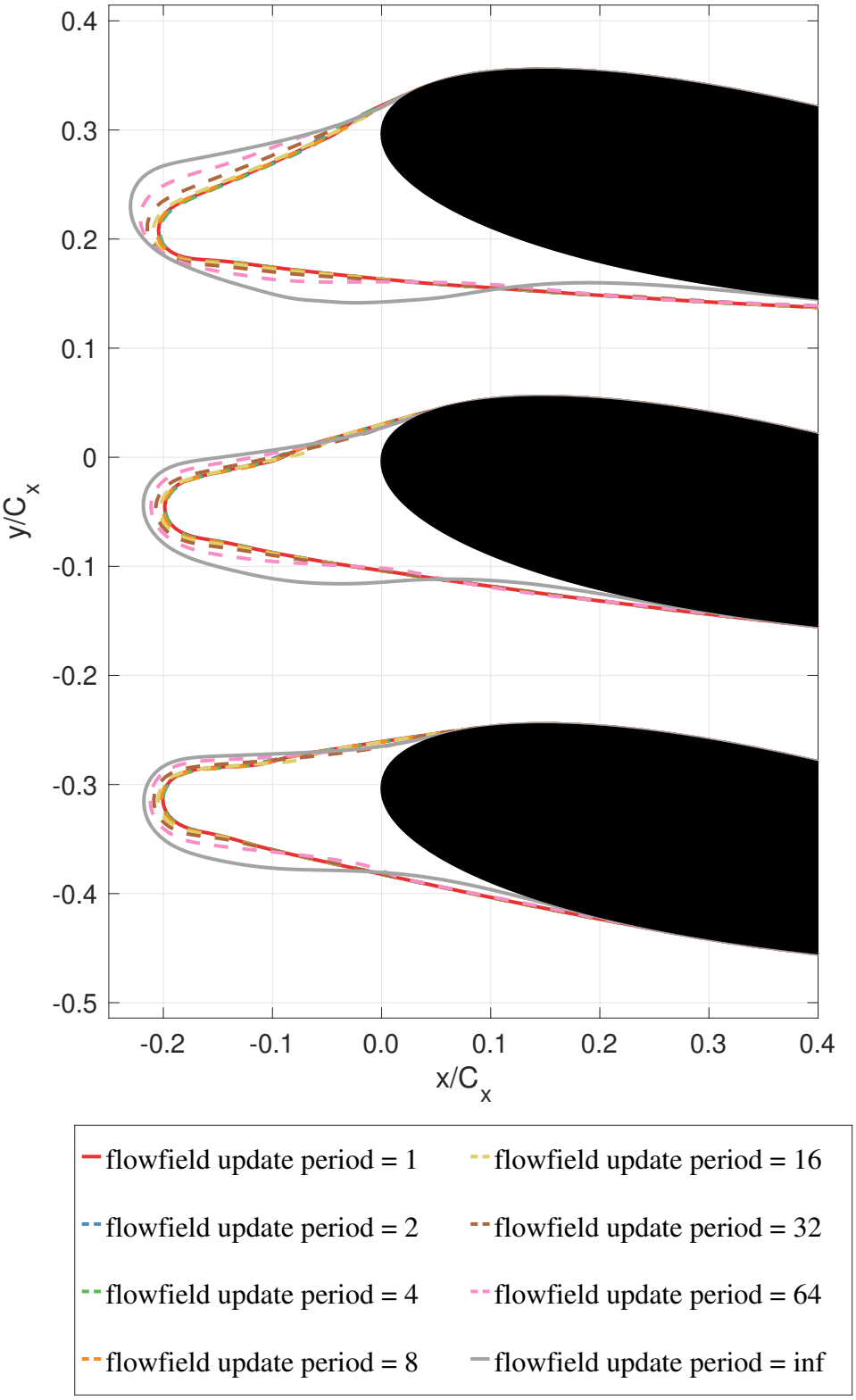

Figure 6.27: Accretion profiles predicted with increasing time periods between the timesteps at which the flowfield is updated. Results shown after 180s of ice exposure (TWC=8g/m^3, mono dispersed d=20μm) for the triple airfoil at 10° angle of attack, Mach 0.2. Update period of infinity means that the flowfield was never updated, i.e. a geometry update solution.

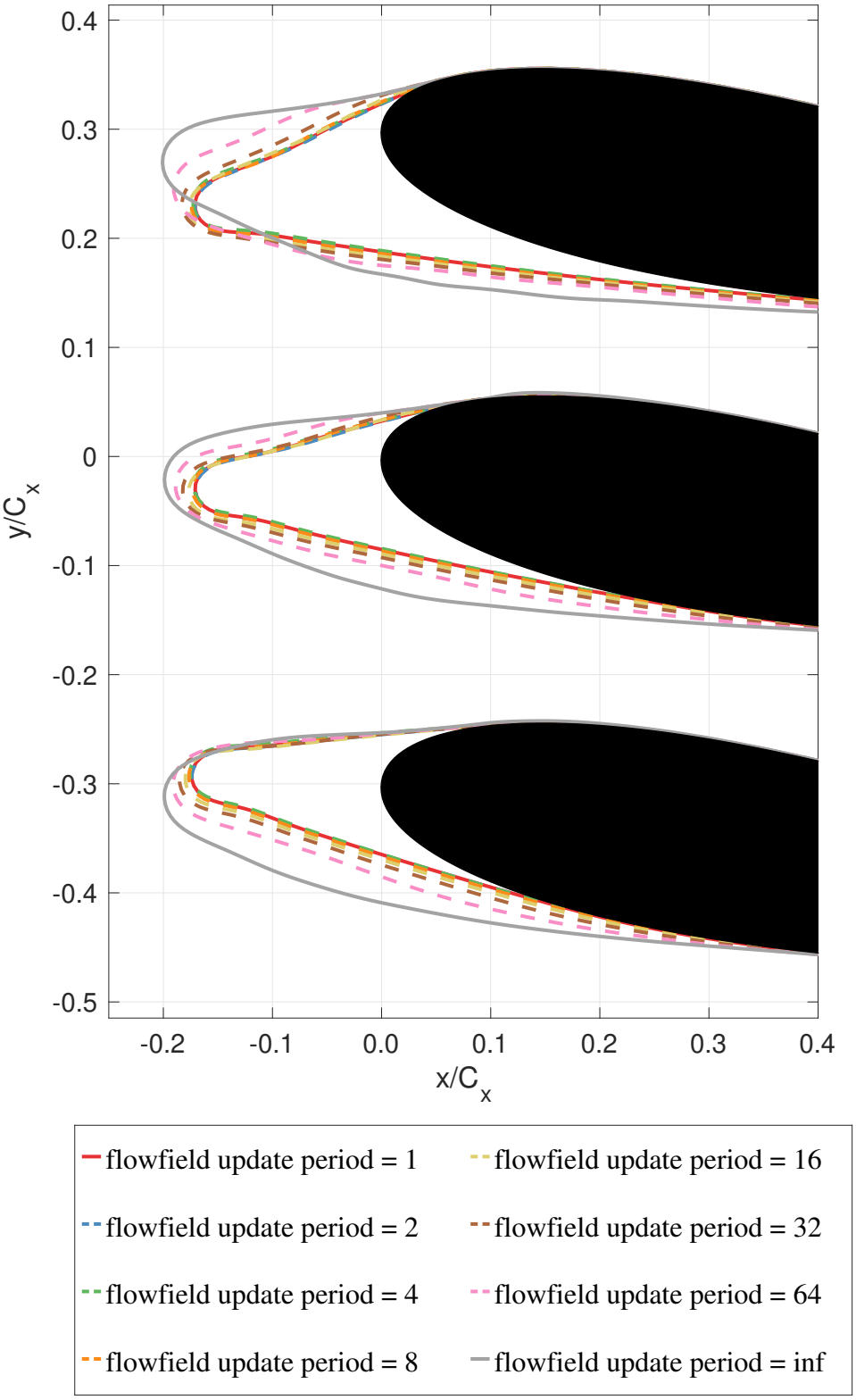

Figure 6.28: Accretion profiles predicted with increasing time periods between the timesteps at which the flowfield is updated. Results shown after 180s of ice exposure (TWC=8g/m^3, mono dispersed d=20μm) for the triple airfoil at 10° angle of attack, Mach 0.3. Update period of infinity means that the flowfield was never updated, i.e. a geometry update solution.

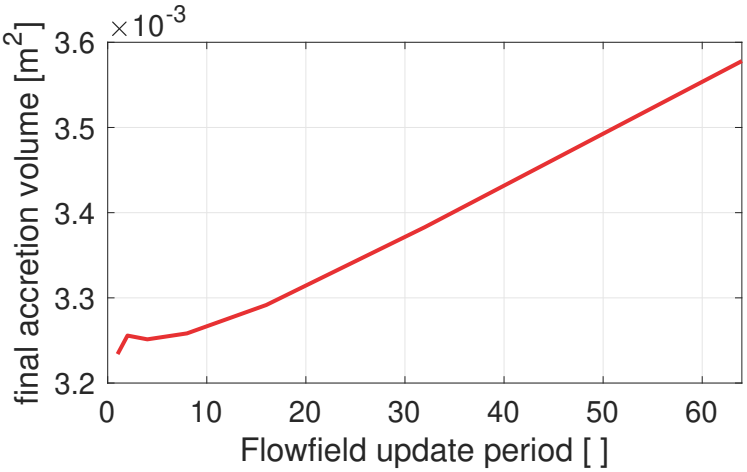

(a) Mach 0.2.

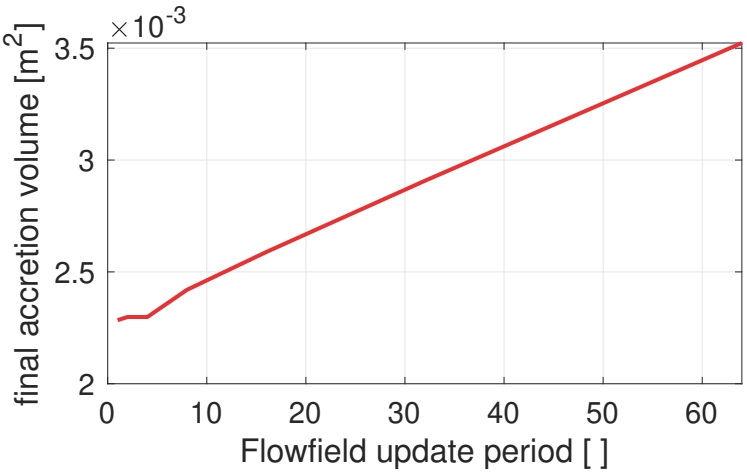

(b) Mach 0.3.

Figure 6.29: Accretion volume numerically predicted with increasing period between the update of the flowfield solution. Results shown after 180s of ice exposure (TWC=8g/m^3, mono dispersed d=20μm) for the triple airfoil at 10° angle of attack, at both Mach 0.2 and Mach 0.3.

at decreasing time intervals, that a converged solution existed. This suggests that for accurate simulations, a convergence study needs to be applied to the rate of update of the flowfield solution. One aim of the work was to conclude the frequency at which this needs to occur, however because it is so heavily dependant on the geometry, flow conditions and particle size, it is concluded that a manual convergence study needs to be conducted.

7 Conclusions and Further Work

7.1 Conclusions

The work conducted for this thesis has enhanced our ability to both experimentally measure the accretion, and also numerically predict the accretion behaviour.

The previous ice crystal icing accretion measurement techniques were simplistic in nature, and at best could only provide quantitative two-dimensional profiles. As the experimental research in the field is progressing away from fundamental geometries where such methods were sufficient, it was deemed necessary to create a measurement system that could measure the three-dimensional accretion profiles, in a non-intrusive manner during the test. Two systems have been developed using bench-top testing; a single laser single camera, and a dual camera single laser. In the first system the laser is calibrated with the camera, and in the latter, the laser is used to enhance the contrast of the stereo system. Both methods have their relative benefits, where the first system (DIP), has a reduced number of components which may be critical in test pieces with limited viewing angles. However, this method requires a calibration method involving a traverse of a planar object, which may not be possible in certain wind tunnels or test pieces. The stereo system has increased complexity with the addition of an additional camera, but the reduced complexity of the calibration procedure (multiple images of a checker-board pattern

at arbitrary position) may make this method more suitable for confined spaces. The DIP measurement technique has been tested in ice crystal icing conditions in RATFac, at the NRC. It was tested on both a single compressor stator blade, and also a combined linear cascade and swan neck duct. For the tests with the stator blade, the accretion was expected to be quasi-two-dimensional - allowing the use of backlit shadography to be used as an alternative data source. Qualitatively good agreement of the data from the DIP and backlit shadography was seen, however because of three-dimensional flow effects the accretion was found not to be two-dimensional. This meant that the data from the backlit shadography could not be used as a validation dataset. Instead, a commercial handheld scanner was used to validate the measurements of the DIP system. This scanner could not be utilised during the test due to the requirements of circular sticker targets being places on the accretion and not being able to image low reflectivity objects. Instead, after the test the altitude chamber was returned to ambient temperatures, the accretion quenched with low temperature gas (to increase the reflectivity), and markers placed on the accretion so that measurements could be taken. Good agreement was observed between the two datasets, with an averaged difference of 0.64 mm. Both systems were able to capture the three-dimensional variations in accretion thickness along the span of the blade - caused by three-dimensional flows. This data could not be captured using previous measurement techniques. The same system was used on the combined linear cascade and swan neck duct test piece, which due to its curvature could not use backlit shadography. This was also compared to data from a handheld scanner at the end of the test, and good agreement was also seen.

Significant work has also gone into the development of the ice crystal icing numerical code, ICICLE. The two-dimensional prediction tool was created by the OTI and had been validated against experimental data of simplistic geometries in certain flow conditions. From the analysis of experimental accretion profiles, it was expected that the accretion would lead to differences in the potential field around the test piece. As part of the work for this thesis, the ability to update the flow solution based on the predicted accretion profile was implemented into ICICLE.

Other improvements to the code included numerical efficiency gains (reducing the computation time of the particle trajectory calculations by over an order of magnitude), and inclusion of more physics in a substrate cooling model and improved water run-back model. The improved code was first tested to determine the number of particle streams required to accurately predict the level of mass sticking to a testpiece. It was found that a much higher number of particle streams were required to reach statistical convergence, compared to what was used in previous simulations.

The code was then tested for the effects of flowfield updating on two test pieces; the compressor stator blade and a triple NACA 18 airfoil. The results from the stator test piece showed that if the particle trajectories are only computed for the clean geometry, then a significant error in the accretion profile is obtained. By updating the geometry and re-computing the trajectory paths, much improved performance was achieved. By also updating the flowfield solution as well as the geometry, it was found that the prediction was similar to that seen with just updating the geometry. It was concluded that this was due to the test piece being isolated in a large flow domain, meaning that the presence of the accretion had little change to the overall blockage.

A new test piece of a triple NACA 18 airfoil was designed and manufactured. This geometry was numerically tested for the effects of flowfield updating. It was found that when used at a positive angle of attack, that significant changes in accretion shape and volume occurred when only updating the geometry compared to also updating the flowfield. It was found that when the flow direction was not aligned with the testpiece leading edge direction that large differences in accretion growth direction occurred. When a larger particle size was studied, the increase in its Stokes number (and hence ballistic nature), meant that it was less affected by the update of the flowfield.

Typically the main risk of ice crystal icing is the damage caused by shed ice, which is dominated by the mass of ice that is shed. This work has shown that for the geometries tested, that a geometry update solution leads to a conservative estimate of the accreted volume. However, if the final accretion shape from the geometry update

solution was analysed for the potential of shedding, it would likely produce the incorrect results due to its geometry being different to the flowfield update solution.

The sensitivity of the frequency at which the flowfield is updated was tested. Due to the complex interaction between the flowfield and particulate behaviour, a criteria for updating the flow solution was not found. However, it was seen that by increasing the frequency at which the flowfield is updated, that a converged solution was obtained. From this result, it was concluded that a convergence study on not only the number of particle streams but also on the frequency at which the geometry and flowfield is updated is necessary for accurate numerical prediction of ice crystal icing.

7.2 Further Work

The physics of ice crystal icing is so complex that numerous areas are still not fully understood. The models utilised for the prediction of the water run back is far from optimal. Without accurate prediction of this water film thickness, it is not possible to predict the likelihood of a particle to stick to the water layer and hence calculate the substrate cooling and successive growth rates.

Heat and mass transfer from the continuous phase to the discrete particle phase is currently accounted for. However, mass and heat transfer due to particle evaporation and sublimation is not returned to the continuous phase. This means that the decrease in free stream temperature with the injection of an ice cloud cannot be predicted, which can dramatically alter the accretion behaviour. This will be particularly beneficial for accurate simulation of the transient change in condition of wind tunnels as the ice flow is initiated, and prediction of the altered conditions in an engine.

Another key model missing is the ability to predict sliding and shed of the accretion. This will require not only an accurate prediction of the local flowfield (to obtain the accretion pressure distribution) but also thermal and stress analysis of the accretion. To determine critical stress limits for the interface with the substrate or within the accretion, the material properties of the accretion need to be known. These properties are likely a function of the impact speed, particle size, melt ratio,

local humidity and accretion temperature. Shedding is the key damage of ice crystal icing, so without accurate numerical prediction it is not possible to certify an engine without additional experimental data.

To validate the work of flowfield coupling shown in this thesis, experimental data of the triple airfoil test piece will need to be obtained. This test piece has been manufactured and is due for test in late 2021.

Experimentally, the accretion measurement methods created in this work will need further testing in complex viewing angles to determine the limits of the system. When imaging accretion in an engine environment, there are limited locations where a camera/laser can be situated. An envelope of acceptable viewing angles and the effect of this on the measurement accuracy will need to be determined.

Finally, experiments need to be conducted to verify the differences in accretion behaviour when different ice generation methods are used. Facilities now exist which can either produce ice via freeze-out of liquid droplets, grinding of ice blocks or in a natural convection cloud chamber - with the latter thought to be the most representative of atmospheric ice. To ensure that our models are capable of accurately predicting ice crystal icing of atmospheric ice, back-to-back comparisons of the different ice generation methods need to be conducted.

Appendices

A

Swan Neck Duct Results

The results of the swan neck duct experimental campaign were submitted as a paper into the 2020 AIAA Aviation conference for which I was lead author. The paper is shown below.

AIAA AVIATION Forum
June 15-19, 2020, VIRTUAL EVENT
AIAA AVIATION 2020 FORUM

10.2514/6.2020-2828

Ice crystal accretion experiments in a combined linear cascade and swan neck duct

Jonathan Connolly *, Myeonggeun Choi †, Xin Yang ‡, Luke Doherty§, David R. H. Gillespie ¶, Matthew McGilvray ‖
University of Oxford, Oxford, OX2 0ES, UK

Benjamin Collier **, Geoff Jones ††
Rolls-Royce Plc, Derby, DE24 8BJ, UK

Fully glaciated ice crystals can be ingested into aero engines, partially melt through the first few stages of compressors and eventually cause large accretions on stationary components. Ice crystals pose a threat due to damage caused by ice shedding. With regulators expanding certification of engines to include the threat of ice crystals, there has been significant research at both the fundamental and complete engine tests. This paper details experiments which lay somewhere between the these two ends of the spectrum; an engine representative stationary geometry with direct control and measurement of the inlet icing conditions. The aim of the experiments is to directly measure ice thickness on complex three dimensional surfaces of a combined linear cascade and swan neck duct. This will enhance our understanding of locations at which there is a large threat to ice accretion and at what conditions this occurs. This paper will detail the test piece geometry, present the results of the experimental campaign and initial analysis and conclusions from the experiments.

Nomenclature

I	=	Image focal point (camera)
L	=	Laser focal point
η	=	Horizontal separation of laser and camera
λ	=	Minimum vertical height of laser/camera
$\vec{FB}$	=	Vertical height of accretion relative to base surface
$\vec{Ab}$	=	Translation of laser node in the cameras perspective
M	=	Mach number
T	=	Temperature
P	=	Pressure
$\dot{Q}$	=	Heater mat heat flux
MR	=	Melt ratio
ICI	=	Ice Crystal Icing
CIKP	=	Compact Iso-Kinetic Probe
PSD	=	Particle Size Distribution
LWC	=	Liquid Water Content
TWC	=	Total Water Content
TC	=	Thermocouple
NRC	=	National Research Council (Canada)
RATFac	=	Research Altitude Test Facility
SND	=	Swan Neck Duct

*PhD Student, Department of Engineering Science, Oxford Thermofluids Institute.
†Postdoc, Department of Engineering Sciences, Oxford Thermofluids Institute.
‡Postdoc, Department of Engineering Sciences, Oxford Thermofluids Institute.
§Senior Postdoc, Department of Engineering Sciences, Oxford Thermofluids Institute
¶Associate Professor, Department of Engineering Science, Oxford Thermofluids Institute.
‖Associate Professor, Department of Engineering Science, Oxford Thermofluids Institute.
**Ice Crystal Tech Focal, Engine Environmental Protection Team, System Design.
††Subject Matter Expert - Icing and Inclement Weather, Engine Environmental Protection Team, System Design.

Subscripts

0 = Total
wb = Wet bulb

I. Introduction

Aero-engines face risk upon ingestion of high altitude ice crystals which has led to regulators expanding certification of engines to include this phenomenon. Commonly termed as ice crystal icing (ICI), the ingested ice crystals can partially melt whilst transiting through the compressor and stick to stationary components. This ice accretion can build to the point of a powerloss event (rollback). Also, when the ice is shed, it can also lead to blade damage, flame out and surge. This has led to a concerted effort from both industry and academia to understand the complex coupled phenomena involved in ICI and develop numerical models of the process.

There has been a large range of high quality experiments undertaken at the fundamental end of the spectrum. This effort has been led by the groups at the NRC and NASA Glenn, with recent additions by the University of Oxford in partnership with Rolls-Royce. These have focused on simple geometries, such as flat plates [1, 2], cones [3, 4], aerofoils [5, 6] and individual stator blades [7]. This has allowed for a much improved understanding of the complex coupled physics involved in ICI and the extraction of quantities needed in empirical models such as sticking efficiencies. Also, these tests have provided simple two dimensional validation datasets to allow validation of ICI numerical codes, notably the NASA GlenICE code [8], ONERA IGLOO2D code [9] and the Oxford/Rolls-Royce ICICLE code [10].

In comparison, there is limited experimental data in the open literature of more engine representative three dimensional geometries. Full engine testing of the Honeywell ALF502 [11] was performed with instrumentation to measure ice accretion downstream of a twin stator. Inter compressor ducting with flow path curvature have been previously tested [12, 13]. Several linear cascades have also been used in ICI experiments [14, 15], with the testing by Fuleki *et al.* using a segment from the Honeywell ALF502. All of these tests have provided valuable qualitative insight to the effects of ICI in more engine like flowfields. However, there is a lack of quantitative engine representative datasets needed for validating ice accretion codes.

With engine architecture from all OEM's moving towards geared fans, this leads to the inclusion of aggressive turning in the inter-compressor ducting typically referred to as swan neck duct (SND), in the early stages of compression. This can be at a location of particularly severe ice accretion due to the radial centrifuging of the ice and concave surface for impact. Although there has been testing of individual components, there is no testing that has coupled the turning effects of a linear cascade and a swan neck duct.

This paper will detail experiments on a combined linear cascade and a swan neck duct under ice crystal icing conditions. The tests apply a digital image projection technique to provide quantitative measurements of the accretion. The testing was performed in the NRC's RATFac wind tunnel by coupling the test piece to the downstream of the cascade rig, providing a controlled and measured inflow condition. Tests were performed over a range of inlet conditions and test piece settings.

II. Test facility, conditions, geometry and optics

RATFac test facility

The test facility used in the study was the Research Altitude Test Facility (RATFac) at the National Research Council of Canada (NRC), Ottawa. The facility comprises a wind tunnel and ice particle generation system, housed in an altitude chamber. A schematic of the facility is shown in Fig. 1. The chamber is divided into a 'cold' section, where an ice grinder produces particles of a target Particle Size Distribution (PSD) at sub-freezing temperatures. These are then fed in the ice injection pipe to the 'warm' part of the chamber, which is maintained at a target total temperature. The particles are fed as a free jet into the bellmouth of the wind tunnel – known as the cascade rig – mixed with any supplemental liquid water from a spray mast. The wet bulb temperature in the test section may be controlled by varying the total temperature, total pressure and/or humidity, the latter controlled by steam injection. The test piece used in this study was connected to the exit of the cascade rig, replacing some of the exhaust system. This allowed the utilisation of the standard facility traverse and instrumentation located in the cascade rig.

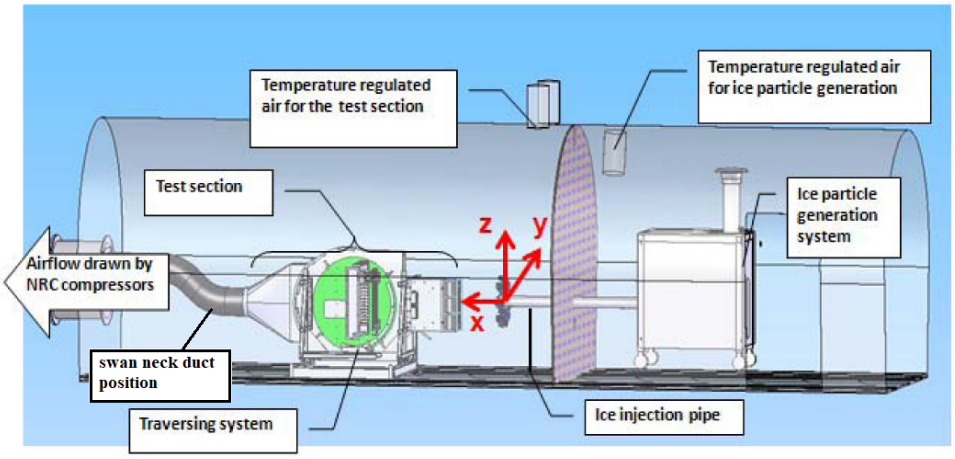

Fig. 1 RATFac altitude chamber, housing the cascade configuration of the icing tunnel. Original image taken from [14], with additional annotation showing location of the swan neck duct test piece.

Aerothermal Measurements

Prior to ice injection the aerothermal conditions were measured to obtain the correct operating point. A Keil probe was traversed onto the tunnel centerline which measured the total temperature and pressure. Static pressure was measured using a tap on the upper surface of the tunnel, upstream of the test section. A rearward facing probe (TAT-RH probe) on the lower surface of the tunnel recorded the total temperature and relative humidity both prior to and during ice injection, allowing the drift in conditions due to the ice cloud to be measured upstream of the test piece. Downstream of the test piece a heated static/pitot probe measured the change in total pressure during the accretion blockage. The change was caused by the increased flow blockage and also the increased levels of loss due to flow separation over the non-aerodynamic accretion profile.

Ice Cloud Measurements

Total water content (TWC) was measured using a compact iso-kinetic probe (CIKP). The probe evaporates all incoming ice, liquid water and air moisture and compares to the background humidity measured by the TAT-RH probe to calculate the total water content of the ice cloud. A SEA multi-element probe was used to measure the liquid water content (LWC). The particle size distribution (PSD) was measured using the NRC Particle Image Velocimetry (PIV) system, which is discussed in more detail in [16, 17]. The approximate plane over which the PSD measurements were taken is shown as a red parallelogram in Fig. 4 (however the region analysed was considerably smaller than the plane shown). The cloud melt ratio is defined as the ratio of liquid to total water content. Measurements from the SEA multi-element probe require corrections to determine the true water content due to the device recording a non-zero LWC with fully glaciated crystals (named the false response), the smallest crystals deflecting around the probe and partially melted crystals not fully shedding their liquid water onto the elements. Bucknell *et al.* [3] determined an empirical relationship for the false response as a function of Mach number, PSD and TWC, and the authors suggested the use of the catch efficiency correction by Struk *et al.* [18]. This same method of melt ratio calculation has been used in this paper. It should be noted that measurements of liquid water content measured by the multi-element probe were taken using the standard RATFac traversing system (shown in Fig. 1), which was located upstream of the swan neck duct blade row. The ice crystals exited the ice injection pipe fully glaciated,and partially melted as they traversed through the test section. The LWC measurements were made approximately 80% along the axial distance from the exit of the ice injection pipe and the blade row of the swan neck duct. Therefore the true melt ratio within in the SND will have been slightly greater than what was measured.

Test conditions

A total of 46 test points were completed with the test article in-situ. In all tests, the mixed phase icing cloud was generated by natural melt of initially glaciated particles in a warm airstream, as opposed to by supplemental liquid water injection. The nominal test point had the following properties: a total pressure of 48.3 kPa; a total air temperature (T_0)

of 10°C; and an upstream initial Mach number of 0.4 (before any accretion). All tests were conducted with a constant particle size distribution with the following parameters; $D_{v10} = 18$, $D_{v50} = 32$, $D_{v90} = 54\ \mu m$. Aerodynamic conditions were obtained indirectly when ice was flowing by measuring parameters (total & static pressure, total temperature and relative humidity) pre-test and superimposing the change in each parameter provided by probes designed to operate in an icing cloud (including the downstream-facing TAT-RH probe).

Test piece geometry

The test geometry used in the study reproduces a typical civil turbofan S-shaped inter-compressor with features that can lead to the accretion on not only stator vanes but also outer annulus skin of the swan neck duct passage, as evident from the experimental results. The linear cascade configuration includes 8 stator vanes upstream of the swan neck duct with a positive lean angle. The vane profile selected was representative of that in an intermediate pressure compressor and the blades had a negative geometric incidence angle. The inner annulus was simplified to be a flat plate to reduce the complexities involved in calibrating the DIP system with distorted optics. The test piece is shown in Fig. 2 and a view of the stator cascade from inside the tunnel is shown in Fig. 3, where the blade camber and outer annulus curvature is clearly visible. In Fig. 3 it can be seen that one of the blades has a penny feature at the intersection with the outer annulus, representative to that in a variable incidence stator. This was implemented to study its effect on the local accretion and it was found to have insignificant impact so is not analysed in this paper. The test piece and the mounting into RATFac is shown in Fig. 4.

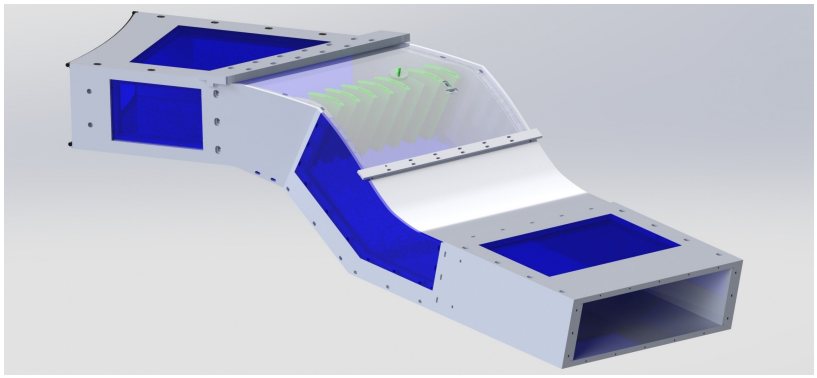

Fig. 2 Swan neck duct test piece. Outer annulus section transparent for clarity

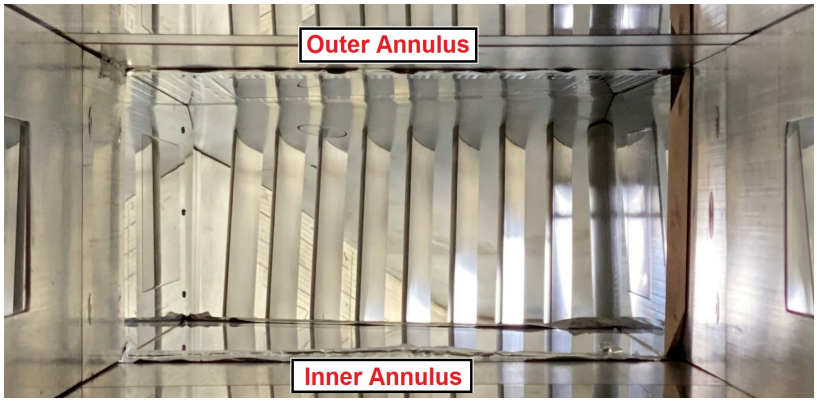

Fig. 3 View of cascade from the RATFac cascade bell-mouth inlet.

The vanes and the swan neck duct outer annulus were machined from a stainless steel resulting in the surface roughness of < 0.8 μm, typical of entry-into-service conditions. The curved outer annulus had a series of cut-outs to receive the stator vanes, then was externally welded and dressed back. The set of vanes was slotted into a 3D printed resin pocket in which itself was mounted into the inner annulus body. The pocket accommodates 7 Perspex windows in

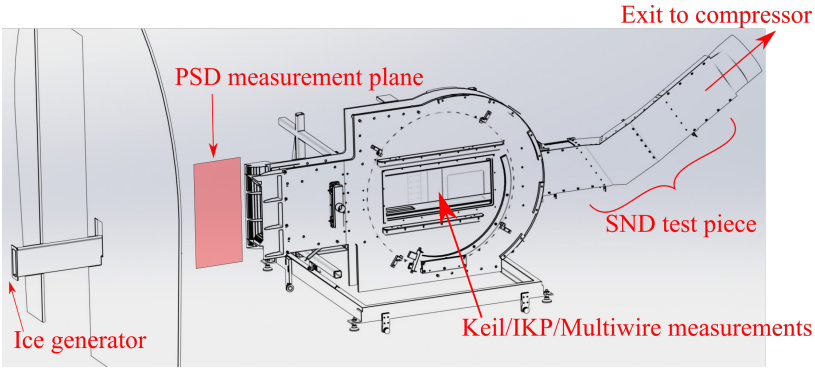

Fig. 4 Schematic of test piece connected onto the cascade rig in RATFac.

between the vane passages for the use of laser projectors looking onto the outer annulus. Downstream of vanes the inner annulus mainly consists of a 10 mm thick Perspex along with a clearly polished Polycarbonate window, allowing full optical access to the domain of interest. The remaining structural parts at both upstream and downstream of the swan neck duct passage were made of an aluminium alloy accommodating additional Polycarbonate windows.

Heating was applied to the outer annulus to study heat transfer effects, and the two side walls which follow the flow turning were heated, and thus minimising passage blockage by unwanted ice build-up. This was done with a set of flexible electrical resistance heater mats mounted on the external of the geometry. These were either controlled by a set of PID controllers for constant temperature operation, or were controlled by constant electrical power input using a Variac and hence had constant heat flux operation. Eight K-type shielded thermocouples were embedded into the external surface of the outer-annulus in regions of highly likely accretion regions, predicted by a preliminary numerical analysis.

Test Piece Thermal Measurements

The outer annulus of the swan neck duct was instrumented with thin film gauges and thermocouples to measure heat transfer and temperatures at discrete points over the surface. The heat transfer data is not discussed in this paper. Eight thermocouples were placed on the outer annulus in the positions shown in Fig. 5. The line normal to the flow path shown between thermocouple (TC) 6 and 7 is the inflection point on the outer annulus.

Cloud biassing

Rotors in an engine centrifuge ice crystals creating a non-uniform radial distribution. To mimic this effect an angled plate was located at the exit of the ice injection pipe (location shown in Fig. 1). Figure 6 shows a schematic drawing of the angled plate upstream of the bell mouth of the cascade. Total water content was measured at three radial positions; 15%, 50% and 90% span over a range conditions (span increasing from inner to outer annulus). Figure 7 shows the radial distribution of TWC, normalised by the value on the centerline. Blue crosses show the raw TWC data points at six different conditions, and the red line is a linear interpolation between the mean value at each span position. A scatter in radial profile was observed due to the angled plate having different effects on the particle trajectories at varying Mach numbers and total pressures.

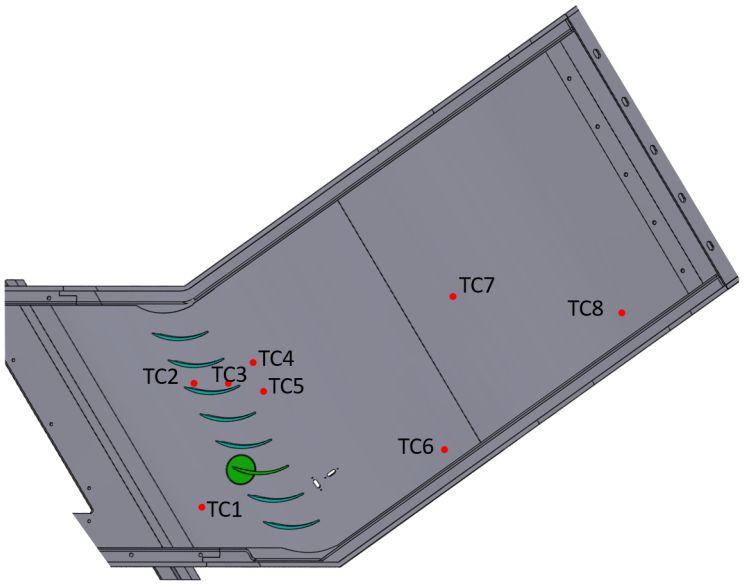

Fig. 5 Thermocouple positions on the outer annulus, as viewed from the inner annulus.

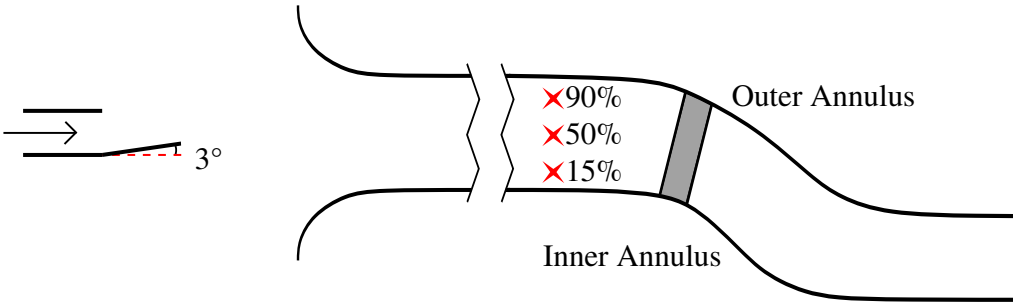

Fig. 6 Ice crystal radial distribution biassing plate.

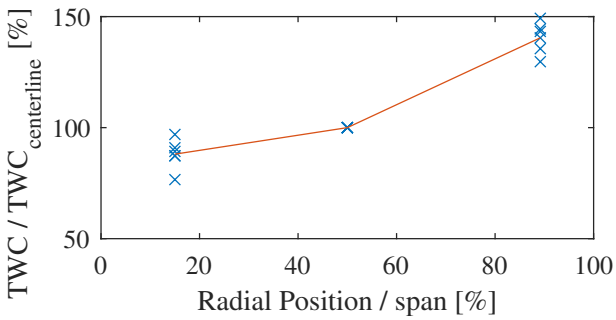

Fig. 7 Radial distribution of total water content normalised by the centerline value.

Qualitative ice accretion cameras

To observe the accretion within the swan neck duct two cameras were installed to view locations of expected ice growth. Both cameras were located on the inner annulus and were directed at the outer annulus. The first camera

recorded the outer annulus in a region upstream of the blade row, and the second recorded a region downstream of the bladerow. The two camera views are shown in Fig.8. The ice cloud passed directly behind the windows which the cameras viewed through, meaning that ice periodically accreted on the window - blocking optical access. The windows were heated with warm air on the outside surface to minimise this effect, however, as seen in the later sections, some window accretion still occurred.

Due to space constraints of this complex test piece with many DIP cameras and lasers as well as standard accretion cameras, it was not always possible to rotate each camera to align the blade rows with the vertical/horizontal axis. During the test campaign the cameras were moved to improve the viewing angles. Post test, the images have been post processed to align the leading/trailing edges with the vertical axis. This has led to some of the images being cropped to a non-rectangular shape.

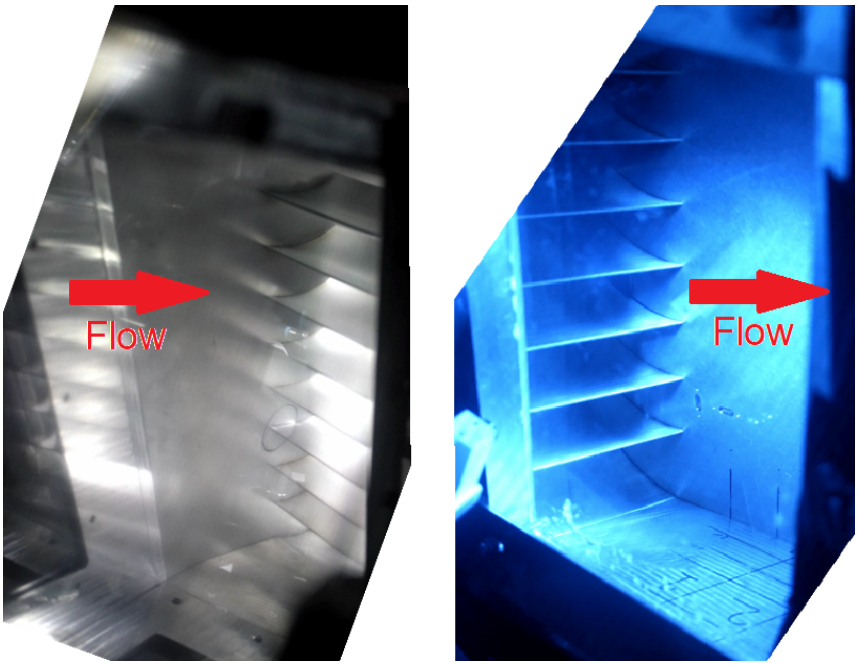

Fig. 8 Main accretion camera views. Both looking at the outer annulus from the inner annulus, in regions upstream (left) and downstream (right) of the blade row. Flow direction is from left to right.

Quantitative ice accretion thickness measurement

To measure the ice crystal accretion thickness during testing, Digital Image Projection (DIP) was applied. A brief summary is provided here of the method, where further details on the novel application of the method to ICI can be found in Connolly *et al.* [19]. Figure 9 shows an idealised DIP system. The system contains a laser projector, which illuminates the surface and a camera positioned to observe the scattered laser from the surface. The laser has a focal point L (position where all projector ray lines diverge from), and the camera has a focal point I. The horizontal separation between the camera and projector is defined as η and the vertical height of the projector/laser from the projection place as λ. For clarity only a single node of the projection array is shown in the diagram. When this node is projected onto a reference plane it is positioned at point A. When a thickness of ice is present above the projection screen, the node originally located at A moves to point B, and again to C with further accretion. From the perspective of the camera, when the node moves spatially from point A to B, the camera observes a translation of the node from point A to b. Point F is defined as the point vertically below B on the projection plane. The goal of this method is to determine ice thickness, $\vec{FB}$, by measuring the displacement of projection nodes, $\vec{Ab}$. From similar triangle relationships, the ratio between $\vec{Ab}$ and $\vec{FB}$ can be related to geometrical parameters of the relative positions of the camera and projector and the ice thickness, equation 1. By re-arranging equation 1, the relationship between ice thickness, $\vec{FB}$ and node displacements, $\vec{Ab}$ can be found (equation 2). Due to equation 2 being an infinite series, an order above which the terms can be ignored needed to be determined. It was found that above the sixth order, convergence had been obtained and

higher order terms were insignificant for the geometries tested in this paper.

The system was calibrated to determine the unknown parameters λ and η. By translating a surface through a known distance $\vec{FB}$ and recording the node translation $\vec{Ab}$, the unknown parameters were found by a curve fitting process. This system can record data during the ice accretion process, however at the point of testing it had not been validated for measuring ice crystal icing accretions. It was decided to compare the DIP data to measurements taken with the Creaform HandyScan 7000 which has a rated accuracy of 0.025 mm for a part size in the range of 0.05-4 m [20]. The device uses a dual camera system with a single structured light source. The method of determining similarity between the two camera sets utilised targets (circular stickers) which were placed onto the object to be scanned, and also used natural features of the object being scanned such as geometrical/colour texture. The device has poor performance when measuring glaze ice with with high transparency. To get the best results, the ice was treated with a low temperature gas to completely freeze out the ice in a non-equilibrium state leading to a surface finish more closely matching rime ice, enhancing the reflectivity. The need to place targets and rapidly freeze the ice structure meant it was not possible to measure the ice thickness during the accretion process. Instead, at the end of the test day the altitude chamber was re-pressurised to atmospheric pressure while maintaining sub freezing conditions ($\approx -10°$). It was then possible to remove the test article from the wind tunnel and complete the ice scan. The ice being scanned is shown in Fig. 10.

Four laser/camera systems were positioned to measure the ice accretion in the folling regions; outer annulus immediately downstream from the trailing edge of a blade, outer annulus further downstream, passage accretion on the outer annulus between the pressure and suction surfaces of one blade pair, and on the suction surface of a blade. Results in this paper show the data from a single DIP system observing the region immediately downstream from the trailing edge. Due to the high computational demand and level user input required to post process the DIP data, it was only possible to process a subsection of the data by the time of publishing this paper. The cameras were primarily used for laser measurements, but also aided in adding additional views of the ice growth. The DIP measurements were taken during most tests, and the laser light can be seen in the main accretion cameras, sometimes leading to overexposure of these images. To minimise this effect on the downstream accretion view, a filter was placed in-front of the camera lens to reduce the intensity of laser light reaching the camera sensor, which caused the blue colouring to this camera view.

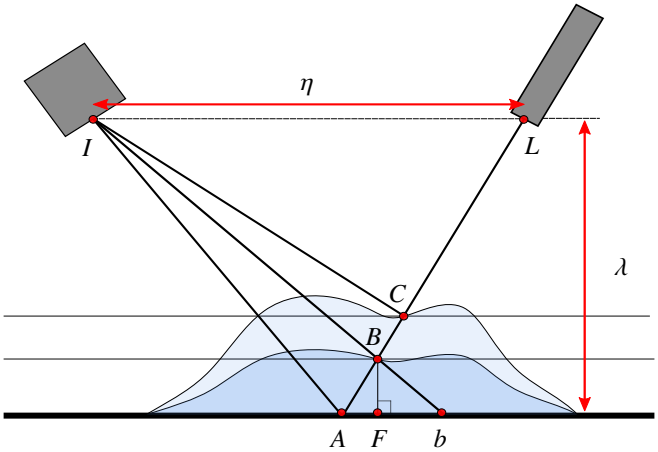

Fig. 9 Relative position of imaging plane (I), projector (P), projector node position at three heights (A,B,C), and equivalent imaging position (b).

$$\frac{\vec{Ab}}{FB} = \frac{\eta}{\lambda - \vec{FB}} \tag{1}$$

$$\vec{FB} = \frac{\frac{\lambda}{\eta}\vec{Ab}}{1+\frac{\vec{Ab}}{\eta}} = \frac{\lambda}{\eta}\vec{Ab} - \frac{\lambda}{\eta^2}\vec{Ab}^2 + \frac{\lambda}{\eta^3}\vec{Ab}^3 - \frac{\lambda}{\eta^4}\vec{Ab}^4 + \ldots \tag{2}$$

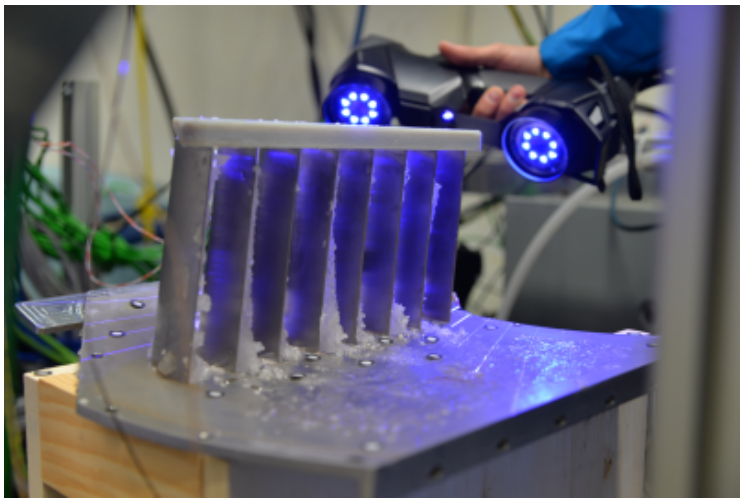

Fig. 10 Scanning of accreted ice using the Creaform HandyScan 7000.

III. Results

The remainder of this paper will discuss the preliminary findings and results from this test campaign. The results will focus on 8 test points from the test matrix, which are detailed in Table 1. The melt ratio values stated were measured on the tunnel centerline, and as mentioned before were upstream of the SND test section. Some conditions had a negative total wet bulb and a melt ratio greater than zero, which for a natural melt tunnel with no supplemental water was initially surprising. The cause of this melt lies in the subtleties of how the tunnel is operated. The 'cold' section of RATFac feeds air and ice into the injection pipe at approximately -20°C, which then mixes with the warmer air in the 'warm' section of RATFac. In the shear layer between the cold stream and warm surroundings the warm air mixes with the cold air, causing the particles to melt in this region. The lensing effect of the inlet bellmouth into the cascade rig causes some of the particles with elevated melt ratio on the edge of the cloud to reach the cloud centerline, hence leading to a non-zero average cloud melt ratio.

Measurements of melt ratio have high levels of uncertainty. It is generally assumed that the recorded values could be up to 0.02 from their true values. Any tests which required matched melt ratios assumed that two values within 0.01 of each-other could be assumed as matched.

Not all tests had matched total water content (ranging between 4.5-6 g/kg), nor did they have equal ice-on durations. Each comparison made in the following analysis had matched masses of injected ice (total water content multiplied by the ice-on duration). The assumption is made that the narrow range in total water content will have insignificant changes on particle-particle interactions and hence the accretion can be temporally scaled.

Effect of Altitude (★,►)

To observe the effects of total pressure, two test cases were studied. Both had the following conditions: $M = 0.4$, $T_0 = 10°C$ and $MR \approx 0.05$, and each had $P_0 = 34.5$ and 49 kPa. These two test cases are labelled as test #'s 2 and 6 in Table 1. The change in pressure could potentially be thought of as a change in altitude or engine operating point. As the engine speed increases the total pressure will rise, but so will the total temperature and Mach number, conversely an increase in altitude (reduction in pressure) will also generally lead to a reduction in temperature. Because the total temperature, Mach number, and humidity were kept constant, they cannot be physically related to an actual change in altitude or engine operating point.

The accretion at the end of each test is shown for the upstream and downstream regions in Figs. 11 and 12 respectively. In both cases the ice initiated on the pressure surface at the intersection of the outer annulus and the trailing edge. At the lower total pressure of 34.5 kPa, the accretion quickly propagated forward up the chord towards the leading edge and also up the span of the blade. The span-wise accretion on the pressure surface was full chord at the outer annulus and tapered off to only the near trailing edge region at the inner annulus. This could be explained by three factors; the location of the ice initiation, the radial TWC profile and the radial PSD profile. The original initiation point was at the pressure surface outer annulus-trailing edge intersection and the ice grew axially and radially outwards from that

Table 1 Aerothermal conditions for each test case. Common symbols under the Alt, Mach, MR and Heaters columns represent the test cases compared for varying Altitude, Mach number, melt ratio and outer annulus heaters, and the TC column symbols show which test cases had the thermocouple traces analysed in this paper. The values of total pressure (P_0) have been rounded to the nearest 0.5 kPa, Mach number to the nearest 0.01, and total temperature (T_0) to the nearest degree. $\dot{Q}$ represents the heat flux into the outer annulus from the heaters

Test #	P_0 [kPa]	M	T_0 [°C]	MR	$T_{wb,0}$ [°C]	$\dot{Q}$ [kW/m^2]	Alt	Mach	MR	Heaters	TC
1	34.5	0.3	10	0.11	0.53	0	★	*			
2	34.5	0.4	10	0.06	-1.64	0	►				
3	34.5	0.4	10	0.12	0.21	0		*			
4	49	0.3	10	0.11	0.64	0	★				
5	49	0.4	10	0.02	0.44	0			•	⌖	χ
6	49	0.4	10	0.05	0.65	0	►		•		
7	49	0.4	10	0.11	1.43	0			•		χ
8	49	0.4	10	0.03	1.23	6.25				⌖	

point. Another factor could have been the reduced TWC at the inner annulus due to the deflector plate. This will have reduced the potential for icing in the inner annulus regions. It could also have been caused by a non-uniform radial particle size distribution. It is thought that the particle deflector plate will have had greater influence on the trajectory of the smaller particles than the larger particles, meaning that there will have been a larger median particle diameter at the inner annulus compared to the outer annulus. The blades had a negative incidence angle relative to the inlet flow, meaning that flow turning was required to reach the pressure surface. The smaller crystals may have had sufficiently small Stokes number that they followed the streamlines and hence impacted onto the pressure surface in the leading edge region, whereas the larger particles will have behaved in a more ballistic nature, meaning that they would be less likely to impinge onto the pressure surface until further along the chord line, hence leading to a greater leading edge accretion at the outer annulus compared to the outer annulus. Unfortunately the PIV system used for particle size distribution measurements recorded measurements in the circumferential plane (shown in Fig. 4), and in order to verify the radial distribution a secondary PIV system would need to be set-up in a plane perpendicular to this.

Once sufficient span-wise accretion had formed, ice then formed on the outer annulus downstream of the blade rows in the wake regions. The wake accretion formed sharp peaks and continued downstream until approximately half the distance from the blade exit and the inflection point of the swan neck duct outer annulus line. Due to the wake accretions initiating after the span accretions, it is thought that sufficient thickening of the wake was required for the particles to have high enough residence time to melt sufficiently and accrete in that region. When the accretion migrated up the chord, it continued past the leading edge into the upstream outer annulus region forming a relatively uniform, thin layer of accretion. Post test, once the ice was turned off and the air flow remained constant, the upstream accretion shed very quickly, often impacting onto downstream outer annulus accretions leading to further shedding.

At the elevated pressure of 49 kPa, initiation also occurred at the outer annulus leading edge intersection. The accretion then similarly progressed up the chord towards the leading edge, however did not initially propagate up the span. At the elevated pressure which had the same Mach number, there was a greater density and dynamic pressure. It is speculated that the increase in drag force on the outer annulus may have led to a reduction in the upstream accretion. Outer annulus wake accretions formed quickly without the requirement of the span-wise pressure surface accretions. Once the accretion reached the leading edge, it propagated upstream on the outer annulus, but had reduced coverage and thickness compared to the lower pressure case. During the test, the downstream wake accretions grew steadily, and ice slowly propagated up the span towards the inner annulus in a uniform thickness along the chord, but with reduced thickness compared to the lower pressure.

Additional pressure comparisons were made at a reduced Mach number of 0.3. These tests had the following conditions; T_0 = 10°C, MR = 0.11, and each at a total pressure of 34.5 and 49 kPa, which corresponds to test #'s 1 and 4 respectively. The end of test accretion in the upstream and downstream outer annulus views are shown in Figs. 13 and 14. At the lower pressure of 34.5 kPa, ice accretion initiated on the pressure surface trailing edge-outer annulus intersection. Instead of then progressing up the chord and span, ice was shed in small amounts along the outer annulus

following the wake paths. Once a stable downstream accretion formed in the wakes, the ice progressed up the chord and span. Thin leading edge accretions then formed, with a slight non-uniform radial growth rate - growing fastest at the outer annulus, slower at the inner annulus. The reduced inner annulus growth rate could have been caused by the radial PSD distribution discussed previously leading to enhanced erosion at the inner annulus, reducing the net growth rate. Once the accretions became sufficiently large, the pressure gradient in the passage bent the leading edge accretion towards the suction surface of the adjacent vane until the accretion and suction surface collided. The large pressure applied to the mid passage blockage (imparted by the oncoming flow), caused the accretion to progressively move down the chord. With further impact of ice crystals, the accretion grew back up the chord until most of the passage was blocked. Looking at the downstream view in Fig. 14 this gave the impression that there was thick pressure surface accretion, however this was caused by the bent leading edge accretion moving downstream through the passage rather than the accretion growing out from the pressure surface. Figure 15 shows a time series of accretion snapshots as the leading edge accretion bent from the pressure surface to the adjacent suction surface. By the end of the test there was full pressure surface span-wise accretion, with most passages blocked. The typical wake accretions on the downstream outer annulus were also present, and accretion was present on the outer annulus upstream of the leading edge. The upstream accretion was growing rapidly after the flow blockages, leading to a premature shut down to prevent the compressor stall due to the reduced mass flow rate through the restricted passages.

At the increased pressure of 49 kPa, accretion also initiated at the pressure surface trailing edge-outer annulus intersection. Accretion then progressed downstream forming the typical wake accretions. Accretion did propagate upstream towards the leading edge, however did not progress upstream of the leading edge, leaving the upstream outer annulus free from accretion. Any accretion which formed in this region quickly shed away before forming a stable accretion. Ice grew partially up the span, up to approximately 20% of the span in some passages but did not progress further up the span.

Table 2 summarises the differences in accretion between the two altitudes. In summary, there was less accretion observed in the upstream outer annulus region and on the pressure surfaces in the higher pressure case compared to the 34.5 kPa. Downstream, similar accretions were observed, with enhanced accretion forming in the regions of the wakes behind each blade. In all cases the ice initiated on the pressure surface at the intersection of the trailing edge and the outer annulus.

Table 2 Comparison of accretions at 34.5 and 49 kPa (test #'s 1,2 & 4,6).

	34.5 kPa	49 kPa
Upstream of leading edge outer annulus	Stable accretion	Reduced accretion
Pressure surface spanwise accretion	Full span accretion	Reduced accretion
Downstream of trailing edge outer annulus	Localised wake accretions	Localised wake accretions

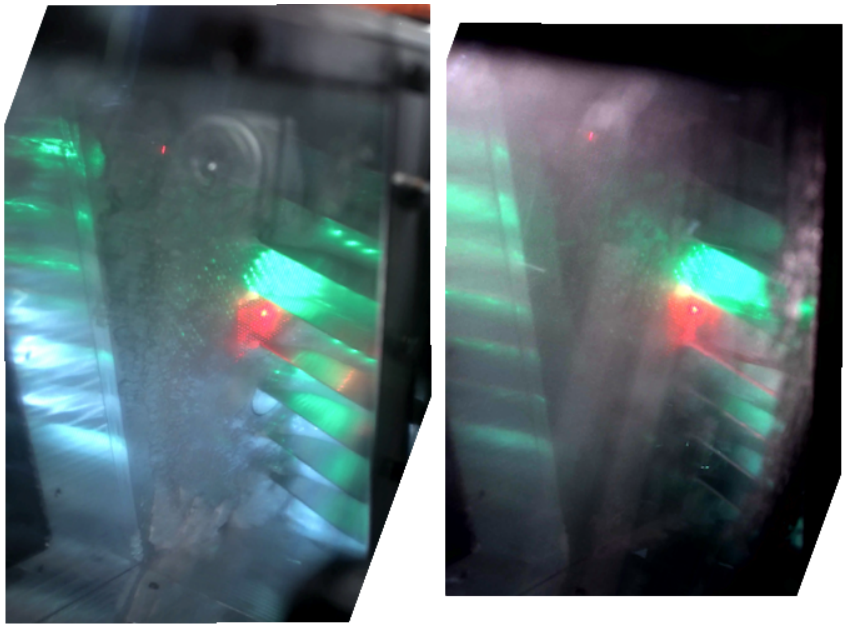

Fig. 11 Upstream camera views at 34.5 kPa (left) and 49 kPa (right). Conditions: T_0 = 10°C, MR = 6‰, Mach = 0.4. Conditions relate to test #'s 2 and 6.

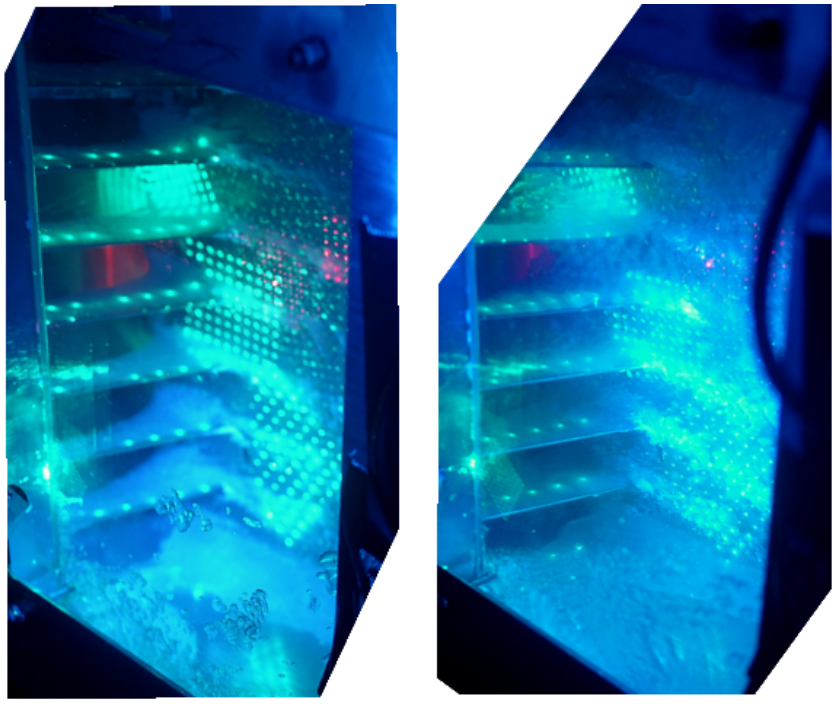

Fig. 12 Downstream camera views at 34.5 kPa (left) and 49 kPa (right). Conditions: T_0 = 10°C, MR = 6‰, Mach = 0.4. Conditions relate to test #'s 2 and 6.

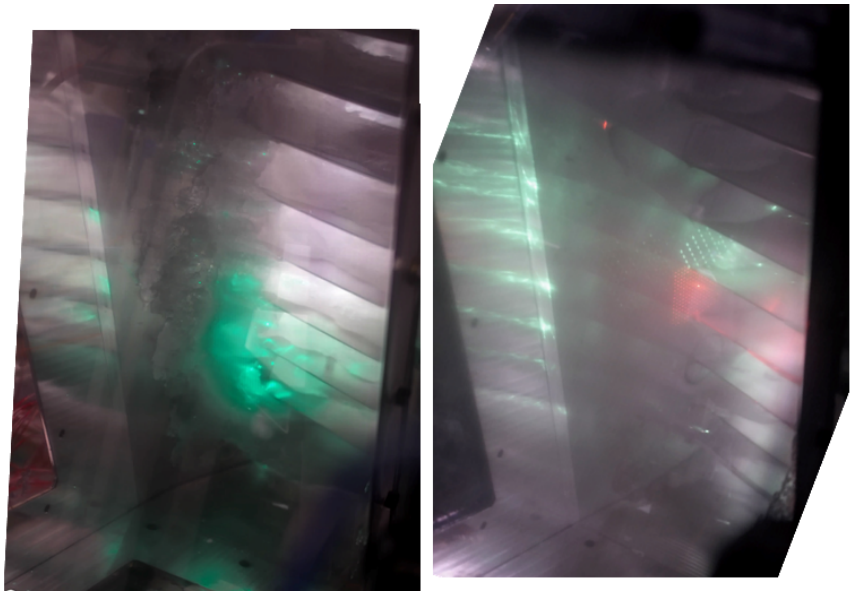

Fig. 13 Upstream camera views at 34.5 kPa (left) and 49 kPa (right). Conditions: T_0 = 10°C, MR = 11%, Mach = 0.3. Conditions relate to test #'s 1 and 4.

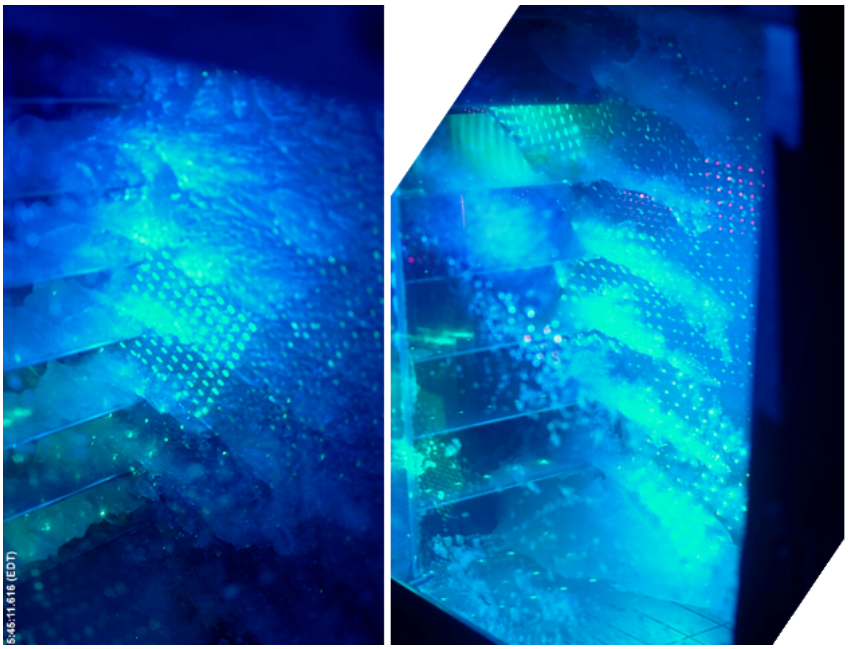

Fig. 14 Downstream camera views at 34.5 kPa (left) and 49 kPa (right). Conditions: T_0 = 10°C, MR = 11%, Mach = 0.3. Conditions relate to test #'s 1 and 4.

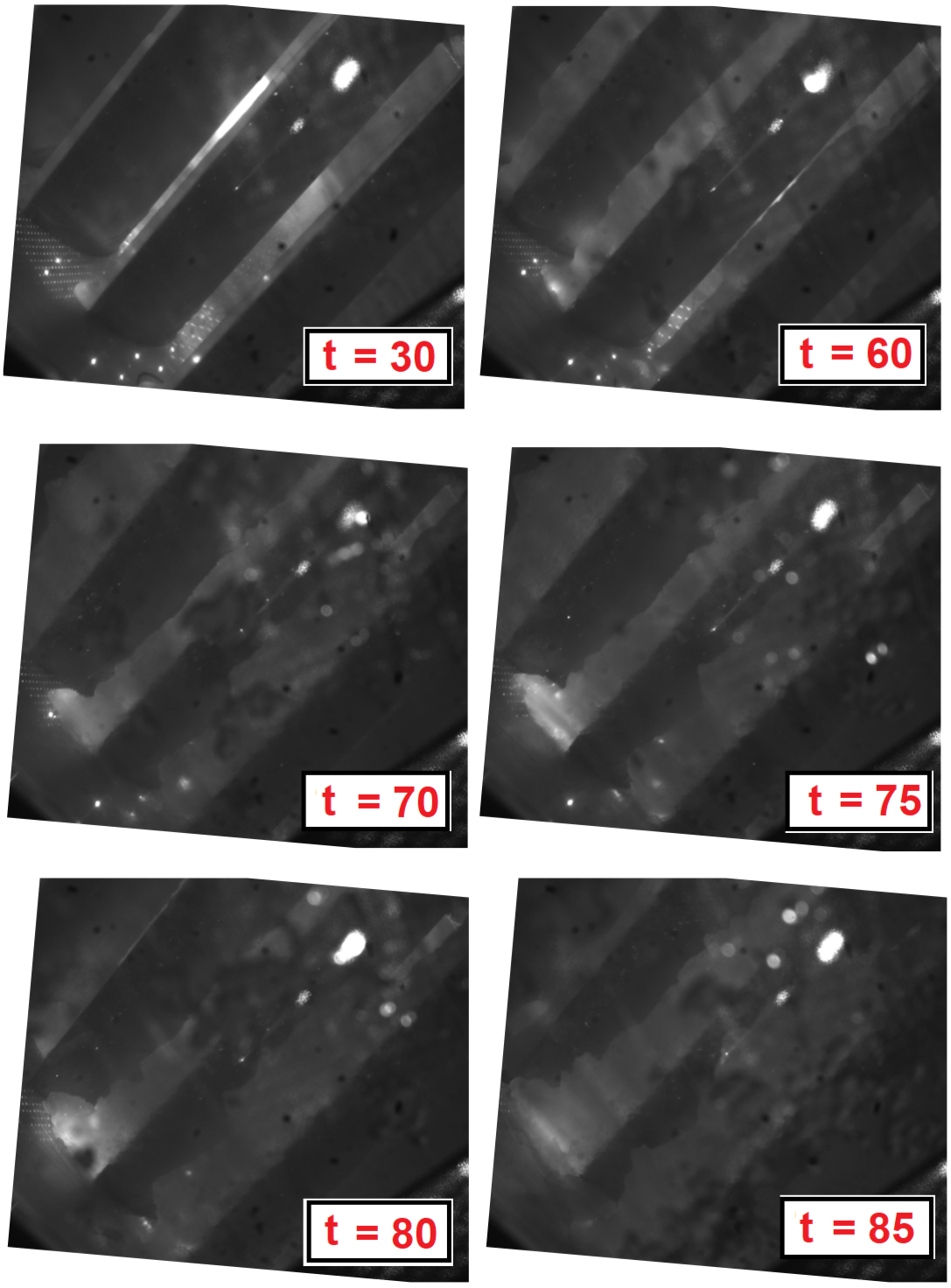

Fig. 15 Leading edge camera view at 34.5 kPa (test # 1). Time series of snapshots of accretion whilst the leading edge accretion bent towards the adjacent suction surface. Time shown in seconds. Conditions: T_0 = 10°C, MR = 11%, Mach = 0.3.

Effect of Mach Number (∗)

To observe the effects of Mach number, another test at the 34.5 kPa pressure was conducted at a Mach number of 0.4 (test # 3), to directly compare to test # 1. The final accretions on the outer annulus upstream and downstream views are shown in Figs. 16 and 17. As previously reported, in test # 1 the accretion initiated at the pressure surface trailing edge-outer annulus intersection, growing wake accretions before leading edge accretions formed. A small radial distribution in leading edge accretion was observed, before the whole accretion bent towards the adjacent suction surface.

Figure 16 shows the accretion formed at the time that the passages blocked in the Mach 0.3 case. At the increased Mach number of 0.4, the non-uniform radial accretion on the leading edge was more pronounced, with much larger accretions being formed at the leading edge-outer annulus intersection and reduced accretion towards the inner annulus. Figure 18 shows the accretion on the leading edges after 30 seconds of ice injection. In both cases enhanced accretion formed on the outer annulus intersection, but the radial taper was more dominant at the Mach 0.4 condition. It is well known that the erosional effect increases with particle kinetic energy [3, 4, 21] which further suggests that the radial distribution in accretion may have been caused by the larger particles at the inner annulus. Part of the radial accretion thickness variation will have been caused by the radial TWC profile. However, because the TWC profile will have been similar in both the Mach 0.3 and Mach 0.4 cases, this effect seems to be insignificant compared to the erosion. Due to the tapered leading edge accretion, the passage pressure gradient was applied to a smaller area, and hence a reduced bending moment was applied to the accretion compared to the Mach 0.4 case. This meant that the adhesion of the inner annulus accretion to the outer annulus was sufficiently strong for the accretion to not bend towards the adjacent suction surface.

Enhanced accretion was also observed on the outer annulus upstream region at the higher Mach number, possibly caused by the increased particle Stoke's numbers causing them to act more balistically and impact onto the outer annulus rather than following the streamline curvature, and due the relatively small PSD at the inner annulus the erosional effect will have been low. Downstream of the blade row, similar maximum accretion thickness's were observed in the wake regions at both conditions, however the accretion at the lower Mach number was thicker between the wakes, creating a more uniform accretion on the outer annulus. The reduced variance in outer annulus accretion in the between the wake and non-wake regions was not observed in other cases at the lower Mach number, so no conclusions could be drawn on the effect of Mach number on the outer annulus downstream regions. In the early stages of accretion prior to the leading edge accretion bending at the lower Mach number, both conditions had similar accretion on the pressure surfaces.

Table 3 compares the main differences observed between the high and low Mach number cases.

Table 3 Comparison of accretions at Mach 0.3 and 0.4 (test #'s 1 and 3).

	Mach 0.3	Mach 0.4
Upstream of leading edge outer annulus	Smaller accretion	Enhanced accretion
Pressure surface spanwise accretion	Similar limited accretion	Similar limited accretion
Downstream of trailing edge outer annulus	Localised wake accretions	Localised wake accretions
Leading edge accretion	Slight radial variance	Large accretion at outer annulus, thin at inner annulus

Effect of MR (•)

Three tests were conducted at constant altitude, Mach number and total temperature, with varying relative humidity to induce melt ratios of 2, 5 and 11%. These tests had the following conditions; P_0 = 49 kPa, M = 0.4, T_0 = 10°C, which corresponds to test #'s 5,6,7. Figures 19 and 20 show the final accretion upstream and downstream accretions. Bucknell *et al.* [3] produced a model of net sticking probability a a function of melt ratio. The peak sticking probability occurred at around 11%, with reduced sticking probability at melt ratios higher and lower than this value. The results of the melt ratio tests agreed with this model with an increasing level of icing severity in all regions with increasing melt ratio, with the highest melt ratio tested coinciding with the value of maximum sticking probability. This is summarised in Table 4.

To aid the quantification of icing severity at each melt ratio, ice thickness measurements were taken using both the DIP system, and also the Creaform HandyScan device. As mentioned previously, the HandyScan device was not able to

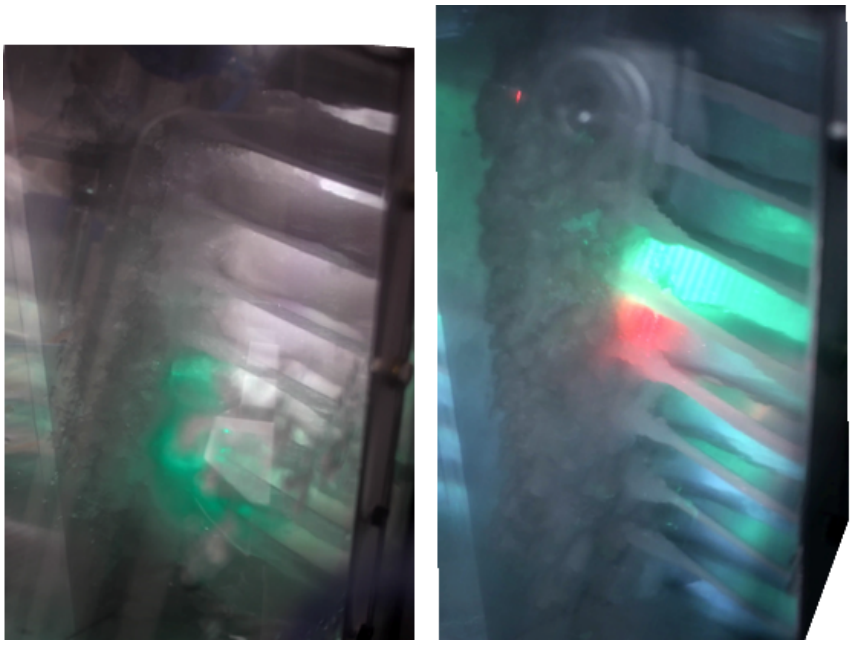

Fig. 16 Upstream camera views at Mach 0.3 (left) and Mach 0.4 (right). Conditions: T_0 = 10°C, MR = 11%, P_0 = 34.5 kPa. Conditions relate to test #'s 1 and 3.

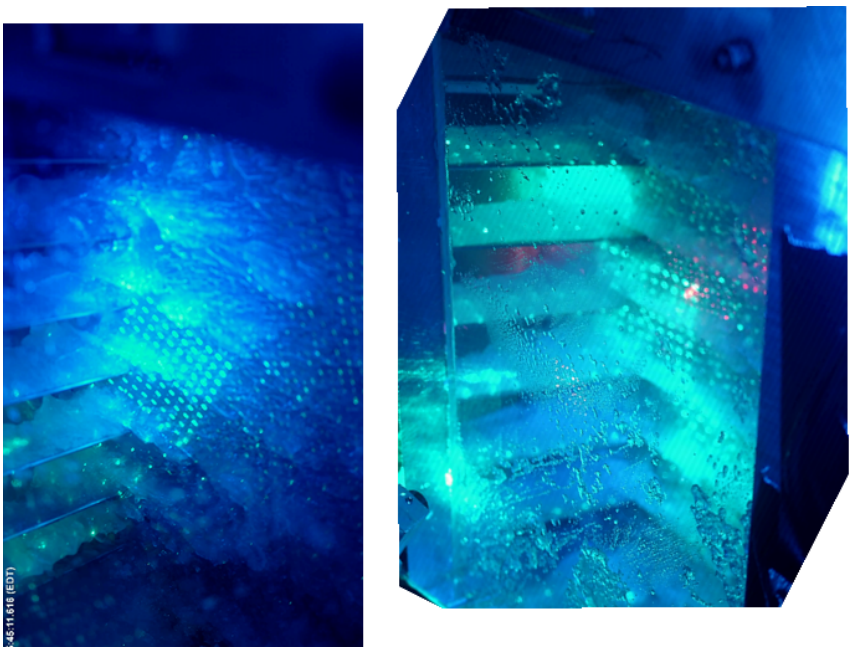

Fig. 17 Downstream camera views at Mach 0.3 (left) and Mach 0.4 (right). Conditions: T_0 = 10°C, MR = 11%, P_0 = 34.5 kPa. Conditions relate to test #'s 1 and 3.

record accretion sizes during the test, and required a tunnel shut-down to atmospheric pressure, and a rapid cooling of the ice. The tunnel shut-down in RATFac takes approximately 10 minutes, and during this period shedding events occurred. Figure 21 shows the downstream outer annulus accretion immediately after ice-off and post shut-down. It can be seen that large sections of accretion had shed off the test piece, notably on the side walls and the pressure surfaces, while the majority of the outer annulus accretion remained intact. The upstream outer annulus accretion also fully shed

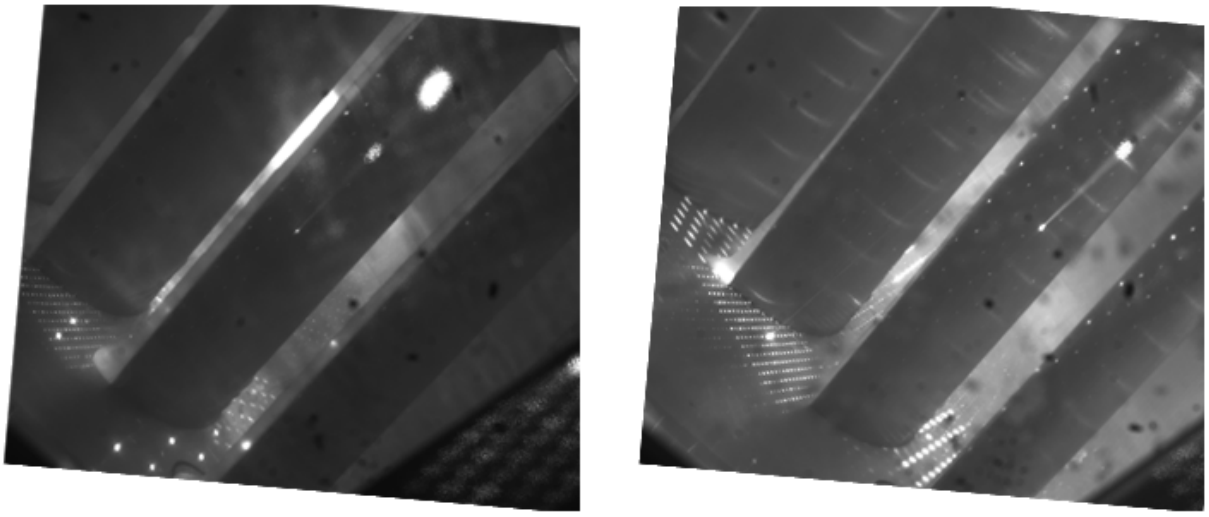

Fig. 18 Leading edge camera view at Mach 0.3 (left) and Mach 0.4 (right). Conditions: T_0 = 10°C, MR = 11%, P_0 = 34.5 kPa. Conditions relate to test #'s 1 and 3.

during the shut-down process. This meant that the data collected from the HandyScan device cannot be taken as true measurements of the accreted ice on the pressure surfaces, side walls and upstream outer annulus regions. Due to the low levels of shedding and evaporation/sublimation on the downstream outer annulus during the shut-down, the data in this region is assumed to be true of the original accreted ice. The green square in Fig. 21 shows the region analysed by the DIP system.

The results of both datasets are shown in as an isometric view and top down view in Figs. 22 and 23, where the accretion thickness has been normalised by the axial chord of the stator blades. This data further shows overall, that the accretion was larger with increasing melt ratio in the conditions studied. Good agreement was observed between the Creaform HandyScan data and the DIP data. The Creaform device has not officially been validated for measuring ice crystal icing accretion thicknesses but is regarded as being an accurate measuring device. The data shows self-similarities between the two datasets, which even though it cannot be used as a validation of the DIP system, suggests that it captures the correct trends.

The ability to capture quantitative data is critical for validating ice crystal icing codes in complex environments, especially in three-dimensional models. This data shows that the DIP method is capable of gathering this data, and once it is suitably validated it will be used extensively in future tests for numerical validation of complex accretion geometries.

Table 4 Comparison of accretions at melt ratio's 2% and 11% (test #'s 5 and 7).

	2% MR	11% MR
Upstream of leading edge outer annulus	Smaller accretion	Enhanced accretion
Pressure surface spanwise accretion	Smaller accretion	Enhanced accretion
Downstream of trailing edge outer annulus	Smaller accretion	Enhanced accretion
Leading edge accretion	Smaller accretion	Enhanced accretion

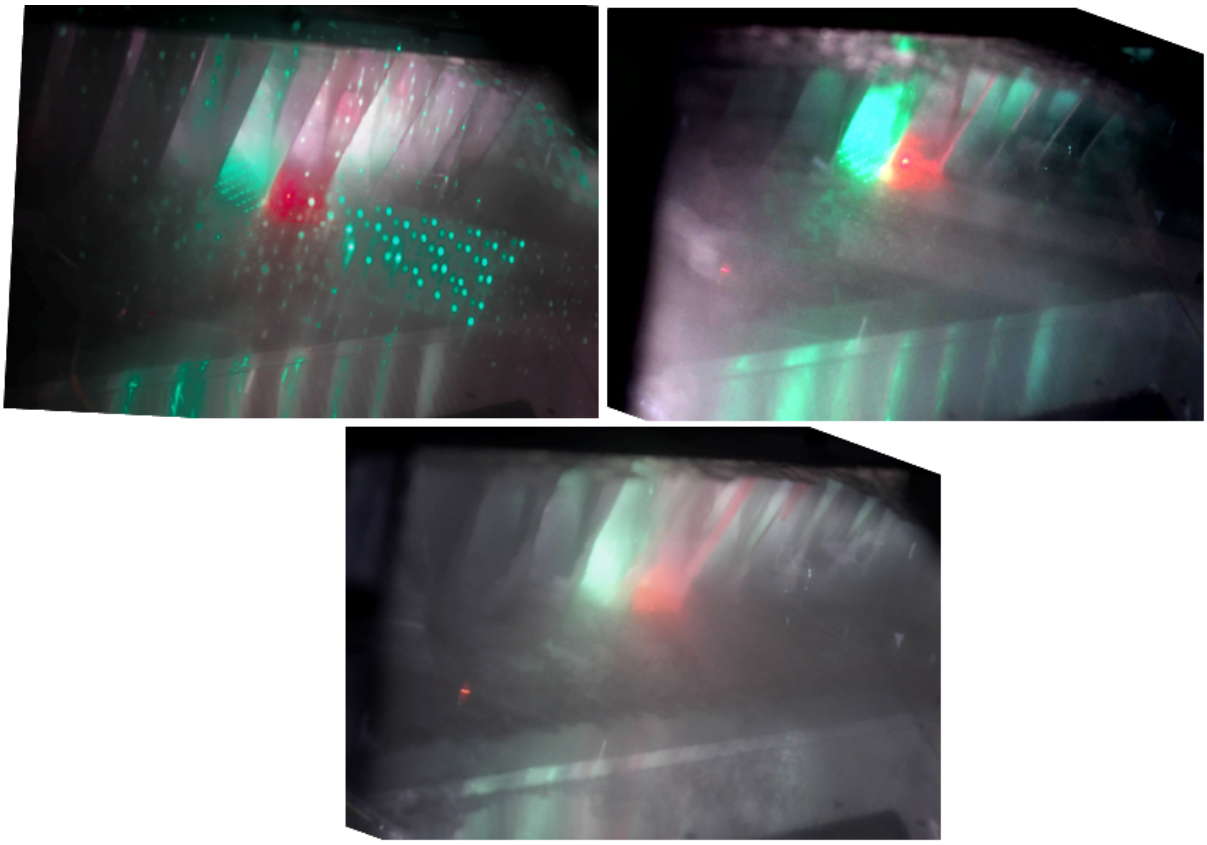

Fig. 19 Upstream camera view at melt ratio of 2% (left), 5% (mid), 11% (right). Conditions: T_0=10°C, MR = 6%, Mach = 0.4. Conditions relate to test #'s 5, 6 and 7.

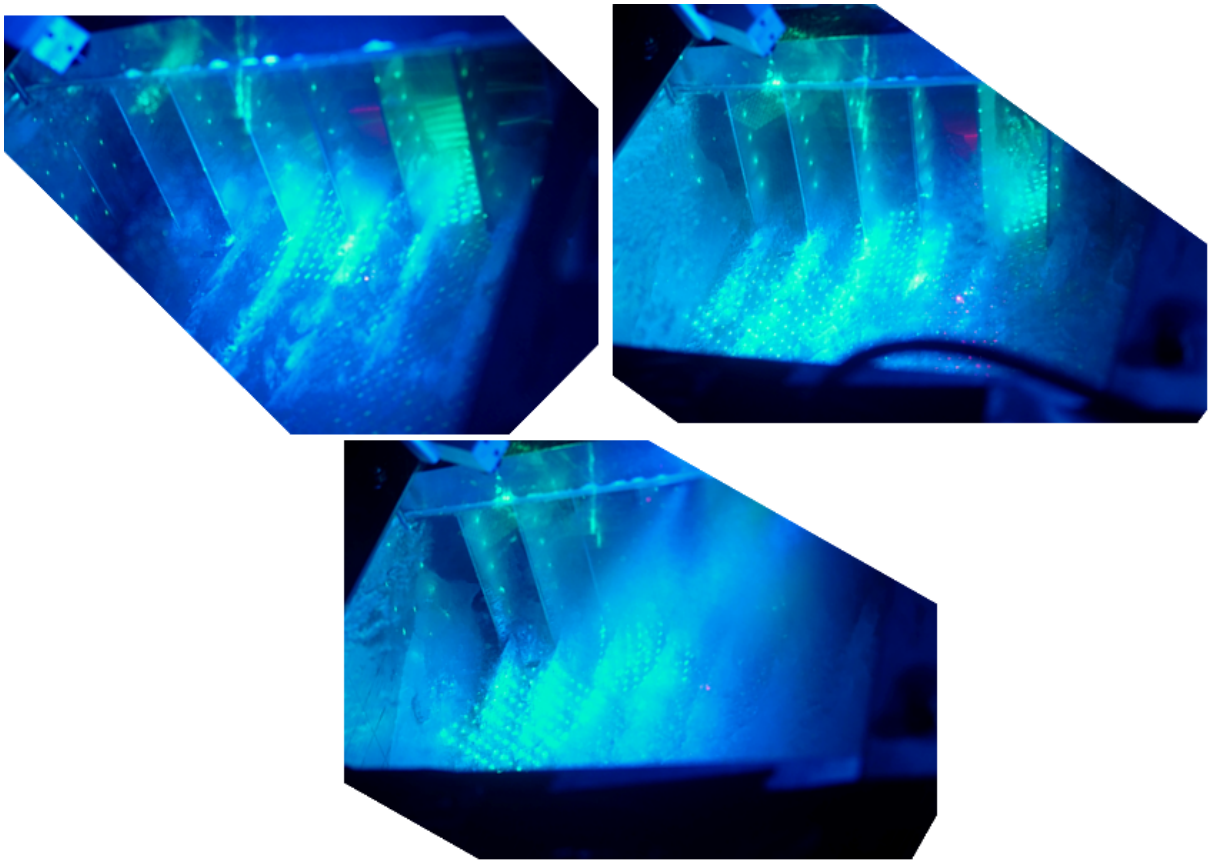

Fig. 20 Downstream camera view at melt ratio of 2% (left), 5% (mid), 11% (right). Conditions: T_0=10°C, MR = 6%, Mach = 0.4. Conditions relate to test #'s 5, 6 and 7.

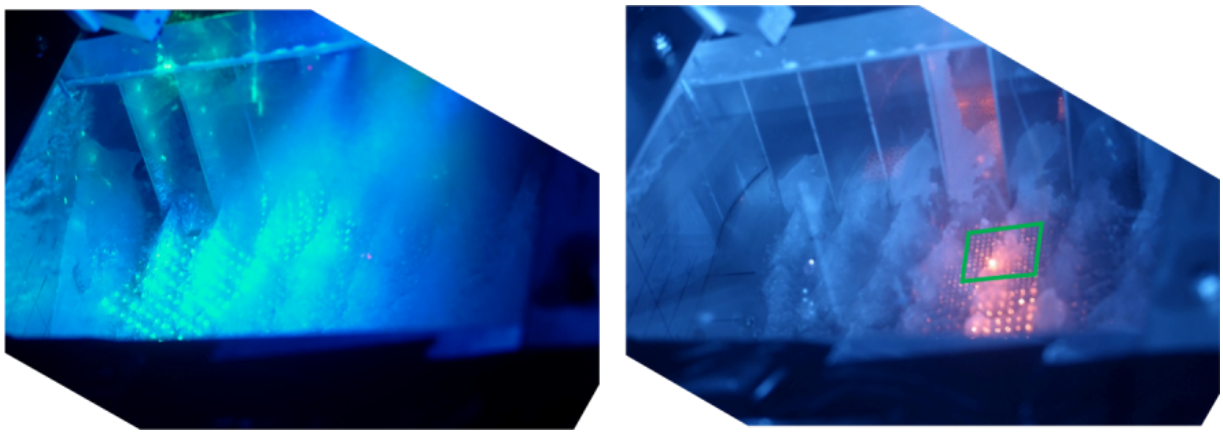

Fig. 21 Downstream camera view at melt ratio of 11%, post ice off (left) and post tunnel shut-down (right). Conditions: T_0=10°C, MR = 6%, Mach = 0.4. Conditions relate to test # 7.

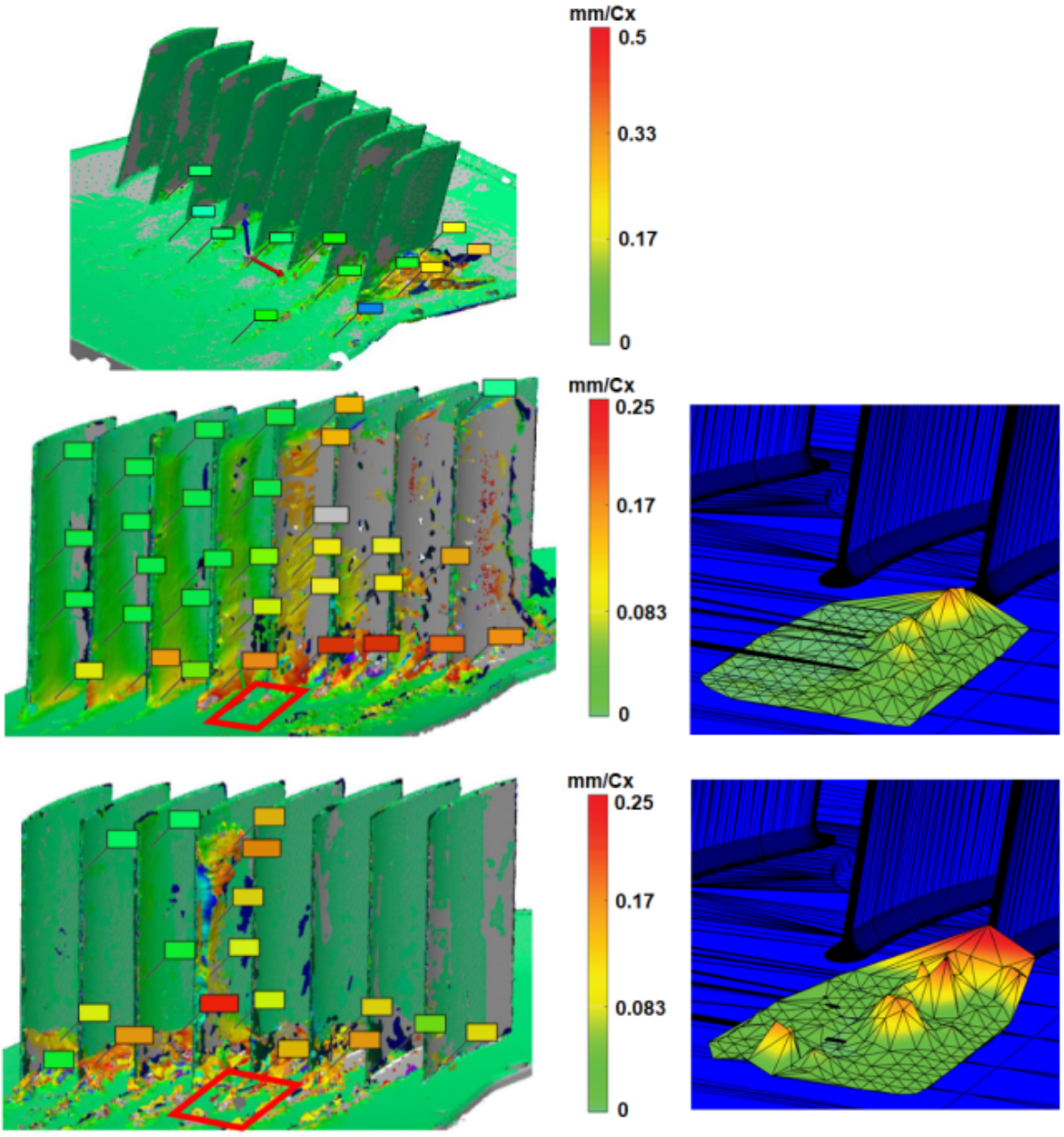

Fig. 22 Isometric view of downstream ice thickness measurements from the Creaform HandyScan (left) and DIP system (right), at melt ratios of 2% (top), 5% (mid), 11% (bottom). Conditions: T_0=10°C, MR = 6%, Mach = 0.4. Note the different colourbar scale shown on the 2% melt ratio data. Conditions relate to test #'s 5, 6 and 7.

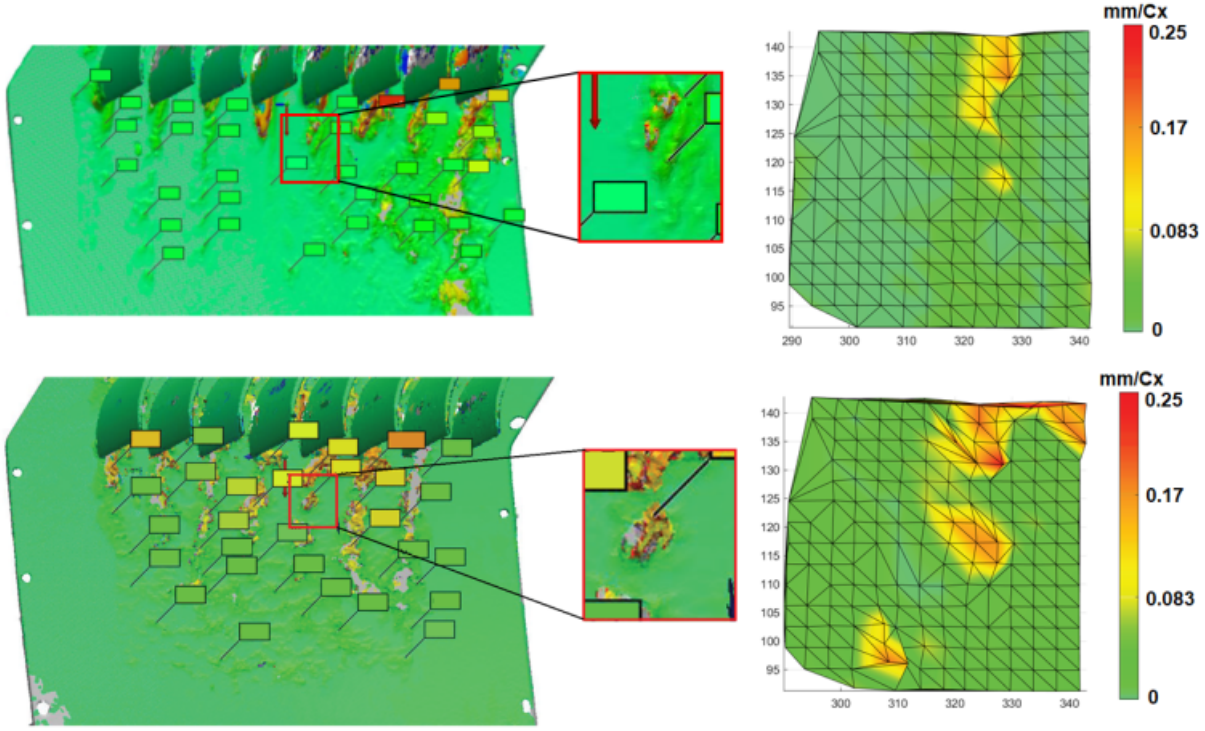

Fig. 23 Top down view of downstream ice thickness measurements from the Creaform HandyScan (left) and DIP system (right), at melt ratios of 5% (top), 11% (bottom). Conditions: T_0=10°C, MR = 6%, Mach = 0.4. Conditions relate to test #'s 6 and 7.

Thermocouples were distributed on the outer annulus, in the locations shown in Fig. 5. The data recorded from these thermocouples is shown in Fig. 24. The data is shown for test #'s 5 and 7 (P_0 = 49 kPa, M = 0.4, T_0 = 10°C), where the melt ratio of 2% is shown on the left and 11% is shown on the right. The black vertical lines show when the ice flow was turned on/off. At the reduced melt ratio, where there was limited accretion on the upstream outer annulus, TC1 recorded a slower decay in temperature. This was expected due to rebounding particles having decrease heat transfer compared to sticking particles. Similar patterns were recorded downstream with thermocouples 7 and 8.

At the increased melt ratio, the enhanced accretion in the outer annulus upstream region caused thermocouple 1 to record a much greater decay in temperature. Downstream, thermocouple 7 also decayed faster, implying that the accretion on the downstream outer annulus extended beyond the inflection point, but not sufficiently far downstream to thermocouple 8. It can be seen that both the total temperature and outer annulus thermocouple readings were at a lower temperature prior to test. In the steady state measurements prior to starting the test, both cases had a total temperature in the region 9.5< T_0 <10.5°C, however in the duration between the steady state scan and the start of test, the higher melt ratio case had drifted down to 9.1°C. It is known that tunnel conditions within RATFac temporally drift, but this further confirms the need to check the conditions in both the steady state scan and during the transient test. It can also be seen that the temperature on the outer annulus is significantly lower than at the lower melt ratio. Because the total temperature and Mach number was the same inside the tunnel and the ambient temperature outside the tunnel was constant, this suggests that the higher melt ratio case had not thermally recovered from the previous icing test. Because of the high rate of decrease in temperature once ice was turned on, both cases reached the steady ice-on temperature in a similar duration in the regions of accretion. This implies that the slightly lower initial temperature will have had only a small effect on the formed accretion. This analysis made the assumption that the lateral heat conduction will have been insignificant compared to the conduction in the direction normal to the surface, meaning that each spatial position where there was a thermocouple could be treated as independent.

While this does not provide much quantitative data, it does give insight into regions where accretion may have occurred. This may be especially useful in regions where optical access is not possible for viewing the ice.

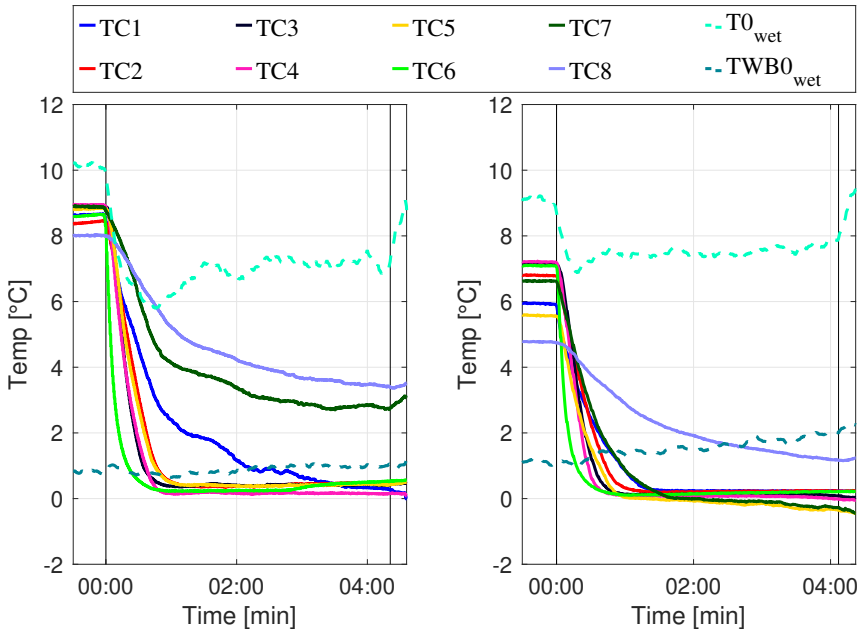

Fig. 24 Thermocouple data at MR = 2% (left) and MR = 11% (right) (test #'s 5 and 7). Conditions: P_0 = 49 kPa, M = 0.4, T_0 = 10°C. Conditions relate to test #'s 5 and 7.

Effect of Outer Annulus Heaters (⌖)

To determine the effect on a positive heat flux through the outer annulus, tests were conducted at constant aero-thermal conditions but with a zero and positive heat flux. A constant 25V was applied to each heater, which produced a constant heat flux of 6.25 W/m^2. These tests were at the following conditions; P_0 = 49 kPa, M = 0.4, T_0 = 10°C and $MR \approx 3\%$.

The test numbers without and with heat flux are 5 and 8. Without the heaters, the ice formation grew in the typical manor seen previously. With the heaters very different ice formations were created on the outer annulus. The initiation was the same as the other tests - on the pressure surface trailing edge-outer annulus intersection, however any ice which propagated downstream into the wake region shed away immediately, preventing any accretion in this region. The camber of the blade prevented the initial ice from shedding, and these ice zones progressively grew in size. Once sufficiently large, the ice on some of the blades then progressed downstream, but into regions between the blade wakes rather than in the wakes. With successive growth, these passage accretion grew to a large size - considerably thicker than the wake accretions typically seen without the heaters applied. The passage accretions also grew up the chord, and in some passages grew past the leading edge into the upstream outer annulus region. The final accretion for test #'s 5 and 8 (without and with heaters) is shown in Figs. 25 and 26, and the observations of the accretion is shown in Table 5.

Other cases with a higher melt ratio (6 and 8%) seemed to be less effected by the heaters, and produced accretions much more similar accretions to what was observed without the heaters applied.

When the heaters were not applied, if large accretions formed they typically had strong bonding to the test piece and took a long time to shed at the end of the test (even with increased humidity and positive outer annulus heat flux). With the heaters on, none of the accretion had strong adhesion to the test piece, and soon after the ice was turned off large sections of ice shed from the test piece. Once of the greatest impacts of ice crystal icing in jet engines is the damage caused by large sections of accreted ice shedding and impacting onto a downstream component. These results suggest that the likelihood of this happening is increased with the application of heat to the outer annulus of the swan neck duct.

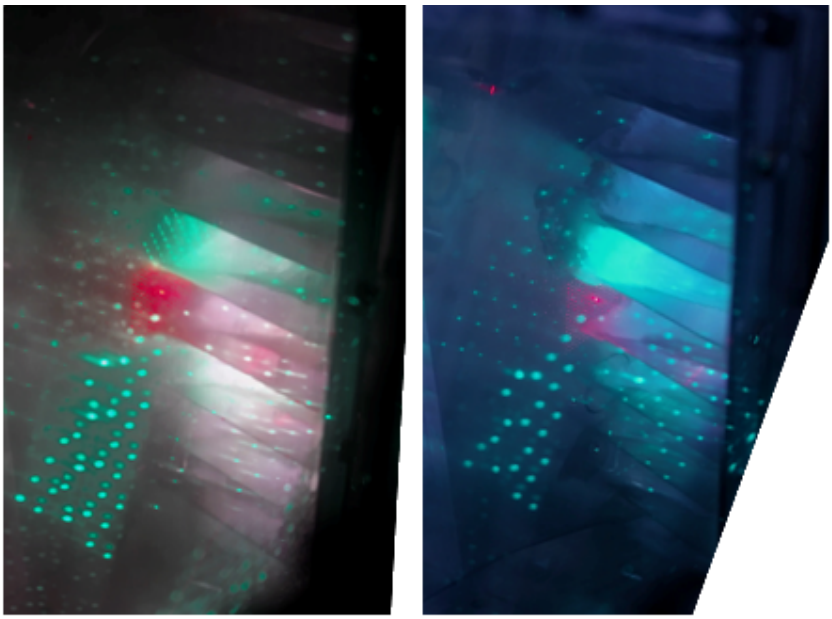

Fig. 25 Upstream camera view without (left) and with (right) outer annulus heat flux. Conditions: T_0 = 10°C, MR ≈ 3%, M = 0.4. Conditions relate to test #'s 5 and 8.

Table 5 Comparison of accretions at with and without outer annulus heaters (test #'s 5 and 8).

	No heaters	With heaters
Upstream of leading edge outer annulus	Similar Accretion	Similar Accretion
Pressure surface spanwise accretion	Similar Accretion	Similar Accretion
Downstream of trailing edge outer annulus	Localised wake accretion	Large accretions in flow path regions

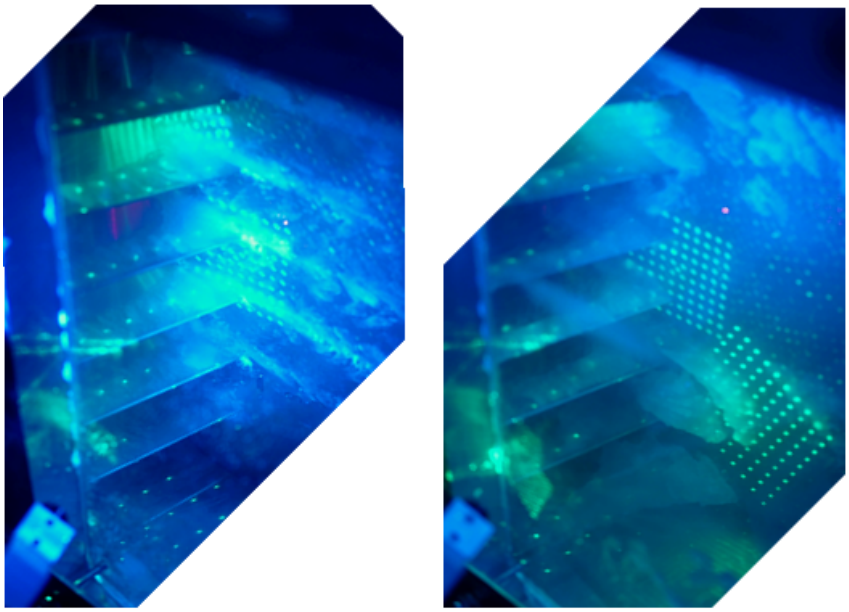

Fig. 26 Downstream camera view without (left) and with (right) outer annulus heat flux. Conditions: T_0 = 10°C, MR ≈ 3%, M = 0.4. Conditions relate to test #'s 5 and 8.

Conclusion

This work has provided the initial results of an experimental campaign studying the ice crystal accretion in a complex three-dimensional engine realistic geometry. It is believed to be the first study involving the streamline curvature imparted by the blade camber, outer annulus radius and blade lean. It was found that in the conditions studied that there were common features in the accretion, notably the peaks of accretion on the outer annulus in the wakes downstream of the blade row. The location of accretion initiation in most conditions occurred at the intersection of the pressure surface trailing edge and the outer annulus. By varying the total pressure the location of accretion changed, with less pressure surface accretion occurring at the higher total pressure of 49 kPa compared to the lower total pressure of 34.5 kPa. The outer annulus upstream of the blade row also had reduced accretion at the higher total pressure. By increasing the Mach number from 0.3 to 0.4, a more significant variation in leading edge accretion occurred, with less accretion occurring at the inner annulus compared to the outer annulus. It is thought that this occurred due to the particle deflector plate biassing a smaller particles to the outer annulus while the larger particles remaining near the inner annulus, hence increasing the erosion on the inner annulus. Future tests involving a radial particle deflector plate should consider an additional particle size distribution measurement plane in the radial direction to confirm this theory (current RATFac measurements are only taken in the circumferential plane). By varying the melt ratio from 2% to 11% an increase in accretion occurred, matching with the sticking probability distribution predicted by Bucknell *et al.* These observations were made using videos recorded using conventional cameras. Additional data was also gathered using two measurement systems; DIP (developed by the University of Oxford) and also using the commercial Creaform Handyscanner. The Handyscanner could only be used once the tunnel was turned off but obtained data over the whole test piece surface, producing a full 3D dataset on the formed accretion. The DIP system also operates during the accretion, allowing for transient data to be gathered. Quantitative ice thickness measurements of the outer annulus have not been possible in previous studies due to the side walls obstructing backlit measurements. The DIP methodology can be applied to a wide range locations, which would not have been possible with traditional measuring techniques. The data collected at the end of the test was compared to the Handyscanner data and good agreement was observed. Collection of 3D accretion profiles will be necessary for validation of ice crystal icing numerical codes in complex test pieces such as engine geometries, and it is hoped with further development that the DIP technology can provide the required data.

In the experiments three-dimensional effects were observed. One condition (test #1) saw the leading edge accretions being bent into the adjacent suction surfaces - blocking the flow path of that passage. This had knock on effects, significantly changing the adjacent flow field and undoubtedly altering the future accretion. For this complex accretion to be numerically predicted the following will need to be implemented; full three-dimensional particle tracking, finite

element analysis of the accretion based on the applied aerodynamic forces and adhesion to local surfaces (predicting bending and/or shedding) and finally a coupled flow solution based on the predicted accretion profile.

The full dataset from this test campaign could not be presented in this one paper. Future publications will explore the data in more detail, especially concerning accretion growth rates from the DIP data and high speed video analysis of the accretion shedding.

Acknowledgement

The authors would like to thank efforts of Marcus Smith, Carol Rance and Rory Clarkson of the EEP team at Rolls-Royce. We would also like to thank the efforts of Scitech, Roke and GKN in support of the tests. The helpful staff of Formaplex, 3D Hub, Getting It Made and our internal Oxford Engineering workshops (with special thanks to David O'Dell) in producing the complex test piece. The staff of the NRC in scoping and conducting the tests, with a very special thanks for Martin Neuteboom.

References

[1] Bucknell, A., McGilvray, M., Gillespie, D. R., Jones, G., Reed, A., and Buttsworth, D. R., "Heat transfer in the core compressor under ice crystal icing conditions," *Journal of Engineering for Gas Turbines Power*, Vol. Vol. 140, No. No. 7, 2018, pp. 1–15. https://doi.org/10.1115/GT2017-63077.

[2] Struk, P. M., Bartkus, T., Tsao, J.-C., Currie, T., and Fuleki, D. M., "Ice Accretion Measurements on an Airfoil and Wedge in Mixed-Phase Conditions," *SAE 2015 International Conference on Icing of Aircraft, Engines, and Structures*, , No. Figure 2, 2015. https://doi.org/10.4271/2015-01-2116, URL http://papers.sae.org/2015-01-2116/.

[3] Bucknell, A., Mcgilvray, M., Gillespie, D. R. H., Jones, G., and Reed, A., "Experimental Studies of Ice Crystal Accretion on an Axisymmetric Body at Engine-Realistic Conditions," *2018 Atmospheric and Space Environments Conference, AIAA AVIATION Forum, (AIAA 2018-4223)*, 2018.

[4] Currie, T. C., Fuleki, D., and Mahallati, A., "Experimental studies of mixed-phase sticking efficiency for ice crystal accretion in jet engines," *Transactions of Japanese Society for Medical and Biological Engineering*, Vol. 51, No. SUPPL., 2013, pp. 1–26. https://doi.org/10.2514/6.2014-3049.

[5] Currie, T., Struk, P., Tsao, J.-C., Fuleki, D., and Knezevici, D., "Fundamental Study of Mixed-Phase Icing with Application to Ice Crystal Accretion in Aircraft Jet Engines," *4th AIAA Atmospheric and Space Environments Conference*, 2012. https://doi.org/10.2514/6.2012-3035.

[6] Struk, P. M., King, M. C., Bartkus, T. P., Tsao, J.-C., Fuleki, D., Neuteboom, M., and Chalmers, J., "Ice Crystal Icing Physics Study using a NACA 0012 Airfoil at the National Research Council of Canada's Research Altitude Test Facility," *2018 Atmospheric and Space Environments Conference*, 2018. https://doi.org/10.2514/6.2018-4224, URL https://arc.aiaa.org/doi/10.2514/6.2018-4224.

[7] Bucknell, A., Mcgilvray, M., Gillespie, D. R. H., Jones, G., and Collier, B., "Experimental Study and Analysis of Ice Crystal Accretion on a Gas Turbine Compressor Stator Vane," *Submitt. SAE Int. Conf. Icing Aircraft, Engines Struct. June 17-21, Minneapolis, MN, USA, 2019.*, 2019. https://doi.org/10.4271/2019-01-1927.

[8] Wright, W., Jorgenson, P., and Veres, J., "Mixed Phase Modeling in GlennICE with Application to Engine Icing," *AIAA Atmospheric and Space Environments Conference*, 2010. https://doi.org/10.2514/6.2010-7674.

[9] Trontin, P., Blanchard, G., Kontogiannis, A., and Villedieu, P., "Description and assessment of the new ONERA 2D icing suite IGLOO2D," *9th AIAA Atmospheric and Space Environments Conference, AIAA AVIATION Forum, (AIAA 2017-3417)*, 2017. https://doi.org/10.2514/6.2017-3417, URL http://dx.doi.org/10.2514/6.2017-3417.

[10] Bucknell, A., McGilvray, M., Gillespie, D., Yang, X., Jones, G., and Collier, B., "ICICLE: A Model for Glaciated & Mixed Phase Icing for Application to Aircraft Engines," *SAE Technical Paper Series*, Vol. 1, 2019, pp. 1–19. https://doi.org/10.4271/2019-01-1969.

[11] Oliver, M., "Ice Crystal Icing Engine Testing in the NASA Glenn Research Center's Propulsion Systems Laboratory: Altitude Investigation," *SAE International Journal of Aerospace*, Vol. 8, No. 1, 2015, pp. 33–37. https://doi.org/10.4271/2015-01-2156.

[12] Mason, J. G., Chow, P., and Fuleki, D. M., "Understanding Ice Crystal Accretion and Shedding Phenomenon in Jet Engines Using a Rig Test," *Journal of Engineering for Gas Turbines and Power*, 2011. https://doi.org/10.1115/1.4002020.

[13] Knezevici, D. C., Fuleki, D., Currie, T. C., Galeote, B., Chalmers, J., and Macleod, J., "Particle Size Effects on Ice Crystal Accretion – Part II," 2013. https://doi.org/10.2514/6.2013-2676, URL http://arc.aiaa.org.

[14] Knezevici, D. C., Fuleki, D., and MacLeod, J., "Development and Commissioning of a Linear Compressor Cascade Rig for Ice Crystal Research," 2011. https://doi.org/10.4271/2011-38-0079, URL http://papers.sae.org/2011-38-0079/.

[15] Fuleki, D., Neuteboom, M., and Chalmers, J., "Ice Crystal Icing Test Design and Execution for the ALF502 Vane Segment in the NRC RATFac Cascade Rig," *SAE Technical Papers*, Vol. 2019-June, No. June, 2019. https://doi.org/10.4271/2019-01-1925.

[16] Galeote, B., "Ice crystal particle measurement using shadowgraph imaging techniques," *AIAA Atmospheric and Space Environments Conference 2010*, , No. August, 2010, pp. 1–11. https://doi.org/10.2514/6.2010-7531.

[17] Fuleki, D., Chalmers, J. L., and Galeote, B., "Technique for Ice Crystal Particle Size Measurements and Results for the National Research Council of Canada Altitude Ice Crystal Test System," *SAE Technical Papers*, Vol. 2015-June, No. June, 2015. https://doi.org/10.4271/2015-01-2125.

[18] Struk, P. M., Bartkus, T. P., Bencic, T. J., King, M. C., Ratvasky, T. P., Zante, J. F. V., and Tsao, J.-C., "An Initial Study of the Fundamentals of Ice Crystal Icing Physics in the NASA Propulsion Systems Laboratory," *Principle Research Scientist, Icing Branch Brookpark Road*, Vol. 7, 2100, pp. 11–2. https://doi.org/10.2514/6.2017-4242, URL http://arc.aiaa.org.

[19] Connolly, J., Mcgilvray, M., Gillespie, D. R., Jones, G., and Collier, B., "Digital Image Projection for 3D Ice Crystal Icing Accretion Measurements," *AIAA Atmospheric and Space Environments Conference 2020*, 2020, pp. 1–16.

[20] "HandyScan 3D," , 2020. URL https://www.creaform3d.com/en/portable-3d-scanner-handyscan-3d.

[21] Trontin, P., Blanchard, G., and Villedieu, P., "A comprehensive numerical model for mixed-phase and glaciated icing conditions," *8th AIAA Atmospheric and Space Environments Conference*, , No. June, 2016. https://doi.org/10.2514/6.2016-3742, URL http://arc.aiaa.org/doi/10.2514/6.2016-3742.

B
Plenoptic Imaging

Conventional cameras integrate the light intersecting each pixel of the CCD array from all ray angles, losing any information on the directionality of the incoming light. The addition of a micro-lens in front of the imaging sensor can act as an optical multiplexer to split the incoming rays based on their incidence angle [115]. A schematic of a conventional and plentoptic camera is shown in Figure B.1. Algorithms can then be applied to each of the images created from each microlens, coupled with geometric calibrations, to form depth maps which can be transformed into world coordinates [116]. A plenoptic camera can be considered as a many-view stereo camera system, where the image from each lenslet acts as a separate camera. Because the dimensions of the microlens array and its distance to the imaging sensor are known (from measurements in the manufacturing process), triangulation between each lenselt image is possible.

A proof of concept experiment was conducted using the icing wind tunnel at USQ using the stator test piece. Lighting was directed onto the test piece at an oblique angle using white LED's to enhance the contrast of the images, which has been found to be of importance for plenoptic imaging [117]. A commercially available plenoptic camera produced by Raytrix (model R29) was used for this study. It has a monochrome CCD sensor, with a resolution of 29 megapixels. All post-processing was computed using the software RxLive 4.0. Calibration of the depth map was

conducted using a dotted target plate and further software packages within RxLive. The data was obtained in collaboration with Stuttgart University [118].

A two-dimensional image rendered from the lightfield data-set is shown in Figure B.2, and the corresponding depth map in Figure B.3. Regions of black colour in the depth map are regions in which there was insufficient contrast to calculate the depth. The depth map can be used to create a three-dimensional surface of the accretion, as shown in Figure B.4. The data shows that the plentopic camera was successful in measuring sub-millimetre variations in ice thickness.

The benefit of using a plentopic camera instead of a stereo system is that only a single optical view of the accretion is required. The use of a light source is still necessary to provide surface contrast, but removes the need for a secondary camera, while also not needing to calibrate the light source as was required in the DIP system. This makes the experimental method very suitable for stationary component tests in a wind tunnel. The main drawbacks are the limited resolution of the image of each lenslet, and the requirement to know the distance from the microlens array to the sensor. Most ice crystal icing wind tunnels have substantial vibrations, as do most engine realistic rotating rigs. Such vibrations will induce errors into the calibration and limit their use unless the camera may be isolated from the vibrations.

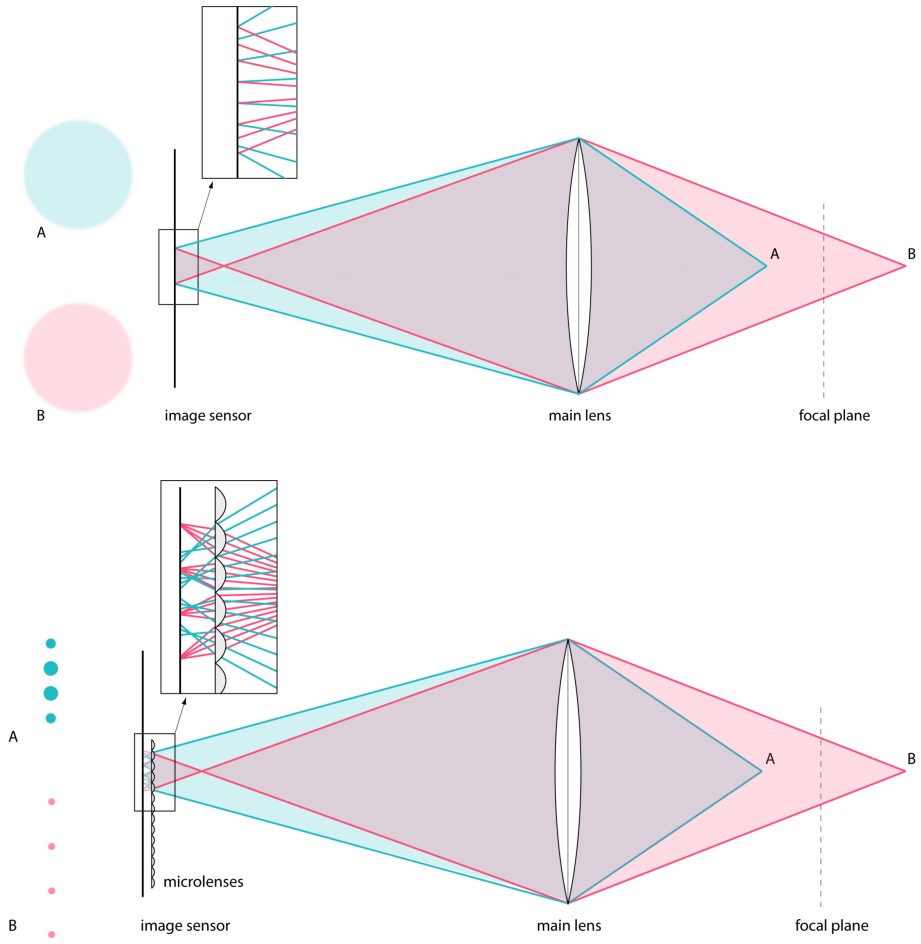

Figure B.1: Comparison of conventional camera (top) and a plenoptic camera (bottom) [118].

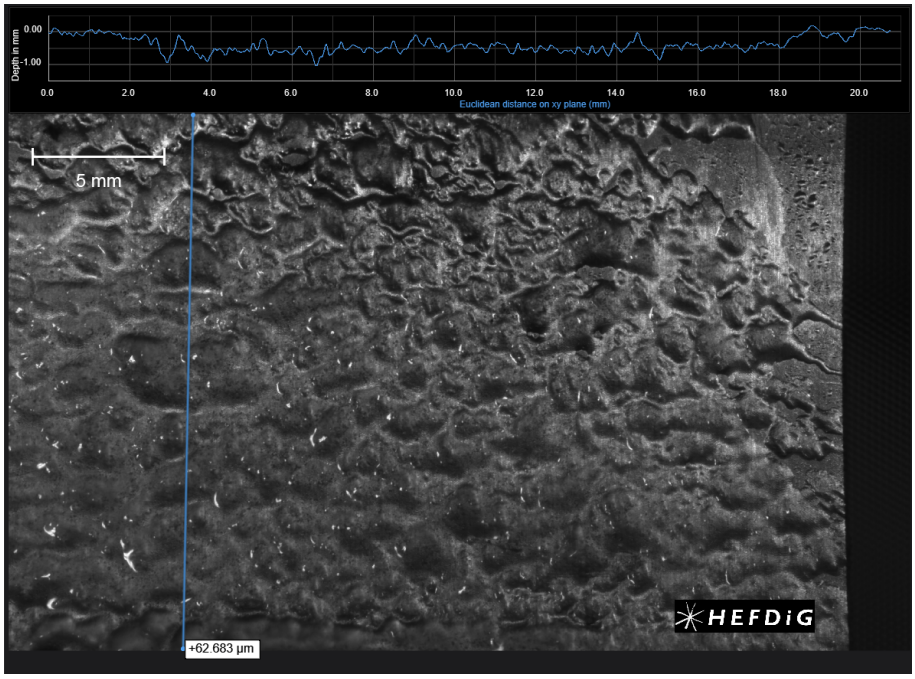

Figure B.2: Two dimensinoal image extracted from the lightfield data. Flow is top to bottom, right hand edge being the free tip of the blade.

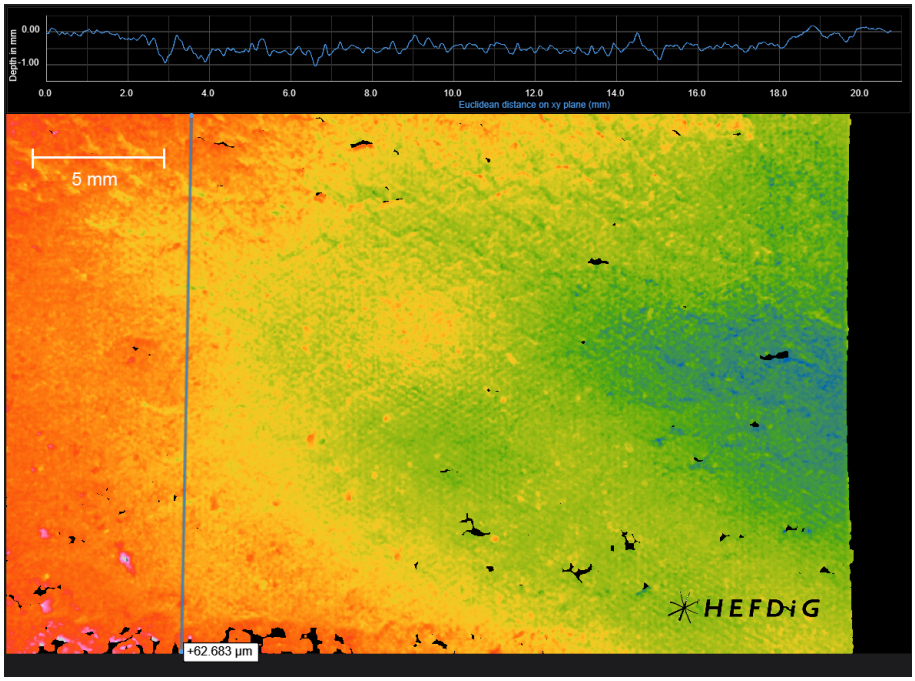

Figure B.3: Depth map computed from the lightfield data. Red color is a shorter distance along the optical axis (thicker ice), blue is further away. Flow is top to bottom, right hand edge being the free tip of the blade.

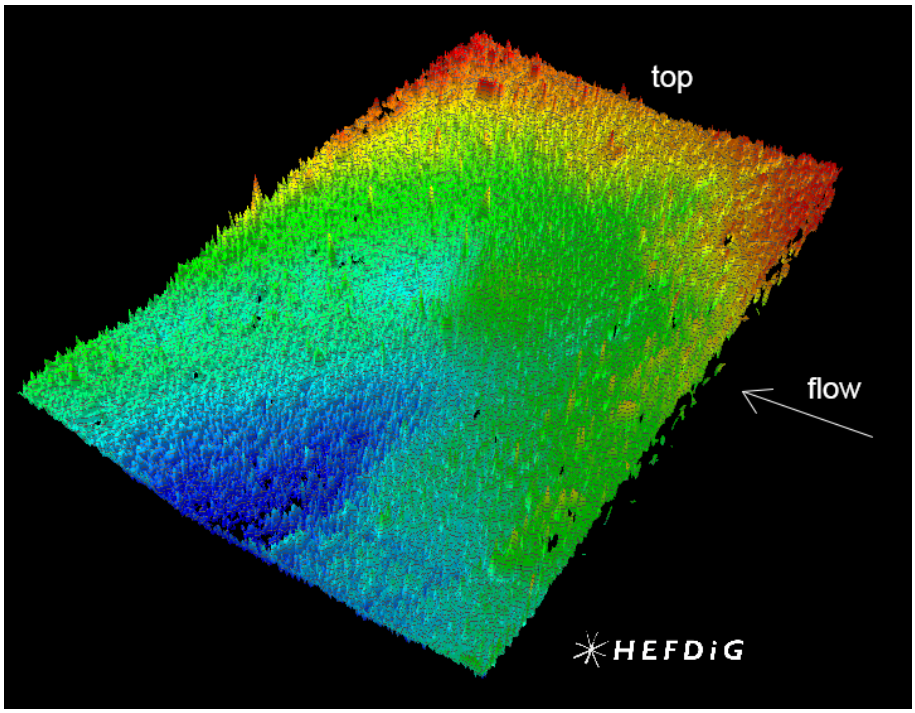

Figure B.4: Three-dimensional surface of the accretion, computed from the lightfield data. Red color is a shorter distance along the optical axis (thicker ice), blue is further away.

C
ICICLE Derivation

This appendix provides a derivations of the key equations used in the ice crystal icing numerical prediction code, ICICLE. Tuning parameters are provided if they are freely available in open literature, otherwise are owned as intellectual property of Rolls-Royce Plc. Sections developed as part of the work in this thesis are referenced to the relevant section in the main thesis, otherwise all other equations have been taken from the work published by Bucknell *et al* [13].

C.1 Particle Size Distributions

Ice particles, both in the atmosphere and icing wind tunnels, can vary in diameter by two to three orders of magnitude, from microns to millimetres. Accurate representation of the particle size distribution is important for multiple elements of the model such as the particle trajectory and impact location, melt percentage, probability of sticking, bouncing or shattering and capacity to erode accretions. The most common type of distribution used is the Weibull distribution, termed the Rosin-Rammler distribution when applied to particulates [119].

The mass fraction of particles with diameter greater than d is given by

$$Y_d = e^{\left(d/\bar{D}\right)^n} \tag{C.1}$$

Where $\bar{D}$ is the diameter constant, defined as the value o Y_d at which $Y_d = e^{-1}$, and n is the spread parameter, given by

$$n = \frac{ln(-ln(Y_d))}{ln(d/\bar{D})} \tag{C.2}$$

C.2 Particle Shape Characterisation

Atmospheric ice particles are inherently non-spherical. The effects of non-sphericity are taken into account in terms of the trajectory dynamics and heat transfer, for which it is assumed that they can be approximated as spheroids. For an equivalent diameter, D_{eq}, the shape is defined by the aspect ratio, E. Aspect ratio values greater than unity create prolate shapes, and oblate for values less than unity - see Figure 2.1 in Chapter 2 for a schematic diagram.

The particle volume is defined by:

$$V_p = V_{eq} = \frac{\pi}{6} {D_{eq}}^3 = \frac{4}{3}\pi a^3 E \tag{C.3}$$

Where a and c are the equatorial radius and length from centre to pole respectively.

Additional particle shape parameters, sphericity, ϕ and crosswise sphericity, $\phi_\perp$, have been taken from [120] and [121] respectively. Crosswise sphericity is defined as the ratio of the cross-sectional area of the volume-equivalent sphere and the actual area of the particle, projected normal to the flow direction, $A_{p,\perp}$. The two sphericity parameters are defined as:

$$\phi = \frac{\pi D_{eq}}{A_p} \tag{C.4}$$

$$\phi_\perp = \frac{\pi D_{eq}^2}{4A_{p,\perp}} \tag{C.5}$$

Where A_p is the surface area of the spheriod. As no particle rotation model has been implemented into ICICLE, it was assumed that the particles would orientate in the most stable orientation, broadside to the flow. When specifying the cloud

characteristics, a distribution of D_{eq} and E is specified, from which the remaining shape parameters can be calculated.

C.3 Lagrangian Particle Tracking

Particle motion is calculated using Lagrangian particle tracking. Eulerian particle tracking was not chosen due to the inability to model the effects of particle/wall interactions. Newtonian motion is used to calculate the velocity and position of the particle on successive time-steps of the model:

$$\boldsymbol{F} = m_p \frac{d\boldsymbol{v_p}}{dt} \tag{C.6}$$

Where $\boldsymbol{F}$ is the particle force vector, m_p is the particle mass, and $\boldsymbol{V_p}$ is the particle velocity vector.

C.4 Time Integration of Particle Motion

The choice of time-step size in the numerical model can have large effects on the numerical accuracy. Choice of infinitesimal time-steps will guarantee accuracy, at the cost of numerical efficiency. For the work done in this thesis, the implicit Euler method has been utilised:

$$\boldsymbol{v_p^{n+1}} = \frac{\boldsymbol{v_p^n} + \Delta t\,(\boldsymbol{g} + \boldsymbol{v_f}/\tau_p)}{1 + \Delta t/\tau_p} \tag{C.7}$$

Where $\boldsymbol{g}$ is the gravity vector, τ_p is the particle relaxation time, $\boldsymbol{v_f}$ is the local fluid flow velocity vector, and Δt is the timestep size. The particle relaxation time assuming Stokes flow is defined as:

$$\tau_p = \frac{4\rho_p D_{eq}^3}{3Re_p C_d \mu_f} \tag{C.8}$$

Where Re_p is the particle Reynolds number, C_d is the particle drag coefficient, and μ_f is the local fluid viscosity. The particle reynolds number is defined as

$$Re_p = \frac{\rho_f |\boldsymbol{v_p} - \boldsymbol{v_f}| D_{eq}}{\mu_f} \tag{C.9}$$

C.5 Particle Forces

Due to the large particle Stokes numbers typically found in ice crystal icing (1-100) [13], it is assumed in ICICLE that only drag and gravity need included for calculating the total forces imparted onto the particle. Other forces such as thermophoresis, turbophoresis, the Basset history force and Saffman's lift force are neglected.

The drag force is calculated as:

$$\boldsymbol{F_d} = -0.5\rho_f C_D A_{p,\perp} |\boldsymbol{v_p} - \boldsymbol{v_f}| (\boldsymbol{v_p} - \boldsymbol{v_f}) \tag{C.10}$$

Where C_D is the drag coefficient, and ρ_f is the local air density. The model for drag coefficient by Hölzer and Sommerfeld [21] has been implemented:

$$C_D = \frac{8}{Re_p\sqrt{\phi_\perp}} + \frac{16}{Re_p\sqrt{\phi}} + \frac{3}{\sqrt{Re_p}\phi^{0.75}} + \frac{0.42\left(10^{0.4(-\log_{10}\phi)^{0.2}}\right)}{\phi_\perp} \tag{C.11}$$

C.6 Particle Phase Change

The particle phase change model of Yang *et al* [122] has been implemented into ICICLE and is summarised here. It is assumed that ice melting consist of three stages; (1) fully solid ice crystals, (2) partially melted ice crystals, and (3) fully melted ice crystals.

During stage (1), the mass transfer is from the sublimation and the heat transfer is from the convection and phase change heat transfer. Particle shape remains unchanged while the particle size changes with particle mass.

During stage (2) the mass transfer is from the evaporation and the heat transfer is from the convection, evaporation/condensation, and melting heat transfer, while the temperature is kept constant at the melting temperature. Particle sphericity gradually approaches unity with the assumption of the fully melted particles being spherical droplets.

During stage (3), the mass transfer is from the evaporation/condensation and the heat transfer is from the convective and phase change heat transfer. Particle temperature is able to increase again while the particle shape remains spherical.

This work assumes that the porosity of the crystal can be accounted by the porosity factor, PF, defined as the ice volume normalised by the volume of the crystal - i.e. a porosity factor of unity is a fully solid crystal with no air pockets:

$$PF = \frac{V_{ice}}{V_{crystal}} \tag{C.12}$$

Stage (1) - frozen ice crystals ($T_p < T_p$)

$$m_p c_{p,i} \frac{dT_p}{dt} = Q_{conv} - \dot{m_{sub}} L_s \tag{C.13}$$

$$\frac{dm_p}{dt} = -\dot{m}_{sub} \tag{C.14}$$

$$Q_{conv} = \frac{\pi D_p}{\phi} Nu^* k_g \left(T_f - T_p\right) \tag{C.15}$$

$$\dot{m_{sub}} = \frac{piD_p}{\phi} Sh^* \rho_f D_{v,f} \left(\gamma_{v,p} - \gamma_{v,g}\right) \tag{C.16}$$

$$T_f = T_{g,s} \left(1 + Pr^(1/3) \frac{\gamma - 1}{2} Ma^2_{p,rel}\right) \tag{C.17}$$

$$\rho_{core} = (1 - PF)\rho_g + PF\rho_i \tag{C.18}$$

$$\rho_p = \rho_{core} \tag{C.19}$$

$$\frac{Nu^*}{Nu} = F_{SB} \tag{C.20}$$

$$\frac{Sh^*}{Sh} = F_{SB} \tag{C.21}$$

$$F_{SB} = \frac{1}{\left(1 + \frac{(T_{g,s} - T_p)\, C_p, p}{L_p}\right)^{0.7}} \tag{C.22}$$

$$C_{p,p} = (1 - MR)C_{p,i} + MRC_{p,w} \tag{C.23}$$

$$L_p = (1 - MR)L_s + MRL_v \tag{C.24}$$

$$Nu = 2\sqrt{\phi} + 0.55Pr^{1/3}\phi^{1/4}\sqrt{Re_P} \tag{C.25}$$

$$Sh = 2\sqrt{\phi} + 0.55Sc^{1/3}\phi^{1/4}\sqrt{Re_P} \tag{C.26}$$

Where, T_p is the particle temperature and T_m is the melting temperature (273.15K); $C_{p,i}$ is the specific heat of the ice, L_s is the total latent heat - the sum of the latent heat of fusion - L_f and evaporation L_v, Nu is the Nusselt number, K_g is the gas thermal conductivity, Sh is the Sherwood number, $D_{v,g}$ is the water vapour diffusivity in the air, $\gamma_{v,p}$ and $\gamma_{v,g}$ are the vapour mass fraction at the particle surface and gas phase, respectively; T_f is the gas temperature local to the particle, $T_{g,s}$ is the local gas static temperature, Pr is the Prandtl number, γ is the specific heat ratio, and $Ma_{p,rel}$ is the particle Mach number based on the slip velocity. The surface blowing factor, F_{SB} determines the enhanced Nusselt and Sherwood numbers, Nu^* and Sh^* respectively. Equations for Nu and Sh are by Villedieu *et al* [19].

Stage (2) - melting ice (T_p - T_m)

$$\dot{m}_{evap}L_v + \dot{m}_{melt}L_f \tag{C.27}$$

$$\frac{dm_p}{dt} = -\dot{m}_{evap} \tag{C.28}$$

$$\frac{dm_{p,i}}{dt} = -\dot{m}_{melt} \tag{C.29}$$

$$m_{p,w} = m_p - m_{p,i} \tag{C.30}$$

$$\dot{m}_{evap} = \frac{\pi D_p}{\phi} Sh^* \rho_g D_{v,g} \left(\gamma_{v,p} - \gamma_{v,g}\right) \tag{C.31}$$

$$\rho_p = 1/\left(\frac{1 - MR}{\rho_{core}} + \frac{MR}{\rho_w}\right) \tag{C.32}$$

$$\phi = MR(1 - \phi_0) + \phi_0 \tag{C.33}$$

Where ϕ_0 is the initial sphericity, and the assumption is made that the particle tends towards spherical when fully melted.

Stage (3) - liquid water ($T_p > T_m$)

$$m_p C_{p,w} \frac{dT_p}{dt} = Q_{conv} - \dot{m}_{evap} L_v \tag{C.34}$$

$$\frac{dm_p}{dt} = -\dot{m}_{evap} \tag{C.35}$$

$$\rho_p = \rho_w \tag{C.36}$$

C.7 Particle Sticking

Sticking on surfaces below freezing

It is assumed that frozen particles bounce off (or shatter) from cold surfaces, and all liquid water sticks to the surface.

$$m_{stuck} = m_p MR \tag{C.37}$$

Sticking on surfaces above freezing

The likelihood of a particle sticking to a surface, P_s is determined by the sticking model derived by Bucknell *et al* [36].

$$m_{stuck} = P_s m_p \tag{C.38}$$

$$P_s = 183MR^5 - 494MR^4 + 478MR^3 - 196MR^2 + 30.2MR - 0.526 \quad for\ 0.02 \leq MR \leq 0.37 \tag{C.39}$$

$$P_s = 0 \quad for\ 0 \leq MR \leq 0.02\ and\ 0.37 < MR \leq 1 \tag{C.40}$$

The value of P_s is used to determine the proportion of each particle stream that sticks to the surface. As the mass of the particle, for which the stream represents, does not change, the scaling factor, SF_p for that stream needs updated:

$$SF_p' = SF_p(1 - P_s) \tag{C.41}$$

C.8 Erosion

An erosion model produced by Bucknell *et al* [36] has been implemented into ICICLE. The effect of sticking and erosion are coupled to produce a "net" sticking efficiency:

$$\eta_{s,net} = P_s\left(1 - \eta_{loss}\right) \tag{C.42}$$

Where the mass loos efficiency, η_{loss}, is given by:

$$\eta_{loss} = min\left(1, \eta_{ero} + \mathcal{H}\right) \tag{C.43}$$

$$\eta_{ero} = A\left(1 + log_{10}\left(KE/KE_0\right)\right)\left(1 + Bsin^2\gamma\right)\left(exp\left(-C\frac{Q_s}{R}\left(\frac{1}{T_w} - \frac{1}{T_f}\right)\right)\right) \tag{C.44}$$

where γ is the angle between the local surface normal and the axial directions, T_w is the accretion surface temperature, R is the specific gas constant of air and Q_s, the surface activation energy of ice, is 4.82E4 $\mathrm{J\,K^{-1}\,mol^{-1}}$. KE is a quasi-kinetic energy parameter, defined in Equation (C.45), where $\bar{D^3_{eq}}$ is calculated by cubing the particle diameter for each bin in the distribution and mass averaging. Model constants $A = 0.2$, $B = 1.0$, $C = 0.3$, $\mathcal{H} = 0.46$.

$$KE = \bar{D^3_{eq}} U^2 \tag{C.45}$$

C.9 Particle Bounce and Shatter

Upon impact with a surface, a particle can either bounce elastically, bounce plastically or shatter. The outcome of particle impact has been studied by Villedieu *et al* [19], and their model has been implemented. Their model computes a dimensionless parameter, $\mathcal{L}$, defined as the ratio of the normal kinetic energy to the surface energy:

$$\mathcal{L} = \frac{\rho_p d_p (v^2_{p,n})}{12 e_\sigma(T_p)} \tag{C.46}$$

Where $v_{p,n}$ is the normal component of the impact velocity (relative to the wall) and $e_\sigma(T_p)$ is the surface energy per unit area of the particle:

$$e_\sigma(T_p) = e_{\sigma,0}\, exp\left[\frac{Q_s}{RT} - \frac{Q_s}{RT_0}\right] \tag{C.47}$$

Where Q_s is the activation energy related to the crack formation. According to Vidaure & Hallet [123], $e_{\sigma,0} = 0.12$ $\mathrm{J\,m^{-1}}$, $T_0 = 253$ K, and according to Higa *et al* [124], $Q_s = 4.82 \times 10^4$ $\mathrm{J\,K^{-1}\,mol^{-1}}$.

Three coefficients of restitution have been defined; tangential restitution coefficient, η_t, normal coefficient of restitution, η_{nn}, and the fraction of normal momentum which is transferred into tangential momentum due to impact, η_{nt}. These are then used to calculate the velocity of the particle after impact, $\boldsymbol{v_p}'$:

$$\boldsymbol{v_p}' = \zeta_t \left(\boldsymbol{v_p} - (\boldsymbol{v_p}.\boldsymbol{n})\,\boldsymbol{n}\right) - (\boldsymbol{v_p}.\boldsymbol{n})\left(\zeta_{nt}\boldsymbol{t} + \zeta_{nn}\boldsymbol{n}\right) \tag{C.48}$$

Elastic Rebound

When $\mathcal{L}$ is less than $\mathcal{L}_{c1}$, the particle elastically rebounds without fracturing nor fragmentation - zero energy loss. It has been found that $\mathcal{L}_{c1} = 0.5$. The normal and tangential coefficnets of restitution, η_n and η_t are given by:

$$\zeta_{nn} = 1 \tag{C.49}$$

$$\zeta_{nt} = 0 \tag{C.50}$$

$$\zeta_t = 1 \tag{C.51}$$

Inelastic Rebound

When $\mathcal{L}_{c1} \leq \mathcal{L} \leq \mathcal{L}_{c2}$, inelastic rebound occurs with particle fracturing but no fragmentation. $\mathcal{L}_{c2} = 90$.

$$\zeta_{nn} = \left(\frac{\mathcal{L}_{c1}}{\mathcal{L}}\right)^{1/3} \tag{C.52}$$

$$\zeta_{nt} = 0 \tag{C.53}$$

$$\zeta_t = 1 \tag{C.54}$$

Highly Inelastic Rebound

When $\mathcal{L}$ is greater than $\mathcal{L}_{c2}$, a highly inelastic rebound occurs with major particle fragmentation.

$$\zeta_{nn} = \left(\frac{\mathcal{L}_{c1}}{\mathcal{L}}\right)^{1/3} \tag{C.55}$$

$$\zeta_{nt} = 0.4\left(1 - \frac{\mathcal{L}_{c2}}{\mathcal{L}}\right) \tag{C.56}$$

$$\zeta_t = 1 \tag{C.57}$$

Villedieu *et al.* found that the maximum diameter of any particle post fragmentation is:

$$d'_p = d_p\left(\frac{\mathcal{L}_{c2}}{\mathcal{L}}\right)^{2/11} \tag{C.58}$$

In ICICLE, it is assumed that a single particle size is re-injected into the flow and that it's size is half that of the maximum size in the fragmented cloud. The scaling factor is adjusted to account for the total mass associated with that stream of particles.

C.10 Accretion growth

The growth rate of the accretion is predicted using the extended messenger model, adapted for ice crystals, EMM-C, derived by Bucknell *et al* [49]. Their paper details the assumptions of the model, most notably neglecting lateral conduction and temporal derivatives of the ice and water temperatures. The model has been implemented in full into ICICLE, with the only modifications being the ability to model the substrate cool down and an alternative water film thickness model, as detailed in section Section 5.6.

No smoothing is applied to the inputs to the accretion model, however the final ice shape is smoothed using a mass conservative smoothing method by Nonato *et al* [111] prior to re-injecting a new stream of particles.

D

Particle Stream Count Convergence

The number of particle streams required to reach statistical convergence for each test piece and condition is shown in the following figures. For more detail on the method please see Section 5.4.2.

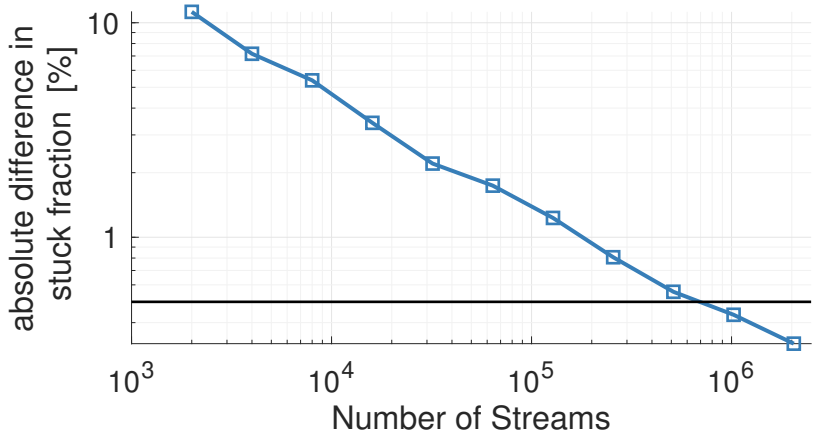

Figure D.1: Convergence of the sticking fraction of incoming particles on the stator test piece at AoA = 0°, Mach = 0.4, $d_{v,50}$ = 34 µm.

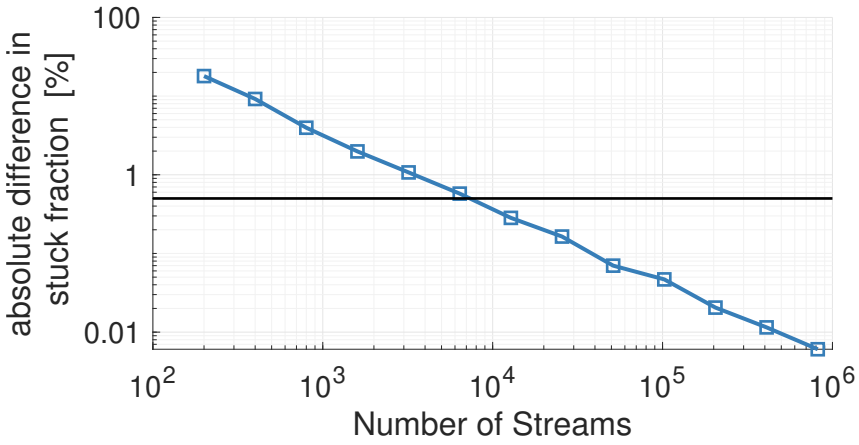

Figure D.2: Convergence of the sticking fraction of incoming particles on the single NACA-0018 airfoil at AoA = 0°, Mach = 0.2, d_p = 20 µm.

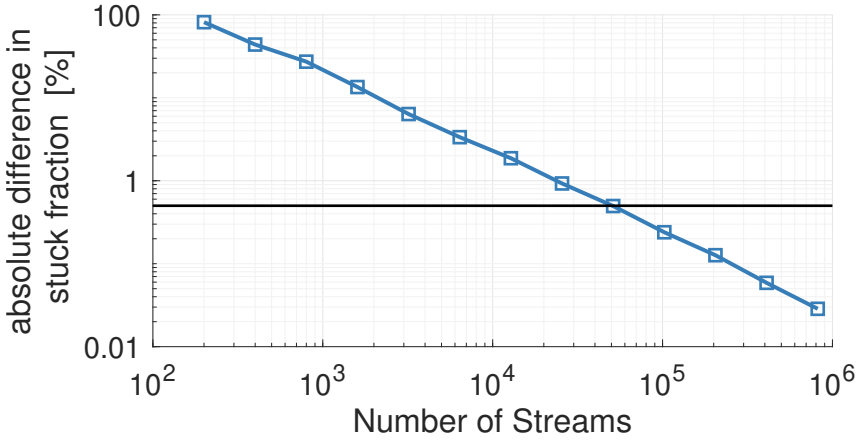

Figure D.3: Convergence of the sticking fraction of incoming particles on the triple NACA-0018 airfoil at AoA = 0°, Mach = 0.2, d_p = 20 µm

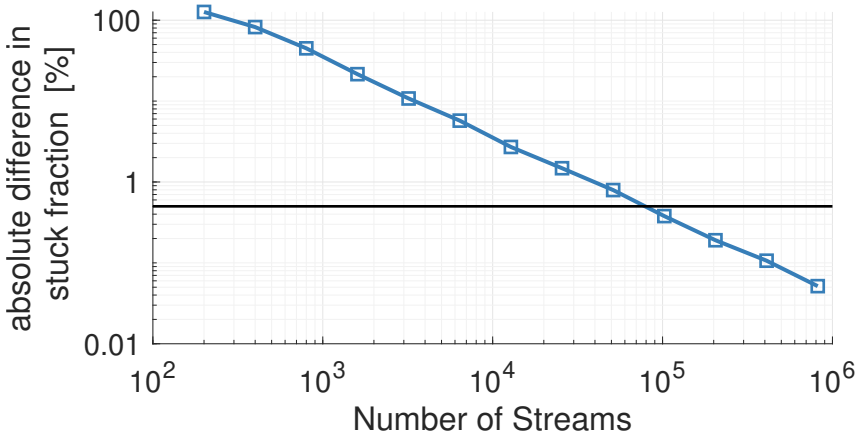

Figure D.4: Convergence of the sticking fraction of incoming particles on the triple NACA-0018 airfoil at AoA = 10°, Mach = 0.2, d_p = 20 µm.

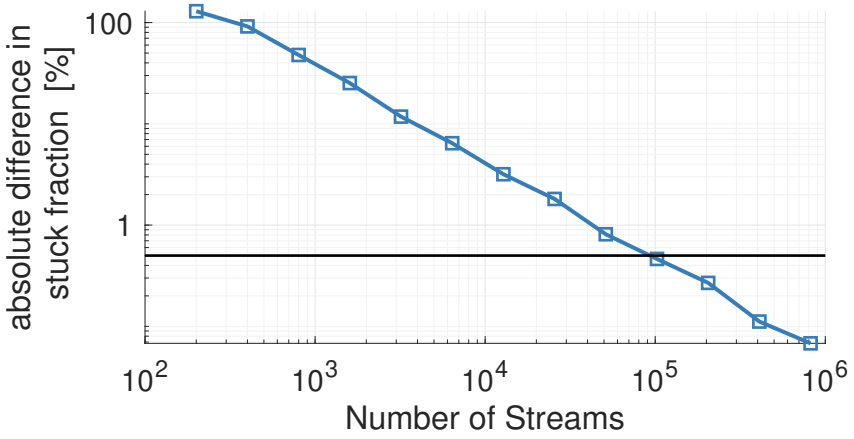

Figure D.5: Convergence of the sticking fraction of incoming particles on the triple NACA-0018 airfoil at AoA = 15°, Mach = 0.2, d_p = 20 µm.

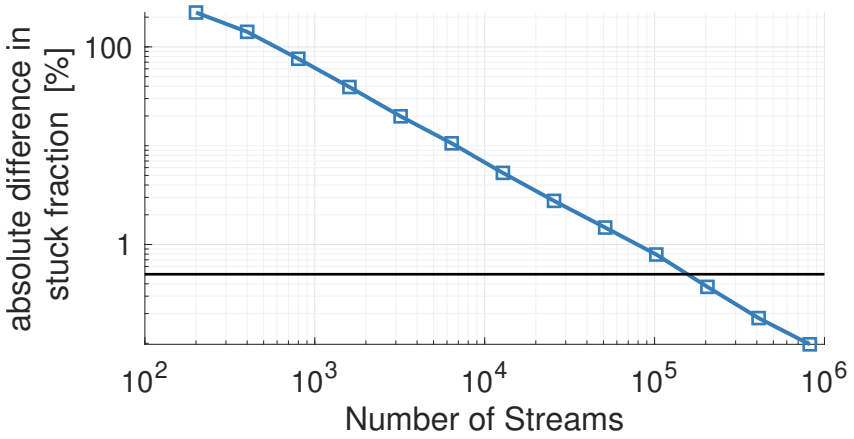

Figure D.6: Convergence of the sticking fraction of incoming particles on the triple NACA-0018 airfoil at AoA = 10°, Mach = 0.3, d_p = 20 µm.

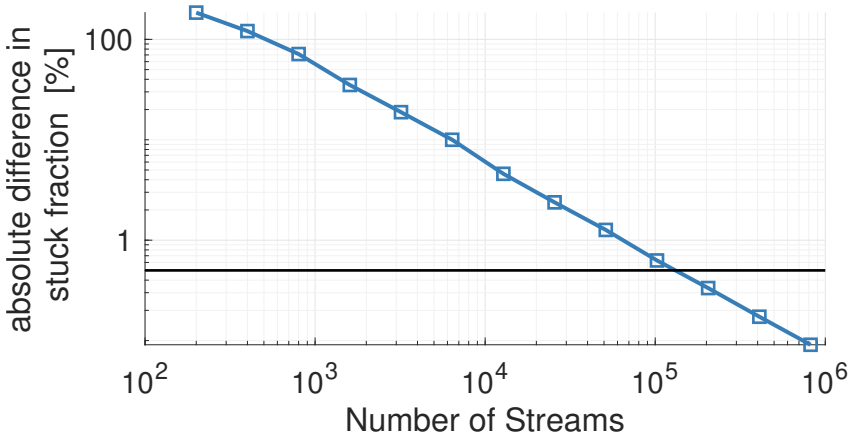

Figure D.7: Convergence of the sticking fraction of incoming particles on the triple NACA-0018 airfoil at AoA = 10°, Mach = 0.2, d_p = 40 µm.

References

[1] Jeanne Mason, Walter Strapp, and Philip Chow. "The Ice Particle Threat to Engines in Flight". In: *44th AIAA Aerospace Sciences Meeting and Exhibit*. 2006.

[2] Federal Register. "Airplane and Engine Certification Requirements in Supercooled Large Drop, Mixed Phase, and Ice Crystal Icing Conditions". In: 79.213 (2014), pp. 65508–65540.

[3] Publishing Office US Government. *Electronic Code of Federal Regulations*. URL: https://www.ecfr.gov/cgi-bin/text-idx?c=ecfr&tpl=/ecfrbrowse/Title14/14tab_02.tpl.

[4] R P Lawson, L J Angus, and a J Heymsfield. "Cloud particle measurements in thunderstorm anvils and possible weather threat to aviation". In: *Journal of Aircraft* 35.1 (1998), pp. 113–121.

[5] A. Protat et al. "The measured relationship between ice water content and cloud radar reflectivity in tropical convective clouds". In: *Journal of Applied Meteorology and Climatology* 55.8 (2016), pp. 1707–1729.

[6] Delphine Leroy et al. "Ice crystal sizes in high ice water content clouds. Part II: Statistics of mass diameter percentiles in tropical convection observed during the HAIC/HIWC project". In: *Journal of Atmospheric and Oceanic Technology* 34.1 (2017), pp. 117–136.

[7] Thomas Ratvasky et al. "Summary of the High Ice Water Content (HIWC) RADAR Flight Campaigns". In: *SAE Technical Paper Series*. 2019, pp. 1–36.

[8] Melissa Bravin, J Walter Strapp, and Jeanne Mason. "An Investigation into Location and Convective Lifecycle Trends in an Ice Crystal Icing Engine Event Database". In: *SAE Technical Paper*. SAE International, 2015. URL: https://doi.org/10.4271/2015-01-2130.

[9] Jeanne Mason. "Current Perspectives on Jet Engine Power Loss in Ice Crystal Conditions: Engine Icing". In: (2009).

[10] Rolls Royce. *UltraFan Cutaway poster*. 2019. URL: https://www.flickr.com/photos/rolls-royceplc/48421626132/in/album-72157644584413758/.

[11] Federal Air Transport Agency of Russia. *Damage to Airbridge Cargo GEnx Engine*.

[12] Paolo Vanacore. "Industry Perspective on Ice Crystal Icing". In: *ASME. Turbo Expo: Power for Land, Sea, and Air, Volume 2D: Turbomachinery* (2018).

[13] Alexander Bucknell et al. "ICICLE: A Model for Glaciated & Mixed Phase Icing for Application to Aircraft Engines". In: *SAE Technical Papers* 2019-June.June (2019), pp. 1–19.

[14] F. Dezitter et al. “HAIC (High Altitude Ice Crystals)”. In: *5th AIAA Atmospheric and Space Environments Conference Aircraft Icing* (2013), pp. 1–15.

[15] J.W. Strapp et al. “The High Ice Water Content Study of Deep Convective Clouds: Report on Science and Technical Plan”. In: (2016), p. 105. URL: http://www.tc.faa.gov/its/worldpac/techrpt/tc14-31.pdf.

[16] Delphine Leroy et al. “HAIC/HIWC Field Campaign - Specific Findings on PSD Microphysics in High IWC Regions from in Situ Measurements: Median Mass Diameters, Particle Size Distribution Characteristics and Ice Crystal Shapes”. In: *SAE Technical Papers* 2015-June.June (2015).

[17] Andrew J Heymsfield et al. “Observations and Parameterizations of Particle Size Distributions in Deep Tropical Cirrus and Stratiform Precipitating Clouds: Results from In Situ Observations in TRMM Field Campaigns”. In: *Journal of the Atmospheric Sciences* 59.24 (2002), pp. 3457–3491. URL: http://dx.doi.org/10.1175/1520-0469(2002)059%3C3457:OAPOPS%3E2.0.CO%5Cn2%5Cnhttp://0.0.0.2.

[18] Clayton T. Crowe et al. *Multiphase Flows with Droplets and Particles*. CRC Press, 2011.

[19] Philippe Villedieu, Pierre Trontin, and Rémi Chauvin. “Glaciated and mixed-phase ice accretion modeling using ONERA 2D icing suite”. In: *Transactions of Japanese Society for Medical and Biological Engineering* 51.SUPPL. (2013), pp. 1–34.

[20] A Haider and O Levenspiel. “Drag Coefficient and Terminal Velocity of Spherical and Nonspherical Particles”. In: *Powder Technology* 58 (1989), pp. 63–70.

[21] Andreas Hölzer and Martin Sommerfeld. “New simple correlation formula for the drag coefficient of non-spherical particles”. In: *Powder Technology* 184.3 (2008), pp. 361–365.

[22] C Tropea et al. “Physics of aircraft icing: A predictive challenge”. In: (2015).

[23] Tobias Hauk, Ilia V. Roisman, and Cameron D. Tropea. “Investigation of the Impact Behaviour of Ice Particles”. In: *6th AIAA Atmospheric and Space Environments Conference* June (2014), pp. 1–15. URL: http://arc.aiaa.org/doi/10.2514/6.2014-3046.

[24] Mario Vargas et al. “Ice Particle Impacts on a Flat Plate”. In: *SAE 2015 International Conference on Icing of Aircraft, Engines, and Structures* (2015). URL: http://papers.sae.org/2015-01-2099/.

[25] German Vidaurre and John Hallett. “Particle impact and breakup in aircraft measurement”. In: *Journal of Atmospheric and Oceanic Technology* 26.5 (2009), pp. 972–983.

[26] Robert L. Jackson, Itzhak Green, and Dan B. Marghitu. “Predicting the coefficient of restitution of impacting elastic-perfectly plastic spheres”. In: *Nonlinear Dynamics* 60.3 (2010), pp. 217–229.

[27] Tobias Hauk, Ilia Roisman, and Cameron Tropea. “Investigation of the melting behaviour of ice particles in an acoustic levitator”. In: *AIAA AVIATION 2014 -11th AIAA/ASME Joint Thermophysics and Heat Transfer Conference* June (2014), pp. 1–17.

[28] Andreas Richter and Petr A. Nikrityuk. "Drag forces and heat transfer coefficients for spherical, cuboidal and ellipsoidal particles in cross flow at sub-critical Reynolds numbers". In: *International Journal of Heat and Mass Transfer* 55.4 (2012), pp. 1343–1354. URL: http://dx.doi.org/10.1016/j.ijheatmasstransfer.2011.09.005.

[29] Xin Yang, Matthew Mcgilvray, and David Gillespie. "Numerical modelling and parametric study of the melting behaviour of ice crystal particles [yet to be published]". In: ().

[30] Tobias Hauk et al. "Theoretical and experimental investigation of the melting process of ice particles". In: *Journal of Thermophysics and Heat Transfer* 30.4 (2016), pp. 946–954.

[31] Thomas C. Currie et al. "Altitude Scaling of Ice Crystal Accretion". In: *5th AIAA Atmospheric and Space Environments Conference* (2013), pp. 1–26. URL: http://arc.aiaa.org/doi/10.2514/6.2013-2677.

[32] Alexander Bucknell et al. "Heat transfer in the core compressor under ice crystal icing conditions". In: *Journal of Engineering for Gas Turbines Power* Vol. 140.No. 7 (2018), pp. 1–15.

[33] Peter Struk et al. "Fundamental Ice Crystal Accretion Physics Studies". In: 2011.

[34] Thomas Currie et al. "Fundamental Study of Mixed-Phase Icing with Application to Ice Crystal Accretion in Aircraft Jet Engines". In: *4th AIAA Atmospheric and Space Environments Conference*. 2012.

[35] Jeanne G. Mason, Philip Chow, and Dan M. Fuleki. "Understanding Ice Crystal Accretion and Shedding Phenomenon in Jet Engines Using a Rig Test". In: *Journal of Engineering for Gas Turbines and Power* (2011).

[36] Alexander Bucknell et al. "Experimental Studies of Ice Crystal Accretion on an Axisymmetric Body at Engine-Realistic Conditions". In: *2018 Atmospheric and Space Environments Conference, AIAA AVIATION Forum, (AIAA 2018-4223)* (2018).

[37] Peter M Struk et al. "Ice Accretion Measurements on an Airfoil and Wedge in Mixed-Phase Conditions". In: *SAE 2015 International Conference on Icing of Aircraft, Engines, and Structures* Figure 2 (2015). URL: http://papers.sae.org/2015-01-2116/.

[38] Tom C. Currie, Dan Fuleki, and Ali Mahallati. "Experimental studies of mixed-phase sticking efficiency for ice crystal accretion in jet engines". In: *Transactions of Japanese Society for Medical and Biological Engineering* 51.SUPPL. (2013), pp. 1–26.

[39] Daniel C Knezevici et al. "Particle Size Effects on Ice Crystal Accretion". In: (2012).

[40] W. Samenfink et al. "Droplet interaction with shear-driven liquid films: Analysis of deposition and secondary droplet characteristics". In: *International Journal of Heat and Fluid Flow* 20.5 (1999), pp. 462–469.

[41] Daniel C Knezevici et al. "Particle Size Effects on Ice Crystal Accretion – Part II". In: (2013). URL: http://arc.aiaa.org.

[42] William B. Wright, Philip C.E. Jorgenson, and Joseph P. Veres. "Mixed phase modeling in GlennICE with application to engine icing". In: *AIAA Atmospheric and Space Environments Conference 2010* August (2010), pp. 1–19.

[43] Pierre Trontin, Ghislain Blanchard, and Philippe Villedieu. "A comprehensive numerical model for mixed-phase and glaciated icing conditions". In: *8th AIAA Atmospheric and Space Environments Conference* June (2016). URL: http://arc.aiaa.org/doi/10.2514/6.2016-3742.

[44] Virgile Charton et al. "Semi-empirical erosion model with particle size and liquid water content effects for ice crystal icing simulations". In: *Aiaa Aviation 2020 Forum* 1 PartF (2020), pp. 1–18.

[45] Benjamin C. Kott, Peter M. Struk, and Tadas P. Bartkus. "A study of ice-crystal icing erosion using the nasa icing research tunnel and propulsion systems laboratory". In: *Aiaa Aviation 2020 Forum* 1 PartF (2020), pp. 1–20.

[46] Bernard L Messingert. "Equilibrium Temperature of an Unheated Icing Surface as a Function of Air Speed". In: *Journal of the Aeronautical Sciences* 20.1 (1953), pp. 29–42. URL: http://arc.aiaa.org/doi/10.2514/8.2520.

[47] Tim G Myers. "Extension to the Messinger Model for Aircraft Icing". In: 39.2 (2001).

[48] William Wright, Phil Jorgenson, and Joseph Veres. "Mixed Phase Modeling in GlennICE with Application to Engine Icing". In: *AIAA Atmospheric and Space Environments Conference*. 2010.

[49] Alexander Bucknell et al. "A Three-Layer Thermodynamic Model for Ice Crystal Accretion on Warm Surfaces: EMM-C". In: *SAE Technical Paper Series* 1 (2019), pp. 1–12.

[50] A Linke-Diesinger. *Systems of Commercial Turbofan Engines: An Introduction to Systems Functions*. Springer Berlin Heidelberg, 2008. URL: https://books.google.co.uk/books?id=bgN2cAxF9OAC.

[51] M. CHU, R. SCAVUZZO, and C. KELLACKEY. "Tensile properties of impact ices". In: *30th Aerospace Sciences Meeting and Exhibit* (1992). URL: http://arc.aiaa.org/doi/10.2514/6.1992-883.

[52] Decang Lou, David Hammond, and Marie-Laure Pervier. "Investigation of the Adhesive Properties of the Ice–Aluminum Interface". In: *Journal of Aircraft* 51.3 (2014), pp. 1051–1056. URL: http://arc.aiaa.org/doi/10.2514/1.C032509.

[53] Andrew H. Work et al. "The Adhesion Strength of Impact Ice Measured Using a Modified Lap Joint Test". In: *2018 Atmospheric and Space Environments Conference* (2018), pp. 1–23. URL: https://arc.aiaa.org/doi/10.2514/6.2018-3341.

[54] A. Reich, R. Scavuzzo, and M. Chu. "Survey of mechanical properties of impact ice". In: *32nd Aerospace Sciences Meeting and Exhibit* (1994). URL: http://arc.aiaa.org/doi/10.2514/6.1994-712.

[55] Andrew Work and Yongsheng Lian. "A critical review of the measurement of ice adhesion to solid substrates". In: *Progress in Aerospace Sciences* 98.January (2018), pp. 1–26. URL: https://doi.org/10.1016/j.paerosci.2018.03.001.

[56] David S. Thompson et al. “Initial Development of a Model to Predict Impact Ice Adhesion Stress”. In: *2018 Atmospheric and Space Environments Conference* (2018), pp. 1–19. URL: https://arc.aiaa.org/doi/10.2514/6.2018-3344.

[57] Rebekah G. Douglass, Jose Palacios, and Grant Schneeberger. “Design, Fabrication, Calibration, and Testing of a Centrifugal Ice Adhesion Test Rig with Strain Rate Control Capability”. In: *2018 Atmospheric and Space Environments Conference* (2018), pp. 1–18. URL: https://arc.aiaa.org/doi/10.2514/6.2018-3342.

[58] H. Farid et al. “An atmospheric ice empirical failure criterion”. In: *Cold Regions Science and Technology* 146.November 2017 (2018), pp. 81–86. URL: https://doi.org/10.1016/j.coldregions.2017.11.013.

[59] R. HENRY. “Development of an electrothermal de-icing/anti-icing model”. In: (1992).

[60] R. J. Scavuzzo, M. L. Chu, and V. Ananthaswamy. “Influence of aerodynamic forces in ice shedding”. In: *Journal of Aircraft* 31.3 (1994), pp. 526–530.

[61] L. Bennani, P. Villedieu, and M. Salaun. “A mixed adhesion-brittle fracture model and its application to the numerical study of ice shedding mechanisms”. In: *Engineering Fracture Mechanics* 158 (2016), pp. 59–80. URL: http://dx.doi.org/10.1016/j.engfracmech.2016.02.050.

[62] D. M. Kintea, I. V. Roisman, and C. Tropea. “Transport processes in a wet granular ice layer: Model for ice accretion and shedding”. In: *International Journal of Heat and Mass Transfer* 97 (2016), pp. 461–472. URL: http://dx.doi.org/10.1016/j.ijheatmasstransfer.2016.01.076.

[63] Y. Wei, R. M. Adamson, and J. P. Dempsey. “Ice/metal interfaces: Fracture energy and fractography”. In: *Journal of Materials Science* 31.4 (1996), pp. 943–947.

[64] Shiping Zhang et al. “FEM analysis of in-flight ice break-up”. In: *Finite Elements in Analysis and Design* 57 (2012), pp. 55–66. URL: http://dx.doi.org/10.1016/j.finel.2012.03.005.

[65] F Erdogan and G C Sih. “On the crack extension in plates under plane loading and transverse shear”. In: (1963).

[66] Jen Ching Tsao, Peter Struk, and Michael Oliver. “Possible mechanisms for turbofan engine ice crystal icing at high altitude”. In: *Transactions of Japanese Society for Medical and Biological Engineering*. 2013.

[67] Khamel Al-Khalil. “Assessment of Effects of Mixed-phase Icing Conditions on Thermal Ice Protection Systems”. In: *Office of Aviation Research, Federal Aviation Administration* (2003).

[68] P. Trontin et al. “Description and assessment of the new ONERA 2D icing suite IGLOO2D”. In: *9th AIAA Atmospheric and Space Environments Conference, 2017* (2017). URL: http://dx.doi.org/10.2514/6.2017-3417.

[69] B Mason. “On the melting of hailstones”. In: (1956), pp. 209–216.

[70] Kamel Al-Khalil, Eddie Irani, and Dean Miller. "Mixed Phase Icing Simulation and Testing at the Cox Icing Wind Tunnel". In: *41st Aerospace Sciences Meeting and Exhibit* 6.September (2003), pp. 2003–903. URL: https://arc.aiaa.org/doi/pdfplus/10.2514/6.2003-903.

[71] Alexander Bucknell et al. "Experimental Study and Analysis of Ice Crystal Accretion on a Gas Turbine Compressor Stator Vane". In: *Submitt. SAE Int. Conf. Icing Aircraft, Engines Struct. June 17-21, Minneapolis, MN, USA, 2019.* (2019).

[72] Lyle Lilie et al. "A Multiwire Hot-Wire Device for Measurement of Icing Severity, Total Water Content, Liquid Water Content, and Droplet Diameter". In: (2005).

[73] Laura E. Steen, Robert F. Ide, and Judith Foss Van Zante. "An assessment of the icing blade and the SEA multi-element sensor for liquid water content calibration of the NASA GRC icing research tunnel". In: *8th AIAA Atmospheric and Space Environments Conference* June (2016), pp. 1–22.

[74] Peter M Struk et al. "An Initial Study of the Fundamentals of Ice Crystal Icing Physics in the NASA Propulsion Systems Laboratory". In: *Principle Research Scientist, Icing Branch Brookpark Road* 7 (2100), pp. 11–2. URL: http://arc.aiaa.org.

[75] Michael J. Oliver. "Validation ice crystal icing engine test in the propulsion systems laboratory at NASA glenn research center". In: *Transactions of Japanese Society for Medical and Biological Engineering* 51.SUPPL. (2013), pp. 1–34.

[76] Philip C E Jorgenson et al. "Analysis of the Honeywell Uncertified Research Engine With Ice Crystal Cloud Ingestion at Simulated Altitudes". In: *Journal of Turbomachinery* 142.6 (May 2020). URL: https://doi.org/10.1115/1.4047187.

[77] Cris Bosetti, Bernard P. Paul, and Adam M. Malone. "Ice shape characterization to aid in replicating ice shapes for subsequent analysis". In: *AIAA Atmospheric and Space Environments Conference 2010*. 2010. URL: https://arc.aiaa.org/doi/abs/10.2514/6.2010-7534.

[78] Sam Lee et al. "Development of 3D ice accretion measurement method". In: *4th AIAA Atmospheric and Space Environments Conference 2012* June (2012), pp. 1–17.

[79] Peter M. Struk et al. "Ice Crystal Icing Physics Study using a NACA 0012 Airfoil at the National Research Council of Canada's Research Altitude Test Facility". In: *2018 Atmospheric and Space Environments Conference* (2018). URL: https://arc.aiaa.org/doi/10.2514/6.2018-4224.

[80] Andrew L. Reehorst and G. Paul Richter. "New Methods and Materials for Molding and Casting Ice Formations." In: *NASA Technical Memorandum* TM-100126.September (1987).

[81] Ramiz Saeed, David Buttsworth, and Khalid Saleh. "A New Wind Tunnel Facility for Ice Crystal Icing Experiments". In: *SAE Technical Papers* 2019-June.June (2019), pp. 1–7.

[82] National Research Council Canada. *Altitude icing wind tunnel*. https://www.nrc-cnrc.gc.ca/eng/solutions/facilities/wind_tunnel/altitude_icing.html. URL: https://www.nrc-cnrc.gc.ca/eng/solutions/facilities/wind_tunnel/altitude_icing.html.

[83] Myron M Oleskiw, Fred H Hyde, and Paul J Penna. “In-Flight Icing Simulation Capabilities of NRC ’ s Altitude Icing Wind Tunnel”. In: July (2014).

[84] Daniel C. Knezevici, Dan Fuleki, and James MacLeod. “Development and Commissioning of a Linear Compressor Cascade Rig for Ice Crystal Research”. In: 2011. URL: http://papers.sae.org/2011-38-0079/.

[85] Arne Baumert, Stephan Bansmer, and Michael Bacher. “Implementation of an innovative ice crystal generation system to the icing wind tunnel Braunschweig”. In: *53rd AIAA Aerospace Sciences Meeting* January (2015), pp. 1–10.

[86] Ashlie B Flegel. “Ice Crystal Icing Research at NASA Glenn Research Center”. In: *AIAA Atmospheric and Space Environments Conference* 9th.June (2017), pp. 1–19. URL: https://arc.aiaa.org/doi/10.2514/6.2017-4085.

[87] Dan Fuleki, Martin Neuteboom, and Jennifer Chalmers. “Ice Crystal Icing Test Design and Execution for the ALF502 Vane Segment in the NRC RATFac Cascade Rig”. In: *SAE Technical Papers* 2019-June.June (2019).

[88] Alex Pasmans and Manj Subiah. “Managing the Global Crisis caused by COVID 19”. In: (2020).

[89] Joaquim Salvi et al. “A state of the art in structured light patterns for surface profilometry”. In: *Pattern Recognition* 43.8 (2010), pp. 2666–2680. URL: http://dx.doi.org/10.1016/j.patcog.2010.03.004.

[90] Kai Zhang, Tian Wei, and Hui Hu. “An experimental investigation on the surface water transport process over an airfoil by using a digital image projection technique”. In: *Experiments in Fluids* 56.9 (2015), pp. 1–16.

[91] Linyue Gao et al. “Quantification of 3D Ice Structures Accreted on a Wind Turbine Airfoil Model”. In: *SAE Technical Papers* 2019-June.June (2019), pp. 1–7.

[92] Torbjørn Taskjelle et al. “Spectral albedo and transmittance of thin young Arctic sea ice”. In: *Journal of Geophysical Research: Oceans* 121.1 (2016), pp. 540–553. URL: https://agupubs.onlinelibrary.wiley.com/doi/abs/10.1002/2015JC011254.

[93] Zhengyou Zhang. “A flexible new technique for camera calibration”. In: *IEEE Transactions on Pattern Analysis and Machine Intelligence* 22.11 (2000), pp. 1330–1334.

[94] Inc. The MathWorks. *Computer Vision Toolbox*. Natick, Massachusetts, United State, 2021. URL: https://uk.mathworks.com/help/vision/.

[95] J. Pagès and J. Salvi. “Coded light projection techniques for 3D reconstruction”. In: *J3eA* 4 (2005), p. 001.

[96] Heiko Hirschmüller. “Stereo processing by semiglobal matching and mutual information”. In: *IEEE Transactions on Pattern Analysis and Machine Intelligence* 30.2 (2008), pp. 328–341.

[97] Stephen Peterson. “Image Sharpness and Focussing the View Camera”. In: *PHOTO Techniques* (1996).

[98] Raymond A Serway and John W Jewett. *Physics for scientists and engineers*. eng. 6th ed. Belmont, Calif. ; London: Thomson/Brooks/Cole, 2004.

[99] Phillip Reu. "All about speckles: Speckle Size Measurement". In: *Experimental Techniques* 38.6 (Nov. 2014), pp. 1–2. URL: https://doi.org/10.1111/ext.12110.

[100] Phillip Reu. "All about Speckles: Speckle Density". In: *Experimental Techniques* 39.3 (May 2015), pp. 1–2. URL: https://doi.org/10.1111/ext.12161.

[101] Sven Bossuyt. "Optimized Patterns for Digital Image Correlation". In: *Imaging Methods for Novel Materials and Challenging Applications, Volume 3*. Ed. by Helena Jin et al. New York, NY: Springer New York, 2013, pp. 239–248.

[102] Y L Dong and B Pan. "A Review of Speckle Pattern Fabrication and Assessment for Digital Image Correlation". In: *Experimental Mechanics* 57.8 (2017), pp. 1161–1181. URL: https://doi.org/10.1007/s11340-017-0283-1.

[103] *HandyScan 3D*. 2020. URL: https://www.creaform3d.com/en/portable-3d-scanner-handyscan-3d.

[104] N Vadgama et al. "Convergence of Spatially Resolved Particle Deposition". In: (2021), pp. 1–10.

[105] MathWorks. *Vectorization*. 2021. URL: https://uk.mathworks.com/help/matlab/matlab_prog/vectorization.html.

[106] Tom C. Currie. "A Physics-Based Model for Predicting Warm Surface Cool-down Resulting from Particle Impingement in Ice Crystal Icing". In: di (2020), pp. 1–18.

[107] Jiliang Ma, Daoyin Liu, and Xiaoping Chen. "Experimental study of oblique impact between dry spheres and liquid layers". In: *Physical Review E - Statistical, Nonlinear, and Soft Matter Physics* 88.3 (2013), pp. 1–9.

[108] S Wittig et al. "Velocity Profiles in Shear-Driven Liquid Films: LDV-Measurements". In: *Developments in Laser Techniques and Fluid Mechanics*. Ed. by R J Adrian et al. Berlin, Heidelberg: Springer Berlin Heidelberg, 1997, pp. 509–522.

[109] M. Thiruvengadam, B. F. Armaly, and J. A. Drallmeier. "Shear-driven liquid film in a duct". In: *Engineering Applications of Computational Fluid Mechanics* 3.4 (2009), pp. 506–513.

[110] Jonathan Connolly et al. "Digital Image Projection for 3D Ice Crystal Icing Accretion Measurements". In: *AIAA Aviation 2020* (2020).

[111] L G Nonato and Norberto Mangiavacchi. "a Mass-Conserving Smooth Method". In: *Small* XXIII.November (2004), pp. 1897–1909.

[112] Hesham El-Batsh and Hermann Haselbacher. "Effect of turbulence modeling on particle dispersion and deposition on compressor and turbine blade surfaces". PhD thesis. 2000.

[113] T. Hedde and D. Guffond. "ONERA three-dimensional icing model". In: *AIAA Journal* 33.6 (1995), pp. 1038–1045.

[114] Peter R. Forsyth, David R.H. Gillespie, and Matthew McGilvray. "Development and applications of a coupled particle deposition - Dynamic mesh morphing approach for the numerical simulation of gas turbine flows". In: *Journal of Engineering for Gas Turbines and Power* 140.2 (2018), pp. 1–15.

[115] Ren Ng. “Digital Light Field Photography”. PhD thesis. Stanford University, 2006.

[116] Christian Perwass and Lennart Wietzke. “Single lens 3D-camera with extended depth-of-field”. In: *Human Vision and Electronic Imaging XVII* 8291.February 2012 (2012), p. 829108.

[117] Martin Eberhart and Stefan Loehle. “Light-field imaging for plasma wind-tunnel application”. In: *Journal of Thermophysics and Heat Transfer* 33.2 (2019), pp. 407–415.

[118] Martin Eberhart et al. “Monitoring of icing on a compressor blade by plenoptic imaging in USQ wind tunnel”. In: IRS-19-IB0 (2019).

[119] P. Rosin and E. Rammler. “The laws governing the fineness of powdered coal”. In: *Journal of the Institute of Fuel* 7 (1933), pp. 29–36.

[120] Hakon Wadell. “Volume, Shape, and Roundness of Quartz Particles”. In: *The Journal of Geology* 43.3 (1935).

[121] David Leith. “Drag on nonspherical objects”. In: *Aerosol Science and Technology* 6.2 (1987).

[122] Xin Yang, Matthew McGilvray, and David Gillespie. “Numerical modeling and parametric study of the melting behavior of ice crystal particles”. In: *AIAA Journal* 59.11 (2021), pp. 4660–4668.

[123] German Vidaurre and John Hallett. “Particle impact and breakup in aircraft measurement”. In: *Journal of Atmospheric and Oceanic Technology* 26.5 (2009), pp. 972–983.

[124] Michiya Higa, Masahiko Arakawa, and Norikazu Maeno. “Size Dependence of Restitution Coefficients of Ice in Relation to Collision Strength”. In: *Icarus* 133.2 (1998).